

On the fracture toughness of polymeric nanocomposites: Comprehensive stochastic and numerical studies

CUMULATIVE DISSERTATION

Zur Erlangung des akademischen Grades

Doktor-Ingenieur (Dr.-Ing.)

an der Fakultät Bauingenieurwesen

der Bauhaus-Universität Weimar

vorgelegt von

Khader M. Hamdia

(interner Doktorand)

geboren am 26 März 1981

in Gaza, Palästina

Gutachter Prof. Dr.-Ing. Timon Rabczuk, Bauhaus-Universität Weimar
Prof. Dr. rer. nat. habil. Klaus Gürlebeck, Bauhaus-Universität Weimar
Prof. Dr. Roberto Brighenti, University of Parma, Italy

Weimar, 20.04.2018

For Eman

Acknowledgements

I am grateful to all people who have supported and helped me so much throughout this research. First of all, I would like to express my sincere gratitude to Prof. Timon Rabczuk for the valuable guidance, assistance, encouragement and for his patience. It has been a great pleasure working with him at Bauhaus-Universität Weimar.

I would also like to thank Dr. Mohammed A. Msekh, Dr. Mohammad Silani, and Dr. Nam Vu-Bac for providing precious materials used in this work. In addition, thanks go to my colleagues at Institute of Structural Mechanics, particularly Navid Valizadeh, S.S.Nanthakumar, and Yamen Khudari bek, for their help and friendly support. I thank Frau. Rosemarie Mayer and Frau. Marlies Terber for helping in several circumstances.

I would like to acknowledge the financial support provided by the International Research Staff Exchange Scheme (IRSES) - Marie Curie Action -MULTIFRAC, the European Research Council-Consolidator Grant (ERC-CoG) under the grant “Computational Modeling and Design of Lithium-ion Batteries (COMBAT)”, and the Deutsche Forschungsgemeinschaft (DFG).

Last but not the least, I wish to express my deepest gratitude to my family. Without their support, I would not be able to accomplish and fulfill my dreams

Abstract

Polymeric nanocomposites (PNCs) are considered for numerous nanotechnology such as: nano-biotechnology, nano-systems, nanoelectronics, and nano-structured materials. Commonly, they are formed by polymer (epoxy) matrix reinforced with a nanosized filler. The addition of rigid nanofillers to the epoxy matrix has offered great improvements in the fracture toughness without sacrificing other important thermo-mechanical properties. The physics of the fracture in PNCs is rather complicated and is influenced by different parameters. The presence of uncertainty in the predicted output is expected as a result of stochastic variance in the factors affecting the fracture mechanism. Consequently, evaluating the improved fracture toughness in PNCs is a challenging problem.

Artificial neural network (ANN) and adaptive neuro-fuzzy inference system (ANFIS) have been employed to predict the fracture energy of polymer/particle nanocomposites. The ANN and ANFIS models were constructed, trained, and tested based on a collection of 115 experimental datasets gathered from the literature. The performance evaluation indices of the developed ANN and ANFIS showed relatively small error, with high coefficients of determination (R^2), and low root mean square error and mean absolute percentage error.

In the framework for uncertainty quantification of PNCs, a sensitivity analysis (SA) has been conducted to examine the influence of uncertain input parameters on the fracture toughness of polymer/clay nanocomposites (PNCs). The phase-field approach is employed to predict the macroscopic properties of the composite considering six uncertain input parameters. The efficiency, robustness, and repeatability are compared and evaluated comprehensively for five different SA methods.

The Bayesian method is applied to develop a methodology in order to evaluate the performance of different analytical models used in predicting the fracture toughness of polymeric particles nanocomposites. The developed method have considered the model and parameters uncertainties based on different reference data (experimental measurements) gained from the literature. Three analytical models differing in theory and assumptions were examined. The coefficients of variation of the model predictions to the measurements are calculated using the approximated optimal parameter sets. Then, the model selection probability is obtained with respect to the different reference data.

Stochastic finite element modeling is implemented to predict the fracture toughness of polymer/particle nanocomposites. For this purpose, 2D finite element model containing an epoxy matrix and rigid nanoparticles surrounded by an interphase zone is generated. The crack propagation is simulated by the cohesive segments method and phantom nodes. Considering the uncertainties in the input parameters, a polynomial chaos expansion (PCE) surrogate model is construed followed by a sensitivity analysis.

Contents

1. Summary	1
1.1. Motivation	1
1.2. Objectives and outline of the thesis	2
1.3. Literature review	5
1.3.1. Fracture Mechanics	5
1.3.2. Phase-field approach for fracture	6
1.3.3. Cohesive segments method and phantom nodes	7
1.3.4. Artificial neural networks	8
1.3.5. Adaptive neuro-fuzzy inference system	9
1.3.6. performance evaluation indices	10
1.3.7. Surrogate models	11
1.3.8. Polynomial chaos expansions	12
1.3.9. Sensitivity analysis	13
1.3.10. Bayesian method for model selection	19
1.4. State of the Art	21
1.4.1. Experimental studies	21
1.4.2. Analysis of toughening mechanisms in nanocomposites	23
1.4.3. Numerical methods to simulate nanocomposites material behaviour	25
1.4.4. Sensitivity analysis	28
1.5. Results and discussion	30
1.5.1. Predicting the fracture energy of polymer/particle nanocomposites using ANN and ANFIS	30
1.5.2. Uncertainty quantification of the fracture toughness of polymeric clay nanocomposites based on phase field modeling	34
1.5.3. Evaluating analytical models used for the prediction of the fracture energy of PNCs by Bayesian method	44

1.5.4. Stochastic model to predict the fracture toughness of particle reinforced polymeric nanocomposites	48
2. Predicting The Fracture Toughness of PNCs: A Stochastic Approach Based on ANN and ANFIS	53
2.1. Introduction	54
2.2. Database	56
2.3. Methods for Predicting Fracture Energy of PNCs	56
2.3.1. Huang and Kinloch	56
2.3.2. Linear Regression	58
2.3.3. Artificial neural networks	58
2.3.4. Adaptive neuro-fuzzy inference system	60
2.4. Results	63
2.4.1. Huang and Kinloch	64
2.4.2. Linear Regression Models	65
2.4.3. Artificial neural networks	65
2.4.4. Adaptive neuro-fuzzy inference system	66
2.4.5. Comparison of the various methods	67
2.5. Parametric Studies	67
2.5.1. Influence of the nanoparticles volume fraction	68
2.5.2. Influence of the nano particle diameter	69
2.5.3. Influence of the matrix fracture energy	69
2.6. Conclusion	69
3. Uncertainty quantification of the fracture properties of polymeric nanocomposites based on phase field modeling	71
3.1. Introduction	72
3.2. Phase-field model for predicting the fracture properties of PNCs	74
3.3. Methods	77
3.3.1. Uncertainty Analysis	77
3.3.2. Sensitivity analysis	77
3.3.3. Convergence	84
3.3.4. Uncertainty quantification	84
3.3.5. Surrogate models	84
3.4. Results	86
3.4.1. Simulation results of Phase-field model	86
3.4.2. Uncertainty Analysis	87

3.4.3. Sensitivity Analysis	89
3.4.4. Quantifying the uncertainty in the fracture toughness of PNCs	96
3.5. Conclusion	97
4. Fracture toughness of polymeric particle nanocomposites: Evaluation of Models performance using Bayesian method	99
4.1. Introduction	100
4.2. Models for predicting the fracture properties of PNCs	102
4.2.1. Huang and Kinloch	102
4.2.2. Williams	105
4.2.3. Quaresimin et al.	106
4.2.4. Discussion	107
4.3. Assessment of PNCs fracture models using Bayesian method	108
4.4. Conclusion	112
5. Stochastic analysis of the fracture toughness of polymeric nanoparticle composites using polynomial chaos expansions	115
5.1. Introduction	116
5.2. Modelling the fracture in the PNCs	118
5.2.1. Fracture Mechanics	118
5.2.2. Numerical simulation of PNC	118
5.3. Modelling the uncertainties in the input parameters	122
5.3.1. Polynomial chaos expansions	122
5.3.2. Sensitivity Analysis	128
5.4. Summary and conclusion	131
6. Sensitivity and uncertainty analysis for multiscale models of collagen bio-structure	135
6.1. Introduction	136
6.2. Materials and Methods	139
6.2.1. Output quantities of interest	141
6.3. Global sensitivity analysis	144
6.3.1. Sobol' method	145
6.3.2. PAWN method	148
6.4. Results and discussion	149
6.4.1. Sensitivity analysis	149
6.4.2. Uncertainty Quantification	154

6.5. Summary	156
7. Conclusions	157
7.1. Summary of findings	157
7.2. Future works	158
A.	161
A.1. Predicted fracture energy of PNCs using ANN and ANFIS: Training Data set	161
A.2. Predicted fracture energy of PNCs using ANN and ANFIS: Testing Data set	163
B.	165
B.1. Evaluation of Models using Bayesian method	165
C. Multiscale constitutive model of collagen fibers	169
C.1. Multiscale constitutive model of collagen fibers	169
Bibliography	173
Ehrenwörtliche Erklärung	194
Curriculum Vitae	195

Chapter 1

Summary

1.1. Motivation

From the past decades, the development of new materials has been the subject of interest for engineers and materials scientists. In this regard, polymeric nanocomposites (PNCs), class of the promising materials, have attracted the attention due to their light weight, low cost and simple fabrication. PNCs are considered for numerous nanotechnology applications such as: nano-biotechnology, nanosystems, nanoelectronics, and nano-structured materials. They are constituted by a combination of polymer (epoxy) matrix and reinforcing rigid filler in the nanoscale size. Three shapes of nanofillers are commonly used: nanoparticles, nanoplatelet (layered), and nanofibrous materials. Due to their inherent characteristic of high crosslink density, epoxy polymers are known to be a relatively brittle material with poor resistance to crack initiation and propagation (poor fracture toughness). The addition of rigid nanofillers to the epoxy matrix has offered great improvements in the toughness without sacrificing other important thermo-mechanical properties. The remarkable improvement in the properties of PNCs even at low loading may be attributed to the large surface area - to - volume ratio of the nanofillers that creates an extreme interfacial zone between the nanofiller and the surrounding matrix [1].

The physics of the fracture of PNCs is extremely complicated phenomenon and is influenced by different uncertain parameters. Consequently, evaluating the improved fracture toughness is a challenging problem. To this end, several experiments have been carried out.

Artificial intelligence techniques, such as artificial neural network (ANN) and adaptive

neuro-fuzzy inference system (ANFIS), have been recently introduced as data driven models. They have the ability to mimic the real-world behavior which can be here the experimental investigations, learn from examples, and identify the data pattern by means of mathematics and statistics methods. Considering the experimental works available in the literature, models such as ANN and ANFIS are still missing for studying the fracture in PNCs.

Unlike the experimental works, several analytical models differing in theory and assumptions have been proposed recently to measure the increase in fracture energy of PNCs. Among others Huang and Kinloch model [2], Williams model [3], and the model according Quaresimin et al. [4] are popular. A methodology to evaluate the quality of these models considering their uncertainties are not available. The uncertainties can be related to the model itself and/or its input parameters. The former might be caused by the simplifications, while the latter can be related to the number and the stochastic variance of the parameters. On the other hand, researchers have developed advanced numerical methods to get a better understanding of nanocomposite material behavior. Most of these methods, however, have focused on predicting thermal and mechanical properties. Few of them have been dedicated to the fracture behavior. As a result of the variance in the factors influencing the fracture, the presence of uncertainty in the predicted output is expected. In the light of this, there is an urgent need for a comprehensive study to measure the influence of the uncertainties in these input parameters. This leads to uncertainty quantification.

1.2. Objectives and outline of the thesis

The Objectives of the study are;

- Constructing artificial neural network (ANN) and adaptive neuro-fuzzy inference system (ANFIS) models to predict the fracture energy of PNCs based on experimental datasets gathered from the literature.
- Evaluating the performance of different analytical models used in predicting the enhanced fracture energy of polymer matrix reinforced by rigid nanoparticles.
- Developing numerical models to predict the fracture and crack propagation in PNCs.

1.2 Objectives and outline of the thesis

- Developing methods for uncertainty quantification in the fracture toughness of polymer/clay nanocomposites through conducting sensitivity analysis that identify the most influence parameters on the uncertainty.

These goals are achieved in the following chapters as following; In Chapter 2, ANN and ANFIS are developed for predicting the fracture energy of PNCs without performing any experiments. The data used for construction the models are gathered from the literature. The performances of the developed models are evaluated based on three performance evaluation indices and are compared to the results of the Huang and Kinloch model [2] and the linear regression models. Finally, parametric studies are carried out to specify the influence of some of the input parameters on the desired output.

Chapter 3 presents a comprehensive sensitivity analysis to identify the influence of input parameters on the fracture toughness of PNCs predicted by a phase-field model. Different methods have been applied to examine the reliability of the implemented SA. These methods are: Standardized Regression Coefficients, Regionalized Sensitivity Analysis, Sobol' Method, EFAST method, and PAWN method. Moreover, an improvement to the PAWN method that reduces the computational cost is developed. The convergence of the sensitivity indices were achieved through the bootstrapping technique. The results of SA are exploited in conducting an uncertainty quantification.

In Chapter 4, the model and parameters uncertainties are taken into account in the assessment of the models used for the prediction of the fracture energy of PNCs. The chapter includes a methodology to evaluate three different analytical models by using the Bayesian method. In particular, Huang and Kinloch model [2], Williams model [3], and the model according Quaresimin et al. [4] are examined. The assessment is carried out based on different reference data (experimental measurements) gathered from the literature. Nevertheless, the same methodology can be applied to evaluate the three models based on other measurements. The prior probabilities are first estimated considering the uncertainties in the parameters. Then, the optimum parameter set which results in best fit of models prognoses is found, and in consequence the coefficient of variation of the models predictions to the measurements are estimated. Eventually, the model selection probability is calculated.

The aim of Chapter 5 is to present a methodology for stochastic modelling of the fracture in the polymer/particle nanocomposites accounting for the interphase zone. A polymer epoxy matrix reinforced by rigid nanoparticles is studied by a 2D finite element model. The phantom node method is employed to model the fracture. The uncertain

1.2 Objectives and outline of the thesis

input parameters considered in the stochastic model are: the volume fraction of the nanoparticles, the diameter of the nanoparticle, Young's modulus of the epoxy matrix, and its maximum allowable principal stress, the thickness, and Young's modulus of the interphase zone. By taking into account the uncertainties in these parameters, a polynomial chaos expansion surrogate model is constructed followed by a sensitivity analysis.

The dissertation has been prepared in the form of cumulative dissertation as follows:

- (i) Chapter 2 has been published in Computational Materials Science (Impact Factor: 2.086).
- (ii) Chapter 3 has been published in Composite Structures (Impact Factor: 3.853).
- (iii) Chapter 4 has been published in Composites Science and Technology (Impact Factor: 3.897).
- (iv) Chapter 5 has been published in International Journal of Fracture (Impact Factor: 1.642).
- (v) Chapter 6 has been submitted for publication (under review).

1.3. Literature review

A brief introduction and relevant literature review of different aspects of the research are provided in this section.

1.3.1. Fracture Mechanics

The fracture toughness is a material property used to measure the ability to fracture resistance of a material containing a crack. The stress intensity factor, K , and the energy release rate, G are common parameters in fracture mechanics. The former is utilized to predict the stress intensity near the crack tip. While the latter is the amount of the energy dissipated per unit of cracked area due to the formation of new surfaces. According to the energy criterion for fracture of Griffith [5], the crack is extended when the energy available for crack growth is sufficient to overcome the resistance of the material. On this basis, Irwin [6] has defined G as the rate of change in potential energy with respect to the crack area.

$$G = -\frac{d\Pi}{dA} \quad (1.1)$$

Fig. 1.1 depicts an infinite plate subjected to tensile stress and initially cracked by $2a$ in length crack. The energy release rate for this case is

$$G = \frac{\pi\sigma^2a}{E} \quad (1.2)$$

where E is the Young's modulus, and σ is the applied stress.

At the moment of fracture, K reaches a critical value called K_c , and known as the fracture toughness. For the mode-I loading, where the principal load tends to open the crack, K_{Ic} is given by

$$K_{Ic} = \frac{P_{max}}{B\sqrt{W}} f\left(\frac{a}{W}\right) \quad (1.3)$$

where P_{max} is the load at fracture, B and W are the thickness and the width of the specimen, a is the crack length, and $f(a/W)$ is a dimensionless function [7].

At this point, the critical energy release rate also reaches a critical value known as the

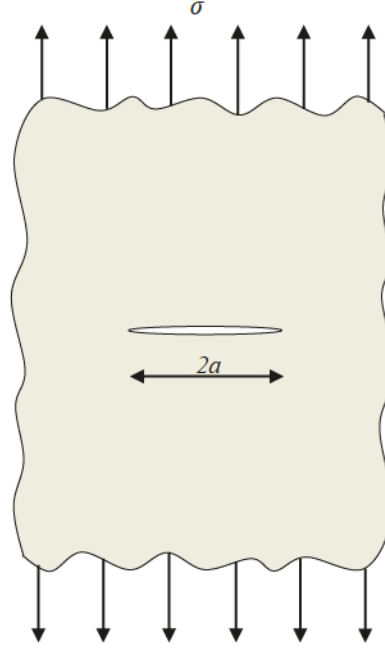


Figure 1.1.: An infinitely wide plate subjected to tensile stress with center crack.

fracture energy. It can be related to K_{Ic} by

$$G_{Ic} = \frac{K_{Ic}^2}{E'} \quad (1.4)$$

For plane stress conditions, $E' = E$, and for plane strain conditions $E' = E/(1 - \nu^2)$, with E being Young's modulus and ν being Poisson's ratio.

1.3.2. Phase-field approach for fracture

The Phase field method is a powerful approach for fracture firstly introduced by [8,9]. It has the ability to deal with crack nucleation, branching and coalesce [10,11]. The total potential energy is decomposed into the surface energy (creation of crack surfaces) and the bulk energy.

$$\Psi = \Psi^s + \Psi^b \quad (1.5)$$

1.3 Literature review

The surface energy in the phase-field approach is equal to the critical energy release rate, G_c , multiplied by the cross sectional area, A , of the crack surface:

$$\Psi^s = G_c \int_{\Omega} \gamma(\phi) d\Omega = G_c \int_A \int_{-\infty}^{\infty} \gamma(\phi) dx dA = G_c A \quad (1.6)$$

the crack surface density function γ is calculated by

$$\gamma(\phi) = \frac{1}{2} \left[\ell_0 \frac{\partial \phi}{\partial x_i} \frac{\partial \phi}{\partial x_i} + \frac{1}{\ell_0} \phi^2 \right], \quad (1.7)$$

where ϕ denotes the phase-field and ℓ_0 is a parameter controls the amount of the crack diffusion.

Interestingly, the phase-field does not require any description of the crack topology.

The bulk energy can be expressed in terms of the strain energy density for an isotropic linear elastic material, $\psi^e(\boldsymbol{\epsilon})$, and a stress degradation function, $g(\phi)$

$$\Psi^b = \int_{\Omega} g(\phi) \psi^e(\boldsymbol{\epsilon}) d\Omega \quad (1.8)$$

1.3.3. Cohesive segments method and phantom nodes

Despite the prominent efficiency of the finite element method (FEM) as a numerical approach in determining the approximate solution of partial differential equations, solving problems which involves presence of discontinuities in the design domain such as cracks remains a challenge. To align the element boundaries with the discontinuity, extremely refined meshes have to be generated. Nevertheless, near the crack tips, the mesh refinement is usually necessary in order to represent the asymptotic fields associated with the crack tips.

Differently, in the XFEM, the crack growth can be modelled without remeshing, where additional degrees of freedom associated to discontinuous shape functions is employed [12]. The Heaviside jump function in the displacement across the crack surfaces and the asymptotic crack tip enrichment function are the two types of enrichment functions considered in XFEM [13–15]. The asymptotic singularity functions is recommended only when modeling stationary cracks.

An alternative approach for modeling moving cracks within the framework of XFEM is the cohesive segments method and phantom nodes. The method is based on traction-separation cohesive behavior. The XFEM-based cohesive segments method can be used

to simulate crack initiation and propagation along an arbitrary, solution-dependent path. The phantom node method in [16, 17] presents special crack tip enrichments allows the crack tip being located inside the element which is important to model fracture in heterogeneous materials. When the crack propagates through an entire element, the crack might end exactly at the material interface which will yield to crack arrest.

A schematic of traction separation curve for modeling cohesive failure is shown in Fig. 1.2. The traction-separation model has been implemented in Abaqus package. It assumes initially linear elastic behavior followed by the initiation and evolution of damage.

1.3.4. Artificial neural networks

Artificial neural network (ANN) is a highly parallel system containing a large number of processing units called neurons or nodes [18]. These units are grouped together into three or more layers. The neighboring layers are connected by weights forming a large network. Inputs from previous layers are linked to a neuron by the corresponding weights and bias. Then, the weighted sums are applied to an activation function to determine the neuron output and consequently passed as inputs for the next layers. The sum at a neuron are calculated by [18]:

$$u_j = \sum_{i=1}^n w_{ji}x_i \quad (1.9)$$

where u_j is the linear combiner output of the j th neuron, n being the number of neurons in the preceding layer, x_i is an input signal, $w_{j1}, w_{j2} \dots, w_{jn}$ are the weights. The bias

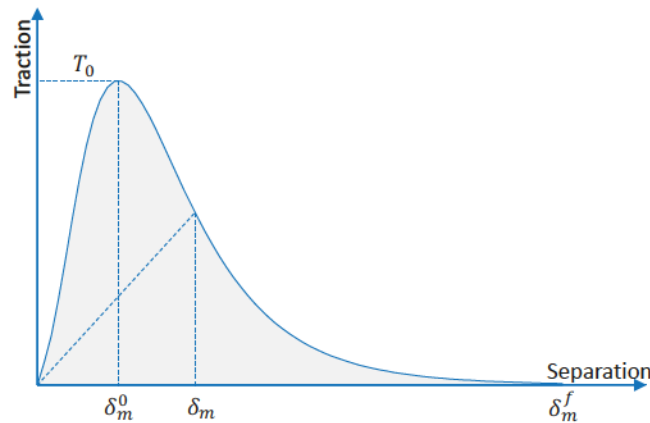


Figure 1.2.: Traction separation curve for modeling cohesive failure. T_0 and δ_m^0 refer respectively to the traction and separation at damage initiation, while δ_m^f is the separation at complete failure

1.3 Literature review

has the effect of applying affine transformation to u_j as

$$net_j = u_j + b_j \quad (1.10)$$

net_j is known here as the induced local field. Then, an activation function is applied to net_j to obtain the neuron output signal. More details about ANN can be found in the literature [18,19].

The multilayer feedforward networks illustrated in Fig. 1.3 with a back propagation algorithm [20] are commonly used. Its first layer receives information from input parameters and transmits it to one or several hidden layers, and then evaluates the predictions through the output layer. The number of input and output variables in the data defines the number of neurons in input and output layers, respectively.

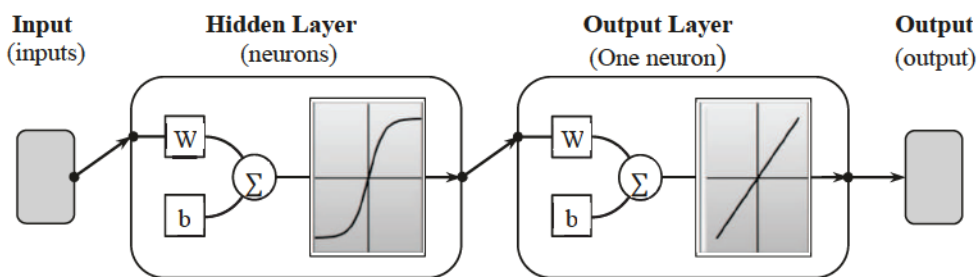


Figure 1.3.: ANN multilayer feedforward networks.

1.3.5. Adaptive neuro-fuzzy inference system

Fuzzy logic (FL) allows partial belongings of an element to a set [21]. Instead of an element belonging to a set or not, the degree of membership, μ , which varies between 0 and 1, describes the partial belongings to a set numerically. Fuzzy inference system (FIS) has the ability to extrapolate the relation between a series of input to an output with the help of fuzzy logic. The process contains integrated and consecutive steps which start with defining the membership functions of fuzzy sets (fuzzification), creating the rules to include all possible relation between input and output, and then merging all the fuzzy rules by a fuzzy inference to produce the results which are finally defuzzified into crisp outputs [22, 23]. One of the commonly fuzzy logic approaches used to solve complex problems, is the Takagi-Sugeno fuzzy model [24], which is characterized by linear or constant terms in the consequent part of the if-then rules. Making use of the merits of FIS and ANN and based on the Sugeno FIS, the adaptive neuro-fuzzy inference system

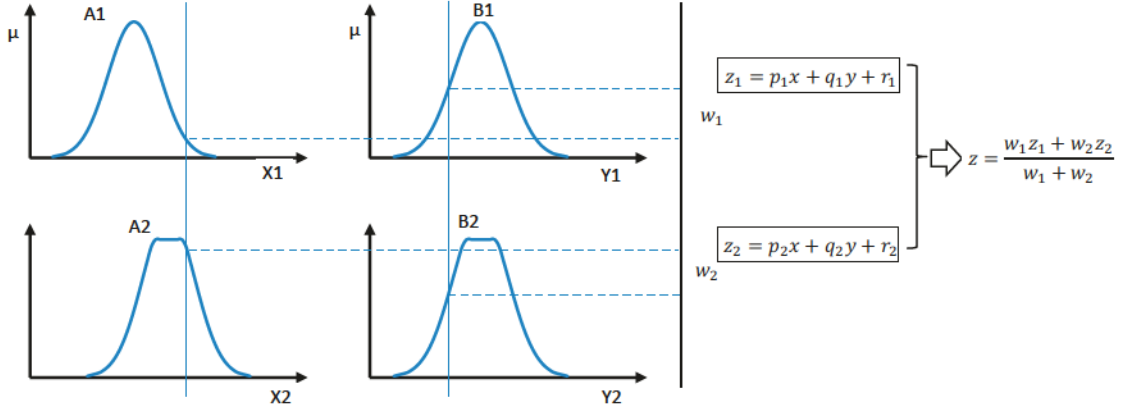


Figure 1.4.: Inference methodology of two input first-order Sugeno-type model with two rules

(ANFIS) have been developed by Jang [25]. Fig. 1.4 shows the inference methodology of a first-order Sugeno with two rules.

1.3.6. performance evaluation indices

Sections 1.3.4 and 1.3.5 presented two methods to build data driven models. The constructed models are evaluated by three evaluation indices: i) The coefficient of determination (R^2), ii) The root mean square error ($RMSE$), and iii) The mean absolute percentage error ($MAPE$). The R^2 is a number between zero and one showing how much the developed model represents the data. One reveals best fit while zero is the worst fit. The $RMSE$ is a positive number used to explain the difference between the actual and predicted data. The $MAPE$ quantifies the relative of overall fit taking values of 0.0% or greater. These statistical parameters are calculated by:

$$R^2 = 1 - \frac{SS_E}{SS_y} \quad (1.11)$$

$$RMSE = \sqrt{\frac{1}{N} SS_E} \quad (1.12)$$

$$MAPE = \frac{1}{N} \sum \frac{t_i - O_i}{t_i} \times 100 \quad (1.13)$$

1.3 Literature review

where t_i and O_i are the actual observation and predicted output, N is the number of datasets, $SS_y = \Sigma(t_i - \bar{t}_i)^2$ is the deviation of the observations from their mean and $SS_E = \Sigma(t_i - O_i)^2$ is the deviation of observation from their predicted value.

1.3.7. Surrogate models

Surrogate models, also known as Meta-models, are commonly used to represent the mechanical models in order to reduce the computational cost. To be built, the mechanical model needs to be evaluated multiple times considering the PDF of the input parameters. Hereafter, the popular polynomial regression method is exploited, where the mechanical model is approximated by linear (LR), quadratic (QR) and quadratic with mixed term (QMR) polynomial regression models with basic function $Z = [X_1, X_2, \dots, X_k, X_1^2, X_2^2, \dots, X_k^2, X_1X_2, \dots, X_{k-1}X_k]$.

Let $\hat{\mathbf{Y}}$ be the linear polynomial regression approximation of the response of the mechanical model \mathbf{Y} and let $\mathbf{X} = (X_1, X_2, \dots, X_k)$ be the input parameters with the basic function $Z = [X_1, X_2, \dots, X_k]$. Then $\hat{\mathbf{Y}}$ can be expressed by

$$\hat{\mathbf{Y}} = \beta_0 + \sum_{i=1}^k \beta_i X_i + \mathbf{e} \quad (1.14)$$

where $\boldsymbol{\beta}$ is the regression coefficient vector and \mathbf{e} is the residual error term that is the difference between the actual values for mechanical model \mathbf{Y} and the values estimated by regression model $\hat{\mathbf{Y}}$. The vector $\hat{\boldsymbol{\beta}}$ is estimated by minimizing the sum of residual squares [26]:

$$\hat{\boldsymbol{\beta}} = \left[[\mathbf{X}]^T [\mathbf{X}] \right]^{-1} \left\{ [\mathbf{X}]^T [\mathbf{Y}] \right\} \quad (1.15)$$

The higher order regression approaches, i.e. QR and QMR are constructed in similar manner.

To describe how well the surrogate model can represents the mechanical model, the coefficient of determination (R^2) as in Eq. (1.11) with

$$SS_E = \left(\mathbf{Y} - \hat{\mathbf{Y}} \right)^T \left(\mathbf{Y} - \hat{\mathbf{Y}} \right); \quad SS_y = \left(\mathbf{Y} - \bar{Y} \right)^T \left(\mathbf{Y} - \bar{Y} \right) \quad (1.16)$$

where \bar{Y} is the the mean value of \mathbf{Y} .

The closer R^2 to one, the better the surrogate model performance. To account for the number of training points, N , as well the number of regression coefficients (k_R), the

adjusted coefficient of determination (R_{adj}^2) is presented

$$R_{adj}^2 = 1 - \frac{N-1}{N-k_R} (1 - R^2) \quad (1.17)$$

If N is significantly larger than k_R , both coefficients will be equal. Once built with accepted R^2 , surrogate models are exploited to perform the SA instead of the mechanical model.

1.3.8. Polynomial chaos expansions

The polynomial chaos expansion (PCE) is an effective stochastic method that can be as a surrogate model. In addition to the ability of the PCE in approximating the response, the randomness in the output is concealed in the expansion coefficients by taking into account the uncertainties in the inputs. According to Ghanem and Spanos [27], Y can be expanded by a spectral expansion using orthogonal polynomials as

$$Y = \sum_{j=0}^{\infty} \beta_j \Psi_j(\boldsymbol{\xi}) \quad (1.18)$$

where $\boldsymbol{\xi}$ is the vector of independent standard normal (Gaussian) random variables, Ψ_j 's are the multivariate Hermite polynomials of order j , and β_j 's are the PCE deterministic coefficients. This decomposition was extended later to distributions other than the Gaussian using orthogonal polynomial basis functions of the Wiener-Askey scheme [28]. The generalized multivariate polynomial, Ψ_j , is obtained by the tensor product of the corresponding univariate polynomials.

$$\Psi_j = \prod_{i=1}^k \psi_{j_i}(\xi_i) \quad (1.19)$$

$\psi_{j_i}(\xi_i)$ being the univariate polynomial of the variable i , and k being the number of independent variables.

The infinite expansion in Eq. (1.18) can be truncated to a polynomial of order n

$$\hat{Y} \approx \sum_{j=0}^{P-1} \beta_j \Psi_j(\boldsymbol{\xi}) \quad (1.20)$$

1.3 Literature review

Hence, the number of unknown deterministic coefficients, P , for k random variables is

$$P = \frac{(k+n)!}{(k!n!)} \quad (1.21)$$

1.3.9. Sensitivity analysis

Sensitivity analysis (SA) is performed to define the influence of the input parameters on the uncertainty of the outputs. Local SA methods study the variation in the output by varying one input parameter while holding other parameters fixed. Contrary, in global SA, the influence of a parameter is defined by varying all the parameters at the same time [29]. In this research global SA methods are implemented. In each method, the model output \mathbf{Y} is expressed as $\mathbf{Y} = f(X_i)$.

The design of experiment was selected by the Latin Hypercube Sampling (LHS) [30], which is an improved sampling strategy that enables a reliable approximation of the stochastic properties even for a small number of samples. The base of the method is the subdivision of the design space of a variable X_i into N classes D_m of equal probability:

$$P[X_i \in D_m]; \quad i = 1, \dots, k; \quad m = 1, \dots, N \quad (1.22)$$

where N and k are the number of samples and the number of input parameters, respectively.

The SA can qualitative screening or quantitative. Variance based methods are based on variance decomposition of the output, while density-based methods are related to the distribution of the model output rather than its variance. The following sections discuss the methods that were employed in this research.

1.3.9.1. Sobol' Method

The Sobol' method is one of the most commonly used global SA approaches that is based on variance decomposition of the output. Given an integrable function f defined on the k -dimensional unit hypercube, the Sobol' functional decomposition [31] is

$$f = f_0 + \sum f_i + \sum_{i=0} \sum_{j=i+1} f_{ij} + \dots + f_{12\dots k} \quad (1.23)$$

The expansion has 2^k terms each of which is a square integrable function of the factors in its index only. Provided that each term has a zero mean value, the summands in the decomposition are orthogonal to each other and the Sobol' decomposition is unique.

The total output of the output can be decomposed as:

$$V = \sum_{i=1}^k V_i + \sum_{i=1}^k \sum_{j=i+1}^k V_{ij} + \dots + V_{12\dots k} \quad (1.24)$$

The Sobol's indices can be obtained through dividing both sides of Eq. (1.24) by V

$$\sum_{i=1}^k S_i + \sum_{i=1}^k \sum_{j=i+1}^k S_{ij} + \dots + S_{12\dots k} = 1 \quad (1.25)$$

The first-order sensitivity index (S_i) measures the part of the variance of the model output due to the input X_i . It is also known as the main effect of the parameters X_i . While the higher order indices (e.g. S_{ij} , which is known as the second-order index), measure the joint effect of the inputs X_i and X_j . S_i is defined as

$$S_i = \frac{V[E(\mathbf{Y}|X_i)]}{V(\mathbf{Y})} \quad (1.26)$$

with $V[E(\mathbf{Y}|X_i)]$ being the variance of the conditional expected value of \mathbf{Y} with respect to X_i and $V(\mathbf{Y})$ is the unconditional variance of \mathbf{Y} .

Accounting for the first-order effect of the input X_i added to all of its higher-order effects due to interactions with other parameters, the total effect sensitivity index (S_{Ti}) is given by

$$S_{Ti} = \frac{E[V(\mathbf{Y}|X_{\sim i})]}{V(\mathbf{Y})} = 1 - \frac{V[E(\mathbf{Y}|X_{\sim i})]}{V(\mathbf{Y})} \quad (1.27)$$

where $X_{\sim i}$ denotes all the input parameters but X_i [29]. The total effect index S_{Ti} is used to estimate how much the variation in the input parameters X_i contributes to the variation in the output. In other words, it is equal to the total value of the first-order term in addition to all high-order terms.

$$S_{Ti} = S_i + S_{i,\sim i} = 1 - S_{\sim i} \quad (1.28)$$

The difference between S_{Ti} and S_i represents a measure of how much X_i interacts with other input parameters.

In total, there are $2^k - 1$ Sobol's indices that required model evaluations (computational cost) of $\mathcal{O}(N2^k)$. This cost can be reduced to $\mathcal{O}(N(k+2))$ by considering the first order and the total indices only [32].

1.3 Literature review

1.3.9.2. PCE-based Sobol' indices

The expansion coefficients of the PCE surrogate model can be utilized to calculate analytically the variance-based Sobol' sensitivity indices [33, 34]. Clearly, the Sobol' decomposition is equivalent to the polynomial chaos expansions in Eq. (1.18). As all the terms of the expansion are orthogonal orthogonal polynomials, the total variance of the response can be approximated by

$$\widehat{V} = \sum_{j=1}^{P-1} \beta_j^2 \mathbf{E} [\Psi_j^2(\mathbf{X})] \quad (1.29)$$

where $\mathbf{E}[\cdot]$ is the mathematical expectation. In accordance to the dependency of each polynomial, the expansion coefficients are assembled and square summed and subsequently normalized in order to obtain the sensitivity indices. Doing so, the complete list of Sobol' indices can be obtained with almost no additional cost. The computational cost required for the calculation of the expansion coefficients is the major cost in this case.

1.3.9.3. Extended Fourier Amplitude Sensitivity Test (EFAST)

Classical Fourier amplitude sensitivity test (FAST) is a variance-based method for sensitivity analysis first presented by Cukier et al. [35]. It transforms a k -dimensional integral into a one-dimensional integral by using a set of parametric equations. Although the classical FAST is limited only to evaluate the first order sensitivity indices, recently an extension of FAST method (EFAST) was proposed to evaluate also the total-effect sensitivity index by [36]. For the input parameter X_i , the transformation (search) function is

$$X_i = F^{-1} \left(\frac{1}{2} + \frac{1}{\pi} \arcsin(\sin(\omega_i s + \varphi_i)) \right) \quad (1.30)$$

where F^{-1} is the inverse cumulative distribution function (CDF), ω_i is a set of integer frequencies, s is a parametric variable varying over the range $[-\pi, \pi]$ and φ_i is a random phase-shift chosen uniformly in the range of $(0, 2\pi)$. Through the derived search function, $f(X_1(s), X_2(s), \dots, X_k(s))$ is transformed into a periodic function $f(s)$. Whenever φ_i 's are positive integers, the period is 2π . Consequently $f(s)$ can be expanded into a Fourier series as

$$\mathbf{Y} = f(s) = \sum_{n=1}^{\infty} \{A_n \cos(ns) + B_n \sin(ns)\} \quad (1.31)$$

with A_n and B_n are the Fourier coefficients given by

$$\begin{aligned} A_n &= \frac{1}{2\pi} \int_{-\pi}^{\pi} f(s) \cos(ns) ds \\ B_n &= \frac{1}{2\pi} \int_{-\pi}^{\pi} f(s) \sin(ns) ds \end{aligned} \quad (1.32)$$

and $n = 1, \dots, (N_s - 1)/2$ with N_s is the size of the sample.

The variance of the model output is approximated by

$$V(\mathbf{Y}) = 2 \sum_{n=1}^{(N_s-1)/2} (A_n^2 + B_n^2) \quad (1.33)$$

To evaluate the spectrum A_n and B_n , a certain frequency, ω_i , for the i -th parameter and a different frequency $\omega_{\sim i}$ for the complementary set including all of the remaining parameters are assigned. Then, the partial variance $V_{\sim i}(\mathbf{Y})$ can be estimated for the fundamental integer frequency $\omega_{\sim i}$ and its higher harmonics $p\omega_{\sim i}$:

$$V_{\sim i}(\mathbf{Y}) = 2 \sum_{p=1}^M (A_{p\omega_{\sim i}}^2 + B_{p\omega_{\sim i}}^2) \quad (1.34)$$

The inference factor M adopted here is set to 4 (usually 4 or 6).

The partial variance $V_i(\mathbf{Y})$ is obtained in a similar way. The minimum sample size to be used is $N_s = N_r(2M\omega_{max} + 1)$, where N_r denotes the number of used curves and ω_{max} is the largest frequency among the set of ω_i frequencies. The first order S_i and the total effect index S_{T_i} are then calculated using Eqs. (1.26) and (1.27).

1.3.9.4. The PAWN method

PAWN is a simple approach proposed recently by Pianosi and Wagener [37] to derive a density-based sensitivity index considering the CDF of the output. The difference between the unconditional and the conditional CDF represents the sensitivity of the parameter X_i . This difference can be calculated by *Kolmogorov–Smirnov statistic* [38] which is denoted here by KS

$$KS = \max |F(\mathbf{Y}) - F(\mathbf{Y} | X_i)| \quad (1.35)$$

where $F(\mathbf{Y})$ and $F(\mathbf{Y} | X_i)$ are the unconditional and the conditional CDF approximated by a sample of size N_u and N_c , respectively. The unconditional sample is generated randomly in the space of the inputs; whereas, the conditioned one is achieved by varying

1.3 Literature review

all inputs while setting X_i fixed n times. The index T_i which can be the maximum or the median over all the fixed values for the parameter X_i is defined as:

$$T_i = \text{stat}[KS(X_i)] \quad (1.36)$$

Trial-and-error is proposed to select the value for n , N_u , and N_c , and $N_u + knN_c$ is the required total model runs (computational cost) [37].

1.3.9.5. Standardized Regression Coefficients

Standardized regression coefficients (SRC) is a screening method which is based on linear regression analysis. The output, $\mathbf{Y} = f(X_1, \dots, X_k)$ is computed using the mechanical model for the input parameters $\mathbf{X} = (X_1, \dots, X_k)$. Once the regression coefficient β_i is computed for the i -th input parameter, X_i , the value of SRC_i can be calculated as

$$SRC_i = \beta_i \frac{\sigma_i}{\sigma_y} \quad (1.37)$$

with σ_i and σ_y being the standard deviations of X_i and \mathbf{Y} , respectively.

1.3.9.6. Regionalized Sensitivity Analysis

The Regionalized Sensitivity Analysis (RSA) is mainly based on a Monte Carlo sampling of the parameter space. The sample is divided into acceptable and unacceptable subsets according to a given criterion for the output. Commonly, the terms of these two subsets in the literature are behavioral (B) and non-behavioral (\bar{B}) [29, 39].

For a set of N Monte Carlo simulations, two subsets are produced by applying a predefined condition which classify the model realizations into acceptable and unacceptable outputs. They are $(X|B)$ and $(X|\bar{B})$ of sizes N_b and N_n , where $N_b + N_n = N$. The probability density functions of each individual parameter in both subsets, $f_{N_b}(X_i|B)$ and $f_{N_n}(X_i|\bar{B})$, are compared. The parameter X_i is influential if it has two significantly different distributions [29]. Considering the null hypothesis that the two distributions are identical, the so called *Kolmogorov – Smirnov test statistic* (D_i) [38] is defined as the maximum vertical distance between the two cumulative distributions to measure

the statistical difference between the two subsets:

$$\begin{aligned}
 H_0 &: f_{N_b}(X_i|B) = f_{N_n}(X_i|\bar{B}) \\
 H_1 &: f_{N_b}(X_i|B) \neq f_{N_n}(X_i|\bar{B}) \\
 D_i &= \max |F_{N_b}(X_i|B) - F_{N_n}(X_i|\bar{B})|
 \end{aligned}
 \tag{1.38}$$

where $F_{N_b}(X_i|B)$ and $F_{N_n}(X_i|\bar{B})$ are the cumulative distribution functions for X_i in the behavioral and non-behavioral realizations. Their difference can be neither lower than zero nor higher than one, and hence, D_i has the range of [0-1]. Clearly, the D_i index depends on the given criterion, so the RSA can be considered as a screening rather than a quantitative method [40].

1.3.9.7. Summary

A summary of the previously described SA methods is listed in Table 1.1 including the comparison of their computation cost, the sensitivity category and the ability to deal with parameters interactions.

Table 1.1.: Characteristics summary of the implemented SA methods

Method	Computation Cost ^a	Screening/ Quantitative	Parameters interactions
Sobol'	$N(k + 2)$	Quantitative	Yes
Sobol' based on PCE	N_{PCE}	Quantitative	Yes
EFAST	$kN_r(2M\omega_{max} + 1)$	Quantitative	Yes
PAWN	$N_u + knN_c$	Quantitative	Yes
Standardized Regression Coefficients	N	Screening	No
Regionalized Sensitivity Analysis	N	Screening	No

^a N : base sample size.

N_{PCE} : number of regression points required to build PCE model.

k : number of input parameters.

M and ω_{max} : the inference factor and the largest frequency.

N_u : and N_c : sample sizes to estimate the unconditional and conditional CDF.

n : number of conditioning points.

1.3 Literature review

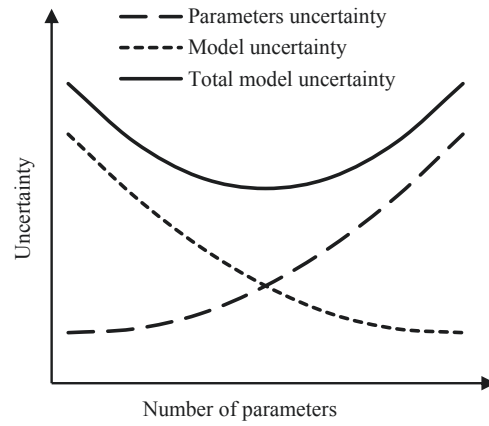


Figure 1.5.: Variation in model, parameter, and total uncertainties with respect to the number of parameters according to [41] .

1.3.10. Bayesian method for model selection

Generally, increasing the model complexity by introducing more factors is expected to result in better predictions and the subsequent decrease in the model uncertainty. However, the parameters uncertainties become more dominant in this case. The model with minimum total uncertainty is the most appropriate model, see Fig. 1.5 [41].

In recent years, Bayesian method has been introduced as an effective tool for evaluating models considering the model and parameters uncertainties based on measurements as reference data [42–45].

In this regard, the Model selection process refers to the problem of selecting one model from a list of candidate models based on available data. The Bayes' rule of statistics has motivated [46] to develop the Bayesian approach for model selection by incorporating the different sources of uncertainties based on response measurements (reference data), D . The model selection probability is represented by the conditional probability of the model M_i given the reference data D . It can be calculated by

$$P(M_i|D) = \frac{P(D|M_i)P(M_i)}{\sum_i P(D|M_i)P(M_i)} \quad (1.39)$$

where $P(M_i)$ is the prior probability of M_i which is based on the user's judgment on the initial plausibility of the models. The data-dependent term $P(D|M_i)$ is the evidence of M_i . It defines the probability that the measurements of reference data D being represented by the predictions of the model M_i . Making use of the theorem of total

probability, the evidence can be calculated by [46]

$$P(D|M_i) = \int P(D|X_i, M_i) P(X_i|M_i) dX_i \quad (1.40)$$

where $P(D|X_i, M_i)$ is the likelihood function and $P(X_i|M_i)$ is the prior probability of the input parameters.

The likelihood is the joint conditional probability of the reference data, D , given the input parameters, X_i . It measures how the model fit the data. A higher likelihood factor corresponds to better fit of M_i to D . The prior probability of the input parameters characterizes what is known about the parameters before any actual observation or modeling being considered. In the presence of measurements and model predictions, the prior probability is updated to posterior probability [47].

Assuming that the posterior probability of the parameters is approximated by a Gaussian distribution, the Laplace's method for asymptotic approximation can be applied to estimate the evidence as [48]

$$P(D|M_i) = P(D|\hat{X}_i, M_i) P(\hat{X}_i|M_i) \left[|H(\hat{X}_i)|/2\pi \right]^{-\frac{1}{2}} \quad (1.41)$$

where \hat{X}_i is the optimal parameter set that maximize the posterior probability and $H(\hat{X}_i)$ is the Hessian matrix of $-\ln [P(D|X_i, M_i) P(X_i|M_i)]$ with respect to X_i calculated at \hat{X}_i . The models are compared according to their model selection probability calculated in Eq. (1.39). The model with the largest probability is the optimum one.

The model uncertainty can be demonstrated by the differences between the predictions and the measurements. This uncertainty is measured by the coefficient of variation (CV).

$$CV_{ij} = \frac{1}{\bar{D}_j} \sqrt{\frac{1}{N_j - 1} \sum_{m=1}^{N_j} (D_m - Y_{im})^2} \quad (1.42)$$

where \bar{D}_j and N_j are the mean value and the number of the individual experiments of the j reference data, D_m is the the measured value, and Y_{im} is the corresponding predicted value of the model M_i .

1.4. State of the Art

1.4.1. Experimental studies

Several experimental studies have been carried out in order to study the fracture behavior of PNCs. The improvement in fracture energy was observed by [49–52] and others. Johnsen et al. [53] showed that the addition of silica nanoparticles led to a significant increase in the toughness of the composite. The mode I fracture energy increased from 100 J/m² for the pure epoxy polymer to 460 J/m² for the epoxy polymer modified with 13 vol% of nanosilica. In the experimental study of Hsieh et al. [54], four different epoxy polymers were investigated. They found that the increased toughness was related to structure/property relationships. Liu et al. [55] studied the toughness of hybrid composites filled with two types of nano-scale particles; silica and rubber. Although, it did not display any synergistic effect, they proposed that hybridization can achieve a good balance of elastic modulus and toughness properties. Liang and Pearson [56] and Dittanet and Pearson [57] studied the influence of different nanoparticle sizes, and they observed that the effect of nanoparticle size was negligible. By studying epoxy resin filled with a mixture of micro and nanometer-size silica particles, Dittanet and Pearson [58] concluded that the enhancement in toughness was higher when the volume fraction of nanoparticles was higher than the volume fraction of microparticles. Zhang et al. [59] reported that the performance of PNCs is dominated by a three-dimensional physical network of interphase material around silica nanoparticles constructed when the interparticle distance is close enough. Wetzel et al. [60] discussed the reinforcing effects of titanium dioxide and aluminium oxide which have average diameters of 300 nm and 13 nm, respectively, and the latter was considerably tougher. At different temperatures, Deng et al. [61] concluded that the nano-silica particles played different roles in enhancing the fracture toughness. It was not affected at 70 °C, clearly increased at 23 and 50 °C, and fewer enhancements were observed at lower temperatures (0 and –50 °C). Hence, they recommended further inspection. Later, Zhang et al. [62] showed that at higher temperature, the addition of nanosilica particles caused larger smooth zone on the fracture surfaces and thus the crack propagation rate was slowed. They further reported that the dominant toughening was local plastic deformation. Considering two epoxy systems, Ma et al. [63] demonstrated that the toughening mechanisms were referred to the formation and development of a thin dilatation zone and nanovoids, both of which were induced, constrained and thwarted by the stress fields of the silica nanoparticles. Zhao et al. [64] presented a comparable study showing the influence of particle-matrix

interface on toughening behavior. With a stronger interface, they noticed larger improvement. More recently, Zappalorto et al. [65] conducted a study on the effect of curing conditions on the mechanical and fracture properties of epoxy/silica nanocomposites. All nanomodified specimens exhibit a fracture toughness higher than that of the pure epoxy, however, post-cured specimens showed higher values of fracture resistance improvement. Zuo et al. [66] considered two thermoplastic copolymers reinforced with three different nano-particle types; two rod-like, cylindrical particle types and spherical particles. For each composite, tensile tests and quasi-static fracture toughness tests were performed at 23 °C. The fracture results were further examined. The nano-rods were more efficient at toughening than nano-spheres because the rod-like particles debond at a lower stress than the spheres and can therefore impart toughness more readily to the composite.

Though they have been widely used in material science, there have been few studies on the application of ANN and ANFIS in prediction and investigation of the behavior of PNCs. Fazilat et al. [67] applied both to predict the mechanical properties of glass fiber reinforced polymers. Polyamide 6 (PA6) with various contents of maleated ethylene- α -propylene-rubber (EPR-g-MA) and reinforced with short glass fiber (GF) composite was investigated. The yield strength, Izod impact strength and modulus were predicted via these methods. Mesbahi et al. [68] studied the performance prediction of a specific wear rate of epoxy composites with various composition content of polytetrafluoroethylen (PTFE), graphite, short carbon fibers (CF) and nano-titanium dioxide particles by means of ANN and ANFIS.

In the present research, the data collected from the literature are exploited to construct ANN and ANFIS models for predicting the fracture energy of spherical particle/polymer nanocomposites. In particular, 115 experimental data gathered from the literature [49–64] are utilized. The collected records were divided into two groups: training set and testing set containing 85 and 30 datasets, respectively. Meanwhile, five parameters are selected to establish the database: the volume fraction of the nano filler (V_f), the diameter of the nano particle (d_n), the fracture energy of the matrix (G_{Im}), the elastic modulus of matrix (E_m), and the yield strength of the matrix (σ_{ym}). These parameters form the input while the fracture energy of PNC (G_{Ic}) forms the output. The minimum, average, and maximum values of the input and the output parameters are listed in Table 1.2.

On the other hand, among the considerable amount of experimental works in the literature that considered clay/epoxy nanocomposites, the study of Wang et al. [69]

1.4 State of the Art

Table 1.2.: Minimum, average, and maximum values for the collected data

Parameters	Min.	Avg.	Max.
<i>Input Parameters</i>			
Volume fraction of the nano filler (%)	0.50	7.63	30
Diameter of the nano particle (nm)	12	39.40	170
Fracture energy of the matrix (J/m ²)	46.5	228.50	606
Elastic modulus of the matrix (GPa)	2.41	3.10	3.53
Yield strength of the matrix (MPa) ^a	757.1	83.13	111
<i>Output</i>			
Fracture energy of PNCs (J/m ²)	58.3	528.73	2156.65

^a Some of these data were not provided by the original literature. It has been assumed based on the property of similar matrices.

is exploited in this research for uncertainty quantification of clay PNCs (Chapter 3). In [69], higher exfoliated morphology of Epoxy/clay nanocomposites was prepared using slurry-compounding. Optical microscopy and transmission electron microscopy (TEM) was used to characterize the microstructures of the nanocomposites. The clay was found to be highly exfoliated and uniformly dispersed. Due to nanomodification, Young's modulus and fracture toughness were increased with different pattern. TEM and scanning electron microscopy (SEM), showed that the dominant microdeformation and fracture mechanisms in the epoxy/ S-clay nanocomposites were the initiation and development of microcracks.

1.4.2. Analysis of toughening mechanisms in nanocomposites

In the recent literature several models have been developed to analyze the toughening mechanisms in nanocomposites. A close form formula of energy dissipation due to the interfacial debonding between the particles and matrix was given by Chen et al. [70] with taking into account the effect of particle size. Lauke [71] studied the energy dissipation phenomena due to particle debonding, voiding and subsequent yielding of the polymer. He concluded that the increase of resistance to crack propagation with decreasing particle size is attributed to the increase in the specific debonding energy. Huang and Kinloch [2] evaluated the increased fracture energy of rubber-toughened epoxy polymers. Latter, the method has been modified for spherical rigid particle/polymer nanocomposites by [51, 53, 56]. The localized plastic shear banding and debonding of nanoparticles which enable plastic void growth of the epoxy matrix are the two dominating terms that taking part

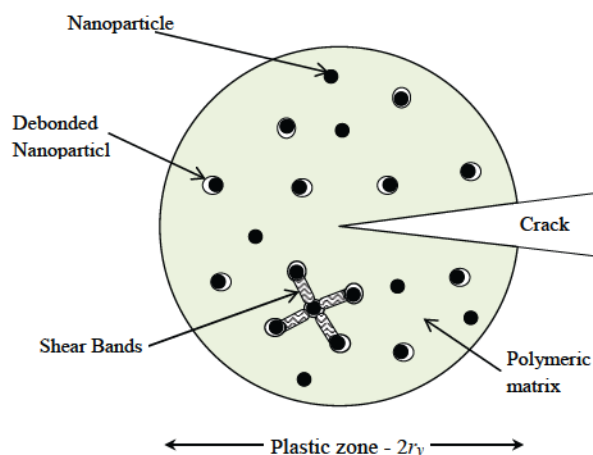


Figure 1.6.: PNCs Toughening mechanisms according to Huang and Kinloch [2] .

in the overall enhancement in the fracture toughness of PNCs, while rubber-bridging mechanism was disregarded. These two mechanisms are demonstrated in Fig. 1.6.

Williams [3] assumed that the energy absorbing mechanism is attributed to the growth of plastic voids around debonded or cavitared particles, which is stimulated by the debonding surface energy. At the first stage, the rigid particles is bonded to the surrounding matrix, and under tensile stress, the interfacial stress increases until debonding occur. This initiates the void growth in the matrix. He also found that the debonding energy is proportional to the particle radius. A large toughness increase was predicted for particle sizes in the nano range when good particle dispersion and sufficient ductility of the epoxy matrix could be achieved. Later, the analysis of Williams [3] for spherical nanoparticles has been extended to cylindrical rods and fibres [66, 72].

A multiscale methodology was adopted by Quaresimin et al. [4] to model the toughening mechanism of PNCs. The authors have considered an interphase zone surrounding the nanoparticle to account for the interactions between the nanoparticles and the matrix. Through its thickness, the interphase layer was assumed to be homogeneous and isotropic [73]. Fig. 1.7 displays the system considered at the nanosized scale. By studying the energy dissipation at the nanoscale, Quaresimin and co-workers [73–75] indicated that the overall fracture toughness of the nanocomposite is composed of three damaging mechanisms: (i) particle debonding, (ii) plastic yielding of nanovoids, and (iii) shear banding of the polymer. Their analysis was based on the energy balance concept around a single nanoparticle.

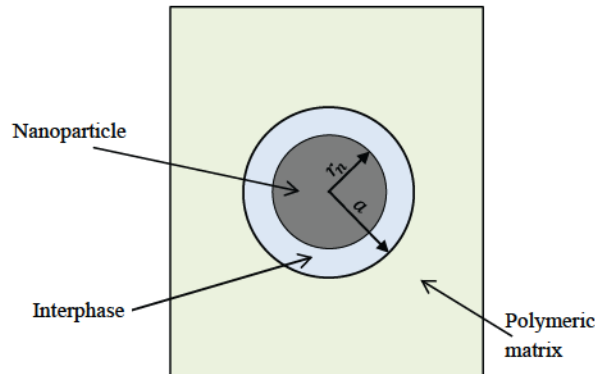


Figure 1.7.: 2D description of the nanoscale system analyzed by Quaresimin et al. [4].

In conclusion, although, the model of Huang and Kinloch [2] accounts for the main damaging mechanisms, it is based on some simplifying assumptions. The values for the volume fraction of voids, V_{fv} , and the volume fraction of debonded particles, V_{fp} , can be measured experimentally using for instance electron micrographs. The knowledge of the increased volume fraction of voids ($V_{fv} - V_{fp}$) is required to evaluate the energy contribution from void-growth mechanism. In turn, a new uncertain parameter to quantify the percentage of debonded particles (V_{dp}) is introduced in this study. The analyses of Williams [3] and Quaresimin et al. [4] were based on the assumption of the absence of particle-to-particle interaction. In turn, the effect of aggregation was ignored. It is widely acknowledged, however, that the nanofillers highly intend to agglomerate in nanocomposites. This may limit the applicability of these models to PNCs with low volume fraction of fillers.

1.4.3. Numerical methods to simulate nanocomposites material behaviour

A hierarchical procedure for obtaining the input parameter necessary to perform polymer-clay-nanocomposite simulations from molecular dynamics simulations was presented by Scocchi et al. [76]. On this basis, their approach included bridging the gap between mesoscopic and atomistic modeling. Mortazavi et al. [77] used a 3D finite element modeling in order to evaluate the interphase effects on the effective elastic modulus and thermal conductivity of nanocomposite reinforced by cylinders, spheres and thin discs nano fillers. A unit cell containing unidirectional nanotube reinforced polymer composites was created to study the influence of the interphase on the viscoelastic

properties of polymer nanocomposites by Qiao and Brinson [78]. Their results demonstrated that relaxation characteristics of nanocomposites were greatly dependent upon the volume of the interphase zone.

Differently and using Molecular Dynamics (MD) simulations, the elastic property and the extent of the interphase thickness were modelled by Odegard et al. [79] and Yu et al. [80]. Tsai et al. [81] presented a multiscale simulation approach to characterize the elastic property of carbon nanotubes (CNTs) reinforced polyimide. They evaluated the degree of non-bonded interaction using MD simulations. Chen et al. [82] considered the binding energy in the MD simulations to study the effect of interfaces on the mechanical properties in clay/epoxy nanocomposites.

Beside these studies, numerous numerical studies have been documented in the literature to simulate and to predict the nanocomposite material behaviour of; polymer/nanoclay [83–85], carbon nanotubes [86–89], and polymer/nanoparticles [90, 91].

In term of stochastic analysis, Vu-Bac et al. [92] studied the influence of the uncertainty in the chain length, the temperature, and the strain rate on the yield stress and the elastic modulus of glassy polyethylene based on united-atom MD simulations. Partial derivatives (local SA) and variance-based methods (global SA) were performed based on surrogate models of polynomial regression and moving least squares. The MD simulations was utilized also to study the effect of the single-walled carbon nanotube (SWCNT) radius, the temperature and the pulling velocity on the interfacial shear stress (ISS) of polymeric carbon nanotube composites [93]. Weibull distribution was the best characteristic distribution of the ISS. For computational efficiency, the SA was based on surrogate models; polynomial regression, moving least squares (MLS) and hybrid of quadratic polynomial and MLS regressions. Similarly, local SA by partial derivatives method, SA based on coefficients of determination, and variance based methods was conducted. Vu-Bac et al. [94] proposed a stochastic multiscale method to investigate the parameters influencing Young's modulus and Poisson's ratio of polymer loaded by carbon nanotube. The parameters at nano-, micro-, meso-, and macro-scales were connected by a hierarchical multiscale approach. The input parameters were; the length of the SWNT, its waviness, its agglomeration and its volume fraction. Different correlated parameters based global SA methods were carried out to evaluate the first-order and the total sensitivity indices. Silani et al. [95], investigated Young's modulus and the damage parameter of clay/epoxy nanocomposites using a stochastic numerical approach damage modelling at the nano-scale including the material properties and distribution of the inclusions and matrix. The overall properties of the nanocomposite were up scaled using

1.4 State of the Art

computational homogenisation. The connection between the matrix and the clay was modelled as a perfectly bonded interface. The key-input parameters influencing the Young's modulus was identified by a stochastic framework based on SA methods [96]. The input parameters included the clay volume fraction, clay aspect ratio, clay curvature, clay stiffness and epoxy stiffness. Later, Almasi et al. [97] refined the method carried out in [95] to analyse the effect of thickness and stiffness of the interphase zone. The results showed that the interphase layer reduced the stiffness of clay/epoxy nanocomposites particularly at higher clay fractions. These studies however, have modelled the PNCs as an elastic material.

Nevertheless, numerous computational methods for material failure have been developed in the past decades. They can be broadly classified into continuum based methods and discrete crack methods. Many popular discrete crack approaches are based on partition-of-unity (PU) enrichment. They modify the original approximation through enrichment functions and introduce additional degrees of freedom into the variational formulation in order to capture the jump in the displacement field. Among the most popular PU enrichment methods are the extended finite element method [98–100], the generalized finite element method [101–103], meshfree [104–109] and extended meshfree methods [110–112], the phantom node method [17, 113, 114], the numerical manifold method [115], and the extended isogeometric analysis (XIGA) [116–118]. An alternative to these PU enriched methods are remeshing procedures with extraneous crack path determination [119, 120] or edge repositioning [119, 121]. They basically align the crack boundary to a new mesh. Classical representatives of the continuum based models are viscous, gradient and nonlocal models [122–124]. An interesting alternative which is also based on continuum mechanics is the phase-field approach to fracture [8, 9]. The phase field is commonly discretised and the evolution of the phase field governed by a second [10] or fourth order [125] differential equation models the nucleation and propagation of cracks. Phase field models have been used in the context of FEM [11], local maximum entropy (LME) [10] and Isogeometric analysis (IGA) [126]. They have been extended to cohesive fracture [127], fracture in thin shells [10] and multi-physics problems [128, 129]. Discrete fracture approaches, in particular the popular partition of unity enriched discrete fracture methods, require a complex enrichment strategy for heterogeneous materials and complex fracture patterns such as PNCs. Phase field models seem due to their simplicity a more suitable alternative for modelling fracture in heterogeneous materials as they do not require a representation of the crack path.

Few numerical works have been dedicated to model the fracture behaviour in the PNCs. Silani et al. [130] measured experimentally and numerically the mechanical properties of clay/epoxy nanocomposites. They found that the increase in clay content reduced the ductility of the nanocomposite. The crack initiation and propagation was simulated using extended finite element method. The stress-strain curves obtained by numerical solution showed good agreement with experimental one. Zhao et al. [131] found that the cohesive energy and equilibrium distances of CNT/graphene, CNT/matrix and two crossing CNTs, which were modelled using continuum modeling of the van der Waals, were largely depended on their size, spacing and crossing angles. Arash et al. [132] applied Coarse-grained model to study the tensile fracture behavior of PMMA polymer matrix reinforced by SWCNTs. The effect of the weight fraction of CNT on the Young's modulus, yield strength, tensile strength and critical strain of the polymer composites were evaluated. They also examined the effect of the orientation and aspect ratio. Moreover, an effective approach for predicting J -integral from the load displacement curve of a single specimen was presented in [133], where, the effects of the CNT weight fraction and covalent cross-links between the polymer matrix and nanotubes, and polymer chains on the fracture behavior of the composites were investigated. Msekh et al. [134] analyzed the behaviour of fully exfoliated clay/epoxy nanocomposites using a phase field approach. The tensile strength, Young's modulus, and J -integral were extracted at different geometric distribution of clay platelets which came from varied clay weight contents and sizes. They reported that at the same boundary conditions, the change in the crack path was affected by the clay platelet distribution.

However, the physics of the fracture in PNCs is rather complicated problem. Various uncertain parameters affect the failure behaviour. None of the above mentioned studies took into account these uncertainties. In this study, this is investigated in Chapter 3 for clay/epoxy nanocomposites. Besides, the analysis of fracture of epoxy polymer loaded with spherical nanoparticle and considering the interphase zone is still missing. This is included in Chapter 5 of the current study.

1.4.4. Sensitivity analysis

Classical Fourier amplitude sensitivity test (FAST) is a variance-based method for sensitivity analysis first presented by Cukier et al. [35]. It transforms a k -dimensional integral into a one-dimensional integral by using a set of parametric equations. Although classical FAST is limited only to evaluate the first order sensitivity indices, recently an extension of FAST method (EFAST) was proposed to evaluate also the total-effect sensi-

1.4 State of the Art

tivity index by Saltelli et al. [36]. The Sobol' indices, another variance-based approach, are known to be good descriptors of the sensitivity of the output to the inputs. They are usually calculated by $\mathcal{O}(N2^k)$ Monte Carlo simulations for model of k parameters. It is unaffordable specially in computationally demanding models. Saltelli [32] developed a method to calculate the full set of first order and total effect indices at cost of $\mathcal{O}(N(k+2))$ with disregarding the second effect indices. He also proposed a more expensive method, cost= $\mathcal{O}(N(2k+2))$, that calculates the the first and total orders, plus estimates all indices of order 2. Later, Sudret [33] extracted the Sobol' indices analytically from the coefficients of the polynomial chaos expansions (PCE) surrogate models. The computation cost is thus transferred to calculating the PCE coefficients, the subsequent post-processing being almost costless. He also proposed a methodology to select an experimental design of minimal size considering non intrusive regression-based approach. More recently, sparse polynomial chaos expansions is introduced in [135, 136].

Differently, Pianosi and Wagener [37] proposed PAWN approach to define density-based sensitivity indices. PAWN sensitivity index measures the influence of the input as the variation in the cumulative distribution function (CDF) of the output when the uncertainty about that input is removed. The difference between the unconditional and the conditional CDF represents the sensitivity of the parameter X_i . This difference can be calculated by *Kolmogorov–Smirnov statistic*. It is computed at several conditioning values and the sensitivity index is a statistic (the maximum or the median) of the individual results. Due to the randomness in the design of experiment, however, a convergence check for the calculated sensitivity indices has to be conducted. Even for a small number of inputs, a large number of total model runs are required when increasing the number of conditional evaluations. On this basis, this study (Section 3.3.2.5) presents an improvement in the original PAWN method to reduce the computational cost.

1.5. Results and discussion

1.5.1. Predicting the fracture energy of polymer/particle nanocomposites using ANN and ANFIS

The fracture energy, G_{Ic} , of polymer/particle nanocomposites was predicted using the ANN and the ANFIS models. It was also compared to the results of the Huang and Kinloch [2] and Quadratic with mixed terms regression model (LR3). The coefficient of variation (COV) of the ratios of the actual experimental to the predicted values for each method is given in Table 1.3. The results reveal a good agreement between the experimental datasets and the corresponding predicted values using ANN and ANFIS.

For Huang and Kinloch [2], the obtained G_{Ic} values against the experimental datasets are presented in Fig. 1.8. At higher values, the predictions show higher scatter. The method produced wide variations on either side of the equality line. This is revealed by the results shown in Table 1.3, where the mean value of the ratios $G_{Icexp}/G_{Icpre.}$ equals 1.011 but its COV is 30.2 %.

Using 85 and 30 training and testing datasets as previously mentioned, the ANN model with five input parameters and one hidden layer with eight neurons was constructed to predict G_{Ic} . From Table 1.3, the mean of $G_{Icexp}/G_{Icpre.}$ was 1.011 with a COV of 12.6 %. Comparing the predicted values of the ANN model with the experimental results for training and testing datasets reveals that the ANN model was successful in learning the relationship between the input parameters and the output. Although the model was not trained for the testing dataset, it yielded good predictions (Figs. 1.9a and 1.9b).

Fig. 1.10 shows the predicted experimental data of the training and testing datasets using the ANFIS model. The output results were very close to the experimental data.

Table 1.3.: Mean and COV of the ratio of experimental to predicted G_{Ic} .

Method	Mean	COV(%)
Huang and Kinloch [2]	1.011	30.2
Quadratic with mixed terms regression model (LR3)	1.076	34.6
ANN	1.011	12.6
ANFIS	1.001	8.6

1.5 Results and discussion

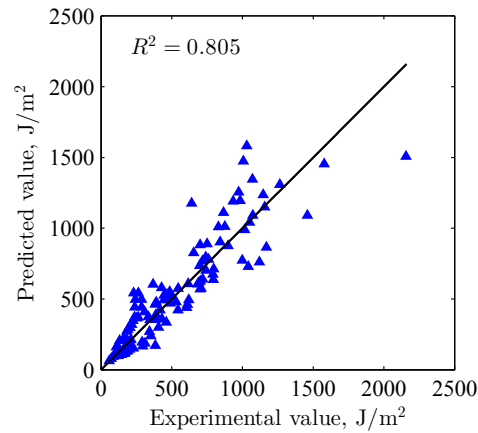


Figure 1.8.: Experimental versus predicted values for Huang and Kinloch [2] model.

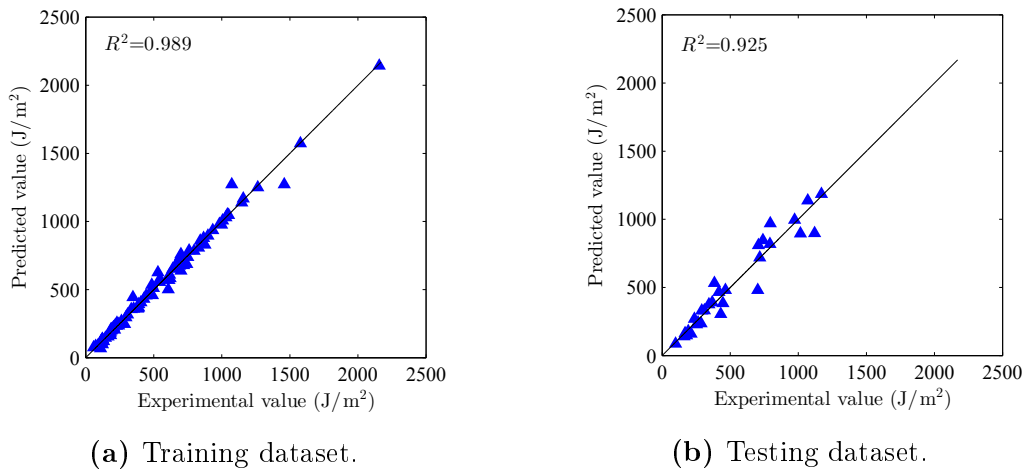


Figure 1.9.: Experimental versus predicted values for ANN model.

Again the testing dataset was not included in the training process but its results verify the robustness of the model. The mean of G_{Icexp}/G_{Icpre} was 1.001 with a COV of 8.6% (Table 1.3).

The predictions of the Huang and Kinloch, LR3, ANN, and ANFIS models were compared with the experimental data. The statistical values of R^2 , RMSE, and MAPE for the results obtained from the training and testing datasets are listed in Table 1.4. The ANN and ANFIS were considerably less scattered from experimental data than the Huang and Kinloch and LR3. This could be attributed to the complex and nonlinear nature of PNCs fracture toughness. For the testing dataset in terms of R^2 , it was 0.768 in the Huang and Kinloch model, 0.864 in the LR3, 0.925 in the ANN, and 0.937 in the ANFIS. The mean absolute percentage error (MAPE) was 12.88 and 12.38 % for ANN and ANFIS while it was 26.75 and 16.39 % for the other two methods. The results of

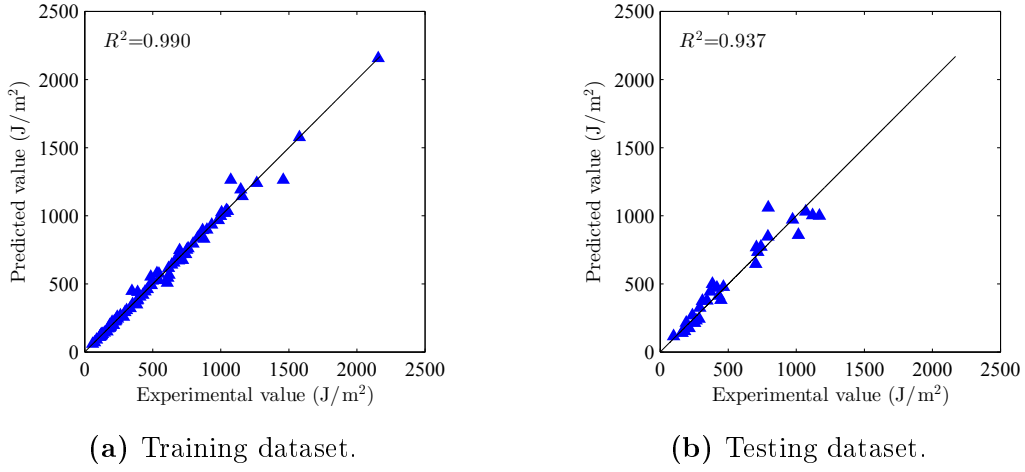


Figure 1.10.: Experimental versus predicted values for ANFIS model.

Table 1.4.: Comparison of the performance indices between modeling methods.

Method	Training Dataset			Testing Dataset		
	R^2	$RMSE$	$MAPE$	R^2	$RMSE$	$MAPE$
Huang and Kinloch	0.813	170.37	25.31	0.768	153.60	26.75
Quadratic with mixed terms regression model (LR3)	0.934	101.13	17.52	0.864	117.50	16.39
Artificial neural networks, ANN	0.989	41.12	6.03	0.925	87.31	12.88
Adaptive neuro-fuzzy inference system, ANFIS	0.990	39.18	3.61	0.937	80.04	12.38

these performance indices clearly indicate a much better performance of the ANN and ANFIS models over the Huang and Kinloch and LR3 models. Moreover, ANFIS shows slightly better results than ANN.

Making use of the constructed models, parametric studies investigating the relationship between the nanoparticles volume fraction, the diameter of the nanoparticle and the matrix fracture energy versus the predicted fracture energy are carried out. Firstly, to understand the effect of the nanoparticles volume fraction, all other input parameters are kept constant: $d_n = 20$ nm, $G_{Im} = 103$ J/m², $E_m = 2.96$ GPa, and $\sigma_{ym} = 61.1$ MPa, whereas V_f varies from 2.5 % to 13.4 %. The predicted and experimental values by Johnsen et al. [53] of G_{Ic} , normalized to the fracture energy of the matrix, G_{Im} , are plotted versus the volume fraction of nanoparticles in Fig. 1.11. Expectedly, the fracture energy of PNCs increases as the volume fraction increases. Moreover, a closer agreement to the experimental data is obtained by the ANFIS and the ANN.

Fig. 1.12 presents the relation between the diameter of the nano particle and the norma-

1.5 Results and discussion

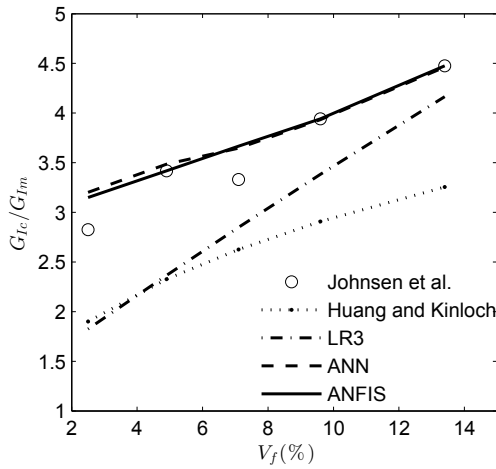


Figure 1.11.: The normalized fracture energy versus the volume fraction.

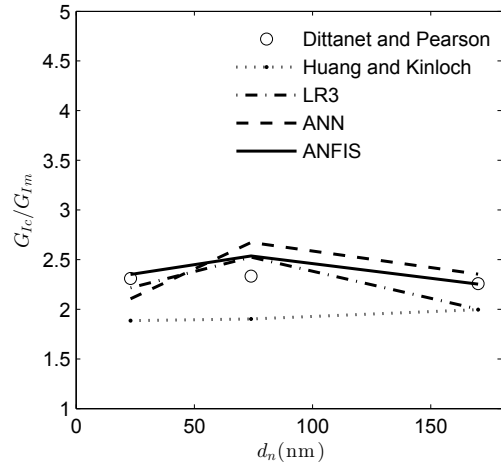


Figure 1.12.: The normalized fracture energy versus nano particle diameter.

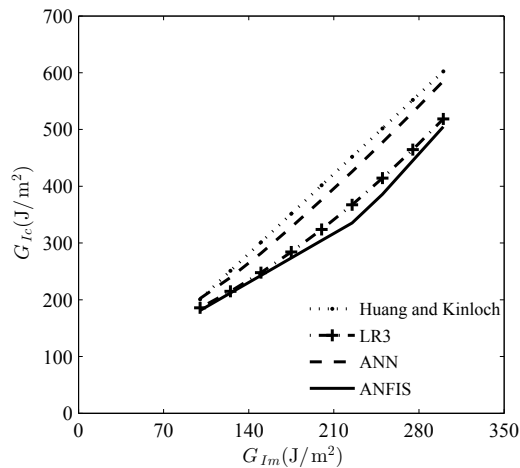


Figure 1.13.: Relationship between the fracture energy of PNCs and the fracture energy of epoxy matrix.

lized fracture energy of PNCs for the predicted and experimental results of Dittanet and Pearson [57]. The other parameters are: $V_f = 2.5\%$, $G_{Im} = 303 \text{ J/m}^2$, $E_m = 3.50 \text{ GPa}$, and $\sigma_{ym} = 85 \text{ MPa}$. The fracture energy of PNCs is slightly affected by the variation of the nano particle size. This is in agreement with the experimental results of [56–58].

The relation between the fracture energy of the epoxy matrix, and the predicted fracture energy of PNCs is investigated by changing the values of G_{Im} while keeping the other input parameters constant as: $V_f = 5.0\%$, $d_n = 20 \text{ nm}$, $E_m = 3.0 \text{ GPa}$, and $\sigma_{ym} = 85 \text{ MPa}$. The results are depicted in Fig. 1.13. As expected, the PNCs fracture energy increases by increasing the fracture energy of the matrix.

1.5.2. Uncertainty quantification of the fracture toughness of polymeric clay nanocomposites based on phase field modeling

1.5.2.1. Simulations of Phase-field model

The phase-field approach is implemented to predict the fracture toughness of polymer/clay nanocomposites. For example, the contour plots (i.e. the crack propagation) at different load steps are illustrated in Figs. 1.14a to 1.14c. The corresponding load displacement curve is shown in Fig. 1.14d. In this example, 20,512 elements were generated. The required CPU time was about 22,830 seconds (6.34 hours.) on a 4 x Twelve-Core AMD Opteron™ Processor of HP ProLiant DL585 G7 system. As an alternative approximation for the response of the mechanical model, the surrogate models were constructed based on LR, QR and QMR regression using six uncertain input parameter. Firstly, we generated the so-called *experimental design* $\mathbf{X} = \{\mathbf{X}^1, \dots, \mathbf{X}^N\}$ by choosing a set of regression points, N , in the probability space of the input parameters using Latin Hypercube Sampling (LHS) [30]. Then, for the generated samples, the fracture toughness were calculated using the mechanical model (phase-field model). The stochastic convergence of R^2 is assumed at a sample size of 10^2 (number of simulations). At this size, the corresponding estimated R^2 and R_{adj}^2 are shown in Table 1.5. The R^2 values indicate that the surrogate models are good approximations of the mechanical model response. Fig. 1.15 presents a scatter plots depicting the predicted outputs of the mechanical model against all the input parameters.

1.5.2.2. Uncertainty Analysis

The histogram for the data distribution of the mechanical model output and the assumed probability distribution functions are shown in Fig. 1.16. The mean value of the fracture toughness is 869.76 KPa. $\sqrt{\text{m}}$ and its coefficient of variation (COV) is 15.39% (Table 1.6). Three different distributions are assumed to represent K_{Ic} , i.e. Normal, Log-normal, and Weibull. The Weibull PDF shows the highest deviations.

Table 1.5.: R^2 and R_{adj}^2 values for the surrogate models.

Surrogate model	R^2	R_{adj}^2
Linear regression (LR)	0.872	0.826
Quadratic regression (QR)	0.897	0.860
Quadratic with mixed term (QMR)	0.934	0.910

1.5 Results and discussion

Table 1.6.: Mean, Standard deviation, and COV of the Output.

	Mean	Standard deviation	COV
K_{Ic} (KPa. \sqrt{m})	869.76	133.88	15.39 %

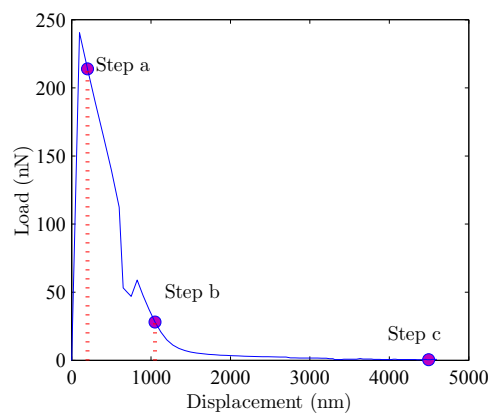
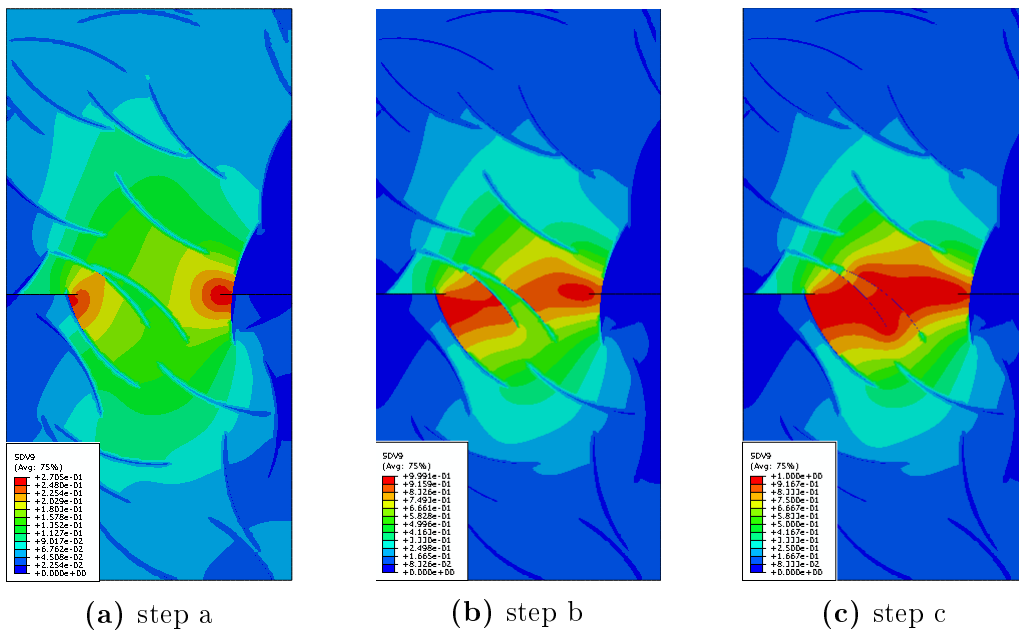


Figure 1.14.: Contour plots and load displacement curve of randomly selected sample (No. of elements=20,512, job time= 22,830 seconds). SDV refers to the phase field parameter (ϕ) with 0.0 and 1.0 indicate, respectively, to non damaged and totally damaged elements.

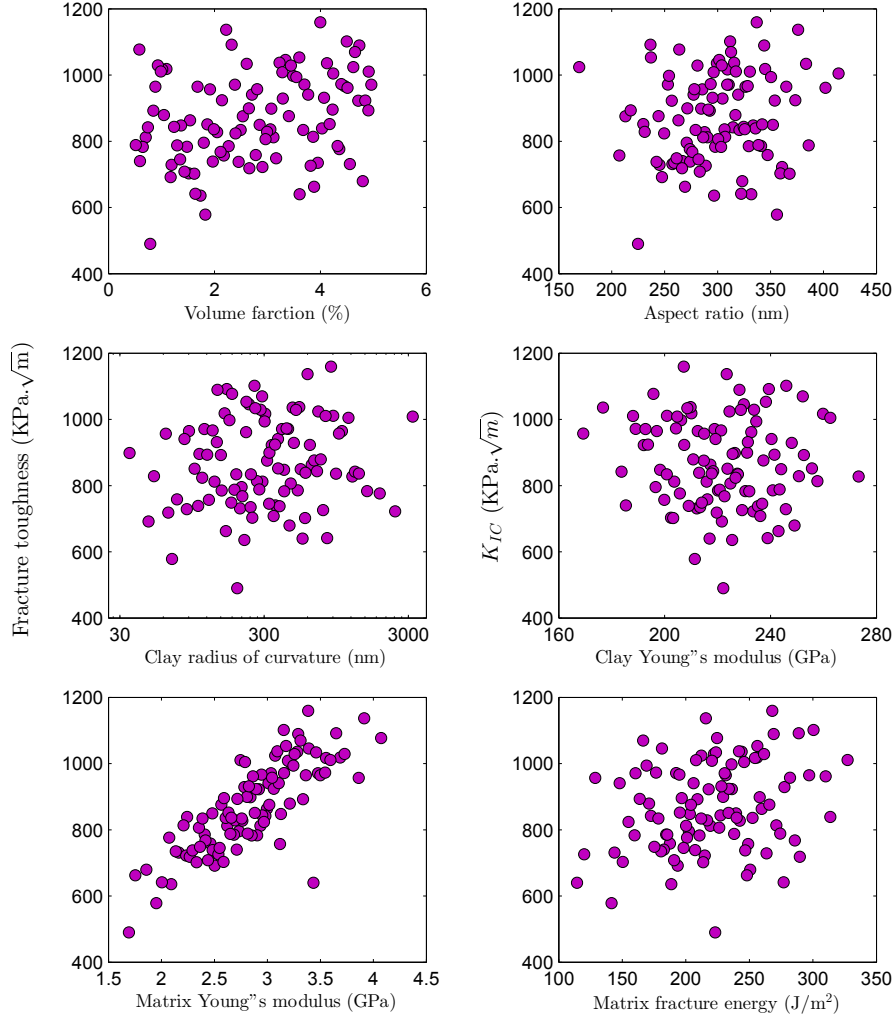


Figure 1.15.: Scatter plots of fracture toughness predicted by the mechanical model versus the input parameters

1.5.2.3. Sensitivity Analysis

In order to examine the reliability of the implemented SA, different methods have been applied. These methods are: Standardized Regression Coefficients (*SRCs*), Regionalized Sensitivity Analysis (RSA), Sobol' Method, EFAST method, and PAWN method. Moreover, we present an improvement to the PAWN method that reduces the computational cost. The convergence of the sensitivity indices were achieved through the bootstrapping technique.

As per Table 1.5, the highest R^2 is obtained by QDR surrogate model. Consequently, it will be utilized to approximate the output of the mechanical model in conducting the following SA methods.

1.5 Results and discussion

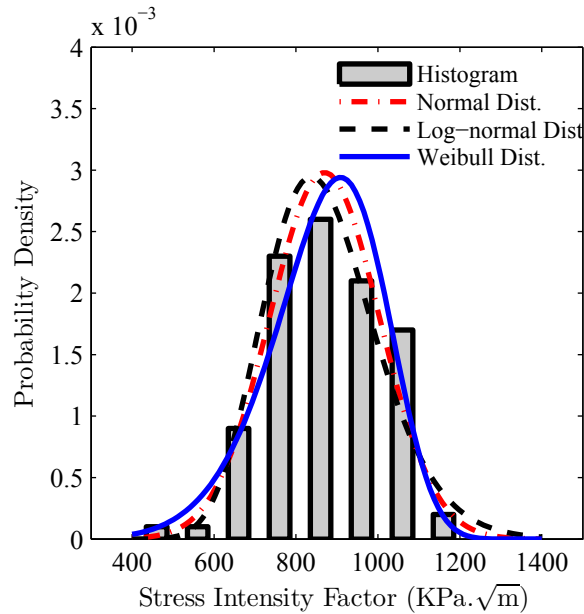


Figure 1.16.: Histogram of the mechanical output and PDFs of the assumed distributions.

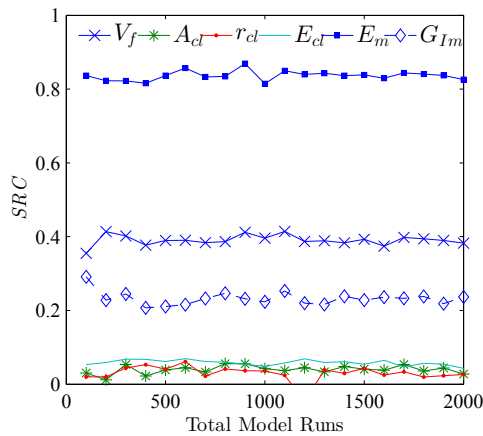


Figure 1.17.: Convergence of SRC method.

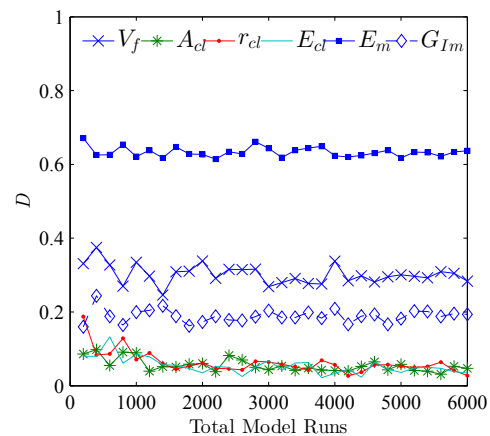


Figure 1.18.: Convergence of RSA method.

Different base sample sizes, N , have been compared as shown in Fig. 1.17 to evaluate $SRCs$. Clearly, 1,200 model run evaluated by the QDR surrogate model for each independent replica can be sufficient to obtain stable sensitivity indices. The most important parameter is the Young's modulus of the matrix (E_m), while the volume fraction of clay platelets (V_f) and the fracture energy of the matrix (G_{Im}) have moderate effects. The aspect ratio (A_{cl}), the radius of the curvature (r_{cl}), and the Young's modulus of the clay platelets (E_{cl}) have insignificant effects on the output.

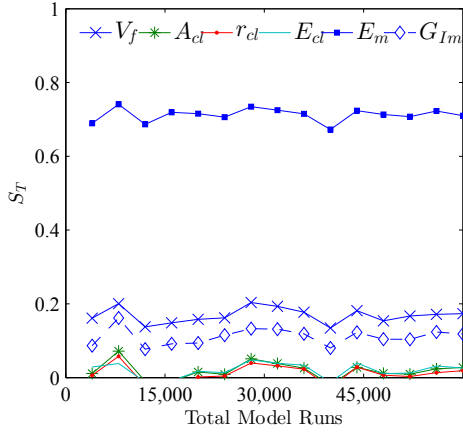


Figure 1.19.: Convergence of Sobol' method.

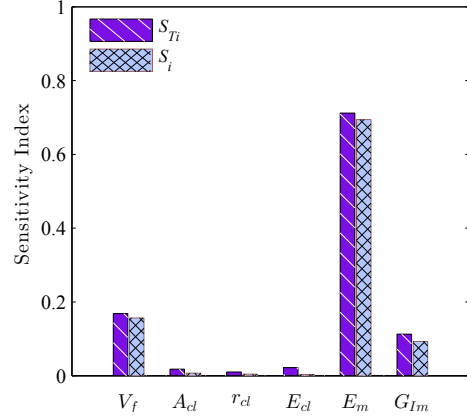


Figure 1.20.: First-order and total-effect sensitivity indices of Sobol' method.

Fig. 1.18 shows the convergence of the D test of RSA method. It is achieved for a sample size of 5,000. RSA also finds E_m as the most influential input parameter for the fracture toughness followed by V_f and G_{Im} . Also, A_{cl} , r_{cl} , and E_{cl} have negligible effects.

The total effect sensitivity indices (S_T) of Sobol' method converge at a base sample size around 5,500 which is equivalent to 44,000(=5,500(6+2)) total model runs for each independent replica (see Fig. 1.19). For non-influential factors, the negative signs appear due to numerical errors in the estimations. The total effect and first-order indices are given in Fig. 1.20. Table 1.7 contains the total and main effect indices and its 95% CIs. The ranking in the last column is based on the total effect, and apparently E_m outranks all other parameters, followed by V_f , and G_{Im} . There are no overlaps between their 95% CIs unlike the remaining insignificant parameters; A_{cl} , r_{cl} , and E_{cl} . The results of S_T were 0.712, 0.168, and 0.113 for E_m , V_f , and G_{Im} , respectively. Whereas the main effect of these parameters constitutes 94.4% (= 0.694+0.157+0.093) of the total variation of the output. The effects of the parameters interactions ($S_{Ti} - S_i$) are almost negligible indicating no interactions between input parameters.

For the EFAST method, we have selected $N_r = 10$ which makes the convergence more stable. Fig. 1.21 shows the convergence of S_T . Compared to Sobol' method, the total effects of the inputs can be estimated quite reliably for a smaller number of model runs. The convergence is achieved at 19,260 total model runs for maximum frequency, $\omega_{max} = 40$. The computed total and first-order indices after bootstrapping are included in Fig. 1.22 and Table 1.8.

1.5 Results and discussion

Table 1.7.: Sensitivity indices based on Sobol' method.

Input parameters	Total Effect		Main Effect		Rank
	S_{Ti}	95% CI	S_i	95% CI	
V_f	0.168	(0.165,0.172)	0.157	(0.155,0.158)	2
A_{cl}	0.018	(0.014,0.021)	0.007	(0.005,0.009)	5
r_{cl}	0.010	(0.007,0.014)	0.004	(0.002,0.006)	6
E_{cl}	0.022	(0.018,0.025)	0.003	(0.002,0.005)	4
E_m	0.712	(0.709,0.715)	0.694	(0.693,0.696)	1
G_{Im}	0.113	(0.109,0.116)	0.093	(0.091,0.094)	3

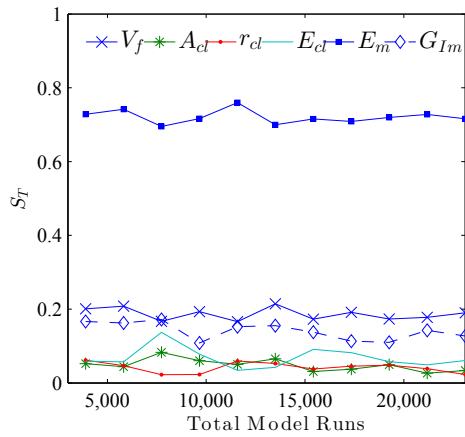


Figure 1.21.: Convergence of EFAST method.

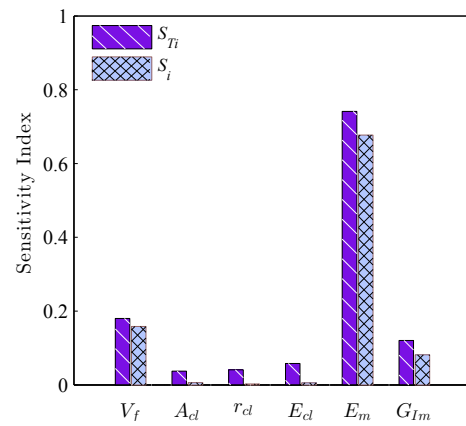


Figure 1.22.: First-order and total-effect sensitivity indices of EFAST method.

Table 1.8.: Sensitivity indices based on EFAST method.

Input parameters	Total Effect		Main Effect		Rank
	S_{Ti}	95% CI	S_i	95% CI	
V_f	0.180	(0.179,0.181)	0.158	(0.157,0.159)	2
A_{cl}	0.037	(0.037,0.038)	0.006	(0.006,0.006)	6
r_{cl}	0.041	(0.040,0.042)	0.003	(0.002,0.003)	5
E_{cl}	0.058	(0.057,0.059)	0.006	(0.006,0.006)	4
E_m	0.741	(0.740,0.743)	0.677	(0.675,0.679)	1
G_{Im}	0.121	(0.120,0.122)	0.081	(0.081,0.082)	3

In the PAWN method, the number of conditioning values, n , for each parameter is set to be 10, while N_u and N_c are both set equal to 150. Fig. 1.23 displays the

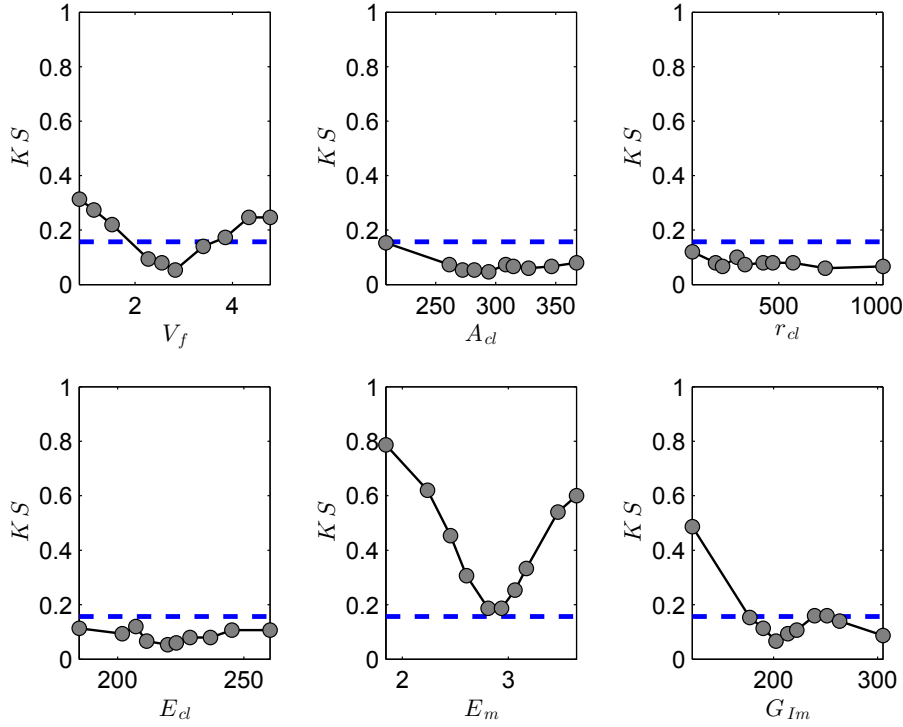


Figure 1.23.: *Kolmogorov – Smirnov statistic (KS)* at different conditioning values of X_i ($n = 10$).

Kolmogorov – Smirnov statistic, KS, for the 10 different conditioning values that were sampled from the space of variation for each of X_i . The dashed horizontal line at $KS = 0.157$ is the critical value of KS considering the confidence level $\alpha = 0.05$ [137]. All the values of KS for A_{cl} , r_{cl} , and E_{cl} are below the critical KS , which confirms that they are non-influential parameters.

Based on the median statistic, Fig. 1.24a displays the convergence of the PAWN indices. The ranking of the parameters are clear but the T index of E_m does not converge to a specific value. When considering the maximum statistic (Fig. 1.24b), the T indices highly fluctuate even for a large sample size.

The maximum KS occurs at the left margin for G_{Im} whereas it occurs at left and right margins for V_f and E_m ranges as shown in Fig. 1.23. Thus, the vector of the conditional values in our improved PAWN approach will be $\mathbf{X} = \{ 0.5, 200, 1000, 178, 1.96, 100 \}$. Fig. 1.24c displays the convergence of the T indices. Obviously, the T indices of the improved PAWN converge faster.

For $N = N_u = N_c = 1100$, the required model runs for both PAWN methods are equal 67,100, while the improved PAWN approach needs only 16,850 model runs. Table 1.9 includes the average sensitivity indices (T), the 95% CIs, and the rankings: E_m has

1.5 Results and discussion

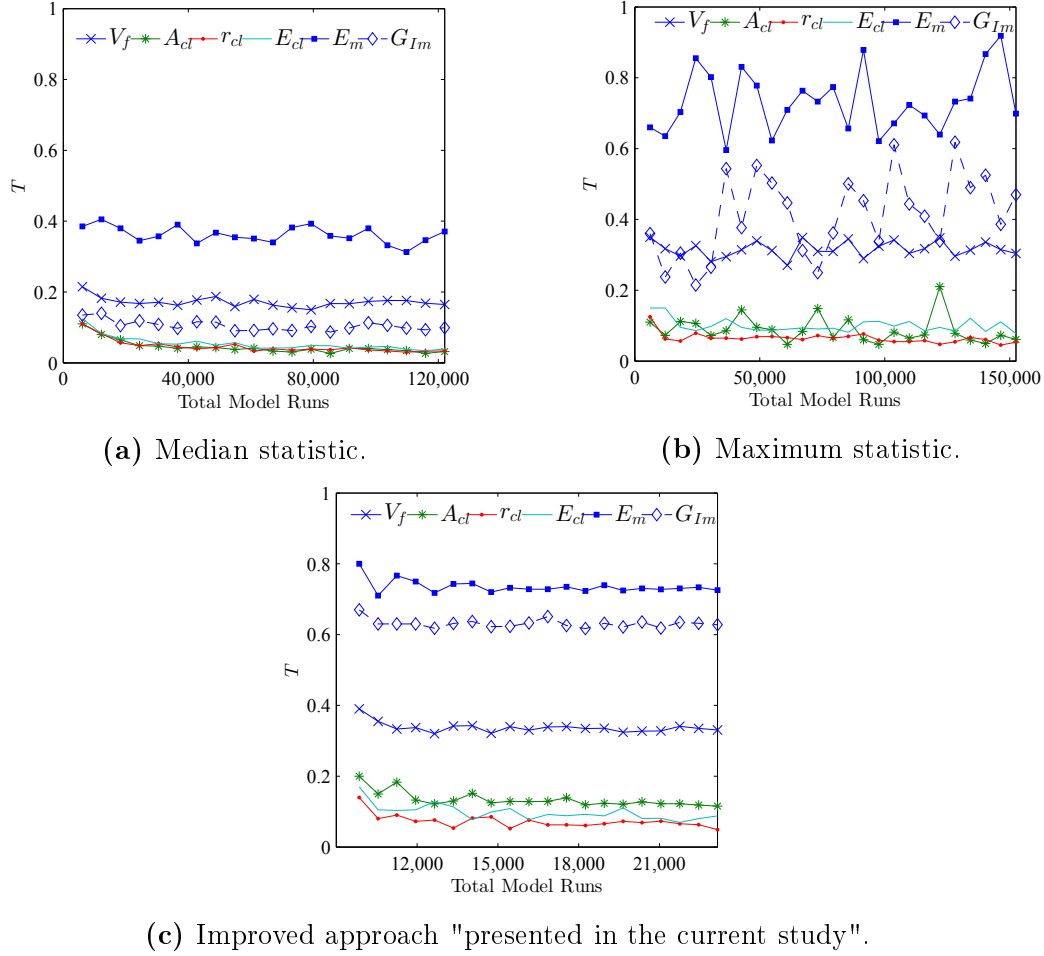


Figure 1.24.: Convergence of PAWN method.

the highest sensitivity index. Similar to the previous SA methods, V_f lies in the second position in ranking based on the median statistic, whereas it is in the third position based on the maximum statistic and improved approach. Also the ranking of the insignificant parameters changed.

Across the various applied SA methods, we can conclude that the matrix Young's modulus was the most influencing parameter followed by the clay platelets volume fraction and the matrix fracture energy. In summary:

- The SRCs and RSA methods qualitatively determined the significant input parameters with few model runs (1,200 and 5,00).
- At higher computational cost, the quantitative methods of Sobol' and EFAST measured the impact of main and total effect of the inputs on the variance of the model

Table 1.9.: Sensitivity indices based on PAWN method.

Input parameters	Median statistic		Maximum statistic		Improved approach		Rank ^a
	<i>T</i>	95% CI	<i>T</i>	95% CI	<i>T</i>	95% CI	
V_f	0.165	(0.165, 0.166)	0.321	(0.320,0.323)	0.336	(0.335,0.337)	3
A_{cl}	0.037	(0.037, 0.037)	0.092	(0.090,0.095)	0.127	(0.126,0.127)	4
r_{cl}	0.038	(0.038, 0.038)	0.071	(0.069,0.072)	0.065	(0.064,0.065)	6
E_{cl}	0.046	(0.046, 0.046)	0.105	(0.103,0.106)	0.094	(0.094,0.095)	5
E_m	0.354	(0.353, 0.355)	0.749	(0.744,0.754)	0.732	(0.732,0.733)	1
G_{Im}	0.100	(0.099, 0.100)	0.367	(0.358,0.375)	0.628	(0.628,0.629)	2

^aThe rank is based on the Total Improved approach

output. However, the Sobol' method required about two times model runs more than EFAST method.

- The required time for Sobol' method was about 5068.5 seconds (1.42 hours) considering the QMR surrogate model, which is much lower than the required time to run *one* mechanical model sample.
- The classical PAWN method that is based on median and maximum statistic required considerable cost, while the improved PAWN showed a faster convergence.
- The improved PAWN showed a faster convergence in comparison to the classical PAWN.
- Similar classification of the parameters importancy can be drawn as a general finding.

1.5.2.4. Quantifying the uncertainty in the fracture toughness of PNCs

The results of SA are exploited in conducting an uncertainty quantification. The input parameters are classified into two groups: important and non-important parameters. The first group includes: E_m , V_f , and G_{Im} , while the second includes: A_{cl} , r_{cl} , and E_{cl} . A Set $G1$ of size 1000 was randomly generated by LHS. Then Set $G2$ was formed with the same as Set $G1$ but the parameters E_m , V_f , and G_{Im} were fixed at 2.85 GPa, 2.75 %, and 220 J/m², respectively. Contrary, Set $G3$ was formed by fixing A_{cl} , r_{cl} , and E_{cl} at any point of their variation range, for example 300 nm, 500 nm, and 221.5 GPa. The scatter of the outputs of Set $G2$ and Set $G3$ against Set $G1$ are displayed in Fig. 1.25. When fixing parameters that are correctly classified as significant as in Set $G2$, the scatter shows a horizontal trend (Fig. 1.25a), whereas fixing the insignificant parameters

1.5 Results and discussion

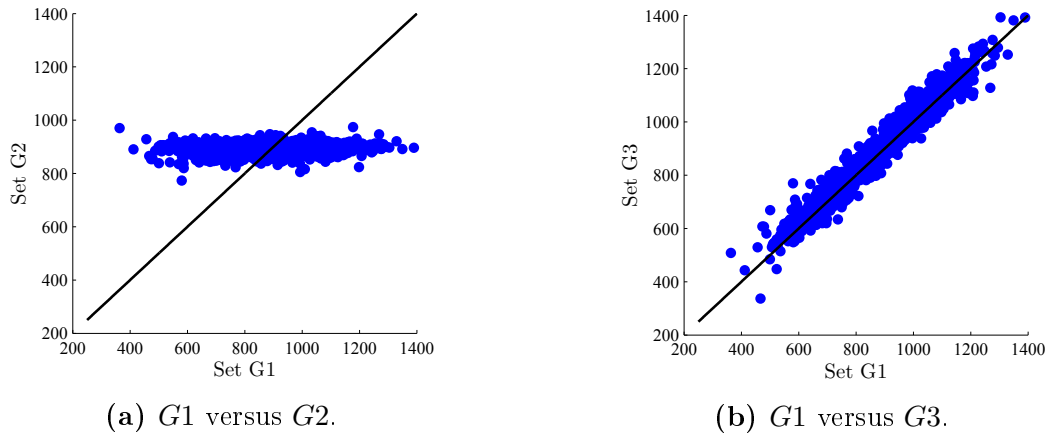


Figure 1.25.: Scatter plot of randomly generated Set, $G1$, versus fixed important parameters Set, $G2$, and non-important parameters, $G3$.

Table 1.10.: Standard deviation and COV of $G1$, $G2$, and $G3$.

Set	Standard deviation	COV
$G1$	146.54	16.82%
$G2$	17.60	1.97%
$G3$	143.70	16.34%

results in linear correlation as in Fig. 1.25b. To assess the loss in variability when fixing the parameters, Table 1.10 lists the standard deviation and COV of the three sets. The COV was considerably reduced from 16.82% for Set $G1$ to 1.97% for Set $G2$, but it remains almost the same in Set $G3$ (16.34%). Obviously, the SA methods used in this research were robust in classifying the parameters.

1.5.3. Evaluating analytical models used for the prediction of the fracture energy of PNCs by Bayesian method

As presented in Section 1.4.2, several models differing in theory and assumptions have been proposed to measure the increase in fracture energy of polymer/particle nanocomposites. The Bayesian method is used to evaluate the model quality of Huang and Kinloch model [2], Williams model [3], and the model according Quaresimin et al. [4]. Hereafter, they are abbreviated by M_1 , M_2 , and M_3 , respectively. These models have been selected due to their popularity and their applicability to different experimental studies. Moreover, they produce explicit predictions of the enhanced fracture energy of PNCs. The prior probabilities of these models is assumed to be equal, i.e. $P(M_1) = P(M_2) = P(M_3) = 1/3$. Regarding the different theory and mechanism assumed, each of them has its own input parameters in addition to the joint parameters. The definitions of the parameters and their stochastic variation are detailed described in Section 4.2. The parameters uncertainty is assumed to be characterized by uniform distribution. Different experimental measurements gathered from the literature [51–53, 55–57, 59, 60, 62, 65] are utilized as reference data. Thanks to the uniform distribution assumed for the input parameters, the prior probabilities of the model parameters, $P(X_i | M_i)$, are constant disregarding the value of the parameter. Considering this, the optimum parameter set which realized the best fit of the model predictions to the measurements are found. Table 1.11 shows the values of selected calculated optimal parameter set.

Interestingly, the incorporation of the parameter V_{dp} (the percentage of debonded particles) in M_1 has enhanced the model predictions to fit the measurements. By the finite-element analysis of [138], the value of the maximum stress concentration for the von Mises stresses around a void, K_{vm} , was estimated to be 2.22 for a matrix of elastic modulus equal 3.2 GPa which agrees well with the optimal values obtained in this study. The interfacial debonding energy, G_a increases as the diameter of the nanofiller increases. Its optimal values were in the range of [0.184, 1.360] and [0.010, 0.046] for M_2 and M_3 , respectively. Similar values of G_a for M_2 were reported in [3] and [66]. The high value of these results may be explained by assuming that the optimal values of G_a were reduplicated since the total energy dissipation in M_2 was attributed only to one mechanism. Based on this, the probability distribution of G_a can be updated to a uniform distribution in the range of [0.1, 1.5] for M_2 and [0.01, 0.1] for M_3 . The elastic property of the interphase was softer than that of the matrix in the measurements; D_{10}

1.5 Results and discussion

and D_{11} ($\chi = 1.162$ and 1.231 , respectively), whereas the matrix showed stiffer elasticity in the remaining measurements.

The models predictions at the calculated optimal parameter set versus the nanofiller volume fraction are depicted in Fig. 1.26.

The CV values for M_1 , M_2 , and M_3 are shown in Fig. 1.27. Except of the measurements: D_8 , D_{11} , D_{12} , and D_{13} , M_1 shows better performance compared to M_2 and M_3 , where its CV values are the least. The predictions of M_2 have the lowest discrepancies from the measurements of D_{11} , D_{12} , and D_{13} . M_3 produces the best fit predictions in the measurements of D_8 only.

When considering both the model and parameters uncertainties in the evaluation, M_1 outperforms M_2 and M_3 for all the different measurements. It has significantly higher

Table 1.11.: Selected input parameters used in the assessment of the models.

Reference Data	All models ^a		M_1^b		M_2^b	M_3^b	
	d_n nm	E_m GPa	K_{vm} –	V_{dp} %	G_a J/m ²	G_a J/m ²	χ –
D_1 [65]	20	3.20	2.227	14.1	0.287	0.015	0.882
D_2 [65]	20	3.20	2.216	11.4	0.309	0.011	0.788
D_3 [52]	12	3.53	2.236	10.4	0.184	0.013	0.644
D_4 [52]	20	3.53	2.18	10.3	0.289	0.016	0.670
D_5 [52]	40	3.53	2.108	13.2	0.473	0.015	0.375
D_6 [57]	23	3.50	2.244	10.8	0.250	0.010	0.742
D_7 [57]	74	3.50	2.236	15.2	0.914	0.046	0.447
D_8 [55]	20	2.86	2.11	16.4	0.374	0.018	0.710
D_9 [51]	20	2.96	2.19	12.5	0.310	0.011	0.758
D_{10} [56]	20	2.41	2.224	14.1	0.363	0.011	1.162
D_{11} [56]	80	2.41	2.239	17.9	1.360	0.046	1.231
D_{12} [62]	25	3.02	2.108	13.3	0.340	0.012	0.676
D_{13} [62]	25	2.78	2.112	16.7	0.383	0.010	0.656
D_{14} [53]	20	2.96	2.229	13.7	0.385	0.011	0.649
D_{15} [60]	13	2.60	2.221	11.1	0.224	0.010	0.770
D_{16} [59]	25	3.27	2.204	14.9	0.322	0.011	0.830

^a The values of d_n and E_m are obtained from the corresponding references.

^b These are the optimal values approximated in the current study.

1.5 Results and discussion

model selection probability, $P(M_i|D)$ (See Table 1.12). It can be concluded that the parameters of M_2 and M_3 have steeper posterior probabilities. Significant changes in their prognoses are expected due to slight variations in the parameters values. One possible explanation is that the natural exponential relation in M_2 and in M_3 results in high values of the determinant of their Hessian matrices.

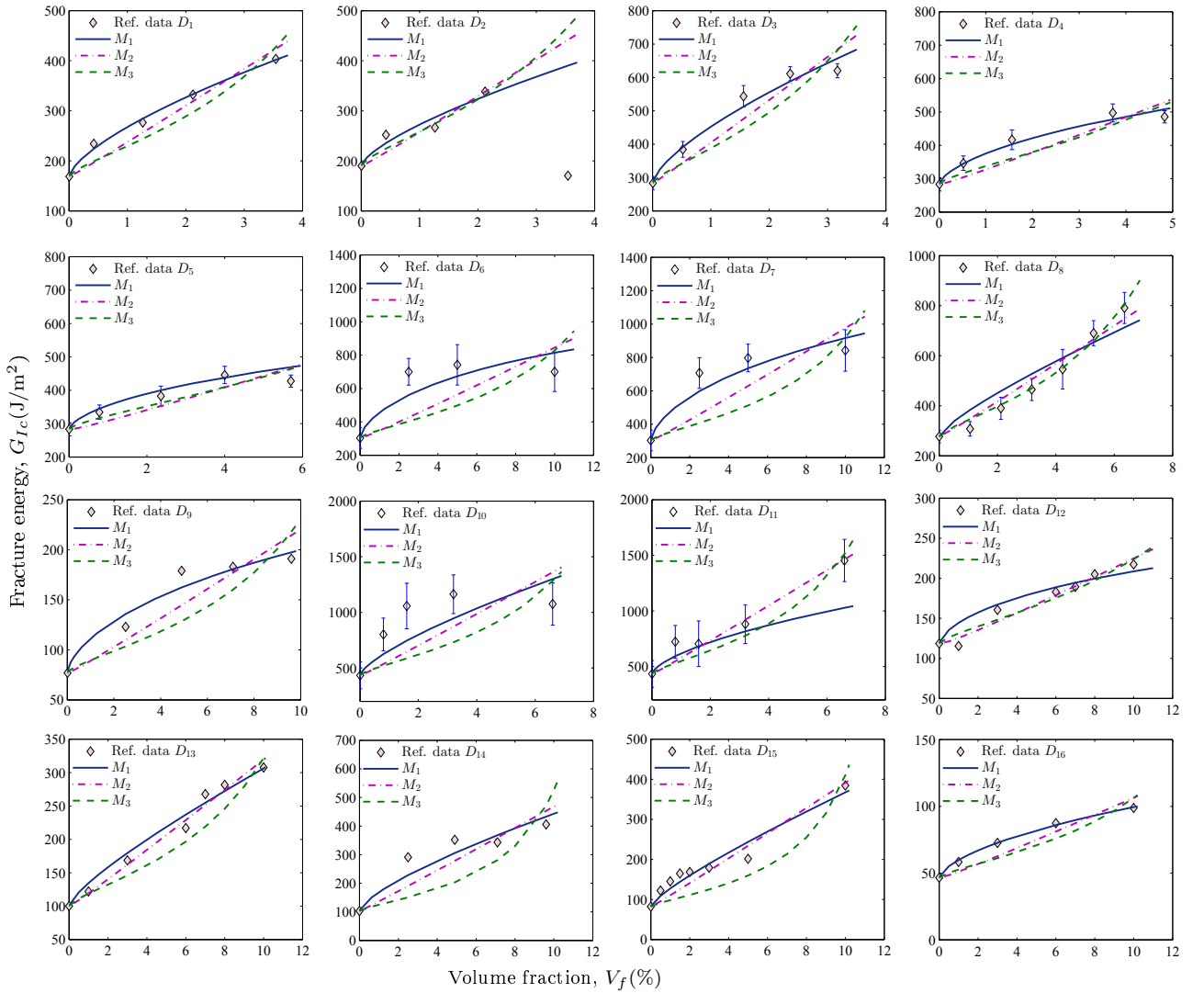


Figure 1.26.: Predictions of the models using the optimal parameter set for the different reference data.

1.5 Results and discussion

Table 1.12.: The models selection probability values for the different reference data

Reference Data		$P(M_i D)^a$		
		M_1	M_2	M_3
D_1	[65]	0.988	0.000	0.012
D_2	[65]	1.000	0.000	0.000
D_3	[52]	1.000	0.000	0.000
D_4	[52]	1.000	0.000	0.000
D_5	[52]	0.805	0.000	0.195
D_6	[57]	0.999	0.000	0.001
D_7	[57]	0.998	0.000	0.002
D_8	[55]	0.998	0.000	0.002
D_9	[51]	1.000	0.000	0.000
D_{10}	[56]	0.995	0.000	0.005
D_{11}	[56]	0.744	0.001	0.255
D_{12}	[62]	1.000	0.000	0.000
D_{13}	[62]	1.000	0.000	0.000
D_{14}	[53]	1.000	0.000	0.000
D_{15}	[60]	1.000	0.000	0.000
D_{16}	[59]	0.997	0.000	0.003

^aThe probability of selecting the model M_i given the different reference data.

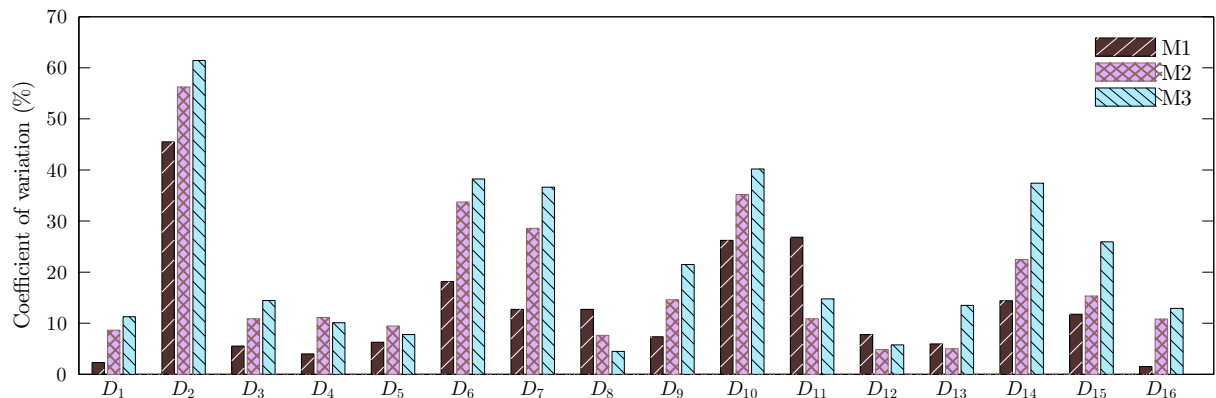


Figure 1.27.: The coefficient of variation for the different references data

1.5.4. Stochastic model to predict the fracture toughness of particle reinforced polymeric nanocomposites

Stochastic finite element modeling is implemented to predict the fracture toughness of polymer/particle nanocomposites. Firstly, a 2D finite element model containing an epoxy matrix and rigid nanoparticles surrounded by an interphase zone is generated. The crack propagation is simulated using XFEM. Fig. 1.28 shows an example of simulation result for PNC specimen reinforced by 4.0 vol.% nanoparticles of 25 nm in diameter, with an interphase of 3.50 nm in thickness. The crack propagates orthogonal to the loading direction through the epoxy and the interphase zone, see Fig. 1.28b. As cleared from the load deflection curve in Fig. 1.28c, the nanoparticles have improved the load carrying capacity and ductility in the PNC compared to the corresponding pure epoxy.

Sequentially, two polynomials, second and third order PCE, were constructed to represent the output as a function of the six input parameters. The calculated value of R^2 and R_{adj}^2 for the constructed PCE are presented in Table 1.13. Although the third order PCE has better coefficient of determination, both have almost identical R_{adj}^2 . Making use of the built PCE stochastic models, the sensitivity of the six input parameters were evaluated. The results PCE-based Sobol' sensitivity indices based on third order polynomial are summarized in Table 1.14. The main effects of all input parameters represent 78.8% of the variance in the output. The sum of the joint effect of two and three parameters, i.e. $\sum S_{ij}$ and $\sum S_{ijl}$ are 12.2% and 9.1%, respectively. The maximum allowable principal stress of the epoxy matrix, σ_{max} , and its stiffness, E_m are the most significant parameter influencing the output variation and σ_{max} is observed clearly to surpass E_m . It is expected that slight changes in these parameters will result in high change in the fracture energy meaning that special care should be considered when measuring these variables. The total effect of the nanoparticle size come in the next place of the ranking. Its effect is dominated by the interaction with other parameters

Table 1.13.: Properties of the constructed PCEs

	Degree of the polynomial	
	$n = 2$	$n = 3$
Coefficient of determination, R^2	0.786	0.877
Adjusted coefficient of determination, R_{adj}^2	0.740	0.738

1.5 Results and discussion

($S_T - S_i$ for d_n is 0.094). The first-order and the total effect sensitivity indices are displayed in Fig. 1.29.

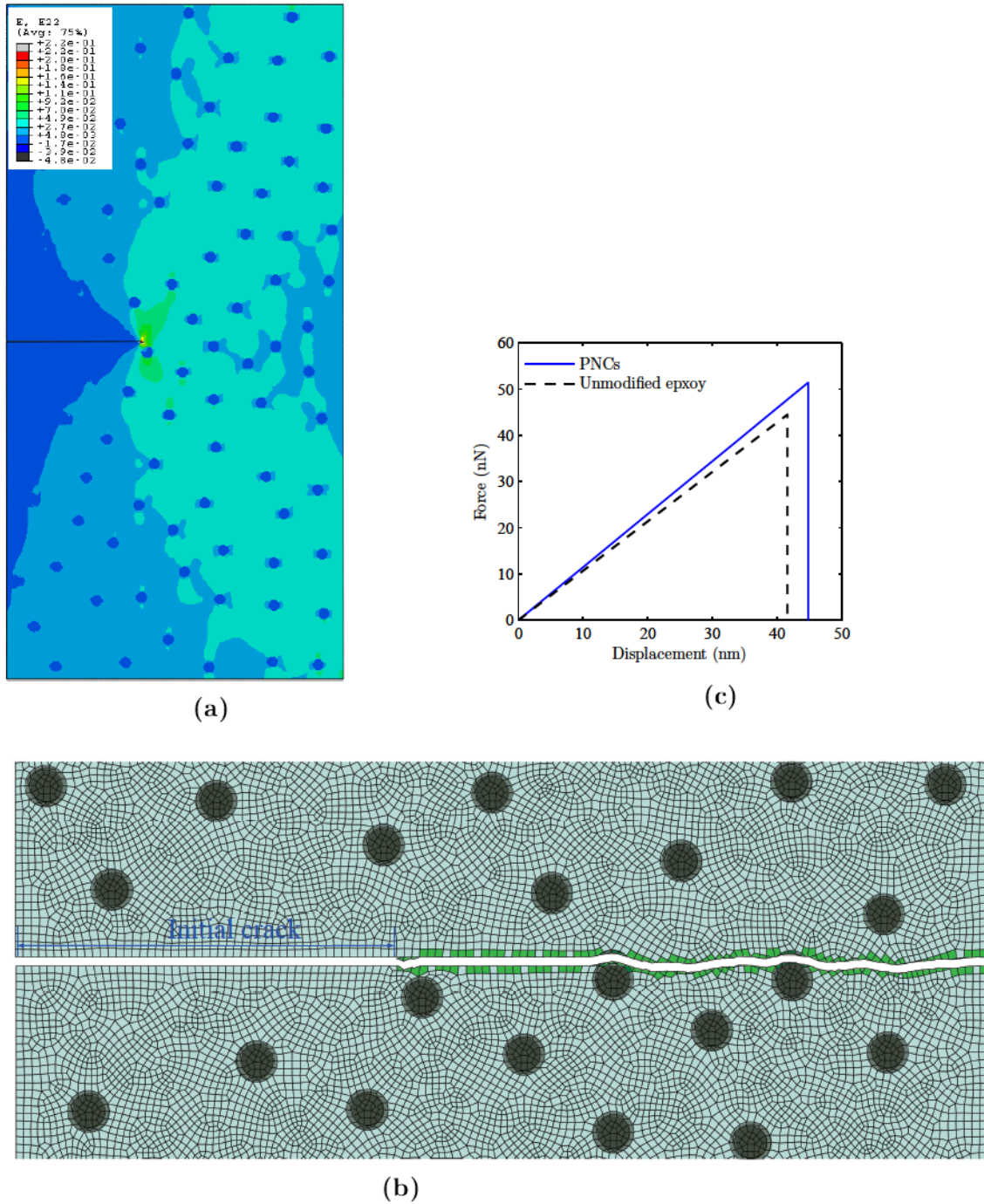


Figure 1.28.: Deformed shape for exemplary particles PNCs specimen: a) The strain in the loading direction just before failure. b) The cracked elements at complete failure. c) Load displacement curves for the unmodified and PNC.

Table 1.14.: Sobol' sensitivity indices based on third order PCE, $n = 3$

	V_f	d_n	E_m	σ_{max}	E_i	t_i
S_i	0.007	0.005	0.237	0.517	0.015	0.007
	$\sum S_i = 0.788$					
S_{ij}						
	S_{1j}	0.006	0.006	0.008	0.001	0.003
	S_{2j}		0.012	0.022	0.001	0.007
	S_{3j}			0.030	0.002	0.014
	S_{4j}				0.001	0.004
	S_{5j}					0.005
	$\sum S_{ij} = 0.122$					
S_{ijl}^a						
		S_{12l}	0.001	0.001	0.002	0.007
		S_{13l}		0.011	0.002	0.003
		S_{14l}			0.005	0.000
		S_{15l}				0.000
		S_{23l}		0.022	0.000	0.005
		S_{24l}			0.001	0.004
		S_{25l}				0.004
		S_{34l}			0.003	0.003
		S_{35l}				0.010
		S_{45l}				0.007
	$\sum S_{ijl} = 0.091$					
S_{Ti}	0.061	0.100	0.359	0.638	0.057	0.084

^a S_{ijl} refers to the third order sensitivity that measures the joint effect of the parameters i , j , and l , e.g. S_{123} is the sensitivity of the interaction between the volume fraction, the diameter of the nanoparticles and the matrix Young's modulus.

In order to show the effect of parameters on the variance of the output, three sets of samples were randomly generated by LHS. Set G_1 is obtained by sampling the entire input parameters space, Set G_2 is formed with the same as Set G_1 but the parameters σ_{max} and E_m are fixed respectively at their mean values, and Set G_3 is formed by fixing the remaining non-influential parameters at any point of their variation range. The corresponding three sets of model output were calculated using the constructed third

1.5 Results and discussion

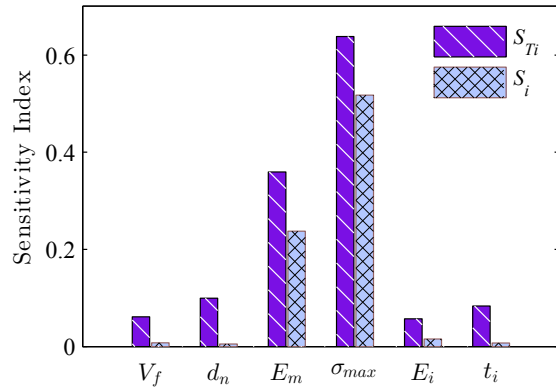


Figure 1.29.: First-order and total-effect PCE-based Sobol' sensitivity indices based on third order PCE polynomial.

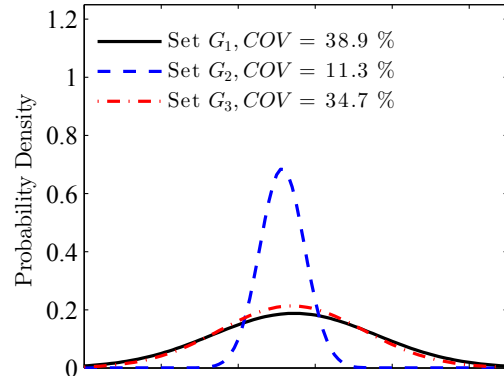


Figure 1.30.: The effect of fixing the influential and non-influential parameters on the variance of the output.

order PCE ($n = 3$) surrogate model. The probability density of the output of the three sets represented by Normal distribution are displayed in Fig. 1.30. Set G_1 and Set G_3 have almost the same range of variation which is considerably higher than Set G_2 . As a measure of relative variance, the coefficient of variations (COV) for Set G_1 and Set G_3 were 38.9 and 34.7 %, respectively, while for Set G_2 was 11.3 %. This manifests that fixing the influential parameters resulted in greatest reduction in the variance of the output.

Chapter 2

Predicting The Fracture Toughness of PNCs: A Stochastic Approach Based on ANN and ANFIS

Contribution of authors

The work presented in this chapter is published in *K.M. Hamdia et al./Computational Materials Science 102 (2015) 304-313*. <http://www.sciencedirect.com/science/journal/09270256>. Impact Factor of the journal: **2.086**. An electronic copy of this publication is available at: <http://dx.doi.org/10.1016/j.commatsci.2015.02.045>.

The original text from this publication is used in this chapter.

- Khader M. Hamdia
 - Conducting literature review.
 - Gathering and classifying experimental results from the literature.
 - Building ANN and ANFIS models for PNCs using matlab.
 - Writing the manuscript.
- Tom Lahmer
 - Discussions in ANN and ANFIS.
 - Reviewing the manuscript before submission.
- Trung Nguyen-Thoi
 - Reviewing the manuscript before submission.
- Timon Rabczuk
 - Mentoring the research progress.
 - Reviewing the manuscript before submission.

2.1. Introduction

Epoxy polymers are often used as matrix in fiber reinforced composites. However, epoxy has a low fracture toughness and poor resistance to crack initiation and propagation. Improving the fracture properties of epoxy polymers without sacrificing some important thermo-physical properties has been the subject of interest for many years. Adding nano filler such as silica, alumina and glass particles to the epoxy matrix has offered exceptional improvements even with low filler contents [139–141].

Various models have been developed to predict the fracture properties of polymeric nanocomposites (PNCs). Williams [3] assumed that the energy absorbing mechanism is attributed to the growth of plastic voids around debonded or cavitated particles, which is stimulated by the debonding surface energy. He also found that the debonding energy was proportional to the particle radius. A large toughness increase was predicted for particle sizes in the nano range when good particle dispersion and sufficient ductility of the epoxy matrix could be achieved. Quaresimin et al. [4] developed a multiscale approach considering three different damaging mechanisms: i) particle debonding, ii) plastic yielding of nanovoids, and iii) shear banding of the polymer. Huang and Kinloch [2] calculated the increase in fracture energy of rubber-toughened epoxy polymers. More recently, Hsieh et al. [51] and other authors [52, 54, 56–58] applied Huang and Kinloch model for PNCs. It was reported that the improvement in the fracture toughness of the epoxy resins reinforced with rigid nanoparticles was dominated by two major mechanisms: localized plastic shear banding and debonding of silica nanoparticles which enable plastic void growth of the epoxy matrix.

On the other hand, several experimental studies have been carried out in order to study the fracture behavior of PNCs. Johnsen et al. [53] showed that adding nanosilica particles led to a significant increase in the toughness of the composite. The mode I fracture energy increased from 100 J/m² for the pure epoxy polymer to 460 J/m² for the epoxy polymer modified with 13 vol% of nanosilica. The improvement in fracture energy was also observed by [49–52, 54, 55] and others. Liang and Pearson [56] and Dittanet and Pearson [57] studied the influence of different nanoparticle sizes, and they observed that the effect of nanoparticle size was negligible. By studying epoxy resin filled with a mixture of micro and nanometer-size silica particles, Dittanet and Pearson [58] concluded that the enhancement in toughness was higher when the volume fraction of nanoparticles was higher than the volume fraction of microparticles. Zhang et al. [59] reported that the performance of PNCs is dominated by a three-dimensional physical network of interphase material around silica nanoparticles constructed when the interparticle distance is

2.1 Introduction

close enough. Wetzel et al. [60] discussed the reinforcing effects of titanium dioxide and aluminium oxide which have average diameters of 300 nm and 13 nm, respectively, and the latter was considerably tougher. The influence of different temperatures was studied by Deng et al. [61] and Zhang et al. [62]. Ma et al. [63] demonstrated that the toughening mechanisms were caused by the formation of a thin dilatation zone and nanovoids. Zhao et al. [64] noticed larger improvement with a stronger particle-matrix interface. In the previous literatures, the fracture toughness was determined experimentally based on a single-edge notch bend (SENB) test or compaction test (CT) [142]. The mode-I stress intensity factor, K_{Ic} , can be given by:

$$K_{Ic} = \frac{P_{max}}{B\sqrt{W}} f\left(\frac{a}{W}\right) \quad (2.1)$$

where P_{max} is the load at fracture, B is the sample thickness, W is the sample width, a is the crack length, and $f(a/W)$ is a dimensionless function [7]. The fracture energy, G_{Ic} , considering plane strain conditions, is calculated by:

$$G_{Ic} = \frac{K_{Ic}^2}{E} (1 - \nu^2) \quad (2.2)$$

with E and ν being the elastic modulus and the Poisson's ratio.

Recently, artificial intelligence techniques such as artificial neural network (ANN) and adaptive neuro-fuzzy inference system (ANFIS) have been effectively used for complex problems in engineering. These stochastic approaches are based on computational intelligence and machine learning tools through correlating the system input parameters to the outputs by means of mathematics and statistics methods. It can be a viable alternative to empirical or to physically based analytical formula which consists of large number of variables. ANN has the ability to learn from examples, identify the data pattern, and process information rapidly, while ANFIS presents a combination of neural network and a fuzzy system which deals with reasoning on a higher level. Disregarding any prior knowledge about the physical phenomenon and the nature of the relationships between input/output variables, both ANN and ANFIS can be used to interpret the behavior of nonlinear complex problems and consequently predict their future reaction. Dependence of data within the range of input parameters being investigated is a shortcoming of these data driven models. Though they have been widely used in material science, there have been few studies on the application of ANN and ANFIS in prediction and investigation of the behavior of PNCs [67, 68].

In the present study, ANN and ANFIS are developed for predicting the fracture energy of PNCs without performing any experiments. The data used for construction the models are gathered from the literature. The performances of the developed models are evaluated based on three performance evaluation indices and are compared to the results of the Huang and Kinloch and the linear regression models. Finally, parametric studies are carried out to specify the influence of some of the input parameters on the desired output.

The rest of this chapter is organized as follows: In the next section, the database is presented. The methods used in this study for predicting the fracture energy of PNC are briefly illustrated in Section 2.3. Section 2.4 presents the results, while Section 2.5 includes parametric studies for input parameters affecting the fracture energy of PNCs. Afterwards, conclusions are summarized in Section 2.6.

2.2. Database

In the present study five parameters were selected to establish the database: the volume fraction of the nano filler (V_f), the diameter of the nano particle (d_n), the fracture energy of the matrix (G_{Im}), the elastic modulus of matrix (E_m) and the yield strength of the matrix (σ_{ym}). These parameters form the input while the fracture energy of PNC (G_{Ic}) forms the output.

For constructing ANN, ANFIS, and the regression models, 115 experimental databases gathered from the literature [49–64] were utilized. The collected records were divided into two groups: training set and testing set containing 85 and 30 datasets, respectively. The training dataset was used to build the relation between the inputs and the output, whereas the testing dataset is applied to prevent over-fitting in ANN and ANFIS and to validate all models. The division was based on the condition that the training and the testing datasets have almost similar distributions. Table 2.1 includes a list of minimum, average, and maximum of the input and the output parameters for both groups.

2.3. Methods for Predicting Fracture Energy of PNCs

2.3.1. Huang and Kinloch

Huang and Kinloch [2] model is used for predicting the fracture toughness in PNCs consisting of an epoxy matrix and nanoparticles. The fracture energy of PNCs, G_{Ic} , is

2.3 Methods for Predicting Fracture Energy of PNCs

Table 2.1.: Range of Input-Output Parameters.

Parameters	Training data			Testing data		
	Min.	Avg.	Max.	Min.	Avg.	Max.
<i>Input Parameters</i>						
Volume fraction of the nano filler (%)	0.50	7.90	30	0.52	6.85	30
Diameter of the nano particle (nm)	12	40.48	170	12	36.35	170
Fracture energy of the matrix (J/m ²)	46.5	228.34	606	46.5	229.0	606
Elastic modulus of the matrix (GPa)	2.41	3.11	3.53	2.41	3.10	3.53
Yield strength of the matrix (MPa) ^a	57.1	83.70	111	57.1	81.53	100
<i>Output Parameter</i>						
Fracture energy of PNCs (J/m ²)	58.3	535.29	2156.65	98.8	510.16	1169.53

^aSome of these data were not provided by the original literature. It has been assumed based on the property of similar matrices.

expressed as:

$$G_{Ic} = G_{Im} + \Psi \quad (2.3)$$

G_{Im} being the fracture energy of the matrix and Ψ is dominated by localized shear banding, ΔG_s , and the plastic void growth, ΔG_v , [2].

$$\Psi = \Delta G_s + \Delta G_v \quad (2.4)$$

with

$$\Delta G_s = \frac{1}{2} \left(1 + \frac{\mu_m}{\sqrt{3}}\right)^2 \left[\left(\frac{4\pi}{3V_f}\right)^{\frac{1}{3}} - \frac{54}{35} \right] V_f \sigma_{yc} \gamma_f r_{yu} K_{vm}^2 \quad (2.5)$$

$$\Delta G_v = \left(1 - \frac{\mu_m^2}{3}\right) (V_{fv} - V_{fp}) \sigma_{yc} r_{yu} K_{vm}^2 \quad (2.6)$$

where μ_m is a material constant (pressure coefficient), σ_{yc} is the compressive yield stress of the epoxy matrix, γ_f is the shear fracture strain of the epoxy matrix, r_{yu} is the radius of plastic zone in the epoxy matrix, K_{vm} is the maximum stress concentration factor of the von Mises stress in the epoxy matrix, and V_{fv} and V_{fp} are the volume fraction of voids and debonded particles, respectively. It is evident that the model has a large number of input parameters that need to be predetermined experimentally even though, the terms V_{fv} and V_{fp} are difficult to be measured. Liang and Pearson [56] assumed that

2.3 Methods for Predicting Fracture Energy of PNCs

the volume of the matrix around the nanoparticles $v_m = v_p/V_{fp} - v_p$ does not change before and after voiding. Hence, the value of $(V_{fv} - V_{fp})$ can be estimated by:

$$(V_{fv} - V_{fp}) = \left(\frac{v_v}{v_v + v_m} - \frac{v_p}{v_p + v_m} \right) \quad (2.7)$$

where v_v and v_p are the average volume of the voids and the nanoparticles.

2.3.2. Linear Regression

Linear Regression can be used to define a mapping between one or more independent and dependent variables. The general form of a regression model is given as:

$$y = a_0 + a_1z_1 + a_2z_2 + \dots + a_mz_m + e = \mathbf{Z}\mathbf{A} + e \quad (2.8)$$

where z_1, z_2, \dots, z_m are basis functions, which can be linear or higher order with or without mixed term polynomials, while a_0, a_1, \dots, a_m are the regression coefficients and e is the residual [26].

The vector \mathbf{A} is determined in such a way that the mean squared difference between the values of the linear regression predictions and the actual experimental data is minimized. The least-square estimate of $\hat{\mathbf{A}}$ is given by:

$$\hat{\mathbf{A}} = \left[[\mathbf{Z}]^T [\mathbf{Z}] \right]^{-1} \left\{ [\mathbf{Z}]^T [\mathbf{Y}] \right\} \quad (2.9)$$

In this study, the training datasets were used to fit linear, quadratic, and quadratic with mixed terms regression models, whereas the testing datasets are applied to the fitted models in order to investigate their applicability. Table 2.2 summarizes the evaluated regression coefficients of the three models.

2.3.3. Artificial neural networks

Artificial neural network (ANN) is a highly parallel system containing a large number of processing units called neurons or nodes [18]. These units are grouped together into three or more layers. The neighboring layers are connected by weights forming a large network. Inputs from previous layers are linked to a neuron by the corresponding weights and bias. Then, the weighted sums are applied to an activation function to determine the neuron output and consequently passed as inputs for the next layers. The sum at a

2.3 Methods for Predicting Fracture Energy of PNCs

neuron are calculated by [18]:

$$u_j = \sum_{i=1}^n w_{ji}x_i \quad (2.10)$$

where u_j is the linear combiner output of the j th neuron, n being the number of neurons in the preceding layer, x_i is an input signal, $w_{j1}, w_{j2} \dots, w_{jn}$ are the weights. The bias has the effect of applying affine transformation to u_j as

$$net_j = u_j + b_j \quad (2.11)$$

net_j is known here as the induced local field. Then, an activation function is applied to net_j to obtain the neuron output signal. More details about ANN can be found in the literature [18, 19].

In this study, we used the multilayer feedforward networks [20]. Its first layer receives information from input parameters and transmits it to one or several hidden layers, and then evaluates the predictions through the output layer. The number of input and output variables in the data defines the number of neurons in input and output layers, respectively. However, there is no accepted rule for setting the number of hidden layers and its neurons. Commonly, a trial and error procedure is adopted.

Table 2.2.: The Evaluated coefficients of the linear regression models.

Regression Model	Regression function, y	Regression coefficients			
First order (LR1)	$a_0 + a_1x_1 + \dots + a_5x_5$	$a_0 = 552.33$ $a_3 = 1.93$	$a_1 = 24.72$ $a_4 = -100.37$	$a_2 = 0.82$ $a_5 = -4.47$	
Quadratic (LR2)	$a_0 + a_1x_1 + \dots + a_5x_5$ $+a_{11}x_1^2 + \dots + a_{55}x_5^2$	$a_0 = 8669.70$ $a_3 = 2.12$ $a_{11} = -0.37$ $a_{44} = 834.81$	$a_1 = 34.28$ $a_4 = -5167.31$ $a_{22} = 0.0042$ $a_{55} = 0.067$	$a_2 = -0.48$ $a_5 = -16.21$ $a_{33} = -0.0011$	
Quadratic with mixed terms (LR3)	$a_0 + a_1x_1 + \dots + a_5x_5$ $+a_{11}x_1^2 + \dots + a_{55}x_5^2$ $+a_{12}x_1x_2 + \dots + a_{45}x_4x_5$	$a_0 = -9854.63$ $a_3 = 6.08$ $a_{11} = -0.13$ $a_{44} = -777.77$ $a_{13} = 0.063$ $a_{23} = 0.073$ $a_{24} = 17.87$ $a_{35} = -0.16$	$a_1 = 116.36$ $a_4 = 5143.23$ $a_{22} = -0.024$ $a_{55} = -0.016$ $a_{14} = -27.92$ $a_{24} = 17.87$ $a_{25} = -0.39$ $a_{45} = -7.50$	$a_2 = -47.67$ $a_5 = 47.79$ $a_{33} = 0.0028$ $a_{12} = 0.067$ $a_{15} = -0.28$ $a_{25} = -0.39$ $a_{34} = 2.23$	

2.3 Methods for Predicting Fracture Energy of PNCs

The multilayer feedforward network considered in this study is illustrated in Fig. 2.1. It has five neurons in the input layer representing the five input parameters ($V_f, d_n, G_{Im}, E_m,$ and σ_{ym}) and one neuron in the output layer for G_{Ic} . The minimum error was observed by using one hidden layer with eight neurons [143]. The activation function for the hidden layer was tan-sigmoid, while it was linear for the output layer. After applying the activation function to the hidden layer, the neuron output O_j is given by:

$$O_j = \frac{e^{\alpha(net_j)} - e^{-\alpha(net_j)}}{e^{\alpha(net_j)} + e^{-\alpha(net_j)}} \quad (2.12)$$

where α is a constant and net_j is the weighted sum calculated from Eq. (2.11). As the tan-sigmoid function in Eq. (2.12) produces output results ranging from -1 to 1, scaling the input and the target vectors in the data set is recommended. The operation is continued forward layer by layer starting from the input layer to the output layer and through the hidden layer. Once all layers are processed, the weights and bias are readapted according to the calculated error comprising the difference between the target and predicted values [20].

2.3.4. Adaptive neuro-fuzzy inference system

Fuzzy logic (FL) allows partial belongings of an element to a set [21]. Instead of an element belonging to a set or not, the degree of membership, which varies between 0 and 1, describes the partial belongings to a set numerically. Fuzzy inference system (FIS) has the ability to extrapolate the relation between a series of input to an output with the help of fuzzy logic. The process contains integrated and consecutive steps which start with defining the membership functions of fuzzy sets (fuzzification), creating the rules to include all possible relation between input and output, and then merging all the fuzzy rules by a fuzzy inference to produce the results which are finally defuzzified into crisp outputs [22, 23]. One of the commonly fuzzy logic approaches used to solve com-

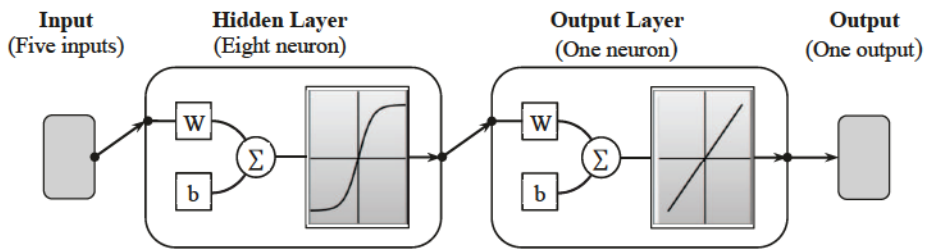


Figure 2.1.: ANN structure for predicting the fracture energy of PNCs

2.3 Methods for Predicting Fracture Energy of PNCs

plex problems, is the Takagi-Sugeno fuzzy model [24], which is characterized by linear or constant terms in the consequent part of the if-then rules. Making use of the merits of FIS and ANN and based on the Sugeno FIS, the adaptive neuro-fuzzy inference system (ANFIS) was implemented in the present study.

The ANFIS was applied to evaluate the fracture energy of PNCs using the five input variables described in Section 2.2. The domain of each variable was divided into a number of fuzzy subsets. Many forms of membership functions such as trapezoidal, triangular, bell-shape, Gaussian function, etc. can be used to characterize the degree of membership. Hereafter, the triangular membership function form was chosen due to its simplicity. For each input, different numbers of triangular fuzzy subsets were tried and the optimal number was chosen based on the minimum error observed during the training process. The number of fuzzy subsets for the input variables V_f , d_n , G_{Im} , E_m , and σ_{ym} was 4, 5, 4, 3, and 4, respectively and the associated membership function plots are shown in Fig. 2.2. Adopting the grid partitioning, a total of 960 rules were obtained [24, 144]:

R_i : If (V_f is V_{fj}) and (d_n is d_{nk}) and (G_{Im} is G_{Imj}) and (E_m is E_{mp}) and (σ_{ym} is σ_{ymj})

Then : (G_{Ic} is G_{Ici})

$i = 1, \dots, 960, j = 1, \dots, 4, k = 1, \dots, 5, p = 1, \dots, 3$

The ANFIS learning method is similar to the common feed-forward neural networks. A hybrid-learning algorithm was employed in the present study, which consists of back-propagation and least squares estimation [144, 145].

Fig. 2.3 explains the corresponding equivalent ANFIS architecture. It comprises of five layers and the characteristics of each layer are described according to Jang [25] as follow:

- Layer 1—For all the input, the output of every node i is the membership function of the fuzzy set calculated by:

$$O_i^1 = \mu_x(x) \quad (2.13)$$

where $\mu_x(x)$ is the membership function of the appropriate fuzzy set for the input x .

- Layer 2—Every node labeled by Π multiplies the incoming signals and sends the product out forming the firing strength of a rule.

$$w_i = \mu_{V_{fj}}(V_f) \times \mu_{d_{nk}}(d_n) \times \mu_{G_{Imj}}(G_{Im}) \times \mu_{E_{mp}}(E_m) \times \mu_{\sigma_{ymj}}(\sigma_{ym}) \quad (2.14)$$

2.3 Methods for Predicting Fracture Energy of PNCs

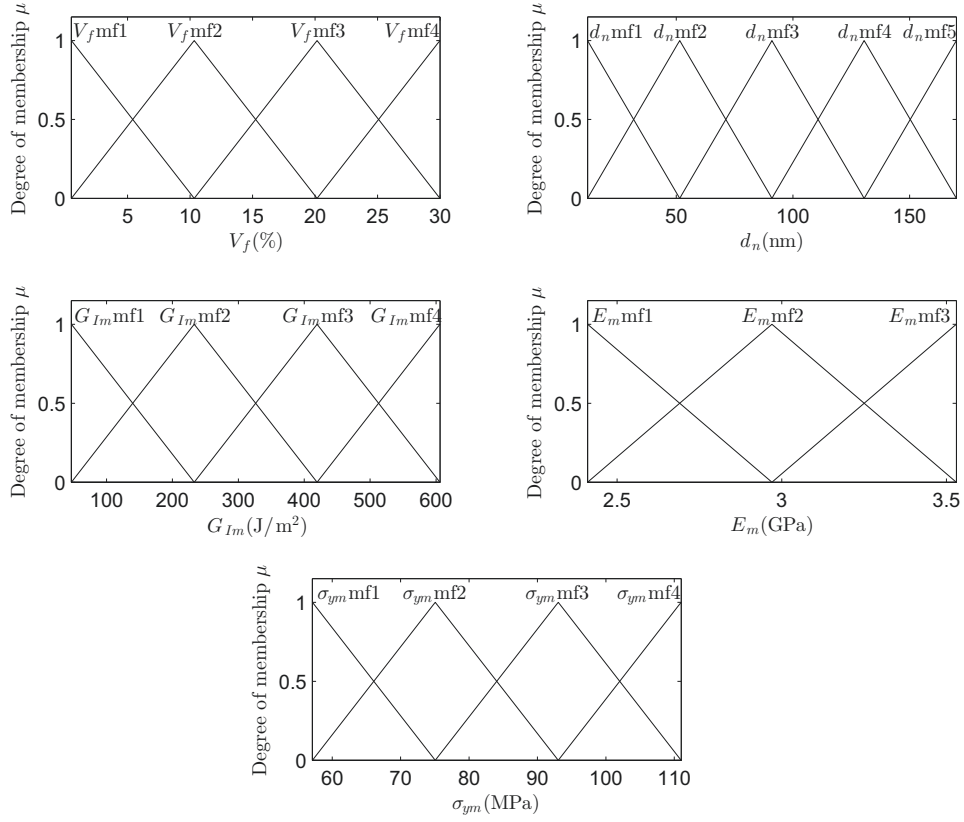


Figure 2.2.: Membership functions of input variables.

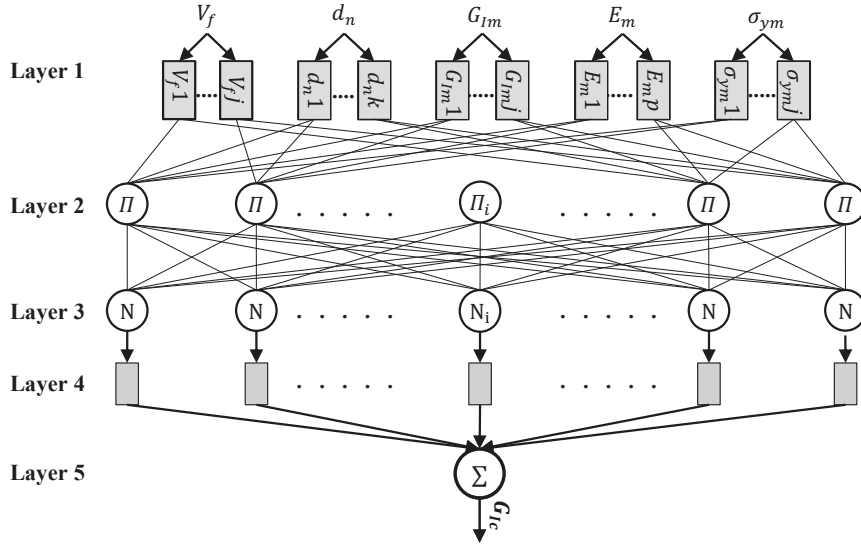


Figure 2.3.: ANFIS architecture.

- Layer 3—The nodes in this layer are labeled by N . The i th node calculates the ratio of the i th rule's firing weight to the sum of all rule's firing weights producing

2.4 Results

the normalized firing strengths.

$$O_i^3 = \bar{w}_i = \frac{w_i}{\sum w_i} \quad (2.15)$$

- Layer 4—Every square node has a function:

$$O_i^4 = \bar{w}_i \cdot f_i \quad (2.16)$$

where \bar{w}_i is the output of layer 3, and f_i is a crisp function which may be linear or constant. In this study, it was selected as constant.

- Layer 5—The signal node in this layer labeled by \sum computes the overall output as the summation of all incoming signals.

$$O_i^5 = \sum \bar{w}_i \cdot f_i \quad (2.17)$$

2.4. Results

The fracture energy, G_{Ic} , of PNCs was predicted using the ANN and the ANFIS models. It was also calculated by the Huang and Kinloch and three different Linear Regression models. The fracture energy of the experimental results and the results predicted by the ANN and the ANFIS models for the training dataset are presented in Table A.1, whereas Table A.2 shows the predicted results for the testing dataset. The coefficient of variation (COV) of the ratios of the experimental to the predicted values for every model is given in Table 2.3. The results reveal a good agreement between the experimental datasets and the corresponding predicted values using ANN and ANFIS. In order to have a comparison of the performance of the models against the experimental datasets, the results of all methods employed were compared by three evaluation indices: i) The coefficient of determination (R^2), ii) The root mean square error ($RMSE$), and iii) The mean absolute percentage error ($MAPE$). The R^2 is a number between zero and one showing how much the developed model represents the data. One reveals best fit while zero is the worst fit. The $RMSE$ is a positive number used to explain the difference between the actual and predicted data. The $MAPE$ quantifies the relative of overall fit taking values of 0.0% or greater. These statistical parameters are calculated

by:

$$R^2 = 1 - \frac{SS_E}{SS_{yy}} \quad (2.18)$$

$$RMSE = \sqrt{\frac{1}{N}SS_E} \quad (2.19)$$

$$MAPE = \frac{1}{N} \sum \frac{t_i - O_i}{t_i} \times 100 \quad (2.20)$$

where t_i and O_i are the actual observation and predicted output, N is the number of datasets, $SS_{yy} = \Sigma(t_i - \bar{t}_i)^2$ is the deviation of the observations from their mean and $SS_E = \Sigma(t_i - O_i)^2$ is the deviation of observation from their predicted value.

2.4.1. Huang and Kinloch

Huang and Kinloch model was applied to the 115 datasets described in Section 2.2. The fracture energy for each dataset was calculated using Eq. (2.3) along with Eqs. (2.4) to (2.7). The obtained G_{Ic} values against the experimental datasets are presented in Figs. 2.4a and 2.4b for the training and testing dataset, respectively. At higher values, the predictions show higher scatter compared to the real experimental data. The method produced wide variations on either side of the equality line. This is revealed by the results shown in Table 2.3 with respect to all data sets, where the mean value of the ratios $G_{Icexp.}/G_{Icpre.}$ equals 1.011 but its COV is 30.2%.

Table 2.3.: Mean and COV of experimental to predicted values ratio.

Method	Mean	COV(%)
Huang and Kinloch	1.011	30.2
First order(LR1)	1.055	65.1
Quadratic(LR2)	1.168	120.5
Quadratic with mixed terms (LR3)	1.076	34.6
ANN	1.011	12.6
ANFIS	1.001	8.6

2.4 Results

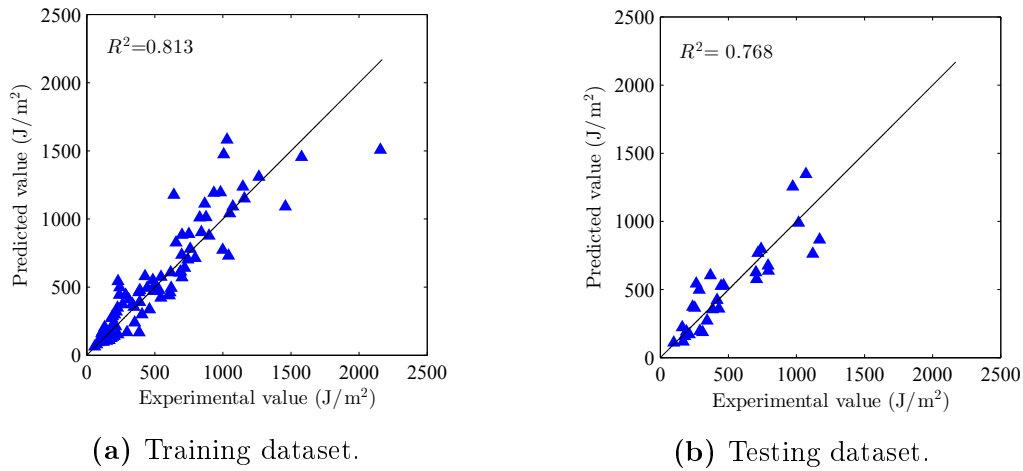


Figure 2.4.: Experimental versus predicted values for Huang and Kinloch model.

2.4.2. Linear Regression Models

Three different linear regression models were employed as presented in Table 2.2. Their evaluation indices for all sets of data are summarized in Table 2.4. The first order linear regression (LR1) had the lowest value of R^2 and the highest value of $RMSE$ and $MAPE$ with the values of 0.82, 156.03, and 33.25, respectively. In contrast, the quadratic with mixed terms (LR3) model had the highest value of R^2 and the lowest value of $RMSE$ and $MAPE$ which were equal to 0.921, 105.64, and 17.23. Therefore, it can be concluded that the LR3 model exhibits better performance than the LR1 and LR2 models. Fig. 2.5 displays the experimental versus the calculated values using LR3.

Table 2.4.: Evaluation of the linear regression models.

Model	R^2	$RMSE$	$MAPE$
First order(LR1)	0.828	156.03	33.25
Quadratic(LR2)	0.853	144.32	32.05
Quadratic with mixed terms (LR3)	0.921	105.64	17.23

2.4.3. Artificial neural networks

Using 85 and 30 training and testing datasets as previously mentioned, the ANN model with five input parameters and one hidden layer with eight neurons was constructed to predict G_{Ic} . From Table 2.3, the mean of $G_{Ic}exp/G_{Ic}pre.$ was 1.011 with a COV of 12.6%. Comparing the predicted values of the ANN model with the experimental results for training and testing datasets reveals that the ANN model was successful in learning

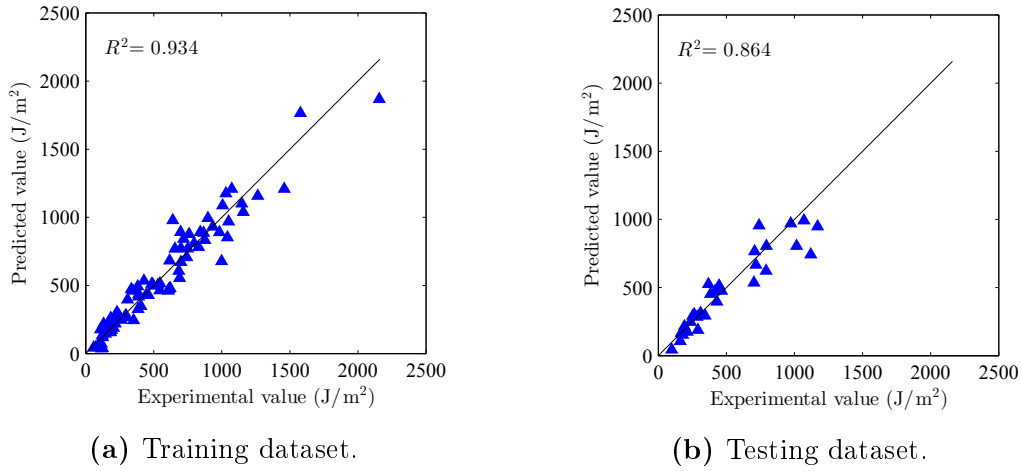


Figure 2.5.: Experimental versus predicted values for LR3.

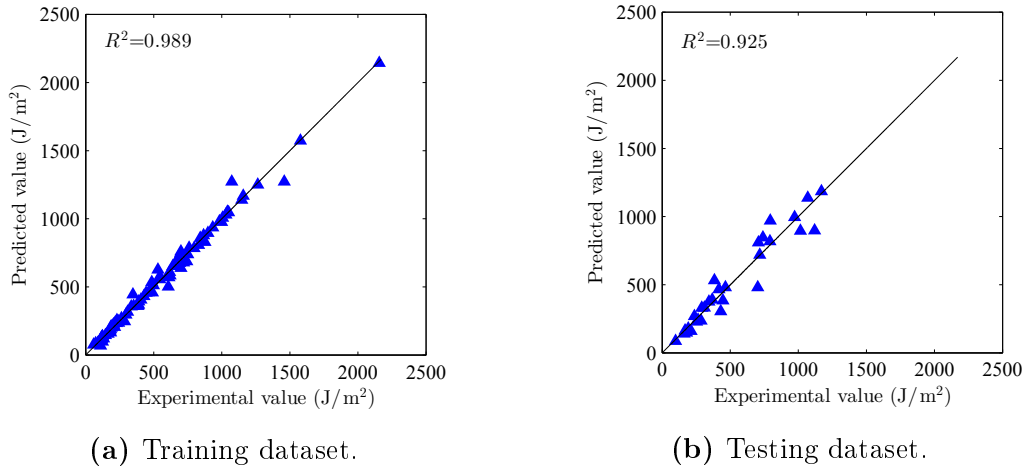


Figure 2.6.: Experimental versus predicted values for ANN model.

the relationship between the input parameters and the output. Although the model was not trained for the testing dataset, it yielded good predictions (Figs. 2.6a and 2.6b).

2.4.4. Adaptive neuro-fuzzy inference system

Fig. 2.7 shows the predicted experimental data of the training and testing datasets using the ANFIS model. The output results were very close to the experimental data. Again the testing dataset was not included in the training process but its results verify the robustness of the model. The mean of $G_{Ic}exp/G_{Ic}pre.$ was 1.001 with a COV of 8.6% (Table 2.3).

2.5 Parametric Studies

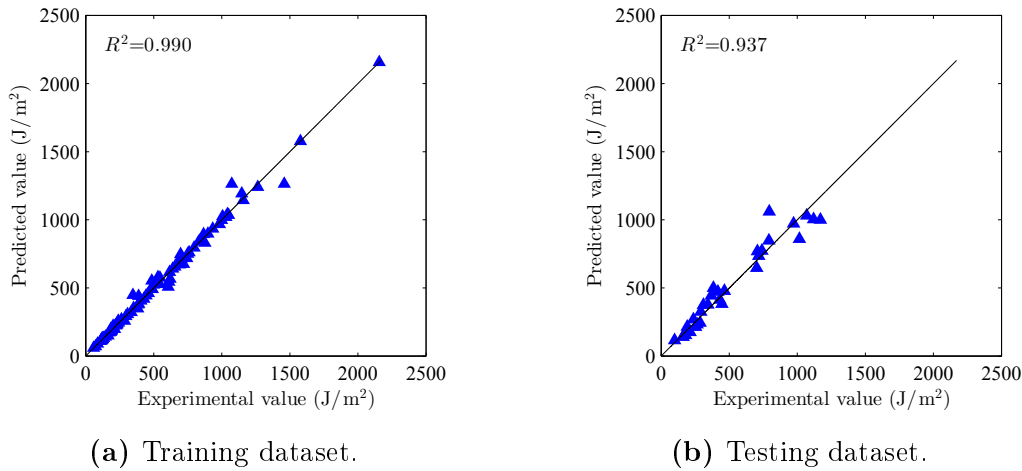


Figure 2.7.: Experimental versus predicted values for ANFIS model.

2.4.5. Comparison of the various methods

The predictions of the Huang and Kinloch, LR3, ANN, and ANFIS models were compared with the experimental data. The statistical values of R^2 , RMSE, and MAPE for the results obtained from the training and testing datasets are listed in Table 2.5. The ANN and ANFIS were considerably less scattered from experimental data than the Huang and Kinloch and linear regression models. This could be attributed to the complex and nonlinear nature of PNCs fracture toughness. For the testing dataset in terms of R^2 , it was 0.768 in the Huang and Kinloch model, 0.864 in the LR3, 0.925 in the ANN, and 0.937 in the ANFIS. The root mean square error ($RMSE$) for ANN and ANFIS are almost equal (87.31 and 80.04 J/m²) but much lower than the Huang and Kinloch and LR3 methods (153.6 and 117.5 J/m²). The mean absolute percentage error ($MAPE$) was 12.88 and 12.38% for ANN and ANFIS while it was 26.75 and 16.39 for the other two methods (Table 2.5). The results of these performance indices clearly indicate a much better performance of the ANN and ANFIS models over the Huang and Kinloch and LR3 models. Moreover, ANFIS shows slightly better results than ANN.

2.5. Parametric Studies

The parametric studies are essential to quantify to which extent a particular parameter affects the fracture energy of PNCs. In this study, parametric studies investigating the relationship between the nanoparticles volume fraction, the diameter of the nanoparticle and the matrix fracture energy versus the predicted fracture energy are carried

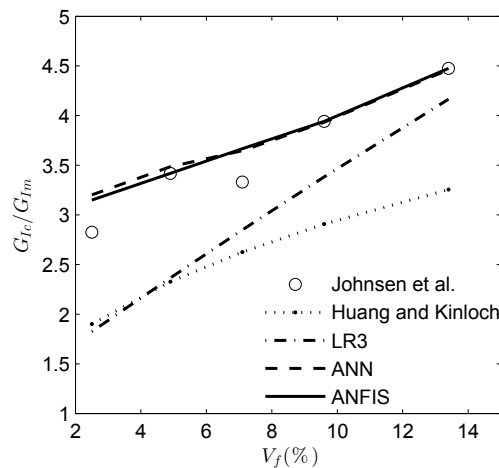
Table 2.5.: Comparison of the performance indices between modeling methods.

Method	Training Dataset			Testing Dataset		
	R^2	$RMSE$	$MAPE$	R^2	$RMSE$	$MAPE$
Huang and Kinloch	0.813	170.37	25.31	0.768	153.60	26.75
Quadratic with mixed terms (LR3)	0.934	101.13	17.52	0.864	117.50	16.39
Artificial neural networks, ANN	0.989	41.12	6.03	0.925	87.31	12.88
Adaptive neuro-fuzzy inference system, ANFIS	0.990	39.18	3.61	0.937	80.04	12.38

out. The first two relations, which investigate the nano filler content and size, are based on experimental data, while no experimental data is available for the last.

2.5.1. Influence of the nanoparticles volume fraction

To understand the effect of the nanoparticles volume fraction, all other input parameters are kept constant: $d_n = 20$ nm, $G_{Im} = 103$ J/m², $E_m = 2.96$ GPa, and $\sigma_{ym} = 61.1$ MPa, whereas V_f varies from 2.5 % to 13.4 %. The predicted and experimental values by Johnsen et al. [53] of the fracture energy of PNCs, G_{Ic} , normalized to the fracture energy of the matrix, G_{Im} , are plotted versus the volume fraction of nanoparticles in Fig. 2.8. Expectedly, the fracture energy of PNCs increases as the volume fraction increases. Moreover, a closer agreement to the experimental data is obtained by the ANFIS and the ANN.


Figure 2.8.: The normalized fracture energy versus the volume fraction.

2.6 Conclusion

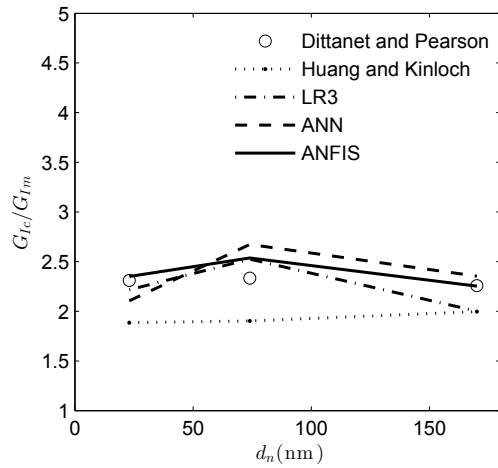


Figure 2.9.: The normalized fracture energy versus nano particle diameter.

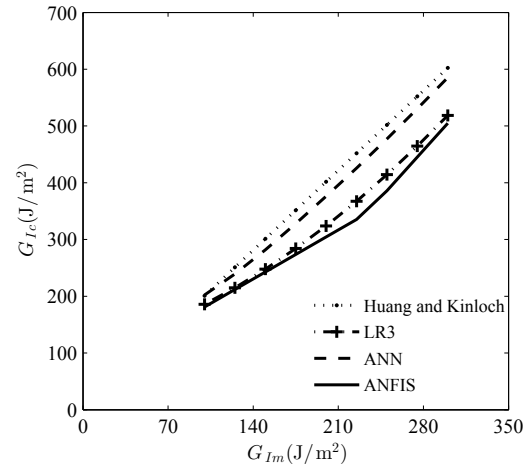


Figure 2.10.: Relationship between the fracture energy of PNCs and the fracture energy of epoxy matrix.

2.5.2. Influence of the nano particle diameter

Fig. 2.9 presents the relation between the diameter of the nano particle and the normalized fracture energy of PNCs for the predicted and experimental results of Dittanet and Pearson [57]. The other parameters are: $V_f = 2.5\%$, $G_{Im} = 303 \text{ J/m}^2$, $E_m = 3.50 \text{ GPa}$, and $\sigma_{ym} = 85 \text{ MPa}$. The fracture energy of PNCs is slightly affected by the variation of the nano particle size. This is in agreement with the experimental results of [56–58].

2.5.3. Influence of the matrix fracture energy

The relation between the fracture energy of the epoxy matrix, and the predicted fracture energy of PNCs is investigated by changing the values of G_{Im} while keeping the other input parameters constant as: $V_f = 5.0\%$, $d_n = 20 \text{ nm}$, $E_m = 3.0 \text{ GPa}$, and $\sigma_{ym} = 85 \text{ MPa}$. The results are depicted in Fig. 2.10. As expected, the PNCs fracture energy increases by increasing the fracture energy of the matrix.

2.6. Conclusion

An artificial neural networks (ANN) and adaptive neuro-fuzzy inference system (ANFIS) methodology has been employed to predict the fracture energy of PNCs. For comparison, the linear regression models and the model proposed by Huang and Kinloch were utilized to approximate the desired output. 115 datasets collected from the

literature [49–64] have been used for constructing the models; 85 datasets were chosen for the training while the remaining data were set for the testing. The data used in constructing the models are arranged in a format of five input parameters: the volume fraction of the nano filler, the diameter of the nano particle, the fracture energy of the matrix, the elastic modulus of the matrix, and its yield strength. The predicted fracture energy of PNCs of the ANN and the ANFIS were very close to the experimental results, with mean values of the ratio *experimental/predicted* fracture energy close to 1.0 and relatively low coefficient of variation. The performance evaluation indices (R^2 , $RMSE$, and $MAPE$) showed that both the methodologies ANN and ANFIS were more efficient compared to the other methods (Table 2.5). With respect to the testing dataset, R^2 value for the ANN and the ANFIS models was 0.925 and 0.937, while it was 0.768 and 0.864 for the Huang and Kinloch model and the quadratic with mixed terms linear regression (LR3) model, respectively. The complex and nonlinear nature of PNCs fracture toughness resulted in scattered predictions of the Huang and Kinloch and the linear regression unlike the ANN and the ANFIS models.

In conclusion, the fracture energy of PNCs can be predicted reliably by the ANN and the ANFIS models with relatively small error in the range of the input parameters being investigated. It was confirmed through the parametric studies, that the results are proportional to the experimental data. The fracture energy of PNCs increases as the nanoparticles volume fraction increases, and as the fracture energy of the epoxy matrix increases, whereas the nano particle size has a negligible influence.

Chapter 3

Uncertainty quantification of the fracture properties of polymeric nanocomposites based on phase field modeling

Contribution of authors

The work presented in this chapter is published in *K.M. Hamdia et al./Composite Structures 133 (2015) 1177-1190*. <http://www.sciencedirect.com/science/journal/02638223>. Impact Factor of the journal: **3.853**. An electronic copy of this publication is available at: <http://dx.doi.org/10.1016/j.compstruct.2015.08.051>.

The original text from this publication is used in this chapter.

- Khader M. Hamdia
 - Conducting literature review.
 - Simulating the fracture behaviour using phase field.
 - Coding sensitivity analysis methods.
 - Writing the manuscript.
- Mohammed A. Msekh
 - Assistance in implementing phase phase field approach in abaqus.
- Mohammad Silani
 - Assistance in Python scripting for generating RVE.
- Nam Vu-Bac
 - Discussion and assistance in Sobol' sensitivity analysis method.

- Xiaoying Zhuang
 - Reviewing the manuscript before submission.
- Trung Nguyen-Thoi
 - Reviewing the manuscript before submission.
- Timon Rabczuk
 - Mentoring the research progress.
 - Reviewing the manuscript before submission.

3.1. Introduction

Polymeric clay nanocomposites (PNCs) are constituted by a combination of polymer (epoxy) matrix and nanoclays as a filler. They are considered for numerous nanotechnology applications such as: nano-biotechnology, nano-systems, nanoelectronics, and nano-structured materials [1].

While there are numerous studies on predicting thermal [77, 146, 147] and mechanical properties [85, 95, 148–150] for intact PNCs, there are comparatively few contributions on predicting fracture properties. Due to different fabrication methods and the complex behaviour at the fine scales, results on experimental studies are contradictory [151–153]. Computational methods are often used in order to complement experiments and to explain physical phenomena that are unaccessible in experimental studies.

Numerous computational methods for material failure have been developed in the past decades. They can be broadly classified into continuum based methods and discrete crack methods.

Many popular discrete crack approaches are based on partition-of-unity (PU) enrichment. They modify the original approximation through enrichment functions and introduce additional degrees of freedom into the variational formulation in order to capture the jump in the displacement field. Among the most popular PU enrichment methods are the extended finite element method [98–100], the generalized finite element method [101–103], meshfree [104–109] and extended meshfree methods [110–112], the phantom node method [17, 113, 114], the numerical manifold method [115], and the extended isogeometric analysis (XIGA) [116–118]. An alternative to these PU enriched methods are remeshing procedures with extraneous crack path determination [119, 120] or edge repositioning [119, 121]. They basically align the crack boundary to a new mesh. Classical representatives of the continuum based models are viscous, gradient and nonlocal models [122–124]. An interesting alternative which is also based on continuum mechanics

3.1 Introduction

is the phase-field approach to fracture [8, 9]. The phase field is commonly discretised and the evolution of the phase field governed by a second [10] or fourth order [125] differential equation models the nucleation and propagation of cracks. Phase field models have been used in the context of FEM [11], local maximum entropy (LME) [10] and Isogeometric analysis (IGA) [126]. They have been extended to cohesive fracture [127], fracture in thin shells [10] and multi-physics problems [128, 129]. Discrete fracture approaches, in particular the popular partition of unity enriched discrete fracture methods, require a complex enrichment strategy for heterogeneous materials and complex fracture patterns such as PNCs. Phase field models seem due to their simplicity a more suitable alternative for modelling fracture in heterogeneous materials as they do not require a representation of the crack path. The crack topology is as mentioned above the outcome of the solution of a differential equation.

Sensitivity analysis (SA) is performed to define the influence of the input parameters on the uncertainty of the outputs. Local SA methods study the variation in the output by varying one input parameter while holding other parameters fixed. Contrary, in global SA, the influence of a parameter is defined by varying all the parameters at the same time [29]. Few studies have been done on the SA of PNCs [93, 94, 96], but they were focused on intact material that is a linear elastic material without fracture model.

In this paper, a comprehensive SA is presented to identify the influence of uncertain input parameters on the fracture toughness of PNCs predicted by a phase-field model. Different methods have been applied to examine the reliability of the implemented SA. These methods are: Standardized Regression Coefficients, Regionalized Sensitivity Analysis, Sobol' Method, EFAST method, and PAWN method. Moreover, we present an improvement to the PAWN method that reduces the computational cost. The convergence of the sensitivity indices were achieved through the bootstrapping technique. The results of SA are exploited in conducting an uncertainty quantification.

The rest of this paper is organized as follows. In the next section, the phase-field is briefly described including the statistical characteristics of all input parameters. The methods implemented for uncertainty and sensitivity analysis are discussed in detail in Section 3.3, while the results are discussed in Section 3.4. Finally, the conclusion is presented in Section 3.5.

3.2. Phase-field model for predicting the fracture properties of PNCs

The clay platelets used in PNCs are considered as linear elastic isotropic material and are not allowed to fracture [69]. A phase-field approach as described in [11] is employed to model quasi-brittle fracture in the epoxy matrix. A rigid bond between the clay reinforcement and the polymer matrix is adopted.

The total potential energy is decomposed into the surface energy (creation of crack surfaces) and the bulk energy.

$$\Psi = \Psi^s + \Psi^b \quad (3.1)$$

The surface energy in the phase-field approach is equal to the critical energy release rate (fracture energy), G_c multiplied by the cross sectional area, A , of the crack surface:

$$\Psi^s = G_c \int_{\Omega} \gamma(\phi) d\Omega = G_c \int_A \int_{-\infty}^{\infty} \gamma(\phi) dx dA = G_c A \quad (3.2)$$

the crack surface density function γ is calculated by

$$\gamma(\phi) = \frac{1}{2} \left[\ell_0 \frac{\partial \phi}{\partial x_i} \frac{\partial \phi}{\partial x_i} + \frac{1}{\ell_0} \phi^2 \right], \quad (3.3)$$

where ϕ denotes the phase-field and ℓ_0 is a parameter controls the amount of the crack diffusion.

Interestingly, the phase-field does not require any description of the crack topology as indicated by Eq. (3.2).

The bulk energy can be expressed in terms of the strain energy density for an isotropic linear elastic material, $\psi^e(\boldsymbol{\epsilon})$, and a stress degradation function, $g(\phi)$

$$\Psi^b = \int_{\Omega} g(\phi) \psi^e(\boldsymbol{\epsilon}) d\Omega \quad (3.4)$$

with

$$\begin{aligned} g(\phi) &= (1 - \phi)^2 + k, \\ \psi^e(\boldsymbol{\epsilon}) &= \frac{1}{2} \lambda \epsilon_{kk} \epsilon_{ll} + \mu \epsilon_{ij} \epsilon_{ij} \end{aligned} \quad (3.5)$$

3.2 Phase-field model for predicting the fracture properties of PNCs

where k is a parameter chosen to keep the system of equations well-conditioned, and λ and μ being the Lame constants.

It can be shown [8,9] that taking variation of Eq. (3.1) leads to the following weak form

$$\begin{aligned} \delta\Psi(\phi, \boldsymbol{\epsilon}) = & \int_{\Omega} [(1 - \phi)^2 + k] \sigma_{ij} \delta\epsilon_{ij} d\Omega + \int_{\Omega} -2(1 - \phi) \delta\phi \psi(\boldsymbol{\epsilon}) d\Omega \\ & + \int_{\Omega} G_c \left(\ell_0 \frac{\partial\phi}{\partial x_i} \frac{\partial\delta\phi}{\partial x_i} + \frac{1}{\ell_0} \phi \delta\phi \right) d\Omega \end{aligned} \quad (3.6)$$

Substituting the discretization of the phase field and the displacement field including their spatial derivatives into the weak form yields the following system of equations:

$$\begin{bmatrix} \mathbf{K}^{\mathbf{u}\mathbf{u}} & \mathbf{K}^{\mathbf{u}\phi} \\ \mathbf{K}^{\phi\mathbf{u}} & \mathbf{K}^{\phi\phi} \end{bmatrix} \begin{Bmatrix} \mathbf{u} \\ \phi \end{Bmatrix} = \begin{Bmatrix} \mathbf{r}^{\mathbf{u}} \\ \mathbf{r}^{\phi} \end{Bmatrix} \quad (3.7)$$

with

$$\mathbf{K}_{IJ}^{\mathbf{u}\mathbf{u}} = \frac{\partial \mathbf{r}_I^{\mathbf{u}}}{\partial \mathbf{u}_J} = \int_{\Omega} [(1 - \phi)^2 + k] \mathbf{B}_I^{\mathbf{u}T} \mathbf{C} \mathbf{B}_J^{\mathbf{u}} d\Omega \quad (3.8a)$$

$$\mathbf{K}_{IJ}^{\mathbf{u}\phi} = \frac{\partial \mathbf{r}_I^{\mathbf{u}}}{\partial \phi_J} = \int_{\Omega} -2(1 - \phi) \mathbf{B}_I^{\mathbf{u}T} \boldsymbol{\sigma} N_J d\Omega \quad (3.8b)$$

$$\mathbf{K}_{IJ}^{\phi\mathbf{u}} = \frac{\partial \mathbf{r}_I^{\phi}}{\partial \mathbf{u}_J} = \int_{\Omega} -2(1 - \phi) N_I \boldsymbol{\sigma}^T \mathbf{B}_J^{\mathbf{u}} d\Omega \quad (3.8c)$$

$$\mathbf{K}_{IJ}^{\phi\phi} = \frac{\partial \mathbf{r}_I^{\phi}}{\partial \phi_J} = \int_{\Omega} G_c \ell_0 \mathbf{B}_I^{\phi T} \mathbf{B}_J^{\phi} d\Omega + \left[\frac{G_c}{\ell_0} + 2\psi(\boldsymbol{\epsilon}) \right] N_I N_J d\Omega \quad (3.8d)$$

where \mathbf{u} and \mathbf{r} represent the displacement and the residual forces respectively. This system can be solved either in staggered or monolithic way. The former are usually more robust but require a stricter step size control. We have employed a monolithic approach which has been implemented into the commercial software package ABAQUS. The model is available at <http://abaqusphasefieldmodel.sourceforge.net>.

The representative volume element (RVE) constitutes of the epoxy matrix filled with randomly oriented and dispersed clay platelets. Initial parameters such as RVE dimensions, mesh size, the aspect ratio and curvature of the clay should be set-up in advance. Then, the clays are placed uniformly without overlapping or intersecting to generate the RVE [95].

In the present work, the fracture toughness was determined considering a double edge notched tension specimen with dimensions 750nm \times 1500nm and initial crack length of

3.2 Phase-field model for predicting the fracture properties of PNCs

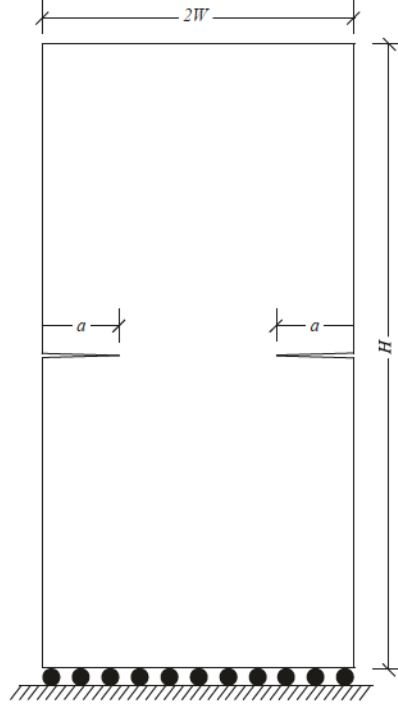


Figure 3.1.: The geometry of the double edge notched tension specimen

187.5 nm as shown in Fig. 3.1. The mode-I stress intensity factor, K_{Ic} , can be given by:

$$K_{Ic} = \frac{P_{max}}{B\sqrt{W}} f\left(\frac{a}{W}\right) \quad (3.9)$$

where P_{max} is the load at fracture, B is the sample thickness, W is the half of the sample width, a is the crack length, and $f(a/W)$ is a dimensionless function [7].

The definition of all the input parameters and their mean value, distribution type, and standard deviation are summarized in Table 3.1. The volume fraction of the clay platelets is varied from 0.5 - 5.0% assuming a Uniform distribution [154]. The range of the aspect ratio of sodium montmorillonite platelets is 200 - 400 nm according to [69] so its distribution is characterized by the Normal distribution with mean value of 300 nm and standard deviation of 6.71 nm. Based on high resolution TEM images of PNCs [69, 130], the histogram of the clay radius reveals that its probability density function is close to a Log-normal distribution with mean of 5.72 nm and standard deviation of 0.91 nm. The Young's modulus of the clay platelets is within the range of 178-265 GPa [155]. We consider its distribution as Normal with mean value of 221.5 GPa and standard deviation of 20 GPa. The Young's modulus of the epoxy matrix ranges from 1.96 to

3.3 Methods

Table 3.1.: Statistical properties of input parameters

Parameter	Definition (unit)	Distribution Type	Mean	Standard deviation	Ref.
V_f	The volume fraction of clay platelets (wt%)	Uniform	2.75	1.299	[154]
A_{cl}	The aspect ratio of the clay (nm)	Normal	300	6.71	[69]
r_{cl}	The radius of the curvature of the clay (nm)	Log-normal	5.72	0.91	[69, 130]
E_{cl}	The Young's modulus of the clay (GPa)	Normal	221.5	20	[155]
E_m	The Young's modulus of the matrix (GPa)	Normal	2.85	0.5	[156]
G_{Im}	The fracture energy of the matrix (J/m ²)	Normal	220	45	[156]

3.53 GPa [156], which can be represented by a Normal distribution with mean value and standard deviation of 2.85 and 0.5 GPa, respectively. A Normal distribution for the epoxy matrix fracture energy is assumed with 220 and 45 J/m² for the mean value and standard deviation [156].

3.3. Methods

3.3.1. Uncertainty Analysis

The uncertainty in the model input parameters inherently creates variation in the model output. Quantifying such variation requires the determination of: range, mean, median and standard deviation of the model output. This can be achieved through estimating the probability density function (PDF) as well as the cumulative distribution function (CDF) for the model output [157].

3.3.2. Sensitivity analysis

Sensitivity analysis (SA) is the study of how much the model output is affected by changes in the model inputs [29]. Although, a variety of SA methods are available in the literature, five methods are implemented in this study. Of these, the first four were chosen due to their popularity and their common application in a variety of scientific domains while the fifth is a new method based on probability density. In order to ensure the reliability of the SA and uncertainty quantification (UQ) we compare the results

of the different methods. In each SA method, the model output \mathbf{Y} is expressed as $\mathbf{Y} = f(X_i)$.

Latin Hypercube Sampling (LHS) [30] is an improved sampling strategy that enables a reliable approximation of the stochastic properties even for a small number of samples. LHS will be used to provide the design points which are spread throughout the design space. The base of the method is the subdivision of the design space of a variable X_i into N classes D_m of equal probability:

$$P[X_i \in D_m]; \quad i = 1, \dots, k; \quad m = 1, \dots, N \quad (3.10)$$

where N and k are the number of samples and the number of input parameters, respectively.

3.3.2.1. Standardized Regression Coefficients

Standardized regression coefficients (SRC) is a screening method which is based on linear regression analysis. The output, $\mathbf{Y} = f(X_1, \dots, X_k)$ is computed using the mechanical model for the input parameters $\mathbf{X} = (X_1, \dots, X_k)$. Once the regression coefficient β_i is computed for the i -th input parameter, X_i , the value of SRC_i can be calculated as

$$SRC_i = \beta_i \frac{\sigma_i}{\sigma_y} \quad (3.11)$$

with σ_i and σ_y being the standard deviations of X_i and \mathbf{Y} , respectively. The larger the value of SRC_i , the more sensitive the model with respect to the input parameter X_i . This method is effective for models with high coefficient of determination, R^2 . In case of fully linear models, i.e. $R^2 = 1$, the SRCs exactly quantifies the amount of the output variance explained by each input parameter. It can still be used to evaluate the parameters' significance for moderately non-linear models ($R^2 \geq 0.7$). However, the regression analysis is inappropriate for smaller values of R^2 [158].

3.3.2.2. Regionalized Sensitivity Analysis

The Regionalized Sensitivity Analysis (RSA) is mainly based on a Monte Carlo sampling of the parameter space. The sample is divided into acceptable and unacceptable subsets according to a given criterion for the output. Commonly, the terms of these two subsets in the literature are behavioral (B) and non-behavioral (\bar{B}) [29, 39].

For a set of N Monte Carlo simulations, two subsets are produced by applying a prede-

3.3 Methods

defined condition which classify the model realizations into acceptable and unacceptable outputs. They are $(X|B)$ and $(X|\bar{B})$ of sizes N_b and N_n , where $N_b + N_n = N$. The probability density functions of each individual parameter in both subsets, $f_{N_b}(X_i|B)$ and $f_{N_n}(X_i|\bar{B})$, are compared. The parameter X_i is influential if it has two significantly different distributions [29]. Considering the null hypothesis that the two distributions are identical, the so called *Kolmogorov – Smirnov test statistic* (D_i) [38] is defined as the maximum vertical distance between the two cumulative distributions to measure the statistical difference between the two subsets:

$$\begin{aligned} H_0 &: f_{N_b}(X_i|B) = f_{N_n}(X_i|\bar{B}) \\ H_1 &: f_{N_b}(X_i|B) \neq f_{N_n}(X_i|\bar{B}) \\ D_i &= \max |F_{N_b}(X_i|B) - F_{N_n}(X_i|\bar{B})| \end{aligned} \quad (3.12)$$

where $F_{N_b}(X_i|B)$ and $F_{N_n}(X_i|\bar{B})$ are the cumulative distribution functions for X_i in the behavioral and non-behavioral realizations. Their difference can be neither lower than zero nor higher than one, and hence, D_i has the range of [0-1]. Clearly, the D_i index depends on the given criterion, so the RSA can be considered as a screening rather than a quantitative method [40].

3.3.2.3. Sobol' Method

The Sobol' method which is based on variance decomposition, is one of the most commonly used GSA approaches. It depends on the variance decomposition of the output \mathbf{Y} [31]:

$$V(\mathbf{Y}) = \sum_{i=1}^k V_i + \sum_{i=1}^k \sum_{j=i+1}^k V_{ij} + \dots + V_{12\dots k} \quad (3.13)$$

where V_i is the main effect (the first-order) of X_i on \mathbf{Y} and V_{ij} , known as the second-order effect, is the joint effect of X_i and X_j minus their first-order effects. The first-order sensitivity index (S_i) that measures the part of the variance of the model output with respect to the input X_i is defined as

$$S_i = \frac{V[E(\mathbf{Y}|X_i)]}{V(\mathbf{Y})} \quad (3.14)$$

with $V[E(\mathbf{Y}|X_i)]$ being the variance of the conditional expected value of \mathbf{Y} with respect to X_i and $V(\mathbf{Y})$ is the unconditional variance of \mathbf{Y} .

Accounting for the first-order effect of the input X_i added to all of its higher-order effects

due to interactions with other parameters, the total effect sensitivity index (S_{Ti}) is given by

$$S_{Ti} = \frac{E[V(\mathbf{Y}|X_{\sim i})]}{V(\mathbf{Y})} = 1 - \frac{V[E(\mathbf{Y}|X_{\sim i})]}{V(\mathbf{Y})} \quad (3.15)$$

where $X_{\sim i}$ denotes all the input parameters but X_i [29]. The total effect index S_{Ti} is used to estimate how much the variation in the input parameters X_i contributes to the variation in the output. In other words, it is equal to the total value of the first-order term in addition to all high-order terms [93].

$$S_{Ti} = S_i + S_{i,\sim i} = 1 - S_{\sim i} \quad (3.16)$$

The difference between S_{Ti} and S_i represents a measure of how much X_i interacts with other input parameters.

Saltelli [32] developed a method to calculate the first order and total effect indices with disregarding the second effect of Sobol' method. Two independent sampling matrices \mathbf{A} and \mathbf{B} of dimension $(N \times k)$ are generated, where N is called a base sample and k is the number of input parameters. Afterwards, a matrix $\mathbf{B}_A^{(i)}$ is defined with entries from \mathbf{B} except the i -th column, which is taken from \mathbf{A} . Once generated, the model output can be calculated for the matrices \mathbf{A} , \mathbf{B} , and $\mathbf{B}_A^{(i)}$ with total computational cost of $N(k+2)$. The approximated unconditional variance, conditional variance with respect to X_i , and conditional variance of all inputs but X_i are given by

$$V(\mathbf{Y}) = \frac{1}{N} \sum_{j=1}^N \left(f(\mathbf{A})_j \right)^2 - f_0^2 \quad (3.17)$$

$$V[E(\mathbf{Y}|X_i)] = \frac{1}{N} \sum_{j=1}^N f(\mathbf{A})_j f(\mathbf{B}_A^{(i)})_j - f_0^2 \quad (3.18)$$

$$V[E(\mathbf{Y}|X_{\sim i})] = \frac{1}{N} \sum_{j=1}^N f(\mathbf{B})_j f(\mathbf{B}_A^{(i)})_j - f_0^2 \quad (3.19)$$

3.3 Methods

with

$$f_0 = \frac{1}{N} \sum_{j=1}^N f(\mathbf{A})_j \quad (3.20)$$

3.3.2.4. Extended Fourier Amplitude Sensitivity Test (EFAST)

Classical Fourier amplitude sensitivity test (FAST) is a variance-based method for sensitivity analysis first presented by Cukier et al. [35]. It transforms a k -dimensional integral into a one-dimensional integral by using a set of parametric equations. Although the classical FAST is limited only to evaluate the first order sensitivity indices, recently an extension of FAST method (EFAST) was proposed to evaluate also the total-effect sensitivity index by [36]. For the input parameter X_i , the transformation (search) function is

$$X_i = F^{-1} \left(\frac{1}{2} + \frac{1}{\pi} \arcsin(\sin(\omega_i s + \varphi_i)) \right) \quad (3.21)$$

where F^{-1} is the inverse CDF, ω_i is a set of integer frequencies, s is a parametric variable varying over the range $[-\pi, \pi]$ and φ_i is a random phase-shift chosen uniformly in the range of $(0, 2\pi)$. Through the derived search function, $f(X_1(s), X_2(s), \dots, X_k(s))$ is transformed into a periodic function $f(s)$. Whenever φ_i 's are positive integers, the period is 2π . Consequently $f(s)$ can be expanded into a Fourier series as [96]

$$\mathbf{Y} = f(s) = \sum_{n=1}^{\infty} \{A_n \cos(ns) + B_n \sin(ns)\} \quad (3.22)$$

with A_n and B_n are the Fourier coefficients given by

$$\begin{aligned} A_n &= \frac{1}{2\pi} \int_{-\pi}^{\pi} f(s) \cos(ns) ds \\ B_n &= \frac{1}{2\pi} \int_{-\pi}^{\pi} f(s) \sin(ns) ds \end{aligned} \quad (3.23)$$

and $n = 1, \dots, (N_s - 1)/2$ with N_s is the size of the sample.

The variance of the model output is approximated by

$$V(\mathbf{Y}) = 2 \sum_{n=1}^{(N_s-1)/2} (A_n^2 + B_n^2) \quad (3.24)$$

To evaluate the spectrum A_n and B_n , a certain frequency, ω_i , for the i -th parameter and a different frequency $\omega_{\sim i}$ for the complementary set including all of the remaining parameters are assigned. Then, the partial variance $V_{\sim i}(\mathbf{Y})$ can be estimated for the fundamental integer frequency $\omega_{\sim i}$ and its higher harmonics $p\omega_{\sim i}$:

$$V_{\sim i}(\mathbf{Y}) = 2 \sum_{p=1}^M (A_{p\omega_{\sim i}}^2 + B_{p\omega_{\sim i}}^2) \quad (3.25)$$

The inference factor M adopted here is set to 4 (usually 4 or 6).

The partial variance $V_i(\mathbf{Y})$ is obtained in a similar way. The minimum sample size to be used is $N_s = N_r(2M\omega_{max} + 1)$, where N_r denotes the number of used curves and ω_{max} is the largest frequency among the set of ω_i frequencies. The first order S_i and the total effect index S_{T_i} are then calculated using Eqs. (3.14) and (3.15).

3.3.2.5. The PAWN method

Unlike the variance based methods, density-based sensitivity indices are related to the distribution of the model output rather than its variance. PAWN is a simple approach proposed recently by Pianosi and Wagener [37] to derive a density-based sensitivity index considering the CDF of the output. The difference between the unconditional and the conditional CDF represents the sensitivity of the parameter X_i . This difference can be calculated by *Kolmogorov – Smirnov statistic* [38] which is denoted here by KS

$$KS = \max |F(\mathbf{Y}) - F(\mathbf{Y} | X_i)| \quad (3.26)$$

where $F(\mathbf{Y})$ and $F(\mathbf{Y} | X_i)$ are the unconditional and the conditional CDF approximated by a sample of size N_u and N_c , respectively. The unconditional sample is generated randomly in the space of the inputs; whereas, the conditioned one is achieved by varying all inputs while setting X_i fixed n times. The index T_i which can be the maximum or the median over all the fixed values for the parameter X_i is defined as:

$$T_i = \text{stat}[KS(X_i)] \quad (3.27)$$

Trial-and-error is proposed to select the value for n , N_u , and N_c , and $N_u + knN_c$ is the required total model runs (computational cost) [37]. Even for a small number of inputs, a prohibitively large number of total model run required when increasing N_c in the order of few thousands to achieve convergence (as will be discussed in Section 3.3.3).

3.3 Methods

Table 3.2.: Characteristics summary of the implemented SA methods

Method		Computation Cost ^a	Screening/ Quantitative	Parameters interactions
Standardized Regression Coefficients	Regress-	N	Screening	No
Regionalized Sensitivity Analysis	Sensiti-	N	Screening	No
Sobol'		$N(k + 2)$	Quantitative	Yes
EFAST		$kN_r (2M\omega_{max} + 1)$	Quantitative	Yes
PAWN		$N_u + knN_c$	Quantitative	Yes
Improved PAWN		$150(1 + 10k) + N(1 + k)$	Quantitative	Yes

^a N : base sample size.

k : number of input parameters.

M and ω_{max} : the inference factor and the largest frequency.

N_u : and N_c : sample sizes to estimate the unconditional and conditional CDF.

n : number of conditioning points.

In this study, we present an improved PAWN method to reduce the computational cost. It requires the following steps:

- Step 1- The values of $N_u = N_c$ and n are fixed at a pre-specified small value, e.g. 150 and 10.
- Step 2 - The conditional vector of \mathbf{X} which produces the maximum KS is found.
- Step 3- By using the fixed conditional value of \mathbf{X} resulted from Step 2, the number of model runs is increased and the convergence of T_i is investigated.

Hence, the input parameter is fixed at one time ($n = 1$) to calculate the sensitivity index T_i in Eq. (3.27). Since there is only one conditional value, T_i will be equal to KS calculated from Eq. (3.26). The computational cost is reduced to $\{150(1 + 10k) + N(1 + k)\}$.

3.3.2.6. Summary

A summary of the implemented SA methods is listed in Table 3.2 including the comparison of their computation cost, the sensitivity category and the ability to deal with parameters interactions.

3.3.3. Convergence

The sampling techniques of the SA are based on a random selection of the input parameters values from its distribution ranges. The total model runs (Sample size) is of an essential object in determining the different sensitivity indices. For limited samples, the uncertainties in the estimated sensitivity indices are more pronounced. However, big samples will be tedious specially for complex models [159]. Hereafter, the proper sample size is determined by observing the convergence and reproducibility of results. To achieve convergence, the evolution of sensitivity indices while increasing the computational cost is investigated. Then, by employing the bootstrap technique [160], the adopted sample size is resampled with replacement B times, and the indices are calculated for each resampling. The value of $B = 1000$ replications is exploited [161], and accordingly, the distributions and their 95% confidence intervals (CI's) for the sensitivity indices are obtained, from which the mean values are considered to represent the sensitivity indices.

3.3.4. Uncertainty quantification

The SA determines how the model output uncertainty is affected by the input parameters. It can define the input parameters that, once fixed, lead to the greatest reduction in the variance of the output, as well the inputs which have negligible influence on the output. To evaluate the effectiveness of the SA methods, three parameter sets, have been constructed: i) Set $G1$ composed of sample of size 1000 drawn randomly, ii) Set $G2$ is the same as $G1$ for the non-important parameters, but the important parameters are fixed to predefined values. iii) Set $G3$ in which the non-important parameters are fixed and the important parameters match $G1$.

The parameters classification as important and non-important is considered proper if the correlation coefficient between the model outputs of $G2$ and $G1$ is close to zero and between the model outputs of $G3$ and $G1$ is close to one. In this case, plotting the outputs of $G2$ in the Y-axis versus $G1$ in the X-axis will produce a horizontal trend, while $G3$ versus $G1$ will produce a linear increasing trend with slope 1. Moreover, the variation of the output of $G1$ and $G3$ are almost the same, but it is considerably lower for $G2$.

3.3.5. Surrogate models

Surrogate models, also known as Meta-models, are commonly used to represent the mechanical models in order to reduce the computational cost. To be built, the mechanical model needs to be evaluated multiple times considering the PDF of the input parameters.

3.3 Methods

Hereafter, the popular polynomial regression method is exploited, where the mechanical model is approximated by linear (LR), quadratic (QR) and quadratic with mixed term (QMR) polynomial regression models with basic function $Z = [X_1, X_2, \dots, X_k, X_1^2, X_2^2, \dots, X_k^2, X_1X_2, \dots, X_{k-1}X_k]$. The SA is done based on the surrogate model. Let $\hat{\mathbf{Y}}$ be the linear polynomial regression approximation of the response of the mechanical model \mathbf{Y} and let $\mathbf{X} = (X_1, X_2, \dots, X_k)$ be the input parameters with the basic function $Z = [X_1, X_2, \dots, X_k]$. Then $\hat{\mathbf{Y}}$ can be expressed by

$$\hat{\mathbf{Y}} = \beta_0 + \sum_{i=1}^k \beta_i X_i + \mathbf{e} \quad (3.28)$$

where $\boldsymbol{\beta}$ is the regression coefficient vector and \mathbf{e} is the residual error term that is the difference between the actual values for mechanical model \mathbf{Y} and the values estimated by regression model $\hat{\mathbf{Y}}$. The vector $\hat{\boldsymbol{\beta}}$ is estimated by minimizing the sum of residual squares [26]:

$$\hat{\boldsymbol{\beta}} = \left[[\mathbf{X}]^T [\mathbf{X}] \right]^{-1} \left\{ [\mathbf{X}]^T [\mathbf{Y}] \right\} \quad (3.29)$$

The higher order regression approaches, i.e. QR and QMR are constructed in similar manner.

To describe how well the surrogate model can represents the mechanical model, the coefficient of determination (R^2) is evaluated by

$$R^2 = 1 - \frac{SS_E}{SS_Y} \quad (3.30)$$

with

$$SS_E = (\mathbf{Y} - \hat{\mathbf{Y}})^T (\mathbf{Y} - \hat{\mathbf{Y}}); \quad SS_Y = (\mathbf{Y} - \bar{Y})^T (\mathbf{Y} - \bar{Y}) \quad (3.31)$$

where \bar{Y} is the the mean value of \mathbf{Y} .

The closer R^2 to one, the better the surrogate model performance.

To account for the number of training points, N , as well the number of regression coefficients (k_R), the adjusted coefficient of determination (R_{adj}^2) is presented

$$R_{adj}^2 = 1 - \frac{N-1}{N-k_R} (1 - R^2) \quad (3.32)$$

Table 3.3.: R^2 and R_{adj}^2 values for the surrogate models.

Surrogate model	R^2	R_{adj}^2
Linear regression (LR)	0.872	0.826
Quadratic regression (QR)	0.897	0.860
Quadratic with mixed term (QMR)	0.934	0.910

If N is significantly larger than k_R , both coefficients will be equal.

Once built with accepted R^2 , surrogate models are exploited to perform the SA instead of the mechanical model.

3.4. Results

3.4.1. Simulation results of Phase-field model

As detailed in Section 3.2, a total of six input parameters has been used to predict the fracture toughness of PNCs using phase-field model. Exemplary, for a randomly selected sample, the contour plots of the phase field model (i.e. the crack propagation) at different load steps are illustrated in Figs. 3.2a to 3.2c. The corresponding load displacement curve is shown in Fig. 3.2d.

20,512 elements were used for this sample, and the CPU time is about 22,830 seconds (6.34 hours.) on a 4 x Twelve-Core AMD Opteron™ Processor of HP ProLiant DL585 G7 system.

As an alternative approximation for the response of the mechanical model, the surrogate models were constructed based on LR, QR and QMR regression. First, the samples were generated based on LHS, and the fracture toughness were calculated using the mechanical model. Then, the R^2 values were evaluated. Fig. 3.3 illustrates the R^2 values versus the size of samples. The stochastic convergence is assumed at a sample size of 10^2 . At this size, the corresponding estimated R^2 and R_{adj}^2 are shown in Table 3.3. The R^2 values are 0.872, 0.897, and 0.934 for LR, QR, and QMR, respectively, indicating that the surrogate models are good approximations of the mechanical model response.

Fig. 3.4 presents a scatter plots depicting the predicted outputs of the mechanical model against all the input parameters. The matrix Young's modulus is clearly the most influential parameter.

3.4 Results

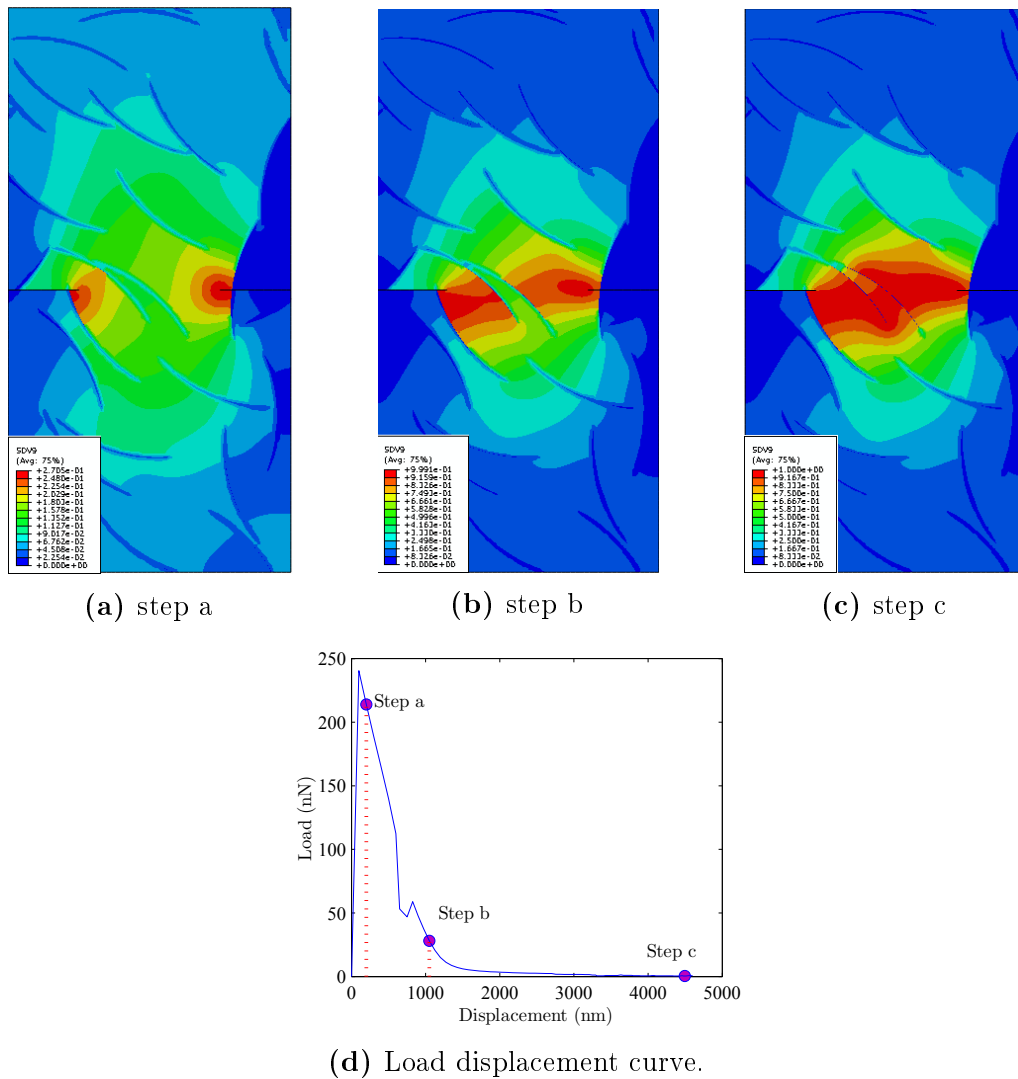


Figure 3.2.: Contour plots and load displacement curve of randomly selected sample (No. of elements=20,512, job time= 22,830 seconds). SDV refers to the phase field parameter (ϕ) with 0.0 and 1.0 indicate, respectively, to non damaged and totally damaged elements. For color version of this figure, the reader is referred to the web version of this article.

3.4.2. Uncertainty Analysis

The histogram for the data distribution of the mechanical model output and the assumed probability distribution functions are shown in Fig. 3.5. The mean value of the fracture toughness is $869.76 \text{ KPa}\cdot\sqrt{\text{m}}$ and its coefficient of variation (COV) is 15.39% (Table 3.4). Three different distributions are assumed to represent K_{Ic} , i.e. Normal, Log-normal, and Weibull, and the parameters of these distributions are included in Table 3.5. The distribution is chosen as a goodness-of-fit of the data, when its cumulative probability plot has the least deviations [162]. In other words, the best fitted distribution of the

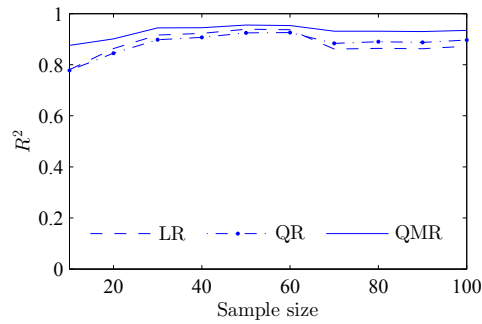


Figure 3.3.: The plot of R^2 versus the number of model simulations (sample size, N).

data is the distribution with the least sum of residual squares (SS_E). The cumulative

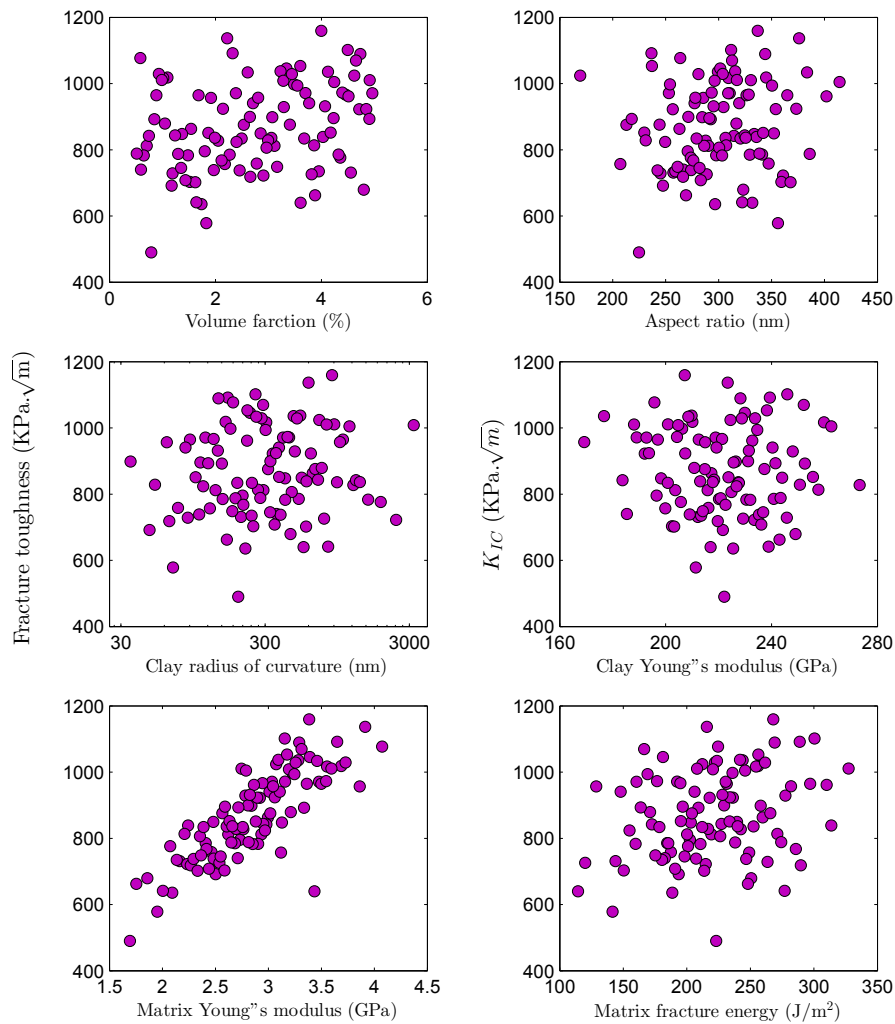


Figure 3.4.: Scatter plots of fracture toughness predicted by the mechanical model versus the input parameters

3.4 Results

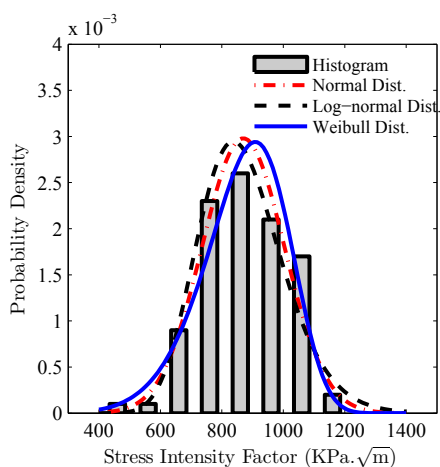


Figure 3.5.: Histogram of the mechanical output and the assumed probability density functions.

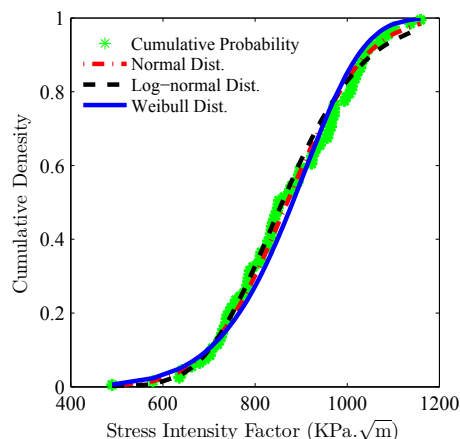


Figure 3.6.: Cumulative probability plots for different types of distributions.

probability plots are depicted in Fig. 3.6, whereas Table 3.5 lists the computed SS_E values. Obviously, the Weibull PDF provides the highest error ($SS_E = 0.191$), while the Normal and Log-normal probability are good approximations with almost the same SS_E equal to 0.077 and 0.075, respectively.

3.4.3. Sensitivity Analysis

According to Section 3.4.1, the highest R^2 is obtained by QDR surrogate model. Consequently, it will be utilized to approximate the output of the mechanical model in

Table 3.4.: Mean, Standard deviation, and COV of the Output.

Output	Mean	Standard deviation	COV
K_{Ic} (KPa.√m)	869.76	133.88	15.39%

Table 3.5.: Uncertainties of mechanical output using the assumed distributions.

	Normal PDF	Log-normal PDF	Weibull PDF
Parameter 1	Mean	Mean	Scale parameter
	869.76	6.75	922.86
Parameter 2	Standard deviation	Standard deviation	Shape parameter
	133.88	0.16	8.01
Error (SS_E)	0.077	0.075	0.191

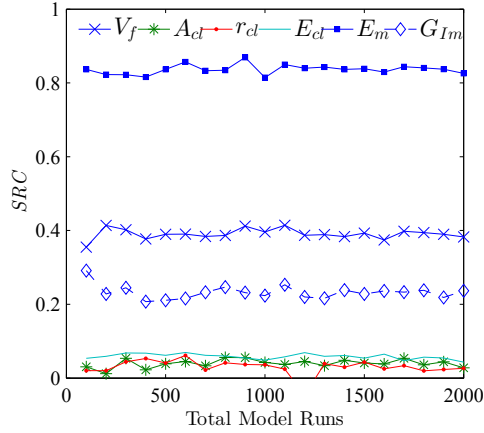


Figure 3.7.: Convergence of SRC method.

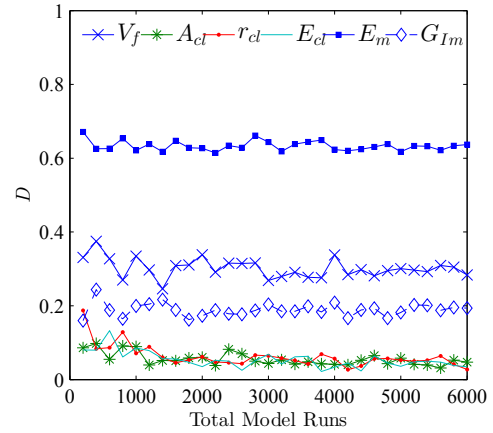


Figure 3.8.: Convergence of RSA method.

Table 3.6.: Sensitivity indices based on SRCs method.

Input parameters	SRC_i	95% CI	Rank
V_f	0.392	(0.392,0.393)	2
A_{cl}	0.039	(0.038,0.039)	5
r_{cl}	0.028	(0.027,0.029)	6
E_{cl}	0.057	(0.056,0.057)	4
E_m	0.833	(0.832,0.833)	1
G_{Im}	0.230	(0.230,0.231)	3

the following SA methods.

Different base sample sizes, N , have been compared as shown in Fig. 3.7 to evaluate $SRCs$. Clearly, 1,200 model run evaluated by the QDR surrogate model for each independent replica can be sufficient to obtain stable sensitivity indices. For this sample size, the converged $SRCs$, 95% CIs, and the rankings estimated based on the bootstrap technique are listed in Table 3.6. The most important parameter is the Young's modulus of the matrix (E_m) with $SRC = 0.833$, while the volume fraction of clay platelets (V_f) and the fracture energy of the matrix (G_{Im}) have moderate effects with SRC equal to 0.392 and 0.230, respectively. The aspect ratio (A_{cl}), the radius of the curvature (r_{cl}), and the Young's modulus of the clay platelets (E_{cl}) have insignificant effects on the output.

Fig. 3.8 shows the convergence of the D test of RSA method. It is achieved for a sample size of 5,000. The calculated indices are listed in Table 3.7. RSA also finds

3.4 Results

E_m as the most influential input parameter for the fracture toughness with $D = 0.632$ followed by V_f and G_{Im} . Though the 95% CI of A_{cl} and r_{cl} are almost identical, both of them have negligible effects. In Fig. 3.9, the CDF is represented by dotted lines for the behavioral set and solid lines for the non-behavioral set. The insignificance of A_{cl} , r_{cl} , and E_{cl} manifests in almost coincided dotted and solid lines.

The total effect sensitivity indices (S_T) of Sobol' method converge at a base sample size around 5,500 which is equivalent to 44,000(=5,500(6+2)) total model runs for each

Table 3.7.: Sensitivity indices based on RSA method.

Input parameters	D_i	95% CI	Rank
V_f	0.295	(0.294,0.295)	2
A_{cl}	0.047	(0.046,0.048)	4
r_{cl}	0.046	(0.045,0.047)	5
E_{cl}	0.041	(0.040,0.042)	6
E_m	0.632	(0.631,0.632)	1
G_{Im}	0.189	(0.188,0.189)	3

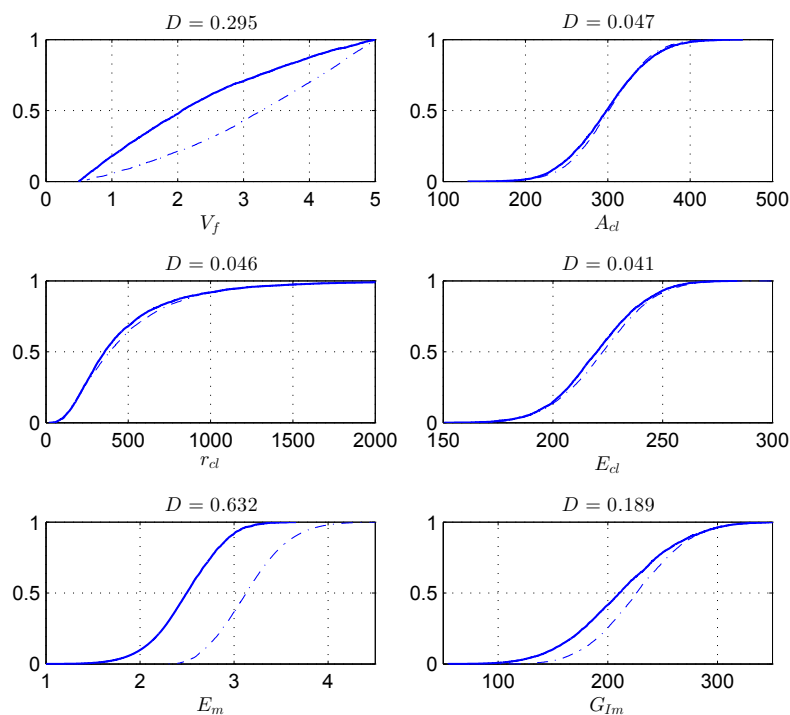


Figure 3.9.: The CDF of the behavioral (dotted line) set and non-behavioral set (solid line) for the input parameters.

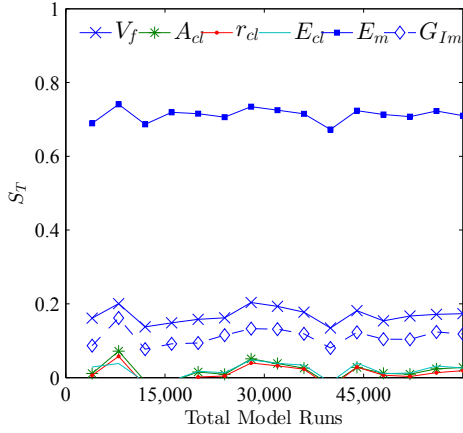


Figure 3.10.: Convergence of Sobol' method.

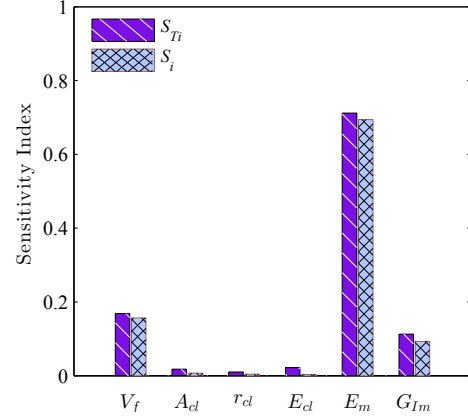


Figure 3.11.: First-order and total-effect sensitivity indices of Sobol' method.

independent replica (see Fig. 3.10). For non-influential factors, the negative signs appear due to numerical errors in the estimations. The total effect and first-order indices are given in Fig. 3.11. Table 3.8 contains the total and main effect indices and its 95% CIs. The ranking in the last column is based on the total effect, and apparently E_m outranks all other parameters, followed by V_f , and G_{Im} . There are no overlaps between their 95% CIs unlike the remaining insignificant parameters; A_{cl} , r_{cl} , and E_{cl} . The results of S_T were 0.712, 0.168, and 0.113 for E_m , V_f , and G_{Im} , respectively. Whereas the main effect of these parameters constitutes 94.4% ($= 0.694+0.157+0.093$) of the total variation of the output. The effects of the parameters interactions ($S_{Ti} - S_i$) are almost negligible indicating no interactions between input parameters.

For the EFAST method, we have selected $N_r = 10$ which makes the convergence more stable. Fig. 3.12 shows the convergence of S_T . Compared to Sobol' method, the

Table 3.8.: Sensitivity indices based on Sobol' method.

Input parameters	Total Effect		Main Effect		Rank
	S_{Ti}	95% CI	S_i	95% CI	
V_f	0.168	(0.165,0.172)	0.157	(0.155,0.158)	2
A_{cl}	0.018	(0.014,0.021)	0.007	(0.005,0.009)	5
r_{cl}	0.010	(0.007,0.014)	0.004	(0.002,0.006)	6
E_{cl}	0.022	(0.018,0.025)	0.003	(0.002,0.005)	4
E_m	0.712	(0.709,0.715)	0.694	(0.693,0.696)	1
G_{Im}	0.113	(0.109,0.116)	0.093	(0.091,0.094)	3

3.4 Results

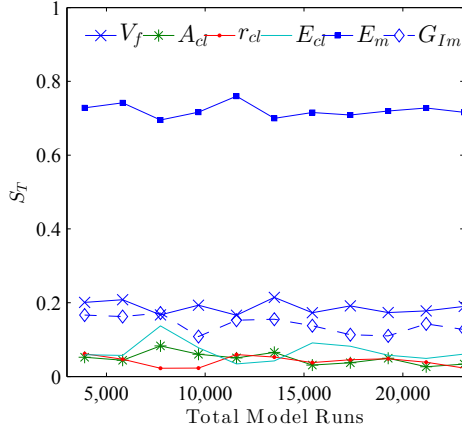


Figure 3.12.: Convergence of EFAST method.

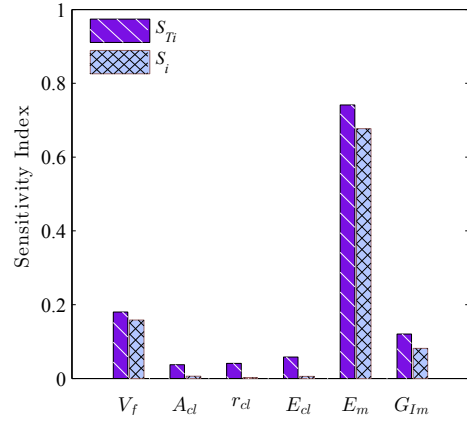


Figure 3.13.: First-order and total-effect sensitivity indices of EFAST method.

total effects of the inputs can be estimated quite reliably for a smaller number of model runs. The convergence is achieved at 19,260 total model runs for maximum frequency, $\omega_{max} = 40$. The computed total and first-order indices after bootstrapping are included in Fig. 3.13 and Table 3.9.

The calculations of the PAWN method were carried out using the Safe Matlab toolbox [163]. The number of conditioning values, n , for each parameter are set to be 10, while N_u and N_c are both set equal to 150. Fig. 3.14 displays the *Kolmogorov – Smirnov statistic*, KS , for the 10 different conditioning values that were sampled from the space of variation for each of X_i . The dashed horizontal line at $KS = 0.157$ is the critical value of KS considering the confidence level $\alpha = 0.05$ [137]. At this significance level, all the values of KS for A_{cl} , r_{cl} , and E_{cl} are below the critical KS , which confirms that they are non-influential parameters.

Table 3.9.: Sensitivity indices based on EFAST method.

Input parameters	Total Effect		Main Effect		Rank
	S_{Ti}	95% CI	S_i	95% CI	
V_f	0.180	(0.179,0.181)	0.158	(0.157,0.159)	2
A_{cl}	0.037	(0.037,0.038)	0.006	(0.006,0.006)	6
r_{cl}	0.041	(0.040,0.042)	0.003	(0.002,0.003)	5
E_{cl}	0.058	(0.057,0.059)	0.006	(0.006,0.006)	4
E_m	0.741	(0.740,0.743)	0.677	(0.675,0.679)	1
G_{Im}	0.121	(0.120,0.122)	0.081	(0.081,0.082)	3

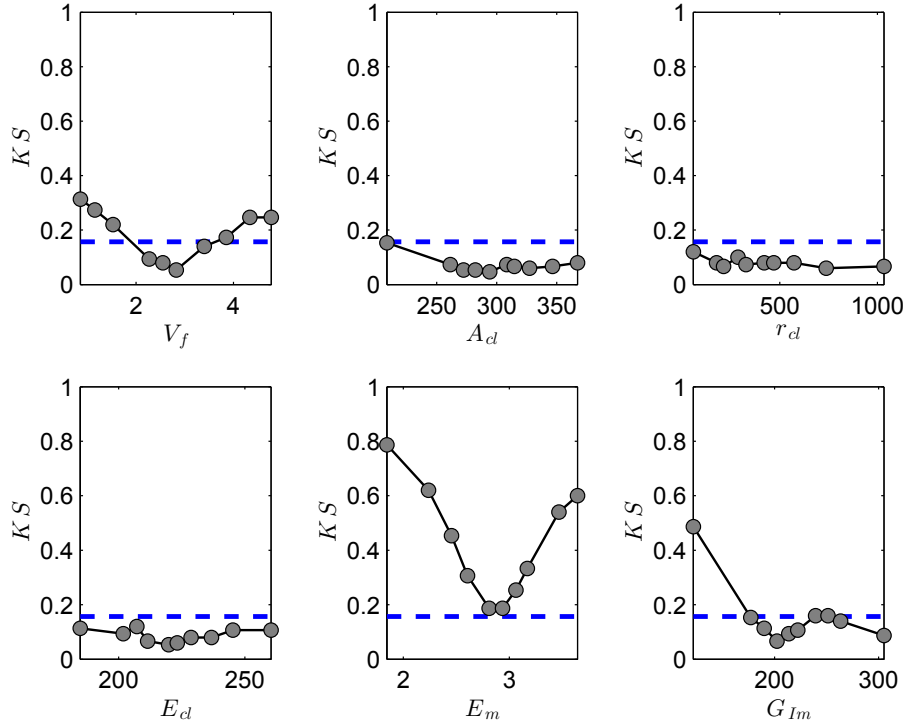


Figure 3.14.: *Kolmogorov – Smirnov statistic (KS)* at different conditioning values of X_i ($n = 10$).

Based on the median statistic, Fig. 3.15a displays the convergence of the PAWN indices with increasing the total model runs. The ranking of the parameters are clear but the T index of E_m does not converge to a specific value. When considering the maximum statistic (Fig. 3.15b), the T indices highly fluctuate even for a large sample size.

The maximum KS occurs at the left margin for G_{Im} whereas it occurs at left and right margins for V_f and E_m ranges as shown in Fig. 3.14. Thus, the vector of the conditional values in our improved PAWN approach will be $\mathbf{X} = \{0.5, 200, 1000, 178, 1.96, 100\}$. Fig. 3.15c displays the convergence of the T indices. Obviously, the T indices of the improved PAWN converge faster.

For $N = N_u = N_c = 1100$, the required model runs for both PAWN methods (based on median and maximum statistic) are equal 67,100, while the improved PAWN approach needs only 16,850 model runs. Table 3.10 includes the average sensitivity indices (T), the 95% CIs, and the rankings: E_m has the highest sensitivity index equal to 0.355, 0.742, and 0.733 based on median statistic, maximum statistic, and improved approach, respectively. Similar to the previous SA methods, V_f lies in the second position in ranking based on the median statistic, whereas it is in the third position based on

3.4 Results

the maximum statistic and improved approach. Also the ranking of the insignificant parameters changed.

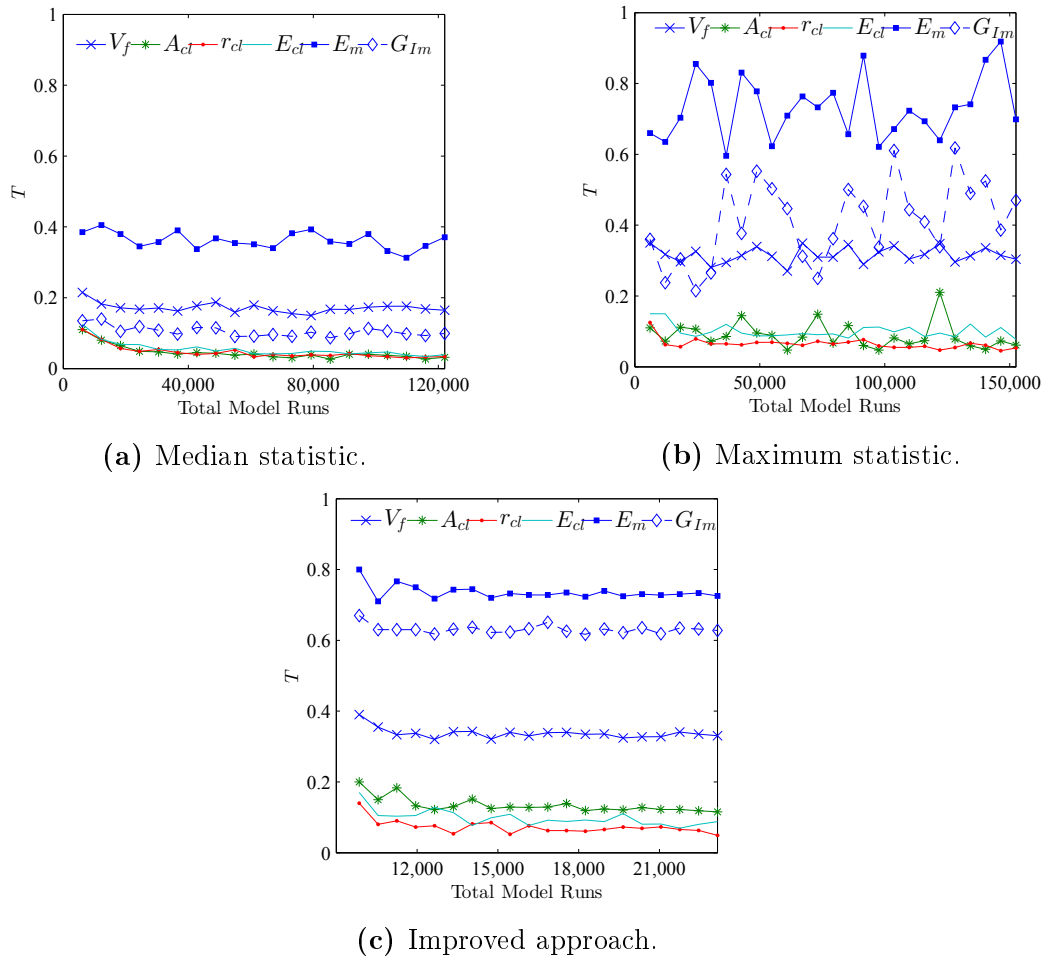


Figure 3.15.: Convergence of PAWN method.

Table 3.10.: Sensitivity indices based on PAWN method.

Input parameters	Median statistic		Maximum statistic		Improved approach		Rank ^a
	T	95% CI	T	95% CI	T	95% CI	
V_f	0.165	(0.165, 0.166)	0.321	(0.320, 0.323)	0.336	(0.335, 0.337)	3
A_{cl}	0.037	(0.037, 0.037)	0.092	(0.090, 0.095)	0.127	(0.126, 0.127)	4
r_{cl}	0.038	(0.038, 0.038)	0.071	(0.069, 0.072)	0.065	(0.064, 0.065)	6
E_{cl}	0.046	(0.046, 0.046)	0.105	(0.103, 0.106)	0.094	(0.094, 0.095)	5
E_m	0.354	(0.353, 0.355)	0.749	(0.744, 0.754)	0.732	(0.732, 0.733)	1
G_{Im}	0.100	(0.099, 0.100)	0.367	(0.358, 0.375)	0.628	(0.628, 0.629)	2

^aThe rank is based on the Total Improved approach

Across the various applied SA methods, we can conclude that the matrix Young's modulus was the most influencing parameter followed by the clay platelets volume fraction and the matrix fracture energy. Within this context, it is worth to restate that we assumed a rigid connection between the clay reinforcement and the polymer matrix. Though, the extent of the impact of clay/polymer interface is principally influenced by the manufacturing techniques as well the curing process. Thereby, a strong or week interface bond can be achieved [164]. Accordingly, in the future, we will construct a phase model considering an interphase zone surrounding the clay platelets. The influence of the size and properties of this zone will be quantified by replicating the approach outlined in this study.

In summary:

- The SRCs and RSA methods qualitatively determined the significant input parameters with few model runs (1,200 and 5,00).
- At higher computational cost, the quantitative methods of Sobol' and EFAST measured the impact of main and total effect of the inputs on the variance of the model output. However, the Sobol' method required about two times model runs more than EFAST method.
- The required time for Sobol' method was about 5068.5 seconds (1.42 hours) considering the QMR surrogate model, which is much lower than the required time to run *one* mechanical model sample.
- The classical PAWN method that is based on median and maximum statistic required considerable cost, while the improved PAWN showed a faster convergence.
- The improved PAWN showed a faster convergence in comparison to the classical PAWN.
- Similar classification of the parameters importancy can be drawn as a general finding.

3.4.4. Quantifying the uncertainty in the fracture toughness of PNCs

According to the results of the SA approaches implemented in this study, the input parameters are classified into two groups: important and non-important parameters. The first group includes: E_m , V_f , and G_{Im} , while the second includes: A_{cl} , r_{cl} , and E_{cl} . A Set $G1$ of size 1000 was randomly generated by LHS (see Section 3.3.4). Then Set

3.5 Conclusion

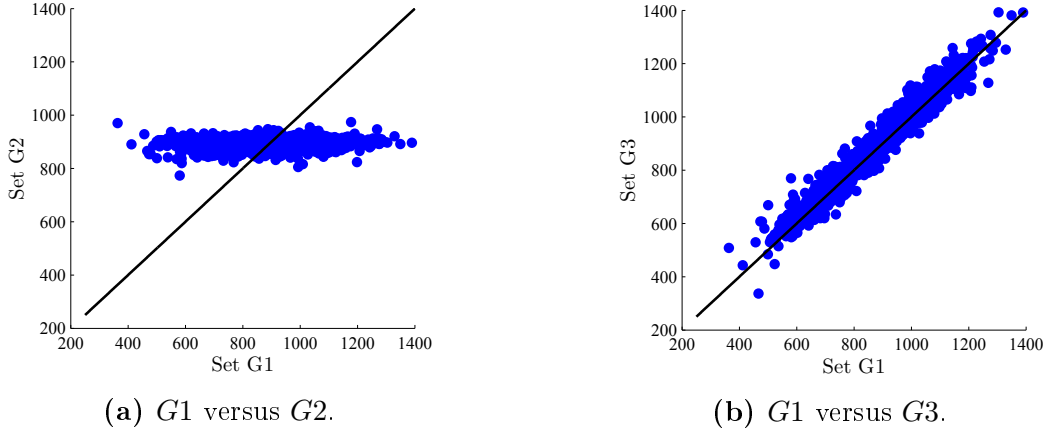


Figure 3.16.: Scatter plot of randomly generated Set, $G1$, versus fixed important parameters Set, $G2$, and non-important parameters, $G3$.

Table 3.11.: Standard deviation and COV of $G1$, $G2$, and $G3$.

Set	Standard deviation	COV
$G1$	146.54	16.82%
$G2$	17.60	1.97%
$G3$	143.70	16.34%

$G2$ was formed with the same as Set $G1$ but the parameters E_m , V_f , and G_{Im} were fixed at 2.85 GPa, 2.75%, and 220 J/m², respectively. Contrary, Set $G3$ was formed by fixing A_{cl} , r_{cl} , and E_{cl} at any point of their variation range, for example 300 nm, 500 nm, and 221.5 GPa. The scatter of the outputs of Set $G2$ and Set $G3$ against Set $G1$ are displayed in Fig. 3.16. When fixing parameters that are correctly classified as significant as in Set $G2$, the scatter shows a horizontal trend (Fig. 3.16a), whereas fixing the insignificant parameters results in linear correlation as in Fig. 3.16b. To assess the loss in variability when fixing the parameters, Table 3.11 lists the standard deviation and COV of the three sets. The COV was considerably reduced from 16.82% for Set $G1$ to 1.97% for Set $G2$, but it remains almost the same in Set $G3$ (16.34%). Obviously, the SA methods used in this research were robust in classifying the parameters.

3.5. Conclusion

In this paper, the fracture toughness of PNCs was predicted based on a fine-scale phase-field model accounting for the following input parameters: the volume fraction of clay

platelets, the aspect ratio of the clay, the radius of curvature of the clay, the Young's modulus of the clay, the Young's modulus of the matrix, and its fracture energy. The uncertainty quantification and prediction of uncertainties in the output are done based on the QMR surrogate model that replicates the output of the mechanical model with coefficient of determination, R^2 , equal to 0.934. Five different SA methods were performed to estimate the influence of the input parameters on the output. These methods were: i) Standardized Regression Coefficients, ii) Regionalized Sensitivity Analysis, iii) Sobol' Method, iv) EFAST method, and v) PAWN method. We also presented an improvement on the PAWN method that reduces the computational cost. The convergence and reproducibility of the sensitivity indices were achieved through the bootstrapping technique. Moreover, comparison and evaluation of the efficiency, robustness, and repeatability of the five SA methods were presented. Almost identical results were produced by the different methods implying the reliability of the implemented SA. All methods revealed that the aspect ratio, the radius of curvature, and the Young's modulus of the clay have negligible effects on the output with different ranking position. The matrix Young's modulus was the most significant parameter, followed by the volume fraction of clay and the fracture energy of the matrix. The latter two parameters swap their ranking in the second and the third position only for the PAWN method. Fixing the important parameters resulted in reducing the COV from 16.82% to 1.97%.

Chapter 4

Fracture toughness of polymeric particle nanocomposites: Evaluation of Models performance using Bayesian method

Contribution of authors

The work presented in this chapter is published in *K.M. Hamdia et al. / Composites Science and Technology 126 (2016) 122-129*. <http://www.sciencedirect.com/science/journal/02663538>. Impact Factor of the journal: **3.897**. An electronic copy of this publication is available at: <http://dx.doi.org/10.1016/j.compscitech.2016.02.012>.

The original text from this publication is used in this chapter.

- Khader M. Hamdia
 - Conducting literature review.
 - Coding the models in matlab.
 - Coding the Bayesian method in matlab.
 - Writing the manuscript.
- Xiaoying Zhuang
 - Reviewing the manuscript before submission.
- Pengfei He
 - Reviewing the manuscript before submission.
- Timon Rabczuk

- Mentoring the research progress.
- Reviewing the manuscript before submission.

4.1. Introduction

Polymeric nanocomposites (PNCs) are commonly formed by an epoxy matrix reinforced with a nanosized filler. Due to its inherent characteristic of high crosslink density, an epoxy polymer is known to be a relatively brittle material [140]. Nanofillers have shown great improvements in the physical and mechanical properties of epoxy-reinforced PNCs. Specifically, they have increased the fracture toughness compared to pristine epoxy. PNCs have numerous applications in nanotechnology such as: nanobiotechnology, nano-systems, nanoelectronics, and nano-structured materials. Generally, there are three categories of fillers: nanoparticles, nanoplatelet (layered), and nanofibrous materials. For this scale, the surface area - to - volume ratio is significantly large. Therefore, the composite properties are highly modified due to the extreme interfacial area between the nanofiller and the matrix [1]. Several experiments have been carried out in order to study the fracture behavior of polymer/particle nanocomposites ([51–53, 55–57, 59, 60, 62, 65] among others). On the other hand, researchers developed numerical and analytical methods to get a better understanding of nanocomposite material behavior. A close form formula of energy dissipation due to the interfacial debonding between the particles and matrix was given by Chen et al. [70] considering the effect of particle sizes. Although, the increased fracture energy of rubber-toughened epoxy polymers was calculated by Huang and Kinloch [2], the model has been modified for PNCs by [51, 53, 56]. The improvement in the fracture toughness was attributed to two major mechanisms: localized plastic shear banding and debonding of silica nanoparticles. Further experimental studies also have implied this supposition [54, 58, 165]. According to the assumption of Williams [3], the energy dissipation is induced by the growth of plastic voids around debonded particles. The author concluded a large toughness increase for nanosize particles. Later, his work has been extended to cylindrical rods and fibres [66, 72]. Quaresimin et al. [4] proposed a multiscale approach to predict the overall increase in the fracture toughness taking into account three different damage mechanisms: particle debonding, plastic yielding of nanovoids, and shear banding of the polymer. Based on experimental data gathered from the literature, a stochastic approach has been presented to predict the fracture energy of PNCs by [156]. In general, all models inherently underlie an amount of uncertainties which can be rela-

4.1 Introduction

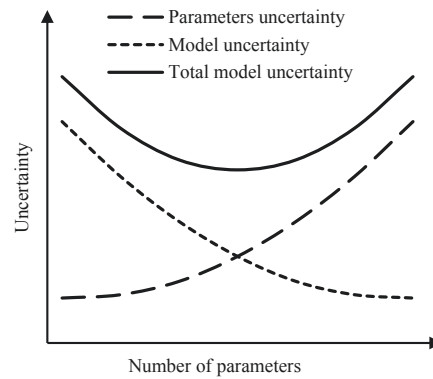


Figure 4.1.: Variation in model, parameter, and total uncertainties with respect to the number of parameters according to [41] .

ted to the model itself and/or its input parameters. The former might be caused by the simplifications of the physical behavior, while the latter can be related to the number and the stochastic variance of the input parameters. Better predictions and the subsequent decrease in the model uncertainty are expected by introducing more factors in the model (increasing the model complexity). However, the parameters uncertainties become more dominant in this case. In light of this, the model with minimum total uncertainty is the most appropriate model, see Fig. 4.1 [41].

In recent years, Bayesian method has been introduced as an effective tool for evaluating models considering the model and parameters uncertainties based on measurements as reference data [42–45].

This paper is the first attempt to consider the model and parameters uncertainties in the assessment of the models used for the prediction of the fracture energy of PNCs. It aims at presenting a methodology to evaluate three different analytical models by using the Bayesian method. In particular, Huang and Kinloch model [2], Williams model [3], and the model according Quaresimin et al. [4] are examined. The purpose of the study is not to give a general recommendation which of the three model to use, but to evaluate their performance with respect to experimentally tested data series. The assessment is carried out based on different reference data (experimental measurements) gathered from the literature [51–53, 55–57, 59, 60, 62, 65]. Nevertheless, the same methodology can be applied to evaluate the three models based on other measurements. The prior probabilities are first estimated considering the uncertainties in the parameters. Then we find the optimum parameter set which results in best fit of models prognoses and in consequence the coefficient of variation of the models predictions to the measurements are estimated. Eventually, the model selection probability is calculated.

The remainder of this paper is organized as follows.. In Section 4.2, the considered models are briefly described. Section 4.3 presents the method for evaluating the models. Finally, the conclusion of this research is presented in Section 4.4.

4.2. Models for predicting the fracture properties of PNCs

Three existing models were chosen to be evaluated; the model of Huang and Kinloch [2], the model of Williams [3], and the model of Quaresimin et al. [4]. Hereafter, they are abbreviated by M_1 , M_2 , and M_3 , respectively. These models have been selected due to their popularity and their applicability to different experimental studies. Moreover, they produce explicit predictions of the enhanced fracture energy of PNCs. Regarding the different theory and mechanism assumed, each of them has its own input parameters in addition to the joint parameters. Table 4.1 includes the definitions of the parameters and their stochastic variation. The uniform distribution was assumed for the parameters uncertainty. The upper and the lower limits of distributions were mostly proposed according to our previous studies [156, 166].

4.2.1. Huang and Kinloch

The model according to Huang and Kinloch [2] was first developed for the toughening mechanisms of rubber-modified epoxy polymers and more recently it has been modified for PNCs [51, 53, 56]. The localized plastic shear banding and debonding of nanoparticles which enable plastic void growth of the epoxy matrix are the two terms that taking part in the overall enhancement in the fracture toughness of PNCs, while rubber-bridging mechanism was disregarded. These two mechanisms are demonstrated in Fig. 4.2.

The improved fracture energy of PNCs, G_{Ic} , is expressed as

$$G_{Ic} = G_{Im} + \Delta G_s + \Delta G_v \quad (4.1)$$

where G_{Im} is the fracture energy of the matrix, and ΔG_s and ΔG_v are the contribution from the localized shear banding and the plastic void growth, respectively.

The term ΔG_s is given by

$$\Delta G_s = \frac{1}{2} V_f \sigma_{yc} \gamma_f F'(r_y) \quad (4.2)$$

4.2 Models for predicting the fracture properties of PNCs

Table 4.1.: The definitions of models' parameters

Parameter	Symbol	Unit	Limits [lower,upper]	Models ^a
The volume fraction of the nano-filler	V_f	%	[0.5,10]	All
The average diameter of the nano-particles	d_n	nm	[10,80]	All
The elastic modulus (The Young's modulus) of the matrix	E_m	GPa	[2.4,3.6]	All
The fracture energy of the matrix	G_{Im}	J/m ²	[40,500]	All
The yield strength of the matrix	σ_{ym}	MPa	[70,120]	All
The Poisson's ratio of the matrix	ν_m	–	[0.33,0.37]	All
The shear fracture strain of the matrix	γ_{fm}	–	[0.70,0.75]	M_1, M_3
The pressure dependency material constant (pressure coefficient)	μ_m	–	[0.175,0.225]	M_1, M_3
The matrix maximum stress concentration factor of the von Mises stress	K_{vm}	–	[2.10,2.25]	M_1
The average diameter of voids around nanoparticles	d_v	nm	[25,120]	M_1
The percentage of the debonded particles	V_{dp}	%	[10,18]	M_1
The interfacial debonding energy	G_a	J/m ²	[0.01,1.5]	M_2, M_3
The shear yielding stress of the matrix	τ_{ym}	MPa	[40,70]	M_3
The thickness of the interphase	t	nm	[1,4]	M_3
The ratio of the shear elastic modulus of the interphase to the shear elastic modulus of the matrix	χ	–	[0.1,2.0]	M_3

^a $M_1, M_2,$ and M_3 refer to Huang and Kinloch model, Williams model, and Quaresimin et al. model, respectively.

where V_f is the volume fraction of the nano-filler, γ_{fm} is the matrix shear fracture strain, and σ_{yc} is the yield stress of the epoxy matrix under compression, which related to the tensile yield stress, σ_{ym} , by [57]

$$\sigma_{yc} = \sigma_{ym} \left(\frac{\sqrt{3} + \mu_m}{\sqrt{3} - \mu_m} \right) \quad (4.3)$$

4.2 Models for predicting the fracture properties of PNCs

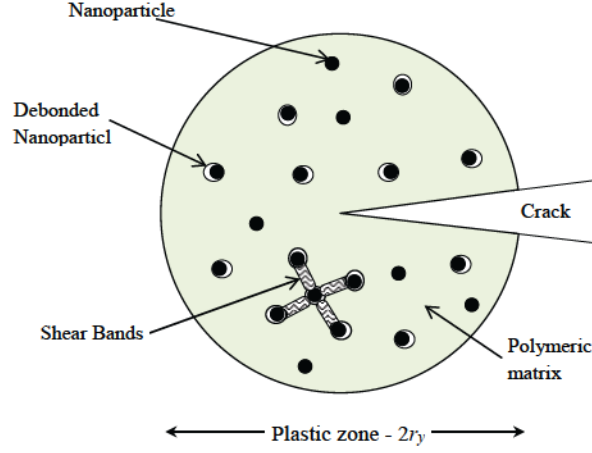


Figure 4.2.: Representative diagram for the toughening mechanisms of PNCs according to Huang and Kinloch [2] .

μ_m is a material constant (pressure coefficient).

The parameter $F'(r_y)$ is a geometric term given by [54]

$$F'(r_y) = r_y \left[\left(\frac{4\pi}{3V_f} \right)^{1/3} \left(1 - \frac{r_n}{r_y} \right)^3 - \frac{8}{5} \left(1 - \frac{r_n}{r_y} \right) \left(\frac{r_n}{r_y} \right)^{5/2} - \frac{16}{35} \left(\frac{r_n}{r_y} \right)^{7/2} - 2 \left(1 - \frac{r_n}{r_y} \right)^2 + \frac{16}{35} \right] \quad (4.4)$$

where $r_n (= d_n/2)$ is the radius of nanoparticles and r_y is the radius of the plastic zone at the crack tip at fracture in the PNCs

$$r_y = \left(1 + \frac{\mu_m}{\sqrt{3}} \right)^2 r_{ym} K_{vm}^2 \quad (4.5)$$

In Eq. (4.5), r_{ym} is radius of the plastic zone of the unmodified epoxy matrix estimated by Irwin's model [6] and K_{vm} is the maximum stress concentration factor of the von Mises stress in the matrix.

The term ΔG_v is calculated by

$$\Delta G_v = \left(1 - \frac{\mu_m^2}{3} \right) (V_{fv} - V_{fp}) \sigma_{yc} r_{ym} K_{vm}^2 \quad (4.6)$$

where V_{fv} and V_{fp} are the volume fraction of voids and the volume fraction of debonded particles. An expression for $(V_{fv} - V_{fp})$ considering the average volume of the voids (v_v)

4.2 Models for predicting the fracture properties of PNCs

and the average volume of nanoparticles (v_p) has been proposed by [53, 56] as

$$(V_{fv} - V_{fp}) = \left(\frac{v_v}{v_p} - 1 \right) V_{fp} \quad (4.7)$$

As reported in the studies of [51, 165], not all of the nanoparticles have been observed to be debonded. Finite element simulations suggest that around 14% of the particles are debonded [165]. On this basis, we include a new factor to quantify the percentage of debonded particles (V_{dp}). It has been assumed to vary from 10% to 18%. The volume fraction of debonded particles, V_{fp} in Eq. (4.7), is substituted by $(V_{dp})(V_f)$

$$(V_{fv} - V_{fp}) = \left(\frac{v_v}{v_p} - 1 \right) (V_{dp})(V_f) \quad (4.8)$$

4.2.2. Williams

The analysis of Williams [3] has referred the energy dissipation to one basic mechanism; the debonding of nanoparticles which initiate the plastic void growth. At the first stage the rigid spherical nanoparticles is bonded to the surrounding matrix, and under tensile stress, the interfacial stress increases until debonding occur. This initiates the void growth in the matrix. The critical interfacial stress (debonding stress), σ_{cr} , is approximated by

$$\sigma_{cr} = \sqrt{\frac{4}{1 + \nu_m} \frac{E_m G_a}{r_n}} \quad (4.9)$$

where G_a is the interfacial debonding energy, and ν_m is the Poisson's ratio of the matrix. If the number of the particles participating in the process is considered to be more than one, then the fracture energy of the PNCs is

$$G_{Ic} = G_{Im} \left(X_t V_f - 1.21 V_f^{2/3} + 1 \right) \quad (4.10)$$

where X_t is toughening factor that is characterized by a critical stress ratio factor, x [3]. Both factors are given by

$$\begin{aligned} x &= \frac{\sigma_{cr}}{\sigma_{ym}} \left[\frac{1 + \nu_m}{2(1 - \nu_m)} \right], \\ X_t &= \frac{(1 + \nu_m)^2}{2\pi(1 - \nu_m)} \left[\frac{e^{(x-1)}}{x} - \frac{5\nu_m - 1}{2(1 + \nu_m)} \right] \end{aligned} \quad (4.11)$$

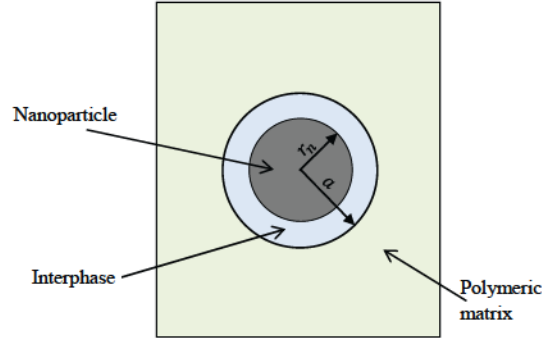


Figure 4.3.: 2D representation of the nanoscale system considered according to Quaresimin et al. [4].

4.2.3. Quaresimin et al.

A multiscale methodology has been adopted by Quaresimin et al. [4] to describe the toughening mechanism of PNCs. The authors have considered the interphase zone surrounding the nanoparticle to account for the interactions between the nanoparticles and the matrix. The adjacent polymer chains are disordered due to the addition of the nanofiller, leading to the formation of interphase zones surrounding the nanoparticles with properties different from that of the bulk matrix. The extent of the impact of particle/polymer interface is principally influenced by the manufacturing techniques and the curing processes. The influence of the interphase was studied experimentally by [167–170] and numerically by [78–80, 91].

Through its thickness, the interphase layer was assumed to be homogeneous and isotropic [73]. Fig. 4.3 displays the system considered at the nanosized scale.

By studying the energy dissipation at the nanoscale, Quaresimin and co-workers indicated that the overall fracture toughness of the nanocomposite is composed of three damaging mechanisms: (i) particle debonding, (ii) plastic yielding of nanovoids, and (iii) shear banding of the polymer [73–75].

The term of toughness improvement due to the debonding of nanoparticle is expressed by

$$\Psi_{dp} = \frac{2G_a}{3\pi r_n} \left(\frac{1 + \nu_c}{1 - \nu_c} \right) \left(\frac{E_c}{\sigma_{cr}^2 C_h^2} \right) \quad (4.12)$$

ν_c and E_c being the Poisson's ratio and the elastic modulus of the nanocomposite, respectively. In this study, ν_c was set equal to the matrix Poisson's ratio, ν_m , while E_c was

4.2 Models for predicting the fracture properties of PNCs

calculated by the Hashin-Shtrikman solution developed in [171]. The debonding stress, σ_{cr} , and the reciprocal of the hydrostatic part of the global stress concentration tensor, C_h , depend on the nanoparticle radius, the interphase thickness, and the matrix and interphase elastic properties [73].

The part of the fracture toughness enhancement caused by the plastic yielding of nanovoids is [74]

$$\Psi_{py} = \frac{4}{9\pi C_h} \frac{E_c}{E_m} \frac{(1 + \nu_c)(1 + \nu_m)}{1 - \nu_c} \frac{\sigma_{ym}}{\sigma_{cr}} \left(\frac{a}{r_n} \right)^{3\left(1 - \frac{\sigma_{ya}}{\sigma_{ym}}\right)} e^{\left(3C_h \frac{\sigma_{cr}}{\sigma_{ym}} - 1\right)} \quad (4.13)$$

where σ_{ya} is the yield stress of the interphase, and a is the external interphase radius (see Fig. 4.3).

The third part, the improvement due to the formation of localised plastic shear bands, is

$$\Psi_{SB} = \frac{I_{SB}}{4\pi\sigma_{yca}^2 (1 - \mu_m/\sqrt{3})^2} \frac{E_c}{1 - \nu_c^2} \Gamma \quad (4.14)$$

I_{SB} is referring to the stress concentration around the nanoparticles, σ_{yca} being the interphase yielding stress under compression, and Γ is quantifying the energy produced at the nanoscale. The shear yielding stress of the matrix, τ_{ym} , in addition to V_f , γ_{fm} , a , and r_n are required to calculate Γ , while I_{SB} is a function of ν_c , μ_m , C_h , and H_{vM} (the deviatoric component of the global stress concentration tensor) [75].

Eventually, the total fracture energy of PNCs is calculated by

$$G_{Ic} = \frac{G_{Im}}{1 - V_f (\Psi_{dp} + \Psi_{py} + \Psi_{SB})} \quad (4.15)$$

The condition: $V_f (\Psi_{dp} + \Psi_{py} + \Psi_{SB}) < 1$, is essential for the applicability of the model in Eq. (4.15). Other values will produce meaningless results. This limits the applicability of the model in determining the fracture energy of PNCs reinforced by small fractions of nanofiller.

4.2.4. Discussion

Although, the model of Huang and Kinloch [2] accounts for the main damaging mechanisms, it is based on some simplifying assumptions. The knowledge of the increased volume fraction of voids ($V_{fv} - V_{fp}$) is required to evaluate the energy contribution from void-growth mechanism, ΔG_v (see Eq. (4.6)). The values for the volume fraction of

voids, V_{fv} , and the volume fraction of debonded particles, V_{fp} , can be measured experimentally using for instance electron micrographs. Instead, based on the expression proposed in [53, 56], we introduced a new uncertain parameter to quantify the percentage of debonded particles (V_{dp}). The proposed formula for ($V_{fv} - V_{fp}$) is shown in Eq. (4.8). On the other hand, the model of Williams [3] assumes that the void growth around debonded particles is the only dominant energy dissipation mechanism. His analysis was based on the energy balance concept around a single nanoparticle and assuming the absence of particle-to-particle interaction. In turn, the effect of aggregation was ignored. A similar assumption, i.e. the absence of particle-to-particle interaction, was considered in the model of Quaresimin et al. [4]. However, three damaging mechanisms through multiscale modelling and the effect of the interphase zone were taken into account. It is widely acknowledged that the nanofillers intend to agglomerate in nanocomposites. This may limit the applicability of the models of Williams [3] and Quaresimin et al. [4] to PNCs with a low volume fraction of fillers. However, since the most important merit of the PNCs is substantial improvements in the fracture toughness at low filler content, this is not a short-coming of the above mentioned models.

4.3. Assessment of PNCs fracture models using Bayesian method

The Model selection refers to the problem of selecting one model from a list of candidate models based on available data. The Bayes' rule of statistics has motivated [46] to develop the Bayesian approach for model selection by incorporating the different sources of uncertainties based on response measurements (reference data), D . The model selection probability is represented by the conditional probability of the model M_i given the reference data D . It can be calculated by

$$P(M_i|D) = \frac{P(D|M_i)P(M_i)}{\sum_i P(D|M_i)P(M_i)} \quad (4.16)$$

where $P(M_i)$ is the prior probability of M_i which is based on the user's judgment on the initial plausibility of the models. The data-dependent term $P(D|M_i)$ is the evidence of M_i . It defines the probability that the measurements of reference data D being represented by the predictions of the model M_i . Making use of the theorem of total

4.3 Assessment of PNCs fracture models using Bayesian method

probability, the evidence can be calculated by [46]

$$P(D|M_i) = \int P(D|X_i, M_i) P(X_i|M_i) dX_i \quad (4.17)$$

where $P(D|X_i, M_i)$ is the likelihood function and $P(X_i|M_i)$ is the prior probability of the input parameters.

The likelihood is the joint conditional probability of the reference data, D , given the input parameters, X_i . It measures how the model fit the data. A higher likelihood factor corresponds to better fit of M_i to D . The prior probability of the input parameters characterizes what is known about the parameters before any actual observation or modeling being considered. In the presence of measurements and model predictions, the prior probability is updated to posterior probability [47].

Assuming that the posterior probability of the parameters is approximated by a Gaussian distribution, the Laplace's method for asymptotic approximation can be applied to estimate the evidence as [48]

$$P(D|M_i) = P(D|\hat{X}_i, M_i) P(\hat{X}_i|M_i) \left[|H(\hat{X}_i)|/2\pi \right]^{-\frac{1}{2}} \quad (4.18)$$

where \hat{X}_i is the optimal parameter set that maximize the posterior probability and $H(\hat{X}_i)$ is the Hessian matrix of $-\ln [P(D|X_i, M_i) P(X_i|M_i)]$ with respect to X_i calculated at \hat{X}_i . The models are compared according to their model selection probability calculated in Eq. (4.16). The model with the largest probability is the optimum one.

In the present work, the models of predicting the fracture energy of PNCs were evaluated. We considered the model of Huang and Kinloch [2] (M_1), the model of Williams [3] (M_2), and the model of Quaresimin et al. [4] (M_3), which were described in Section 4.2. The prior probabilities of these models were assumed to be equal, i.e. $P(M_1) = P(M_2) = P(M_3) = 1/3$.

Thanks to the uniform distribution assumed for the input parameters, the prior probabilities of the model parameters, $P(X_i|M_i)$, are constant disregarding the value of the parameter. The input parameters V_f , d_n , E_m , and G_{Im} were fixed as deterministic parameters, while we calculated the most probable value (optimal parameter value), which realized the best fit of the model predictions to the measurements, for the remaining parameters. Different experimental measurements gathered from the literature [51–53, 55–57, 59, 60, 62, 65] have been utilized as reference data. For each, Table 4.2 shows the values of the calculated optimal parameter set.

4.3 Assessment of PNCs fracture models using Bayesian method

Interestingly, the incorporation of the parameter V_{dp} in M_1 has enhanced the model predictions to fit the measurements. By the finite-element analysis of [138], the value of the maximum stress concentration for the von Mises stresses around a void, K_{vm} , was estimated to be 2.22 for a matrix of elastic modulus equal 3.2 GPa which agrees well with the optimal values obtained in this study. The interfacial debonding energy, G_a increases as the diameter of the nanofiller increases. Its optimal values were in the range of [0.184, 1.360] and [0.010, 0.046] for M_2 and M_3 , respectively. Similar values of G_a for M_2 were reported in [3] and [66]. The high value of these results may be explained by assuming that the optimal values of G_a were reduplicated since the total energy dissipation in M_2 was attributed only to one mechanism. Based on this, the probability distribution of G_a can be updated to a uniform distribution in the range of [0.1, 1.5] for M_2 and [0.01, 0.1] for M_3 . The elastic property of the interphase was stiffer than that of the matrix in the measurements; D_{10} and D_{11} ($\chi = 1.162$ and 1.231, respectively), whereas the matrix showed stiffer elasticity in the remaining measurements. Exploiting the optimal parameter sets, the models predictions versus the nanofiller volume fraction are depicted in Fig. 4.4. Obviously, M_2 and M_3 mostly have a similar ascending trend but it differs slightly from M_1 .

The model uncertainty can be demonstrated by the differences between the predictions and the measurements. This uncertainty is measured by the coefficient of variation (CV).

$$CV_{ij} = \frac{1}{\bar{D}_j} \sqrt{\frac{1}{N_j - 1} \sum_{m=1}^{N_j} (D_m - Y_{im})^2} \quad (4.19)$$

where \bar{D}_j and N_j are the mean value and the number of the individual experiments of the j reference data, D_m is the the measured value, and Y_{im} is the corresponding predicted value of the model M_i .

The CV values for M_1 , M_2 , and M_3 are shown in Fig. 4.5. Except of the measurements: D_8 , D_{11} , D_{12} , and D_{13} , M_1 shows better performance compared to M_2 and M_3 , where its CV values are the least. The predictions of M_2 have the lowest discrepancies from the measurements of D_{11} , D_{12} , and D_{13} . M_3 produces the best fit predictions in the measurements of D_8 only.

When considering both the model and parameters uncertainties in the evaluation, M_1 outperforms M_2 and M_3 for all the different measurements. It has significantly higher model selection probability, $P(M_i|D)$ (See Table 4.3). It can be concluded that

Table 4.2.: The values of the input parameters used in the assessment of the models

Reference	All models ^a		M_1^b							M_2^b			M_3^b							
	d_n nm	E_m GPa	σ_{ym} MPa	ν_m -	γ_{fm} -	μ_m -	K_{vm} -	d_v nm	V_{dp} %	σ_{ym} MPa	ν_m -	G_a J/m ²	σ_{ym} MPa	ν_m -	G_a J/m ²	γ_{fm} -	μ_m -	τ_{ym} MPa	t nm	χ -
D_1 [65]	20	3.20	71.6	0.35	0.732	0.194	2.227	37.7	14.1	72.3	0.36	0.287	85.1	0.36	0.015	0.722	0.184	66.0	3.00	0.882
D_2 [65]	20	3.20	115.8	0.36	0.740	0.203	2.216	43.5	11.4	80.0	0.36	0.309	77.6	0.35	0.011	0.746	0.197	52.9	2.26	0.788
D_3 [52]	12	3.53	80.5	0.33	0.728	0.206	2.236	25.5	10.4	76.9	0.36	0.184	81.4	0.34	0.013	0.730	0.204	67.3	2.24	0.644
D_4 [52]	20	3.53	107.1	0.34	0.730	0.192	2.180	25.5	10.3	86.5	0.36	0.289	110.4	0.34	0.016	0.747	0.184	69.6	1.95	0.670
D_5 [52]	40	3.53	118.4	0.34	0.704	0.177	2.108	45.0	13.2	82.7	0.36	0.473	97.0	0.36	0.015	0.727	0.214	59.0	2.90	0.375
D_6 [57]	23	3.50	71.6	0.34	0.715	0.210	2.244	25.1	10.8	75.8	0.36	0.250	117.5	0.36	0.010	0.727	0.189	65.1	2.7	0.742
D_7 [57]	74	3.50	71.6	0.37	0.745	0.222	2.236	91.2	15.2	75.8	0.35	0.914	110.1	0.34	0.046	0.727	0.188	63.4	2.18	0.447
D_8 [55]	20	2.86	118.6	0.34	0.704	0.191	2.110	47.4	16.4	81.7	0.35	0.374	87.2	0.33	0.018	0.713	0.184	68.5	2.97	0.710
D_9 [51]	20	2.96	70.5	0.36	0.737	0.205	2.190	25.7	12.5	80.2	0.35	0.310	112.5	0.36	0.011	0.745	0.192	62.6	1.08	0.758
D_{10} [56]	20	2.41	70.3	0.35	0.747	0.208	2.224	42.2	14.1	73.5	0.36	0.363	94.8	0.35	0.011	0.710	0.187	67.3	1.32	1.162
D_{11} [56]	80	2.41	70.7	0.36	0.730	0.223	2.239	118.8	17.9	71.5	0.37	1.360	88.5	0.34	0.046	0.716	0.184	63.8	1.20	1.231
D_{12} [62]	25	3.02	118.4	0.34	0.704	0.177	2.108	29.8	13.3	81.8	0.34	0.340	109.6	0.34	0.012	0.734	0.203	48.3	3.91	0.676
D_{13} [62]	25	2.78	116.7	0.36	0.704	0.181	2.112	56.6	16.7	72.7	0.34	0.383	87.2	0.34	0.010	0.709	0.220	60.2	3.78	0.656
D_{14} [53]	20	2.96	71.5	0.37	0.741	0.222	2.229	42.0	13.7	77.4	0.33	0.385	79.0	0.36	0.011	0.708	0.185	50.8	3.43	0.649
D_{15} [60]	13	2.60	80.6	0.36	0.705	0.181	2.221	35.3	11.1	71.1	0.35	0.224	97.1	0.36	0.010	0.749	0.176	67.4	2.83	0.770
D_{16} [59]	25	3.27	117.1	0.33	0.708	0.185	2.204	36.4	14.9	83.5	0.36	0.322	110.0	0.36	0.011	0.731	0.215	46.4	3.89	0.830

^a The values of d_n and E_m are obtained from the corresponding references.

^b These are the optimal values approximated in the current study.

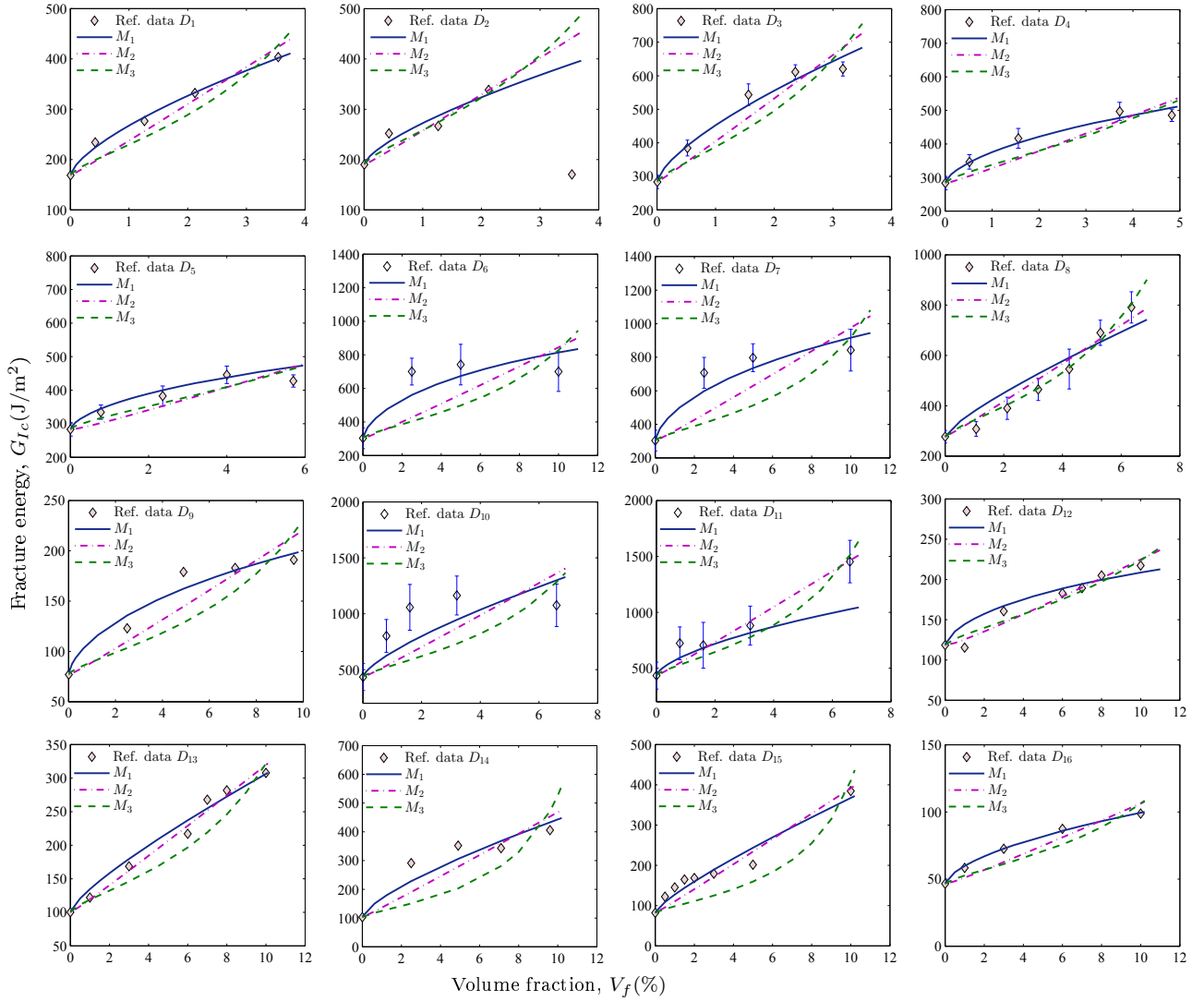


Figure 4.4.: Predictions of the models using the optimal parameter set for the different reference data.

the parameters of M_2 and M_3 have steeper posterior probabilities. Significant changes in their prognoses are expected due to slight variations in the parameters values. One possible explanation is that the natural exponential relation in M_2 and in M_3 results in high values of the determinant of their Hessian matrices.

4.4. Conclusion

Three existing models used for the prediction of the fracture toughness of PNCs were evaluated. The Bayesian method was employed to quantify the model selection probabilities of Huang and Kinloch [2] model, Williams [3] model, and Quaresimin et

4.4 Conclusion

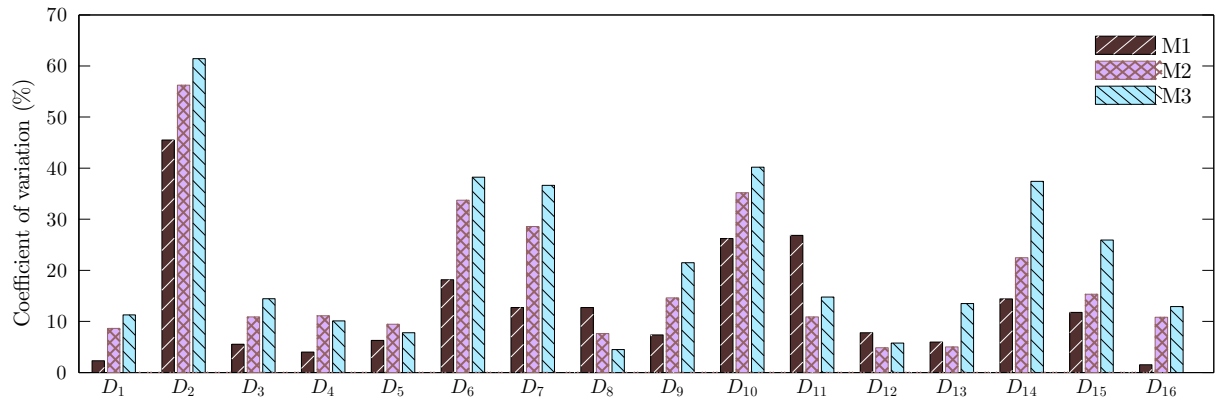


Figure 4.5.: The coefficient of variation for the different references data

Table 4.3.: The models selection probability values for the different reference data

Reference Data	$P(M_i D)^a$		
	M_1	M_2	M_3
D_1 [65]	0.988	0.000	0.012
D_2 [65]	1.000	0.000	0.000
D_3 [52]	1.000	0.000	0.000
D_4 [52]	1.000	0.000	0.000
D_5 [52]	0.805	0.000	0.195
D_6 [57]	0.999	0.000	0.001
D_7 [57]	0.998	0.000	0.002
D_8 [55]	0.998	0.000	0.002
D_9 [51]	1.000	0.000	0.000
D_{10} [56]	0.995	0.000	0.005
D_{11} [56]	0.744	0.001	0.255
D_{12} [62]	1.000	0.000	0.000
D_{13} [62]	1.000	0.000	0.000
D_{14} [53]	1.000	0.000	0.000
D_{15} [60]	1.000	0.000	0.000
D_{16} [59]	0.997	0.000	0.003

^aThe probability of selecting the model M_i given the different reference data calculated by Eq. (4.16).

al. [4] model. The model and parameters uncertainties were considered in the assessment based on the experimental measurements of [51–53, 55–57, 59, 60, 62, 65]. The optimal models predictions with respect to these measurements were obtained using the optimal parameter sets. In contradiction to the references data of D_8 , D_{11} , D_{12} , and D_{13} , the optimal predictions of Huang and Kinloch model showed better performance compared to the other two models. However, for all the reference measurements, the model of Huang and Kinloch showed a distinctly higher model selection probability. On this base, we can conclude that it is the most robust model with regard to the applied reference measurements.

Chapter 5

Stochastic analysis of the fracture toughness of polymeric nanoparticle composites using polynomial chaos expansions

Contribution of authors

The work presented in this chapter is published in *K.M. Hamdia et al. / International Journal of Fracture 126 (2017) 122-129*. Impact Factor of the journal: **1.642**. An electronic copy of this publication is available at: <http://dx.doi.org/10.1007/s10704-017-0210-6>. The original text from this publication is used in this chapter.

- Khader M. Hamdia
 - Conducting literature review.
 - Simulating the fracture behaviour using XFEM.
 - Coding sensitivity analysis methods.
 - Writing the manuscript.
- Mohammad Silani
 - Assistance in Python scripting for generating 2D FE.
- Xiaoying Zhuang
 - Reviewing the manuscript before submission.
- Pengfei He
 - Reviewing the manuscript before submission.
- Timon Rabczuk
 - Mentoring the research progress.
 - Reviewing the manuscript before submission.

5.1. Introduction

Polymers are considered a promising material in several applications. Adding particles to the polymer matrix results in major improvements in the properties of the created composite. Incorporating rigid fillers at the nano-scale has shown an improved fracture toughness without sacrificing other important thermo-mechanical properties. Three shapes of nanofillers are commonly used: spherical particles (e.g. silica, alumina and glass), layered (e.g. clay and graphite) and fibrous materials (nanotubes). Thanks to the low density and simple fabrication methods, polymeric nanocomposites (PNCs) have become a popular multifunctional material in numerous nanotechnology applications [1].

The remarkable improvement in the properties of the produced composite may be attributed to the large surface area - to - volume ratio of the nanofillers that creates an extreme interfacial zone between the nanofiller and the surrounding matrix. Due to the nanofillers, the adjacent polymer chains are disordered forming interphase zones of different properties surrounding the nanoparticles. The extent of the impact of particle/polymer interface is principally influenced by the manufacturing techniques and the curing processes. Studying the nanostructure of composite considering the interphase effect remains a challenging problem. Experimental investigations of the material at the nanoscale size are cumbersome, expensive and in some cases impractical. Instead, numerous numerical studies have been documented in the literature that simulate and predict the mechanical behavior of nanocomposites such as; polymer/nanoclay [76,85,95], carbon nanotubes [86,87,89], and polymer/ nanoparticles [78,90,172]. These studies however, have modelled the PNCs as an elastic material without fracture. Although there are different analytical solutions [2-4], few numerical works have been dedicated to model the fracture behavior of the PNCs. In this regard, it is worth to mention the work on modeling fracture in PNCs reinforced by; graphene sheets [131], carbon nanotubes [132,133], and nanoclays [130,134,166]. The focus of this study is on particle reinforced nanocomposites accounting for uncertainties in the input parameters.

Various uncertain parameters affect the PNCs failure behavior. Hence, there is an urgent need for a comprehensive study to measure the influence of the uncertainties in these input parameters. This can be achieved by means of sensitivity analysis (SA). In contrary to the local SA, the global SA intends to quantify the significance of the input parameters and their joint effects on the output by varying all the parameters at the same time. Variance-based SA methods that are based on decomposing the variance of the output are among the most popular ones [29]. Few SA works have been dedicated

5.1 Introduction

to study the properties of PNCs. The effect of different parameters on the uncertainty of the mechanical properties of single-walled carbon nanotube and nanoclay were investigated by Vu-Bac et al. [93], [94], and [96], respectively.

In order to get a proper estimate of the sensitivity indices, the required number of model evaluations (cost of the analysis or the computational cost) shall be in the order of thousands. However, fracture simulations are computationally expensive utilizing several minutes to hours of CPU usage, and therefore are not practically feasible to provide the 'full' data for the sensitivity analysis. Instead, *surrogate models*, also known as *meta-models*, can be used in order to mitigate the computational expense. The surrogate model is constructed based on a set of output values generated from the original mechanical model. Recently, the use of polynomial chaos expansions (PCE) [27, 28] surrogate modeling has been widely exploited to express the random response of a mechanical model using orthogonal polynomials in the random input variables. In PCE, the variance-based Sobol' sensitivity indices can be extracted by gathering expansion coefficients of the constructed PCE according to the dependency of each basis polynomial [33, 34, 173].

The aim of this paper is to present a methodology for studying fracture in polymer/particle nanocomposites accounting for the interphase zone. In order to quantify the uncertainty in the fracture energy of PNCs, we employ a global sensitivity analysis. A polymer epoxy matrix reinforced by rigid nanoparticles is presented by a 2D finite element model. The phantom node method [16, 17, 113, 114, 174] is employed to model the fracture. The uncertain input parameters considered in the stochastic model are: the volume fraction of the nanoparticles, the diameter of the nanoparticle, Young's modulus of the epoxy matrix, the maximum allowable principal stress, the thickness, and Young's modulus of the interphase zone. By taking into account the uncertainties in these parameters, a PCE surrogate model is constructed and the sensitivity of the input parameters is evaluated.

The paper is organized as follow; Section 5.2 presents the methodology for fracture modeling of PNCs. The polynomial chaos expansions, the stochastic inputs, and the parameters sensitivity are discussed in detail in Section 5.3. Section 5.4 concludes and summarizes the manuscript.

5.2. Modelling the fracture in the PNCs

5.2.1. Fracture Mechanics

The fracture toughness is a material property used to measure the ability to fracture resistance of a material containing a crack. The stress intensity factor, K , predicts the stress intensity near the crack tip, while the energy release rate, G , is the amount of the energy dissipated per unit area due to the formation of new surfaces. According to the energy criterion for fracture of Griffith [5], the crack is extended when the energy available for crack growth is sufficient to overcome the resistance of the material. On this basis, Irwin [6] has defined G as the rate of change in potential energy with respect to the crack area.

$$G = -\frac{d\Pi}{dA} \quad (5.1)$$

When fracture occurs, K reaches a critical value K_c , which is known as the fracture toughness. For the mode-I loading, where the principal load tends to open the crack, K_{Ic} is given by

$$K_{Ic} = \frac{P_{max}}{B\sqrt{W}} f\left(\frac{a}{W}\right) \quad (5.2)$$

where P_{max} is the load at fracture, B and W are the thickness and the width of the specimen, a is the initial crack length, and $f(a/W)$ is a dimensionless function [7].

The critical energy release rate also reaches a critical value known as the fracture energy. It is related to K_{Ic} by

$$G_{Ic} = \frac{K_{Ic}^2}{E'} \quad (5.3)$$

For plane stress conditions, $E' = E$, and for plane strain conditions $E' = E/(1 - \nu^2)$, with E being Young's modulus and ν being Poisson's ratio.

5.2.2. Numerical simulation of PNC

In the present work, we assume small strain theory, quasi-brittle fracture without cyclic loading simplified a two-dimensional model. Therefore, we have employed the phantom node method [16, 17, 113, 114, 174] in order to model fracture in PNCs. When the crack propagates through an entire element, the crack might end exactly at the material interface which will yield to crack arrest. The phantom node method in [16, 17]

5.2 Modelling the fracture in the PNCs

presents special crack tip enrichments which allows the crack tip being located inside the element which is important to model fracture in heterogeneous materials. A rigid cohesive zone model as proposed by Areias and Rabczuk [175] has been exploited in our simulation. For further details, the interested reader is referred to the above mentioned manuscripts and the references reported therein.

We investigate system of PNCs formed by an epoxy matrix reinforced with randomly dispersed spherical nanoparticles surrounded by an interphase zone.

Determining the properties and the size of the interphase zone experimentally is challenging and to our best knowledge, no direct experimental data is available up to date. However, the radial extension of the interphase zone was predicted by Odegard et al. [79] and Yu et al. [80] through Molecular Dynamics (MD) simulations and by Le et al. [176] through a probabilistic multiscale analysis. Their MD results showed that the polymer chains are attracted by the filler surface, which generates a spherical transverse isotropy indicating that the interphase zone is much less isotropic. Although the system studied by Le et al. [176] is not the same as the one considered in this study, it paves the way for further uncertainty analysis for the influence of the anisotropic phase. On the other hand, other researchers, who investigated similar PNCs system, have assumed isotropic interphase [73, 77, 90, 91, 177]. Accordingly, in the current study, we choose the interphase zone to be homogeneous and isotropic through its thickness.

Also the size of the interphase zone is arguable and several contradictory results have been reported in the literature. It may be equal to a couple of nanometers as in [4, 77], half the diameter of the particle as in [178], range from half to one times the diameter as in [91], or [0.5, 3.25] times the diameter as in [78]. It is also stated in several manuscript [179] that the size of the interphase zone is strongly affected by the processing/manufacturing quality and the better the quality the smaller the interphase zone. In view of the rapid improvement on processing techniques for PNCs, we therefore adopt the range of [1, 4] nm for the interphase zone thickness from [77].

The epoxy and the interphase zone are considered as a quasi-brittle isotropic material. The nanoparticles are much stiffer than the epoxy matrix and are not allowed to fracture. Furthermore, we neglect the agglomeration of the inclusions and assume no particle debonding occurs and the dominant failure mechanism is considered to be the fracture in the polymer matrix and/or the interphase zone. Note that the fracture energy of PCNs might also be influenced by the chemical composition of constituents, the morphology of filler, manufacturing techniques and the curing processes which have not been taken into account herein.

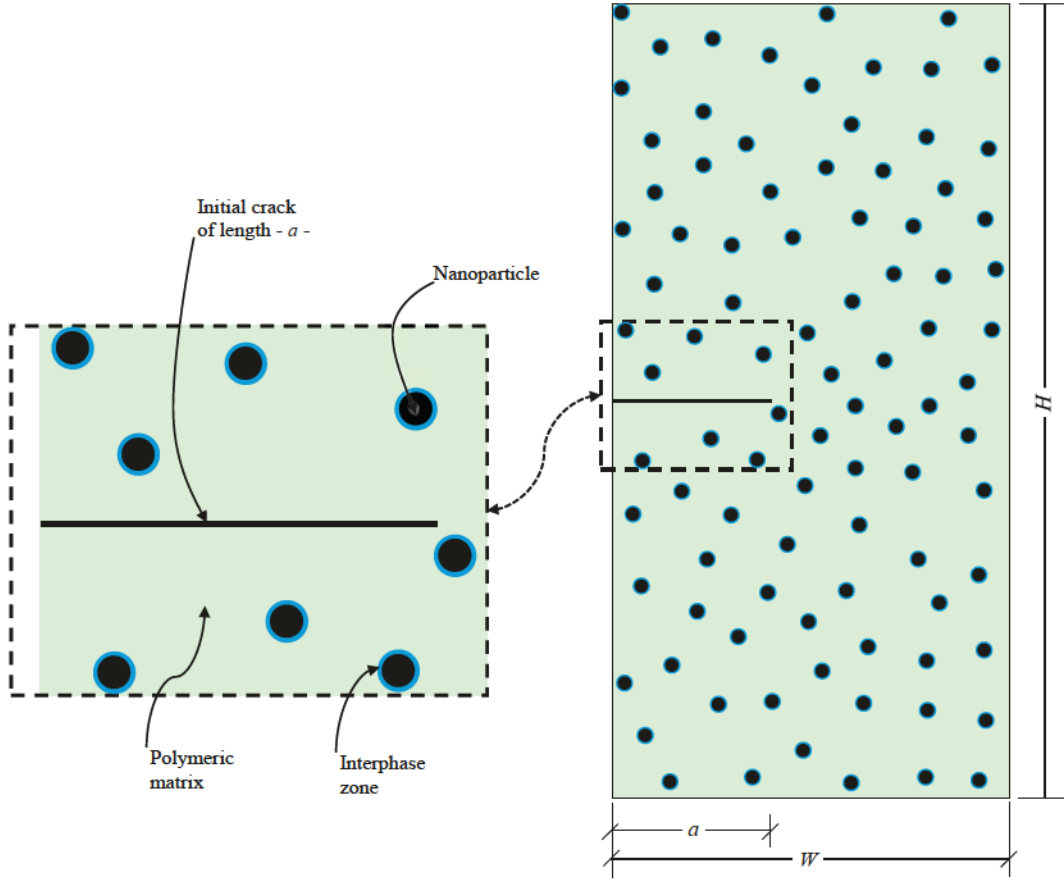


Figure 5.1.: Schematic geometry of the Single Edge Notched Tension specimen of PNCs including the interphase zones.

Plane stress conditions are assumed to model the fracture and the maximum principal stress criterion is adopted for the crack initiation. The fracture toughness is determined considering a Single Edge Notched Specimen under tensile loading as illustrated in Fig. 5.1. The dimensions of the specimen are $W=750$ nm and $H=1500$ nm, and the initial notch length is 300 nm.

The flowchart of the modeling approach is illustrated in Fig. 5.2. At the beginning, initial parameters (mesh size, volume fraction of the filler, size of the nanoparticles and the interphase zone) are defined. The required number of nanoparticles are placed sequentially based on the random sequential addition algorithm (RSA). A non-overlapping condition between a new and the existing sequence is checked during placing the nanoparticles inside the matrix. Since we are interested in studying the effect of the interphase zone, a well dispersion of the particles is also confirmed. Once all particles are inserted, the mesh is generated; we employ the 4-node phantom elements described in [16, 17]. Displacement boundary conditions are applied on the top surface. The displacements

5.2 Modelling the fracture in the PNCs

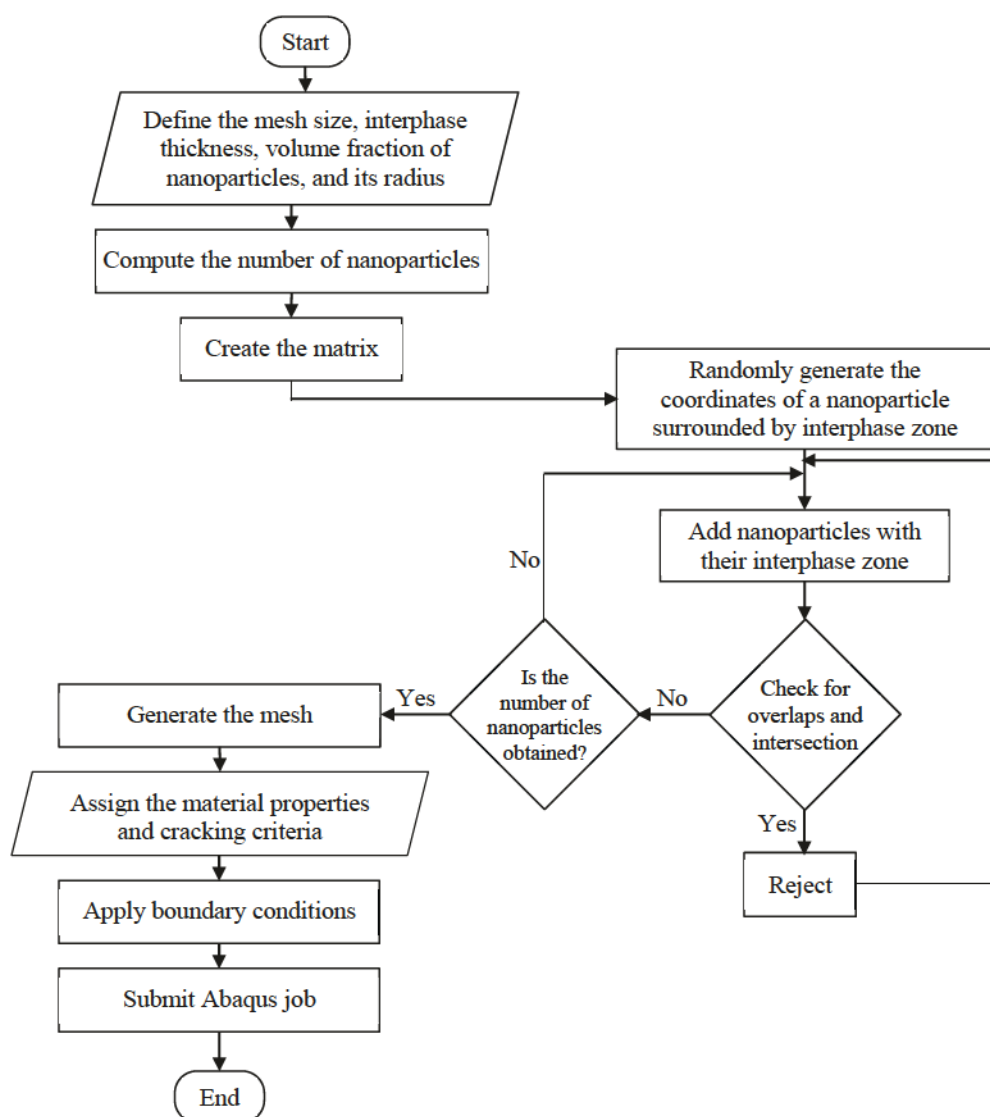


Figure 5.2.: Flowchart of the modeling algorithm.

along the loading direction are fixed at the bottom edge resulting in mode-I dominated fracture.

Fig. 5.3 shows the deformed shape of PNCs exemplary specimen reinforced by 4.0 vol.% nanoparticles of 25 nm in diameter, with an interphase of 3.50 nm in thickness. Other material properties are given in Table 5.1. The crack propagates orthogonal to the loading direction as illustrated at different load steps in Figs. 5.3a to 5.3c. Fig. 5.3d shows that the nanoparticles have improved the load carrying capacity and ductility in the PNC compared to the corresponding pure epoxy. We also tested different realizations with different particles spatial distributions for the same parameters properties. The coefficient of variation of 10 different realizations for the Young's modulus and the frac-

5.3 Modelling the uncertainties in the input parameters

Table 5.1.: Material properties for the exemplary PNCs specimen shown in Fig. 5.3

The volume fraction of the nanoparticles (%)	4.0
The nano-particles size (nm)	25
The epoxy matrix Young's modulus (GPa)	2.85
The epoxy matrix maximum allowable principal stress (MPa)	425
The interphase zone thickness (nm)	3.5
The interphase zone Young's modulus (GPa)	4.0
The coefficient of variation ^a of:	
-Young's modulus of the nanocomposite	0.5%
-The fracture energy of the nanocomposite	2.7%

^aThe coefficient of variation of 10 realizations simulated by different spatial distributions of the nanoparticles.

ture energy of the PNCs are displayed in Table 5.1. The fracture energy has a higher variation than the Young's modulus but both have a relatively low variability in relation to their means values.

5.3. Modelling the uncertainties in the input parameters

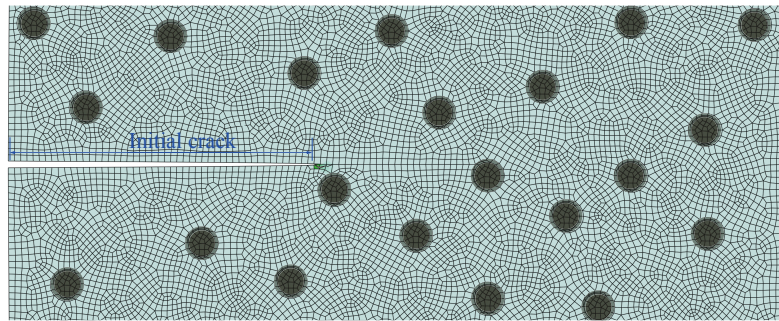
5.3.1. Polynomial chaos expansions

The output of interest of a physical system can be expressed mathematically as a dependent variable, Y , that is a function of independent variables, $fX = (X_1, \dots, X_k)$, i.e. $Y = f(\mathbf{X})$.

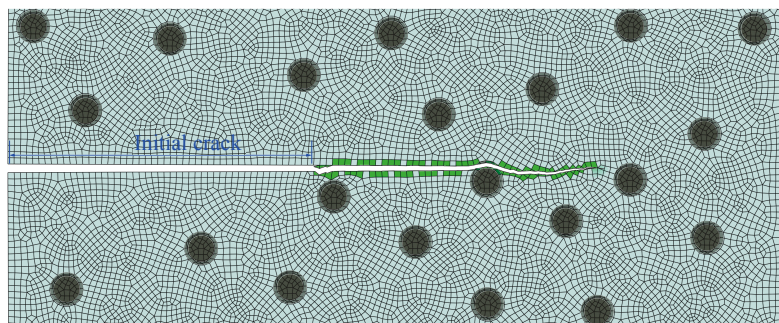
As mentioned previously, the response of the mechanical model can be approximated by a surrogate model. The polynomial chaos expansions (PCE) is an effective stochastic tool that can be utilized for this purpose. In addition to the ability of the PCE in approximating the response, the randomness in the output is concealed in the expansion coefficients by taking into account the uncertainties in the inputs. According to Ghanem and Spanos [27], Y can be expanded by a spectral expansion using orthogonal polynomials as

$$Y = \sum_{j=0}^{\infty} \beta_j \Psi_j(\boldsymbol{\xi}) \quad (5.4)$$

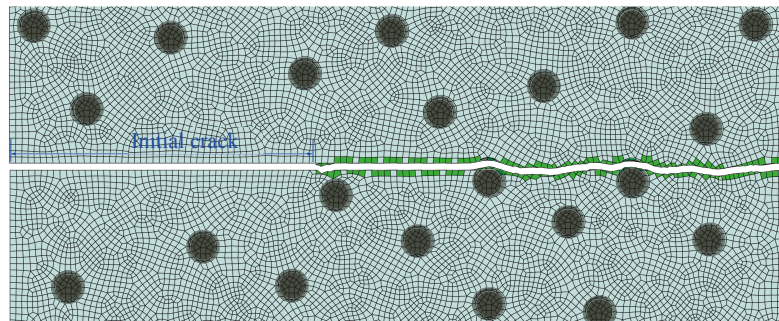
5.3 Modelling the uncertainties in the input parameters



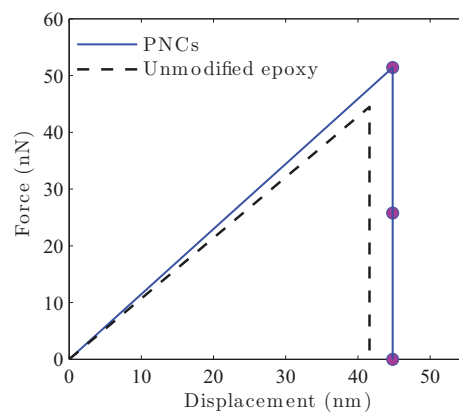
(a) Step a



(b) Step b



(c) Step c



(d) Load-displacement

Figure 5.3.: Deformed shape for an exemplary PNCs specimen and the associated load-displacement curve.

5.3 Modelling the uncertainties in the input parameters

where $\boldsymbol{\xi}$ is the vector of independent standard normal (Gaussian) random variables, Ψ_j 's are multivariate Hermite polynomials of order j , and β_j 's are the PCE deterministic coefficients. This decomposition was extended later to distributions other than the Gaussian using orthogonal polynomial basis functions of the Wiener-Askey scheme [28]. For instance, the uniform distributions over $[-1, 1]$ can be associated to Legendre polynomials. The expressions for Hermite and Legendre polynomials are described in Eqs. (5.5) and (5.6), respectively [180].

$$H_{e0}(x) = 1, \quad H_{e1}(x) = x, \quad H_{e2}(x) = x^2 - 1, \quad (5.5)$$

$$P_0(x) = 1, \quad P_1(x) = x, \quad H_2(x) = \frac{1}{2}(3x^2 - 1), \quad (5.6)$$

The generalized multivariate polynomial, Ψ_j , is obtained by the tensor product of the corresponding univariate polynomials.

$$\Psi_j = \prod_{i=1}^k \psi_{j_i}(\xi_i) \quad (5.7)$$

$\psi_{j_i}(\xi_i)$ being the univariate polynomial of the variable i , and k being the number of independent variables.

The infinite expansion in Eq. (5.4) can be truncated to a polynomial of order n

$$\hat{Y} \approx \sum_{j=0}^{P-1} \beta_j \Psi_j(\boldsymbol{\xi}) \quad (5.8)$$

Hence, the number of unknown deterministic coefficients, P , for k random variables is $P = (k+n)!/(k!n!)$. The statistical properties of the model output can be obtained directly once the PCE coefficients are available.

Two classes of methods are popular for computing the PCE coefficients, namely the intrusive and the non-intrusive methods. In the intrusive method, a weak form of the mathematical model is developed based on the minimization of the residual in the balance equation in the Galerkin scheme where an alteration in the original finite element code is imposed [27, 181]. The non-intrusive method is easier to implement. As the name implies, it can be carried out utilizing a set of realizations of the deterministic model without modifying the finite element code. From various non-intrusive methods, the regression method in [33, 182, 183] is exploited in this study. The regression met-

5.3 Modelling the uncertainties in the input parameters

hod which known also as stochastic collocation is based on least square minimization of error between a variable and its truncated approximation [184, 185]. Accordingly, the expansion coefficients are determined by least-squares regression of the exact solution (the finite element model) with respect to the expected results of PCE surrogate model. Firstly, we generate the so-called *experimental design* $\mathbf{X} = \{\mathbf{X}^1, \dots, \mathbf{X}^N\}$ by choosing a set of regression points, N , called samples, in the probability space of the input parameters using Latin Hypercube Sampling (LHS) [30]. Compared to classical Monte Carlo sampling method, LHS is an improved strategy that enables a reliable approximation of the stochastic properties of the random variables. The base of the method is the subdivision of the design space of a variable X_i into N classes D_m of equal probability:

$$P[X_i \in D_m]; \quad i = 1, \dots, k; \quad m = 1, \dots, N \quad (5.9)$$

where N and k are the number of samples and the number of input parameters, respectively. Thereby, the occurrence of X_i is insured to be equally probable in its design space.

By then, the matrix Ψ is formulated considering the transformation of the values of \mathbf{X} into standard variables of ξ . For the generated sample, the model is evaluated at each point and the corresponding vector of exact model simulations is \mathbf{Y} . The final step is to calculate the expansion coefficients. The sum of the squares of the residuals, S , between \mathbf{Y}_s and the approximated solution of PCE, $\hat{\mathbf{Y}}$, is

$$S = \sum_{s=1}^N \left(Y_s(\xi^s) - \sum_{j=0}^{P-1} \beta_j \Psi_j(\xi^s) \right)^2 \quad (5.10)$$

where ξ^s is the transformed standard random vector of the sample point \mathbf{X}^s . Eq. (5.10) can be minimized by taking its partial derivative with respect to each of the coefficients and setting the resulting equation equal to zero

$$\frac{\partial S}{\partial \beta_j} = 0; \quad j = 0, \dots, P-1 \quad (5.11)$$

Solving the resulting system of linear equations yields the expansion coefficients. It can be expressed in matrix notation as

$$\beta = (\Psi^T \Psi)^{-1} \Psi^T \mathbf{Y} \quad (5.12)$$

5.3 Modelling the uncertainties in the input parameters

An appropriate choice for the number of model evaluations, N , is crucial. A very small N may not adequately cover the input parameters space and will not yield an effective representative surrogate model. On the other hand, a very large N unnecessarily increases the computational cost without improving the accuracy of the results significantly. There are yet only empirical methods to determine an adequate sample size. In all cases, to solve Eq. (5.12), N must be greater than the number of unknowns (P). In this study, the experimental design is built iteratively by increasing N until the convergence of the coefficient of determination (R^2) is achieved. Further, to account for the number of expansion coefficients, P , the adjusted coefficient of determination (R_{adj}^2) is also examined.

$$R_{adj}^2 = 1 - \frac{N - 1}{N - P - 1} (1 - R^2) \quad (5.13)$$

The degree of polynomial of the PCE (order) has to be a priori chosen. There are no guidelines for selecting directly the lowest order of the polynomials (n) that achieve the best fit of actual model. This optimum order depends mainly on the considered problem. The coefficient of determination, R^2 , is a measure to assess the performance of the selected PCE degree. At this point we should keep in mind that as n increases, the number of unknowns increases requiring more model simulations (higher computational cost). Hence, higher n values is recommended in the case of high accuracy meta models required or when we are deeply looking into the higher order interaction between the input parameters.

We consider the fracture energy of PNCs, G_{Ic} , as the output of interest. Six input parameters has been assumed being non-deterministic independent variables.

The definition of the input parameters and their distribution type, mean value, and standard deviation are summarized in Table 5.2. The volume fraction of the nanoparticles (V_f) is assumed to vary uniformly from 0.5 - 10.0% [186]. The distribution of the particles size is characterized by the logarithmic normal distribution [70]. In our simulations, this distribution is truncated at 10 and 80 nm as minimum and maximum bounds of the nanoparticle diameter (d_n). A uniform distribution is assumed for Young's modulus of the epoxy matrix (E_m) with mean value of 2.85 GPa and standard deviation of 0.520 GPa [187, 188]. A Gaussian Normal distribution is assumed for the maximum allowable principal stress (σ_{max}) with mean value and standard deviation of 425 and 45 MPa. The probability distribution functions of the thickness (t_i) and Young's modulus (E_i) of the interphase zone are uniform with the limits of [1,4] nm and [1,7.5] GPa,

5.3 Modelling the uncertainties in the input parameters

Table 5.2.: The definitions and the statistical properties of the uncertain input parameters.

Parameter definition	Unit	Symbole	Distribution Type	Mean	Standard deviation
The volume fraction of the nanoparticles	%	V_f	Uniform	5.25	2.742
The diameter of the nano-particles	nm	d_n	Log-Normal ^a	25.0	20.0
The elastic modulus (Young's modulus) of the epoxy matrix	GPa	E_m	Uniform	2.85	0.520
The maximum allowable principal stress	MPa	σ_{max}	Normal	425	45
The elastic modulus (Young's modulus) of the interphase zone	GPa	E_i	Uniform	4.25	1.876
The thickness of the interphase zone	nm	t_i	Uniform	2.5	0.866

^aThe distribution of the particles size is truncated at lower and upper bounds of 10 and 80 nm.

respectively.

The variables with Normal and Log-Normal distributions were expressed as a series expansion of Hermite polynomial. They were transferred to standard normal distribution with zero mean and unit standard deviation in advance, while the uniform distributions are mapped linearly onto $[-1, 1]$ prior to be represented using Legendre chaos polynomials.

Two polynomials, second and third order PCE ($n = 2$ and $n = 3$), are constructed to represent the output as a function of the six input parameters. The calculated value of R^2 and R_{adj}^2 for the constructed PCE are presented in Table 5.3. Although the third order PCE has better coefficient of determination, they have almost identical R_{adj}^2 .

Table 5.3.: Properties of the constructed PCEs

	Degree of the polynomial	
	$n = 2$	$n = 3$
Number of expansion coefficients, P	28	84
Coefficient of determination, R^2	0.786	0.877
Adjusted coefficient of determination, R_{adj}^2	0.740	0.738

5.3.2. Sensitivity Analysis

The fracture energy of the PNCs is expected to be a random variable as a result of the randomness in the input parameters. Measuring the relative significance of the effect of each individual input parameter on the variance of the output is achieved by means of sensitivity analysis. The Sobol' method [31] is one of the most commonly used global SA approaches that is based on variance decomposition of the output. Given an integrable function f defined on the k -dimensional unit hypercube, the Sobol' functional decomposition is

$$f = f_0 + \sum f_i + \sum_{i=0} \sum_{j=i+1} f_{ij} + \dots + f_{12\dots k} \quad (5.14)$$

The expansion has 2^k terms each of which is a square integrable function of the factors in its index only. Provided that each term has a zero mean value, the summands in the decomposition are orthogonal to each other and the Sobol' decomposition is unique.

In this framework, the analysis of variance (ANOVA) decomposition can be written as;

$$V = \sum_{i=1}^k V_i + \sum_{i=1}^k \sum_{j=i+1}^k V_{ij} + \dots + V_{12\dots k} \quad (5.15)$$

Accordingly and by dividing both sides of Eq. (5.15) by V , the Sobol' indices can be

$$\sum_{i=1}^k S_i + \sum_{i=1}^k \sum_{j=i+1}^k S_{ij} + \dots + S_{12\dots k} = 1 \quad (5.16)$$

The first-order sensitivity index (S_i) measures the part of the variance of the model output due to the input X_i . It is also known as the main effect of the parameter X_i . Whilst, the higher order indices (e.g. S_{ij} , which is known as the second-order index), measure the joint effect of the input parameters. The total sensitivity index S_{T_i} is used to estimate how much the variation in X_i contributes to the variation in the output. It equals the sum of the first-order and all high-order terms. The difference between S_{T_i} and S_i determines how much the parameters interact with each others.

The Sobol' indices are obtained usually using Monte Carlo simulations. In total, there are $2^k - 1$ Sobol's indices that require $\mathcal{O}(N2^k)$ model evaluations (computational cost) which is unaffordable particularly in the time consuming finite element simulations. This cost can be reduced to $\mathcal{O}(N(k+2))$ by considering the first order and the total indices

5.3 Modelling the uncertainties in the input parameters

only as proposed by [32] which is still unaffordable particularly for computationally demanding models.

Alternative to the sampling-based methods, the variance-based Sobol' sensitivity indices can be computed analytically from the expansion coefficients of the PCE [33,34]. Clearly, the Sobol' decomposition is equivalent to the expansions of PCE in Eq. (5.4). As all the terms of the expansion are orthogonal polynomials, the total variance of the response can be approximated by

$$\hat{V} = \sum_{j=1}^{P-1} \beta_j^2 \mathbb{E} [\Psi_j^2(\mathbf{X})] \quad (5.17)$$

where $\mathbb{E}[\cdot]$ is the mathematical expectation. In accordance to the dependency of each polynomial, the expansion coefficients are assembled, square summed and subsequently normalized in order to obtain the sensitivity indices. Thereby, the complete list of Sobol' indices can be obtained with almost no additional cost. The computational cost required for the calculation of the expansion coefficients is the major cost in this case.

Making use of the PCE from Section 5.3.1, the sensitivity of parameters influencing the fracture energy of PNCs are evaluated using Eqs. (5.16) and (5.17). For the second order PCE, the first order, second order, and total effect sensitivity indices are summarized in Table 5.4. The main effects of the input parameters are the substantial source of the variance in the output that constitute 93.4%. The maximum allowable principal stress of the epoxy matrix, σ_{max} , outranks its stiffness, E_m , as the most two influential parameters. Their main effect is 90.3% ($= 0.628 + 0.275$) of the total variance of the output. Fig. 5.4a depicts the first-order and the total effect sensitivity indices of the six parameters.

On the other hand, when considering third order PCE, the main effects of all input parameters are 78.8%. The sum of the joint effect of two and three parameters, i.e. $\sum S_{ij}$ and $\sum S_{ijl}$ are 12.2% and 9.1%, respectively (Table 5.5). σ_{max} and E_m are also, as in the second order PCE, the most significant parameter influencing the output variation and σ_{max} is observed clearly to surpass E_m . The total effect of the nanoparticle size come in the next place of the ranking. Its effect is dominated by the interaction with other parameters ($S_T - S_i$ for d_n is 0.094). This result may explain the contradictions in experimental results in the literature. For instance, [56] and [57] reported that the fracture energy of PNCs is slightly affected by the variation of the nano particle size, while the study of [52] showed a significant influence of the variation of the nano particle size on the fracture energy. The remaining parameters have also considerable interaction

5.3 Modelling the uncertainties in the input parameters

Table 5.4.: Sobol' sensitivity indices based on Second order PCE, $n = 2$

	V_f	d_n	E_m	σ_{max}	E_i	t_i
S_i	0.008	0.005	0.275	0.628	0.014	.004
	$\sum S_i=0.934$					
S_{ij}^a						
S_{1j}	0.001	0.000	0.003	0.002	0.000	
S_{2j}		0.013	0.021	0.002	0.001	
S_{3j}			0.021	0.000	0.001	
S_{4j}				0.000	0.000	
S_{5j}						0.001
	$\sum S_{ij}=0.066$					
S_{Ti}	0.015	0.042	0.309	0.674	0.019	0.007

^a S_{ij} refers to the second order sensitivity that measures the joint effect of the parameters i and j , e.g. S_{12} is the sensitivity of the interaction between the volume fraction and the diameter of the nanoparticles.

effects that contribute to the variance. The first-order and the total effect sensitivity indices are displayed in Fig. 5.4b.

From the preceding analysis, the allowable principal stress of the epoxy, and Young's modulus of the epoxy can be considered as the most significant parameter that dominate the variance in the fracture energy of PNCs. It is expected that slight changes in these parameters will result in high change in the fracture energy. This implies that special care should be taken when measuring these variables.

In order to show the effect of parameters on the variance of the output, three sets of samples are randomly generated by LHS. Set G_1 is obtained by sampling the entire input parameters space, Set G_2 is formed with the same as Set G_1 but the parameters; σ_{max} and E_m are fixed respectively at their mean values, and Set G_3 is formed by fixing the remaining parameters at any point of their variation range. The corresponding three sets of model output are calculated using the constructed third order PCE ($n = 3$). The probability density of the output of the three sets represented by Normal distribution are displayed in Fig. 5.5. Set G_1 and Set G_3 have almost the same range of variation which is considerably higher than Set G_2 . As a measure of relative variance, the coefficient of variations (COV) for Set G_1 and Set G_3 are 38.9 and 34.7 %, respectively, while for Set G_2 is 11.3 %.

5.4 Summary and conclusion

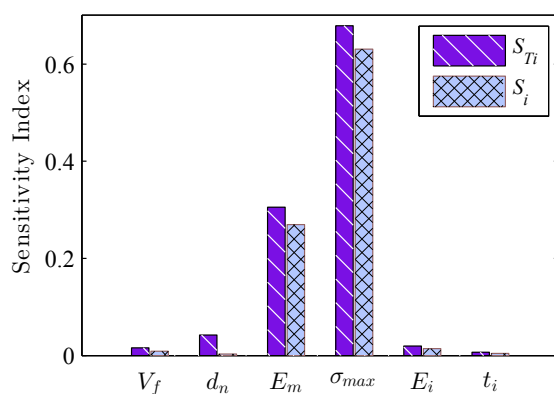
Table 5.5.: Sobol' sensitivity indices based on Third order PCE, $n = 3$

	V_f	d_n	E_m	σ_{max}	E_i	t_i
S_i	0.007	0.005	0.237	0.517	0.015	0.007
$\sum S_i = 0.788$						
S_{ij}						
S_{1j}		0.006	0.006	0.008	0.001	0.003
S_{2j}			0.012	0.022	0.001	0.007
S_{3j}				0.030	0.002	0.014
S_{4j}					0.001	0.004
S_{5j}						0.005
$\sum S_{ij} = 0.122$						
S_{ijl}^a						
		S_{12l}	0.001	0.001	0.002	0.007
		S_{13l}		0.011	0.002	0.003
		S_{14l}			0.005	0.000
		S_{15l}				0.000
		S_{23l}		0.022	0.000	0.005
		S_{24l}			0.001	0.004
		S_{25l}				0.004
		S_{34l}			0.003	0.003
		S_{35l}				0.010
		S_{45l}				0.007
$\sum S_{ijl} = 0.091$						
S_{Ti}	0.061	0.100	0.359	0.638	0.057	0.084

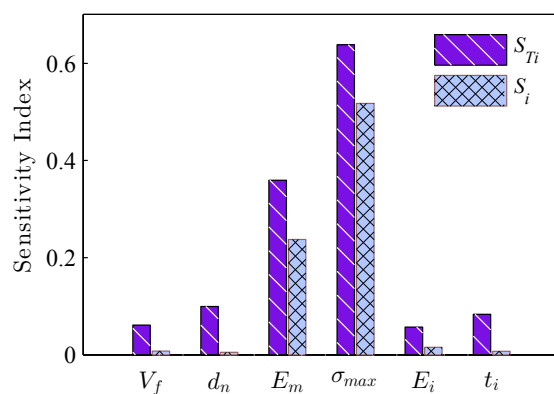
^a S_{ijl} refers to the third order sensitivity that measures the joint effect of the parameters i , j , and l , e.g. S_{123} is the sensitivity of the interaction between the volume fraction, the diameter of the nanoparticles and the matrix Young's modulus.

5.4. Summary and conclusion

The fracture toughness of the polymer can be considerably enhanced by the addition of nanosize rigid inclusions. In the presence of nanofiller, interphase zones are formed connecting the rigid inclusions with the surrounding matrix. In this study, the fracture in epoxy polymers reinforced by spherical nanoparticles was investigated accounting for the interphase zone. Fracture was modelled by the phantom node method. Due to the uncertainty in the parameters influencing the damage of PNCs, the frac-



(a) Second order PCE, $n = 2$



(b) Third order PCE, $n = 3$

Figure 5.4.: First-order and total-effect Sobol' sensitivity indices.

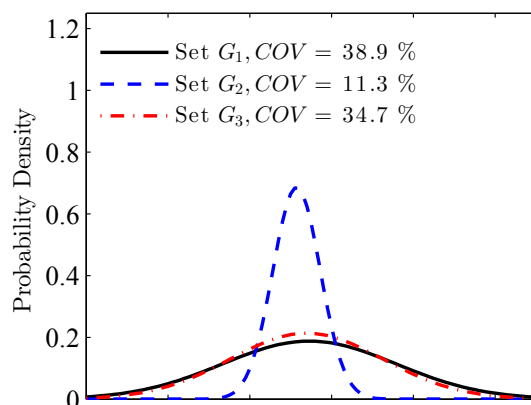


Figure 5.5.: The effect of fixing the influential and non-influential parameters on the variance of the output.

ture energy was considered as a random variable in constructing the polynomial chaos

5.4 Summary and conclusion

expansions (PCE) surrogate model. The uncertain independent parameters were: the volume fraction of the nanoparticles, the diameter of the nanoparticle, Young's modulus of the epoxy matrix, the maximum allowable principal stress, the thickness, and Young's modulus of the interphase zone.

The developed second and third order PCE showed almost the same performance measured by the adjusted coefficient of determination, R_{adj}^2 . Also, both produced an identical parameters sensitivity ranking. The sensitivity analysis results revealed that the maximum allowable principal stress and Young's modulus of the epoxy matrix are the most significant parameters. High variation in the fracture energy of PNCs is expected due to small changes in these parameters, hence, they should be determined precisely.

In the future, we will develop the work to 3D stochastic modeling of PNCs considering the debonding mechanism and the anisotropy in the interphase zone.

Chapter 6

Sensitivity and uncertainty analysis for multiscale models of collagen bio-structure

Contribution of authors

The work presented in this chapter is submitted for publication. The original text from this publication is used in this chapter.

- Khader M. Hamdia
 - Conducting literature review.
 - Coding sensitivity analysis methods.
 - Performing uncertainty quantification.
 - Writing the manuscript.
- Michele Marino
 - Conducting literature review regarding Collagen Bio-structures.
 - Modeling of Collagen Bio-structures.
 - Assisting in writing the manuscript.
- Xiaoying Zhuang
 - Mentoring the research progress.
 - Reviewing the manuscript before submission.
- Timon Rabczuk
 - Mentoring the research progress.
 - Reviewing the manuscript before submission.

6.1. Introduction

Soft tissues provide the essential link and support for organs and biological structures throughout the whole human body, such as tendons, ligaments, skin, muscles, blood vessels, heart, cornea and intestine. Therefore, the mechanical response of soft tissues highly affects the functionalities of many body systems in health and disease (e.g., musculoskeletal, cardiovascular, digestive). Soft biological tissues consists of cells, collagen, elastin and ground matrix, if not being mineralized. Tissue constituents are organized in agreement with a multiscale hierarchical principles from the nanoscale (i.e., the quaternary structure of polypeptides), through the mesoscale (i.e., cross-linked molecular assemblies), up to the microscale (i.e., fibers), which determines tissue mechanical response.

However, the understanding of the relationship between the multiscale structural arrangement of constituents and their biomechanical performances remains an open issue [189]. For instance, the role of tissue remodeling on the non-functional behavior of biological structures associated with ageing or cardiovascular pathologies (e.g., aortic restenosis, dissecting aneurysms) is not clear. Though a number of literatures have addressed the collagen constituents, alterations in the crimp and the thickness of fibers [190, 191], in the density of intermolecular cross-links [192, 193], or in the molecular flexibility [194, 195], a better understanding of the phenomenon and mechanism requires the multiscale structure-mechanics relationship in soft tissues is a significant step-forward in biomechanics.

The mechanical response of soft tissues can be characterized by nonlinear stress-strain relationships with a strong anisotropic character, mostly due to the presence of collagen fibers. The basic building blocks of collagen fibers are tropocollagen molecules, that is proteins made up by three polypeptide strands twisted together into a triple helix quaternary structure. Collagen molecules exhibit labile domains, also referred to as molecular kinks. Since the length of labile domains is comparable with the persistence length of collagen triple-helices, molecular kinks are activated by thermal fluctuations (see Fig. 6.1).

In soft tissues, tropocollagen molecules self-assemble to form long and continuous cylinder-like structures, named fibrils, characterized by a diameter between 50 to 500 nm. In particular, molecules interact each other by means of inter-molecular covalent cross-links and the density of the links affect the prevalence of molecular sliding with respect to the molecular elongation.

6.1 Introduction

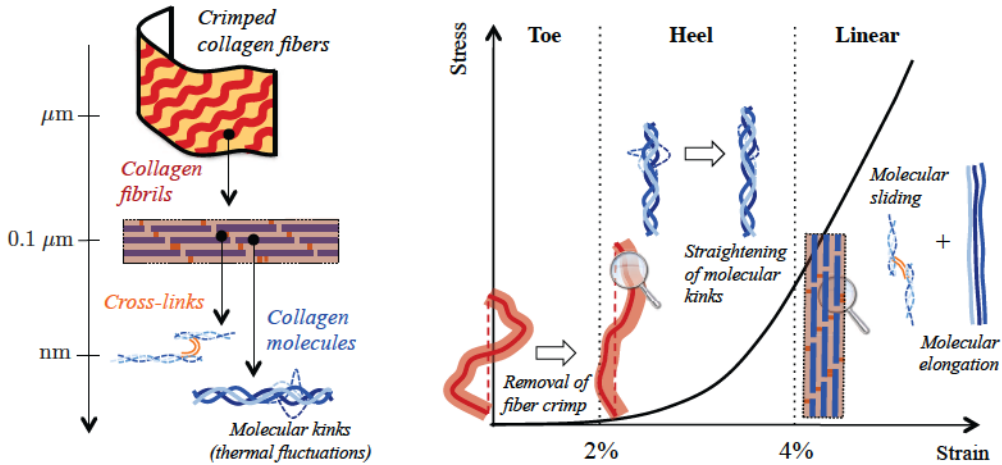


Figure 6.1.: Multiscale hierarchical arrangement of constituents (left) and structure-mechanics relationship (right) in soft biological tissue.

Collagen fibers in soft tissues are characterized by a crimped collagen fiber microstructure. Fibers appear indeed as periodic-like curvilinear structures with characteristic length in the order of μm . As schematically depicted in Fig. 6.1, the underlying nonlinearities in tissue constituents are responsible for a characteristic J-shaped stress-strain curve in the case of a uniaxial traction applied along the collagen fiber direction. For describing tissue nonlinear behavior, low and high strain tangent moduli, as well as transition (from a low to a high stiffness region) strain and stress values are relevant output quantities, commonly employed in the specialized literature.

The nonlinear mechanical response of biological tissues is often modeled by introducing hyperelastic strain-energy functions. Constituents non-linearities are indeed generally taken into account by choosing a suitable analytical form of the strain-energy density (e.g., polynomial, exponential) as in a phenomenological approach [196–198]. These approaches generally exhibit a weak relationship between model parameters and tissue histological/biochemical features, because they are based on phenomenological expressions of fiber strain-energy functions, with fiber orientation being the only structural information. Employing classical phenomenological-based constitutive approaches, common physiopathological alterations in the structure and organization of tissue constituents can be accounted for only via a suitable calibration of a set of phenomenological parameters.

Alternatively, a multiscale constitutive approach has been recently proposed for the description of the mechanical properties of soft tissues [199–202]. This approach is based

on the development of models for the dominant mechanisms occurring at the different length scales, coupled by means of inter-scale compatibility and equilibrium relationships. Generalizing the early ideas by Lanir on microstructural-based models [203], multiscale constitutive models allocate macroscopic stress to different micro- and nanostructural mechanisms with a special insight on the structure-mechanics relationship.

Thanks to the explicit description of the hierarchical collagen organization, the multiscale constitutive approach introduces only parameters corresponding to measurable structural properties, opening to a straightforward model calibration based on clinical evidence. Calibration can be simplified first by identifying the most influential parameters. Moreover, addressing the variation of clinically-relevant histological, biochemical or biophysical features, the proposed approach opens to a better understanding of the relationship between tissue structure and mechanical properties in health and disease. The uncertainties in the model structure, the estimates of the model input parameters, and their stochasticity are highly expected. These uncertainties propagate through the model and lead to uncertainty of the output quantities. Evaluating how these uncertainties are affected by collagen related structural features is essential. For this purpose, sensitivity analysis (SA) can be applied effectively, where the relative importance of each input parameter is evaluated.

This work presents an extensive study of parametric sensitivities analyses which gives a statistically-relevant quantitative correlation between mechanical output quantities (e.g, low- and high-strain tangent moduli, transition stress and strain) and collagen-related structural features (i.e., fiber crimp amplitude and thickness, density of inter-molecular cross-links, molecular persistence length). This research is of value to gain insight understanding into the multiscale mechanical behaviour of soft tissue, that greatly help in making future investigations about which parameters to target in a field study and model calibration. To the best of our knowledge, quantitative results in the context of stochastic analysis has not yet been investigated in the literatures.

Results can be employed in the framework of:

- the identification of the dominant/insignificant parameters for model order reduction;
- direct approaches for the calibration of constitutive models from histological, biochemical and biophysical measurement;
- inverse approaches for estimating histological, biochemical or biophysical features from mechanical tests;

6.2 Materials and Methods

- growth and remodeling formulations for understanding the rationale behind remodeling strategies in pathological and healing conditions;
- tissue engineering applications for tuning structural features in biological constructs in order to obtain targeted mechanical properties.

6.2. Materials and Methods

Collagen fibers in soft biological tissues are arranged in agreement with a regular (e.g., tendons) or an irregular (e.g., skin) pattern. The arrangement of collagen fibers in regular tissues follows a predefined pattern and these can be conveniently classified in uni- (e.g., tendons, ligaments) or multi- (e.g., arterial walls, hearth valves) directional tissues [189]. In unidirectional tissues, collagen fibers can be retained as parallel one to each other. A multidirectional tissue is intended to be made up of a number of stacked thin layers, each of them with a regular unidirectional fiber arrangement. In this framework, collagen fibers are classically split in different families where each family is identified by a given direction.

Soft biological tissues undergo both uniaxial and biaxial loading conditions under *in vivo* applications. In particular, unidirectional tissues undergo uniaxial stress states, mainly along the fiber direction. On the other hand, multidirectional tissues are generally subjected to biaxial stress states, where the single sub-layer carries loads along the local fiber main direction.

Accordingly, unidirectional tissues under uniaxial traction are endowed with the essential features which characterize the nonlinear mechanics of soft biological tissues in terms of the underlying structure-mechanics relationship. The obtained mechanical response is indeed affected by microstructural and nanoscale mechanisms. The ones that are herein addressed refer to collagen fibers. As also shown in Fig. 6.1, the mechanisms that will be addressed in the present work are:

- upon tissue deformation, the crimped aspect of fibers at microscale straighten out, increasing the stiffness of the overall tissue along the fiber-chord direction;
- upon fiber straightening, fibrils' stretch increases, associated with two *in series* elongation mechanisms at mesoscale, that is intermolecular sliding and molecular stretch;

- upon molecular stretching, the thermal fluctuations of molecular kinks progressively disappear and molecular backbone straightens out at the nanoscale. The former mechanism is known as a source of entropic elasticity and it extinguishes when molecular end-to-end length reaches its contour length, as well captured by the Worm-Like Chain model. On the other hand, the stretching of molecular backbone is referred to as energetic elasticity and it is associated with the unravelling of collagen triple-helix, as elucidated by atomistic computations through molecular dynamics simulations.

As a result of the underlying nonlinearities, the stress-strain curve of unidirectional tissues under along-the-fiber uniaxial traction is J-shaped. It has been described as subdivided into three main regions [189]: the toe region (within the nominal strain range $\approx 0-2\%$), the heel region (within the strain range $\approx 2-4\%$), and the linear region (within the strain range $\approx 4-10\%$). Mechanisms occurring at very different length scales are dominant within each region, associated with collagenous constituents and described in Section 6.2.1 (see Fig. 6.1).

Since the aim of the present work is to shed a novel light on the multiscale relationships between mechanical and structural features in soft biological tissues, the analysis is restricted to unidirectional tissues under uniaxial traction, with collagen fibers aligned along the traction direction. In particular, a displacement-based test is addressed, where stretch $\lambda \in [1, \lambda_{\max}]$ is the control-variable and λ_{\max} is the maximum stretch. Moreover, in order to isolate the role of collagenous constituents, the contribution P_F to tissue nominal stress associated with collagen fibers is considered only.

In order to conduct physically-meaningful sensitivity analyses, the relationship between fiber nominal stress P_F and the values of structural features is obtained employing a constitutive approach based on a multiscale structural rationale. The latter has been recently proposed in [199, 200, 202] and it is described in Appendix C for the sake of completeness. As shown by Eq. (C.3) in Appendix C, the employed approach allows to obtain the stress-stretch relationship $P_F = P_F(\lambda)$ in function of (among others) the following structural features:

- collagen fiber crimp amplitude $H_{F,o}$;
- collagen fiber radius r_F ;
- intermolecular cross-link stiffness density $\Lambda_K = \Lambda_c k_c$, with Λ_c being the (mole fraction) density and k_c the stiffness of intermolecular cross-links;

6.2 Materials and Methods

- molecular persistence length ℓ_p , being the maximum contour length over which the corresponding molecular segment appears as straight under thermal fluctuations.

The sensitivity of function $P_F(\lambda)$ on the set of structural features \mathcal{S} ,

$$\mathcal{S} = \{H_{F,o}, r_F, \Lambda_K, \ell_p\}, \quad (6.1)$$

will be obtained. To this aim, relevant output quantities, physically-meaningful from the mechanical point of view and highly affected by \mathcal{S} , are introduced (see Fig. 6.2). Apart from fiber stress and introducing collagen volume fraction V_F , these quantities are defined by means of:

- the effective tangent modulus $E_F = E_F(\lambda)$ of crimped collagen fibers (see Eq. (C.3)):

$$E_F(\lambda) = \frac{1}{V_F} \frac{\partial P_F}{\partial \lambda}; \quad (6.2)$$

- the amplitude $H_F = H_F(\lambda)$ of crimped collagen fibers (see Eq. (C.4c));
- the stretch $\lambda_f = \lambda_f(\lambda)$ of collagen fibrils;
- the contribution $\lambda_m = \lambda_m(\lambda)$ of the elongation of collagen molecules to fibril stretch λ_f ;
- the contribution $\lambda_s = \lambda_s(\lambda)$ of entropic elongation-mechanisms to molecular stretch λ_m .

6.2.1. Output quantities of interest

The output quantities of interests, that will be object of sensitivity analyses, are introduced on the basis of the dominant mechanisms occurring within each region of the J-shaped stress-strain curve of unidirectional tissues under along the fiber uniaxial traction.

The toe region is a low stiffness region, mainly associated with the straightening of the microscopic crimp in collagen fibers. Within this region, relevant mechanical output quantities are (see Fig. 6.2):

- the minimum fiber tangent modulus E_{\min} :

$$E_{\min} = \min_{\lambda \in [1, \lambda_{\max}]} (E_F(\lambda)) . \quad (6.3)$$

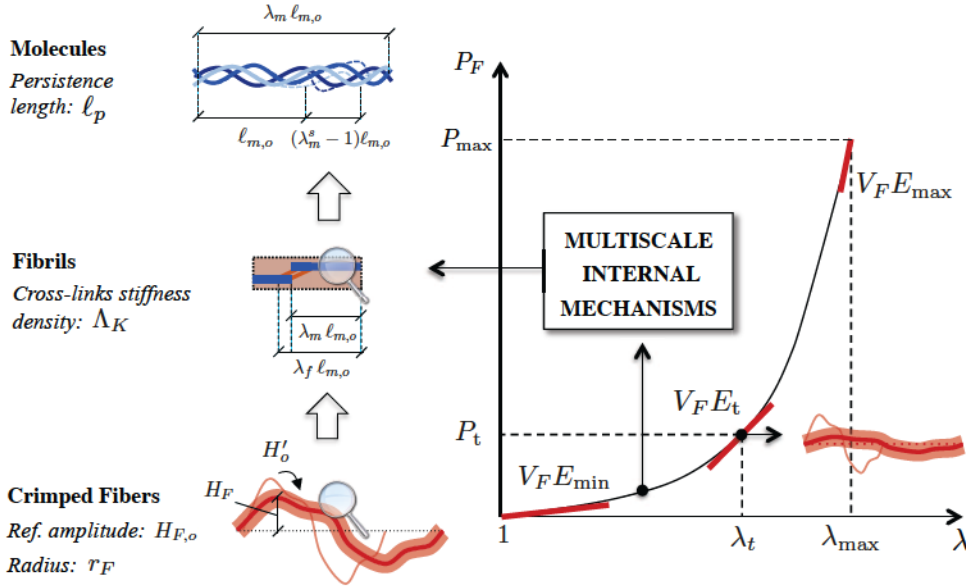


Figure 6.2.: Relevant structural features in collagen fibers, fibrils and molecules, affecting physically-meaningful output quantities in the stress-stretch relationship $P_F(\lambda)$.

Due to the monotonic stiffening response associated with fiber straightening in hyperelasticity, it results $E_{\min} = E_F(1)$ (i.e., the one at nominal strain $\varepsilon = \lambda - 1 = 0$) and it is referred to as the small-strain modulus. This quantity contributes to the small-strain tissue tangent modulus, classically referred to as the “elastin slope”. The latter nomenclature is misleading, since collagen fibers, although crimped in the initial strain-range, may significantly contribute;

- the initial straightening rate H'_o of collagen fibers

$$H'_o = \left. \frac{\partial H_F}{\partial \lambda} \right|_{\lambda=1}. \quad (6.4)$$

The heel region is associated with a significant stiffening response due the complex interplay between the straightening of the microscopic crimp and fibril elongation. It is recalled that fibril elongation is, in turn, a combination of molecular entropic-energetic elongation and sliding. Accordingly, both nano- and micro-scale mechanisms occur, and the prevalence of ones versus the others is given by the values of structural features at hand. Therefore, although entropic effects (i.e., the straightening of molecular kinks) have been reported as the most prevalent in the heel region [189], alterations in the value of the persistence length can affect the different amount of internal deformation

6.2 Materials and Methods

mechanisms. Relevant mechanical output quantities that can be analyzed within the heel region are (see Fig. 6.2):

- the transition stretch λ_t :

$$\lambda_t = \min_{\lambda \in [1, \lambda_{\max}]} (\{\lambda \mid H_F(\lambda) \leq \delta_H\}), \quad (6.5)$$

that is the minimum stretch over which fiber crimp H_F is lower than a given (small) amplitude $\delta_H \approx 0$. In other words, collagen fibers are fully straighten out at the transition stretch λ_t . Hence, the geometric nonlinear effects associated with fiber straightening vanish at λ_t and fibril strain is the unique deformation mode beyond λ_t ;

- the transition fiber stress P_t :

$$P_t = P_F(\lambda_t); \quad (6.6)$$

- the transition fiber modulus E_t :

$$E_t = E_F(\lambda_t); \quad (6.7)$$

- the transition molecular-to-fiber stretch ratio $\Delta\lambda_t^{mf}$:

$$\Delta\lambda_t^{mf} = \frac{\lambda_m(\lambda_t)}{\lambda_f(\lambda_t)} - 1; \quad (6.8)$$

which gives a measure of the prevalence of molecular straightening mechanisms over intermolecular sliding in the small-strain regime (i.e., up to λ_t).

- the transition energetic-to-entropic stretch ratio $\Delta\lambda_t^{sm}$:

$$\Delta\lambda_t^{sm} = \frac{\lambda_s(\lambda_t)}{\lambda_m(\lambda_t)} - 1; \quad (6.9)$$

which gives a measure of the prevalence of entropic over energetic molecular elongation mechanisms in the small-strain regime (i.e., up to λ_t).

The linear region is a high stiffness region. The fiber crimp can be retained fully extinguished during the linear region, whose mechanical response is fully dominated

by collagen molecular elongation and sliding. Relevant mechanical output quantities characterizing the linear region are (see Fig. 6.2):

- the maximum fiber tangent modulus E_{\max} :

$$E_{\max} = \max_{\lambda \in [1, \lambda_{\max}]} (E_F(\lambda)) . \quad (6.10)$$

Due to the monotonic stiffening response of collagen fibers in hyperelasticity, it results $E_{\max} = E_F(\lambda_{\max})$. Hence, it will be also referred to as the finite-strain fiber tangent modulus. This quantity is the main determinant for the tissue tangent modulus at high strains, also known as “collagen slope”;

- the maximum fiber stress P_{\max} :

$$P_{\max} = \max_{\lambda \in [1, \lambda_{\max}]} (P_F(\lambda)) . \quad (6.11)$$

resulting $P_{\max} = P_F(\lambda_{\max})$ due to collagen monotonic response;

- the finite-strain molecular-to-fiber stretch ratio $\Delta\lambda_{\text{fin}}^{mf}$:

$$\Delta\lambda_{\text{fin}}^{mf} = \frac{\lambda_m(\lambda_{\max})}{\lambda_f(\lambda_{\max})} - 1 . \quad (6.12)$$

which gives a measure of the prevalence of molecular straightening mechanisms over intermolecular sliding in the finite-strain regime (i.e., up to λ_{\max}).

- the finite-strain energetic-to-entropic stretch ratio $\Delta\lambda_{\text{fin}}^{sm}$:

$$\Delta\lambda_{\text{fin}}^{sm} = \frac{\lambda_s(\lambda_{\max})}{\lambda_m(\lambda_{\max})} - 1 . \quad (6.13)$$

which gives a measure of the prevalence of entropic over energetic molecular elongation mechanisms in the finite-strain regime (i.e., up to λ_{\max}).

6.3. Global sensitivity analysis

Global Sensitivity analysis (GSA) methods are mathematical tools that can be used in order to quantify the uncertainty in the numerical models. The relative influence of each individual input parameter on the the output is expressed by scaler value through varying all the parameters at the same time [29]. The GSA approaches may be divided into two classes; variance-based and density-based, as will be illustrated in the following.

6.3.1. Sobol' method

The Sobol' method [31] is one of the most commonly used GSA approaches based on the variance decomposition of the output as a sum of contributions of each input variables, or combinations thereof (Variance based approach).

Given an integrable function, $Y = f(X)$, defined on the k -dimensional unit hypercube, the Sobol' functional decomposition is based on the decomposition of f into terms of increasing dimensionality

$$f = f_0 + \sum_i^k f_i + \sum_i^k \sum_{j=i+1}^k f_{ij} + \dots + f_{12\dots k} \quad (6.14)$$

where the constant term, f_0 , is the the mean value of the function. The expansion has 2^k terms each of which is a square integrable function of the factors in its index only. For instance; $f_i = f_i(X_i)$ for the input factor X_i ; $f_{ij} = f_{ij}(X_i, X_j)$ for the input factors X_i and X_j ; and so on. Provided that each term has a zero mean value, the summands in the decomposition are orthogonal to each other and accordingly, the Sobol' decomposition is unique.

In this framework, the analysis of variance (ANOVA) decomposition can be written as;

$$V = \sum_{i=1}^k V_i + \sum_{i=1}^k \sum_{j=i+1}^k V_{ij} + \dots + V_{12\dots k} \quad (6.15)$$

where, $V = V(f)$ is the total variance of the model output, $V_i = V(f_i)$ is the variance in the output due to the effect of the parameter X_i , $V_{ij} = V(f_{ij})$ is the variance in the output due to the joint effect of the parameters X_i and X_j , and so on. The Sobol' sensitivity indices can be achieved through dividing both sides of Eq. (6.15) by V .

$$\sum_{i=1}^k S_i + \sum_{i=1}^k \sum_{j=i+1}^k S_{ij} + \dots + S_{12\dots k} = 1 \quad (6.16)$$

Here, (S_i) refers to the first-order sensitivity index which measures the part of the variance of the model output due to the input X_i . Sometimes, S_i also known as main effect of the parameter X_i . Whilst, the higher order indices $(S_{ij}, S_{ijl}, \dots \text{etc.})$ measure the joint effect of the input parameters. The total sensitivity index S_{T_i} is used to estimate how much the variation in X_i contributes to the variation in the model output. It equals the sum of the first-order and all high-order terms.

The Sobol' indices can be obtained through classical Monte Carlo simulation. In total,

there are $2^k - 1$ Sobol's indices that require $\mathcal{O}(N2^k)$ model evaluations (N here refers to the base sample size). Saltelli et al. [32] proposed, however, a methodology to reduce this cost to the order of $\mathcal{O}(N(k+2))$ by considering the first order and the total indices.

Alternatively, polynomial chaos expansion (PCE), which is an analytical representation of orthonormal polynomials, is used for the response decomposition [33, 34]. The response (output) is represented in a suitable function space spanned by a polynomial basis known as a polynomial chaos [27]. Each of these polynomials are orthogonal with respect to the joint distribution of the input parameters. According to Ref. [27], the output of interest of any given model (Y) can be expanded by a spectral expansion using orthogonal polynomials as

$$Y = \sum_{j=0}^{\infty} \beta_j \Psi_j(\boldsymbol{\xi}) \quad (6.17)$$

where $\boldsymbol{\xi}$ is the vector of independent standard normal (Gaussian) random variables, Ψ_j 's are multivariate Hermite polynomials of order j , and β_j are the PCE deterministic coefficients. In the following, this decomposition was extended to other types of distributions other than the Gaussian distribution using orthogonal polynomial basis functions of the Wiener-Askey scheme [28], which is well known as Generalised Polynomial Chaos. The multivariate polynomial, Ψ_j , is obtained by the tensor product of the corresponding univariate polynomials.

$$\Psi_j = \prod_{i=1}^k \psi_{j_i}(\xi_i) \quad (6.18)$$

$\psi_{j_i}(\xi_i)$ being the univariate polynomial of the variable i , and k being the number of independent variables.

For the purposes of numerical computation, the infinite expansion in Eq. (6.17) can be truncated to a finite number of terms in order to approximating response function.

$$\hat{Y} \approx \sum_{j=0}^{P-1} \beta_j \Psi_j(\boldsymbol{\xi}) \quad (6.19)$$

where P is the number of unknown deterministic expansion coefficients which is mainly controlled by the number of variables (k) and the order of polynomials (p). It increases

6.3 Global sensitivity analysis

exponentially with k and p .

$$P = \binom{k+p}{p} = \frac{(k+p)!}{k!p!}. \quad (6.20)$$

In this study, expansion coefficients are determined by least-squares regression of the output realizations with respect to the expected results of PCE as detailed in Ref. [204], where the model is solved repetitively for a number of discrete points in the probability space of the input parameters. For this purpose, we generate the so-called *experimental design* $\mathbf{X} = \{\mathbf{X}^1, \dots, \mathbf{X}^N\}$ by choosing a set of regression points, N , called samples, using Latin Hypercube Sampling (LHS) [30]. In matrix form, Eq. (6.19) can be rewritten as

$$\hat{\mathbf{Y}} = \Psi \boldsymbol{\beta} \quad (6.21)$$

The matrix Ψ is formulated considering the transformation of the values of \mathbf{X} into standard variables of $\boldsymbol{\xi}$. For the generated \mathbf{X} , the model is evaluated at each point. The corresponding vector of exact model simulations (realizations) is \mathbf{Y} . By minimizing the sum of the squares of the residuals, the approximated expansion coefficients can be calculated by

$$\boldsymbol{\beta} = \left([\Psi]^T [\Psi] \right)^{-1} \left([\Psi]^T \{\mathbf{Y}\} \right) \quad (6.22)$$

Once the PCE coefficients are obtained, the statistical properties of the model output can be gained directly. The total variance of the response is approximated by

$$\hat{V} = \sum_{j=1}^{P-1} \beta_j^2 \mathbf{E} [\Psi_j^2(\mathbf{X})] \quad (6.23)$$

where $\mathbf{E}[\cdot]$ is the mathematical expectation which is a weighted average of all the possible values where each value being weighted according to the probability distribution function. In accordance to the dependency of each polynomial, the expansion coefficients are assembled, square summed and subsequently normalized in order to obtain the sensitivity indices which called PC-based Sobol' indices [33].

6.3.2. PAWN method

The density-based sensitivity analysis methods take into account the entire Probability Density Function (PDF) of the output rather than its variance. The variations in the output PDF due to removing the uncertainty in one input can be considered as the sensitivity index of that input. Recently, Pianosi and Wagener [37] proposed a simple approach called PAWN (derived from the authors names) to formulate a density-based sensitivity index considering the cumulative distribution function (CDF). In the probability theory, the CDF refers to the probability, P , that a real random variable will be less than or equal to a deterministic value. The cumulative distribution function for single random variable X is given by

$$F_X(x) = P[X \leq x]. \quad (6.24)$$

With the same context, the probability density function, PDF, is defined as the derivative of the CDF respect to x .

According to Pianosi and Wagener [37], the sensitivity of the parameter X_i can be expressed by the difference between the entire unconditional and conditional CDF of a given model output Y . Keeping in mind that Y can be considered as a single real random variable. This difference is calculated by *Kolmogorov – Smirnov statistic (KS)*

$$KS_i = \max |F(\mathbf{Y}) - F(\mathbf{Y} | X_i)| \quad (6.25)$$

where $F(\mathbf{Y})$ and $F(\mathbf{Y} | X_i)$ are the unconditional and the conditional CDF approximated by samples of size N_u and N_c , respectively as shown in Fig. 6.3. The unconditional

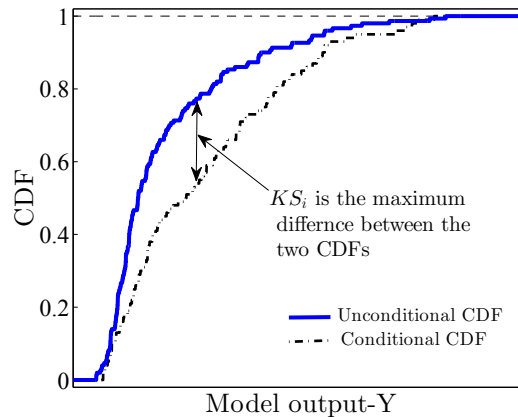


Figure 6.3.: Example of unconditional and conditional CDF at one conditioning point

6.4 Results and discussion

sample (with size N_u) is generated randomly in the space of the inputs; whereas the conditioned one (with size N_c) is achieved by varying all inputs while setting the input parameter X_i fixed n times. Hence, in addition to the unconditional CDF, for each parameter we have n conditional CDF and n different KS_i values. Thus the computational cost in terms of total number of model runs required to compute the sensitivity indices is $N_u + knN_c$ [163]. More recently, the PAWN method has been improved in Ref. [166] to reduce this computational cost when considering the convergence of the solution. The sensitivity index T_i has been taken in this study as the median of KS_i 's over all the n fixed values for the parameter X_i .

$$T_i = \underset{KS_i^{(1)}, \dots, KS_i^{(n)}}{\text{median}} [KS_i] \quad (6.26)$$

By definition, T_i has the range of [0-1], see Fig. 6.3, with 1 refers to the highest significant index. For insignificant parameters, the unconditional and the conditional CDF are almost coincided meaning that their KS values are close to zero. Accordingly, the two-sample *Kolmogorov – Smirnov* test can be used to determine these insignificant parameters, where the hypothesis that the two distributions are coincided is accepted at a confidence level, α , if

$$KS \leq c(\alpha) \sqrt{\frac{N_u + N_c}{N_u N_c}} \quad (6.27)$$

where $c(\alpha)$ is the critical value for the confidence level α [137]. In other words, the parameters with KS lower than the significance level defined by Eq. (6.27) can be considered as non-influential parameters.

6.4. Results and discussion

6.4.1. Sensitivity analysis

A total of four input parameters has been identified to be potentially contribute the uncertainty of the multiscale model predictions. The parameters are; (1) the collagen fiber crimp amplitude ($H_{F,o}$), (2) the collagen fiber radius (r_F), (3) the intermolecular cross-link stiffness density (Λ_K), and (4) the molecular persistence length (ℓ_p). Table 6.1 lists the definitions for the input parameters and their reference values. These parameters are assumed to vary in the range of [0.1-2.0] multiplied by their respective reference value and uniformly distributed over this range. Samples are generated in the probability space

Table 6.1.: Reference values for the input parameters

Parameter	Symbol	Unit	Reference value	Source
The collagen fiber crimp amplitude	$H_{F,o}$	MPa	13.04×10^{-3}	[202]
The collagen fiber radius	r_F	nm	1.63×10^{-3}	[202]
The intermolecular cross-link stiffness density	Λ_K	pN/nm	7.0×10^{-6}	[202]
The molecular persistence length	ℓ_p	mm	14.5×10^{-6}	[202]

of the input parameters using LHS. Sequentially, the model is evaluated at each set of sampled input parameters and the corresponding sensitivity indexes is calculated. In the different examination cases, a value close to 1 of the sensitivity indices means a large (dominant) contribution to the uncertainty in the output.

Considering the J-shaped stress-strain curve of Collagen, the total PCE-Sobol', S_{T_i} , sensitivity indices for the four parameters along the strain axis are demonstrated in Fig. 6.4a. As shown, the collagen fiber radius, r_F , has insignificant effect on the stress, where its S_{T_2} values are almost zero along the stretch axis. Likewise, the molecular persistence length, ℓ_p , has relatively limited effect. S_{T_4} has a maximum value of 8.8%. On the other hand, the collagen fiber crimp amplitude, $H_{F,o}$ (S_{T_1}), is the most significant parameter in the toe, heel and linear regions ($\lambda < 10\%$), and its effect decreases as the stretch increases. Reciprocally is the effect of the intermolecular cross-link stiffness density, Λ_K , which increases as the stretch increases, refer to S_{T_3} in Fig. 6.4a. Similar results are obtained by PWAN method (Fig. 6.4b) except of the results for sensitivity indices for r_F (T_2), which shows moderate effects and even higher than Λ_K and ℓ_p at low stretch region but descends along the stretch axis. Moreover, the PWAN sensitivity index for $H_{F,o}$ (S_{T_1}) has ascending trend in the toe region before declines. Meanwhile, Fig. 6.4c shows the values of $S_{T_i} - S_i$ for the input parameters. The interaction effect is in tune with the parameter sensitivities. Though, the relatively low values of $S_{T_i} - S_i$ implies that the variance in the output is mostly dominated by the first order effect (S_i) of the input parameters.

Similarly, sensitivity analyses have been conducted to investigate the effect of the uncertainties in the four input parameters on the different output quantities of interest. The main orders of sensitivity indices for input parameter in addition to their interaction orders and total effects are calculated using PCE-Sobol' and PAWN methods, see Fig. 6.5.

6.4 Results and discussion

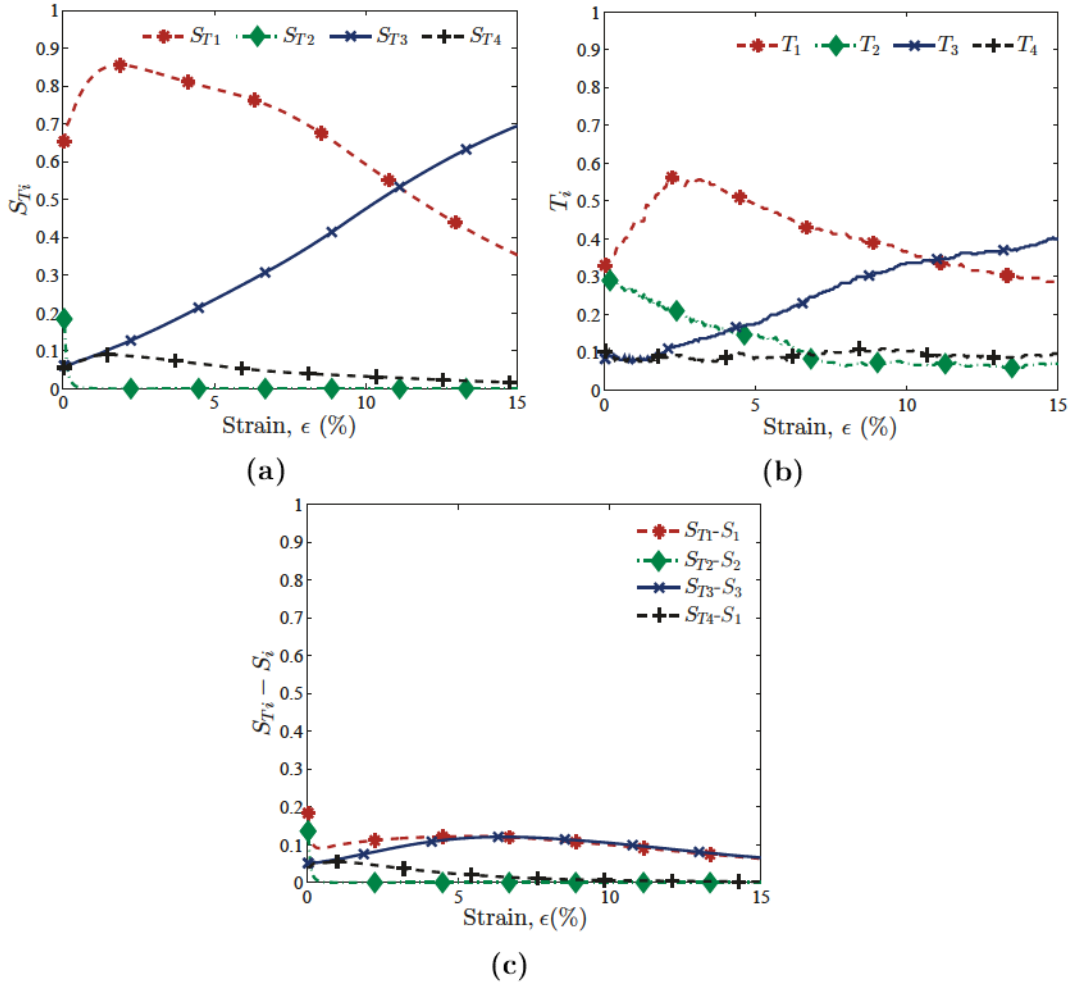


Figure 6.4.: Sensitivity indices along the strain axis of J-shaped stress-strain curve of Collagen; using PCE-Sobol' method (a), using PAWN method (b), and the parameters interaction sensitivity (c).

In line with the results of PAWN sensitivity indices, Fig. 6.6 displays the *Kolmogorov–Smirnov statistic*, KS_i , for 10 different conditioning points (n) that were sampled from the space of variation for each input parameter X_i range uniformly from 0.1 to 2.0 times the respective reference value. The critical value of KS equals 0.157 considering the confidence level of $\alpha = 0.05$ is represented by a dashed horizontal blue line as the significance level. Below this line, the conditional and unconditional CFD are hypothetically coincided indicating insignificant parameter effect. The KS values of the collagen fiber amplitude, $H_{F,o}$, are extremely higher than the critical value at all the conditioning points in λ_t , H'_o , and $\Delta\lambda_{fin}^{mf}$. This also is confirmed by the highest and dominating sensitivity indices for $H_{F,o}$, see Figs. 6.5a, 6.5f and 6.5h. The KS values for $H_{F,o}$ are almost similar to r_F and Λ_K considering the outputs E_{min} , and $\Delta\lambda_t^{sm}$ and P_{max} , respectively.

6.4 Results and discussion

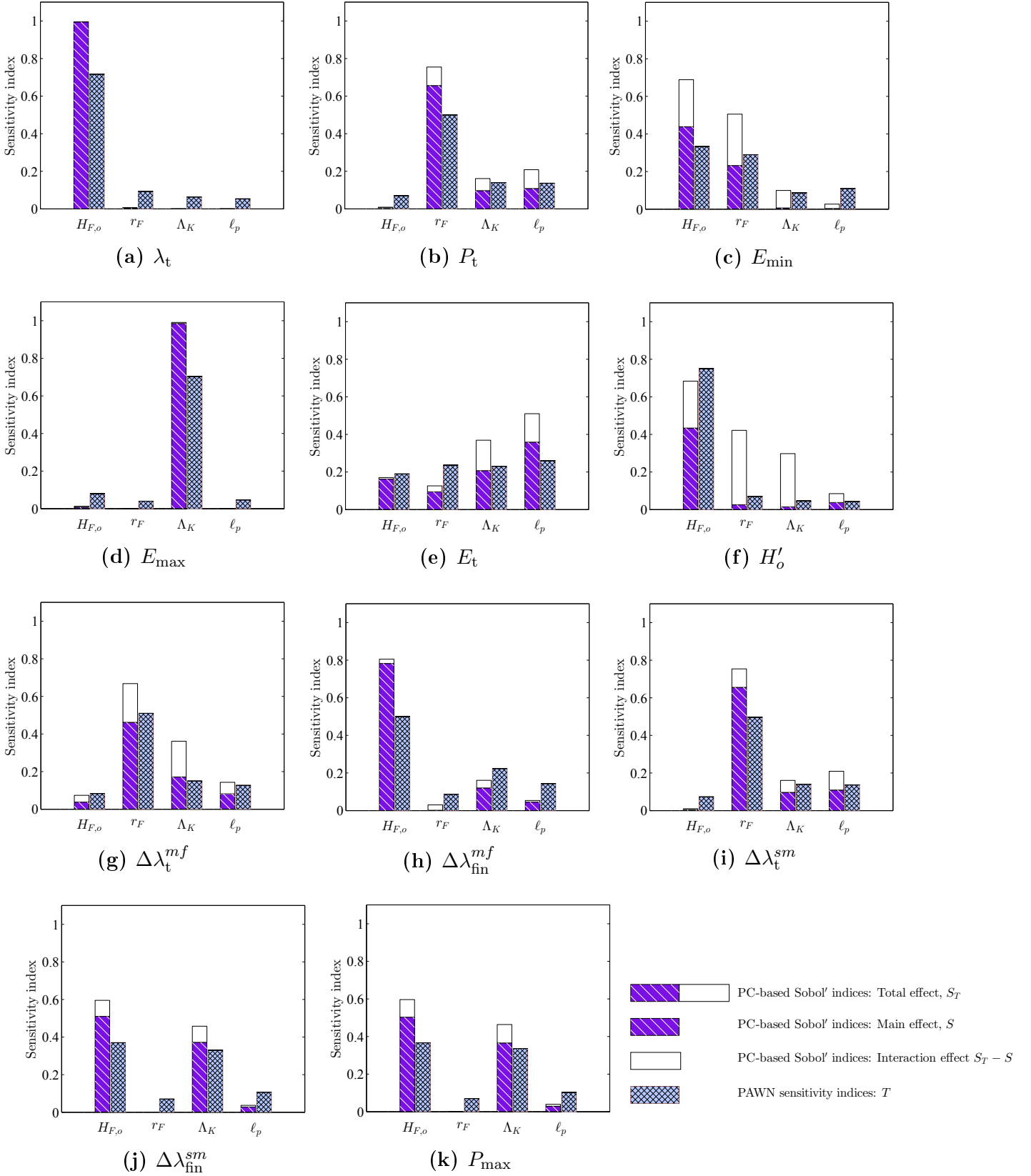


Figure 6.5.: Sensitivity analyses for output quantities of interest.

6.4 Results and discussion

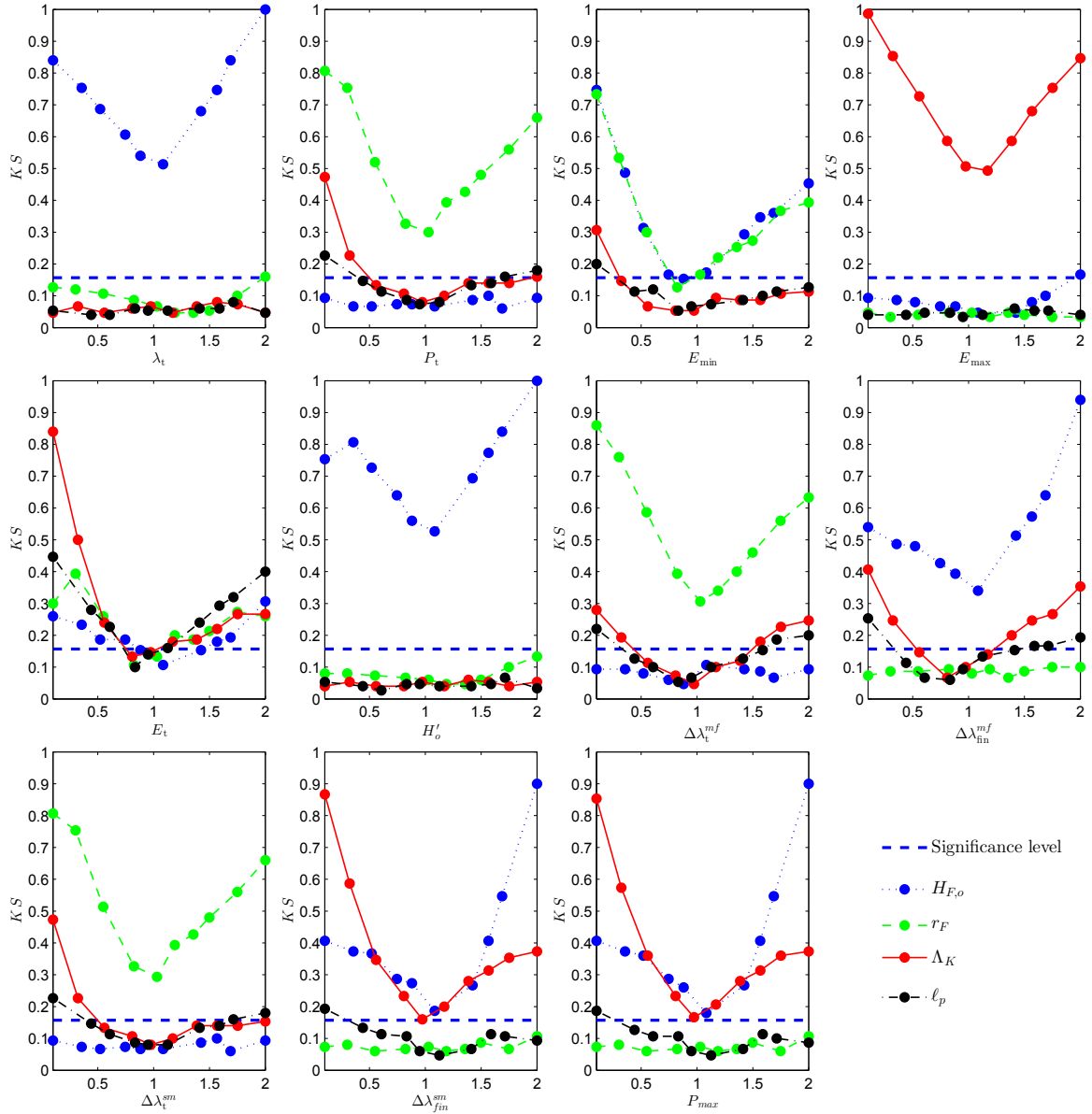


Figure 6.6.: *Kolmogorov – Smirnov statistic (KS_i) at different conditioning points of X_i s ($n=10$).*

Moreover, as clearly displayed in Fig. 6.6, $H_{F,o}$ can affect output once it be fixed at its extreme bounds. More specifically, around 2 times its reference value for; λ_t , H'_o , $\Delta\lambda_{fin}^{mf}$, $\Delta\lambda_{fin}^{sm}$, and P_{max} , and around 0.1 times its reference value for; E_{min} . Fixing $H_{F,o}$ at any point of its range will not affect the variation in the remaining outputs. In similar way, the KS values and the conditioning point for the remaining input parameters that most affect the variation of the different outputs can be extracted from Fig. 6.6.

6.4.2. Uncertainty Quantification

Making use of the results from Section 6.4.1, the uncertainties in the models' predictions can be quantified by fixing the significant parameters. For this purpose, hereafter we examine firstly the effect of fixing the different input parameters on the variation of the J-shaped stress-strain curve of Collagen. The model has been simulated in different five cases. In *Case A*, all the parameters are varied in their range of variation in order to generate the samples space using LHS. In *Case B*, the parameter $H_{F,o}$ is fixed at its reference value while others are the same as in *Case A*. Similarly, in *Cases: C, D, and E*, the parameters r_F , k_c , and ℓ_p are respectively fixed at their reference values. As a measure of the variance, the standard deviation (square root of the variance) of the different cases are depicted in Fig. 6.7. Clearly, the standard deviations of *Case A* and *Case C* are identical, meaning that fixing r_F did not affected the variance. Remember it was non influential parameter on the variation of the J-shaped stress-strain curve of Collagen (see Fig. 6.4). While, fixing ℓ_p has revealed modest impact. Most of the uncertainty has been eliminated by considering the stochasticity of the collagen fiber amplitude, $H_{F,o}$ in the toe region (stretch $\leq 2.5\%$ in Fig. 6.7), where the standard deviation approaches to zero in this region for *Case B*. At strain greater than 10% the most influential parameter is Λ_K and fixing this parameter in *Case D* given rise to slow down the rate of increasing the variation compared to *Case A*. Worth to mention, the decrease in the variation in the different cases is consonant with the results of sensitivity analysis shown in Fig. 6.4. In addition, the mean response of the J-shaped curve in the five cases are illustrated in Fig. 6.8, in which *Case B* presents the best fit to the results of experiments of Hansen et al. [205].

Secondly, the uncertainties in the other different output quantities of interest are investigated. Based on the design space of the input parameters, three sets of samples are generated, also, using LHS. *Set G1* is obtained by sampling the entire input parameters space. Then *Set G2* is formed by considering the stochasticity in the insignificant parameters, where the significant parameters are fixed at their reference values for each output of interest. On the contrary, *Set G3* is formed by fixing the remaining insignificant parameters. The model is simulated for the generated sets and the uncertainty analysis is performed for the outputs. According to the central limit theorem, when independent random variables are added together, their sum tends toward a normal (Gaussian) distribution even if the original variables themselves are not normally distributed. Hence, the output parameters of interest can be described to follow a Gaussian distribution despite of uniform distributions were adopted for the input parameters.

6.4 Results and discussion

This uncertainty quantification provides clear understanding regarding the relative influence of the stochasticity of input parameters on the probability distribution of the corresponding output. Table 6.2 includes the mean response and the standard deviation for each of the output of interest. From the table, *Sets G1* and *G3* had almost the same standard deviations which is considerably higher than the corresponding one in *Set G2*.

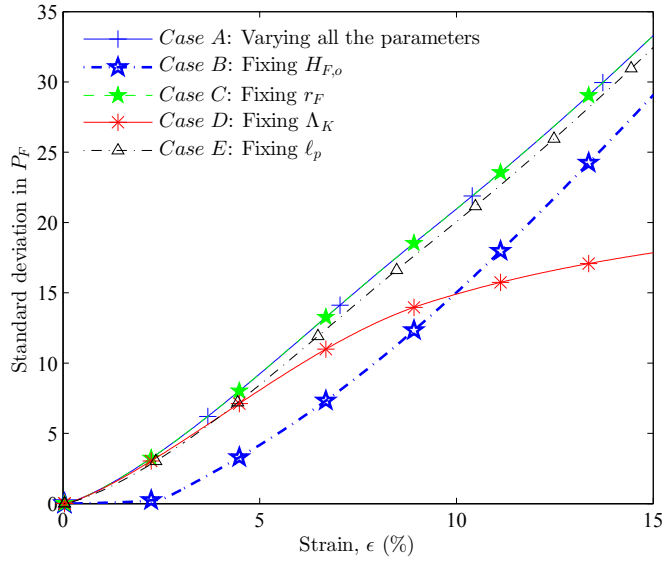


Figure 6.7.: Standard deviation in the J-shaped stress-strain curve obtained due to stochasticity in different input parameters

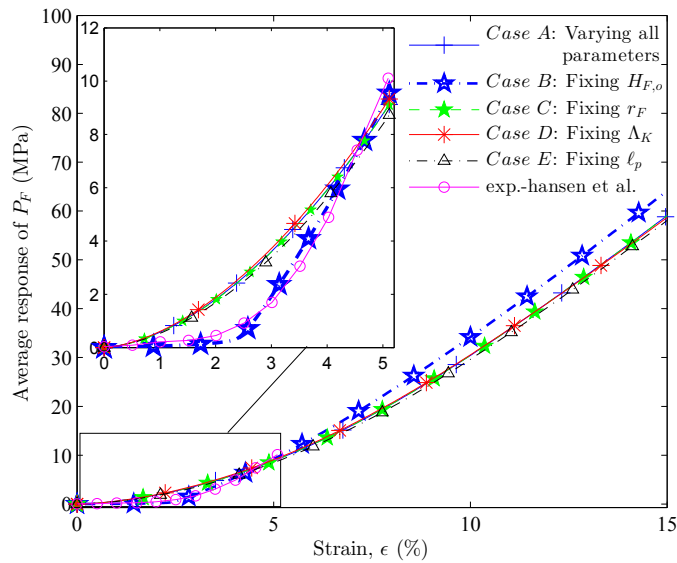


Figure 6.8.: Mean response of the J-shaped stress-strain curve obtained due to stochasticity in different input parameters compared to the experiments of Hansen et al. [205].

Table 6.2.: Comparison of mean, standard deviation and coefficient of variation for the different outputs obtained due to stochasticity in all (G_1), insignificant (G_2), and significant parameters (G_3)

Output	Set of the Significant Parameters	G1		G2 ^a		G3 ^b	
		Mean	STD	Mean	STD	Mean	STD
λ_t	$H_{F,o}$	1.034	0.027	1.026	0.002	1.034	0.027
P_t	$\{r_F\}$	0.647	0.683	0.457	0.226	0.646	0.535
E_{\min}	$\{H_{F,o}, r_F\}$	13.57	33.25	3.21	1.596	13.22	29.05
E_{\max}	$\{\Lambda_K\}$	643.2	319.2	625.4	31.3	654.3	323.0
E_t	$\{H_{F,o}, r_F, \Lambda_K, \ell_p\}$	218.6	131.3	232.4	0.0	218.6	131.3
H'_o	$\{H_{F,o}\}$	-0.397	0.392	-0.273	0.004	-0.385	0.294
$\Delta\lambda_t^{mf} (10^{-3})$	$\{r_F\}$	-0.9	0.9	-0.7	0.3	-0.8	0.7
$\Delta\lambda_{\text{fin}}^{mf}$	$\{H_{F,o}\}$	-0.038	0.019	-0.043	0.008	-0.036	0.017
$\Delta\lambda_t^{sm} (10^{-3})$	$\{r_F\}$	-0.14	0.14	-0.10	0.05	-0.14	0.11
$\Delta\lambda_{\text{fin}}^{sm} (10^{-3})$	$\{H_{F,o}, \Lambda_K\}$	-5.8	3.8	-6.7	0.7	-5.7	3.3
P_{\max}	$\{H_{F,o}, \Lambda_K\}$	30.31	20.70	34.49	3.81	29.61	20.02

^aThe significant parameters are fixed at their reference values.

^bThe insignificant parameters are fixed at their reference values

6.5. Summary

The biological structures of soft tissues which characterised by very different length scales led us to adopt hierarchical multiscale modeling approach in order to study the tissue mechanical properties. As the uncertainties in the model input parameters propagated leading to uncertainty in the outputs of interest, sensitivity analysis was presented to evaluate the effect of the collagen related structural features. The following structural features were considered: fiber crimp amplitude and thickness, density of inter-molecular cross-links, molecular persistence length. In this regard, two sensitivity analysis approaches were employed, namely; Sobol' and PAWN methods. While the former is based on the variance decomposition of the output, the latter is a density-based sensitivity takes into account its cumulative distribution function.

The collagen fiber crimp amplitude and the intermolecular cross-link stiffness density were the key parameters influencing the stress-stretch relationship. They have reciprocal effect along the strain axis. Fixing the collagen fiber amplitude resulted in eliminating the variance and the average response of the J-shaped curve were in substantial agreement with the experimental measurements of Hansen et al. [205]. Moreover, the results of sensitivity analysis manifested the multiscale interdependence of output quantities of interests and the collagen structural features. We can conclude that both sensitivity analysis methods were able to refer the uncertainty in the model prognosis to the different input parameters in similar tone.

Chapter 7

Conclusions

7.1. Summary of findings

This study was devoted to the stochastic and numerical investigations of fracture properties for polymeric nanocomposites. Stochastic data driven models were constructed to predict the fracture energy of polymer/particle nanocomposites. ANN, and ANFIS were trained and tested using 85 and 30 dataset, respectively, gathered from the literature. Moreover, Bayesian model selection method was applied for the first time to PNCs. Three analytical models differing in theory of fracture mechanisms were evaluated by taken into account the model and parameters uncertainties. The assessment was based on experimental measurements of 16 different references. Meanwhile, uncertainty quantification was performed to quantify the key parameters influencing the fracture in PNCs by means of various global SA methods. Comparison and evaluation of the efficiency, robustness, and repeatability of the SA methods were also presented. Computational models were presented for the analysis of crack propagation in clay PNCs using the phase-field method and in particles PNCs using the extended finite element method.

The fracture energy of particles PNCs can be predicted reliably by the ANN and the ANFIS models with relatively small error in the range of the input parameters being investigated. Although testing dataset was not included in the training process, both ANN and ANFIS produced good predictions verifying their robustness. Parametric studies, which were conducted using ANN and ANFIS, revealed that the fracture energy of PNCs increases as the nanoparticles volume fraction increases, and as the fracture energy of the epoxy matrix increases, whereas the nano particle size has a negligible influence.

Using the Bayesian method, the optimal models predictions with respect to sixteen different experimental reference data were obtained using the optimal parameter sets. The model predictions of Huang and Kinloch [2] model showed better predictions in 12 of the 16 reference measurements compared to the models according to Williams [3], and Quaresimin et al. [4]. Whilst, it showed a distinctly higher model selection probability. On this base, it can be conclude that Huang and Kinloch [2] model is the most robust model with regard to the applied reference measurements.

The phase-field method showed high ability in detecting the crack propagation of clay PNCs. Five different global SA methods were performed to estimate the influence of the input parameters on the fracture toughness. Almost identical results were produced by the different SA methods implying the reliability of the implemented SA. All methods revealed that the aspect ratio, the radius of curvature, and the Young's modulus of the clay have negligible effects on the fracture toughness. The matrix Young's modulus was the most significant parameter, followed by the volume fraction of clay and the fracture energy of the epoxy matrix. Fixing the important parameters resulted in reducing the coefficient of variation from 16.82% to 1.97%.

The fracture in particle/polymer nanocomposites was modeled by the cohesive segments method and the phantom nodes. Polynomial chaos expansions (PCE) surrogate model was constructed accounting the uncertainties in different input parameters. The sensitivity analysis results revealed that the maximum allowable principal stress and Young's modulus of the epoxy matrix are the most significant parameters. High variation in the fracture energy of PNCs is expected due to small changes in these parameters, hence, they should be determined precisely.

7.2. Future works

The presented investigated work the fracture behaviour of PNCs accounting for a set of uncertain parameters. A further improvement for the ANN and ANFIS method should be considered to cover higher range of of input parameters being investigated. For this purpose an extra experimental works that study the fracture at different values of the parameters are required. Moreover, studying the effects of extra parameters should be considered. The temperature effect on the fracture behaviour is one of the parameters that should be taken into account. Also, quantifying the temperature effects by mean of computational modeling using phase-field is a future aim.

7.2 Future works

Measuring the effect debonding between nanofiller and the epoxy experimentally is infeasible. Contrary, the computational simulations will be an effective alternative tool. To account the anisotropy, the interphase zone can be modelled using molecular dynamics (MD) simulations. In this regard, the cross-link density is required to be included in the analysis. 3D simulation is a challenge in terms of computational cost. However, future improvements in the presented work for 3D simulation is suggested considering the fast evolution in software program and computing machines.

Appendix A

A.1. Predicted fracture energy of PNCs using ANN and ANFIS: Training Data set

Table A.1.: Experimental and predicted results of fracture energy for the training dataset.

Exp.	ANN	ANFIS	Ref.	Exp.	ANN	ANFIS	Ref.
123	136.17	123.03	[51]	760	786.28	759.99	[58]
183	164.25	182.94	[51]	750	738.11	750	[58]
212	204.84	198.02	[51]	352	358.99	352	[53]
543.6	554.92	526.29	[52]	406	405.2	406	[53]
611.4	570.05	543.64	[52]	461	459.58	461	[53]
620.2	583.36	566.55	[52]	998	976.44	998	[49]
346.5	443.03	447.06	[52]	640	651.39	640	[49]
497.2	510.49	523.53	[52]	189.34	200.66	185.61	[50]
485.5	534.19	552.83	[52]	229.51	254.85	236.75	[50]
334.5	355.03	321.79	[52]	295.1	295.53	291.59	[50]
382.6	358.67	348.6	[52]	308	316.61	306.48	[55]
427.4	430.89	418.62	[52]	390	392.78	382.54	[55]
184	204.84	198.02	[54]	546	577.6	574	[55]
444	455.54	444.02	[54]	690	675.15	670.95	[55]
490	457.82	490	[54]	58.3	74.91	58.8	[59]
616	608.19	616	[54]	72.6	85.36	70.17	[59]
114	115.5	113.99	[54]	87.4	87.74	90.26	[59]
172	172.88	172.02	[54]	123.1	97	121.21	[59]
1040.77	1050.33	1040.76	[56]	115.1	126.97	116.06	[59]

Continued on next page

A.1 Predicted fracture energy of PNCs using ANN and ANFIS: Training Data set

Table A.1 – continued from previous page

Exp.	ANN	ANFIS	Ref.	Exp.	ANN	ANFIS	Ref.
1072.96	1271.87	1262.92	[56]	122.37	134.63	130.46	[60]
1577.25	1572.51	1577.24	[56]	145.16	145.3	141.19	[60]
719	678.61	674.91	[56]	164.8	154.9	150.1	[60]
697.4	745.7	747.48	[56]	179.36	180.49	177.65	[60]
897.8	895.69	898.11	[56]	201.52	217.74	220.42	[60]
1459.2	1271.87	1262.92	[56]	384.51	364.5	377.85	[60]
2156.65	2143.02	2156.64	[56]	388.55	368.83	439.76	[61]
700	637.88	712.36	[57]	606.22	500.98	506.91	[61]
742	687.36	717.76	[57]	530.4	626.01	578.5	[61]
700	759.88	729.6	[57]	115.42	119.85	119.13	[62]
876	829.29	830.79	[57]	182.94	190.72	176.6	[62]
866	878.42	893.47	[57]	189.33	208.54	189	[62]
934	936.07	933.99	[57]	204.97	223.3	201.47	[62]
797	783.47	795.15	[57]	217.34	238.23	223.96	[62]
842	858.97	849.68	[57]	225.27	232.96	225.1	[62]
1050	1047.1	1035.06	[57]	655	669.8	654.99	[63]
1157	1168.07	1143.27	[57]	109	67.92	108.98	[63]
1146	1138.93	1192.91	[57]	132	121.12	132.02	[63]
1264	1250.55	1239.89	[57]	239	246.17	257.25	[64]
684	713.29	682.74	[57]	242	235.78	244.48	[64]
830	807.08	837.26	[57]	230	242.14	231.59	[64]
983	980.97	967.62	[57]	262	269.16	268.43	[64]
1006	1005.92	1025.25	[57]	286	246.17	257.25	[64]
1030	1030.24	1020.11	[57]				

A.2 Predicted fracture energy of PNCs using ANN and ANFIS: Testing Data set

A.2. Predicted fracture energy of PNCs using ANN and ANFIS: Testing Data set

Table A.2.: Experimental and predicted results of fracture energy for the testing dataset.

Exp.	ANN	ANFIS	Ref.	Exp.	ANN	ANFIS	Ref.
179	147.57	154.06	[51]	343	375.52	377.69	[53]
191	177.78	214.77	[51]	1016	894.88	859.56	[49]
384.4	531.4	499.44	[52]	310.66	330.95	374.53	[50]
416.7	465.38	471.87	[52]	465	480.65	477.87	[55]
445.8	383.95	382.79	[52]	791	818.54	847.52	[55]
212	160.04	175.02	[54]	1120	897.83	1003.47	[55]
702	480.44	646.3	[54]	98.8	86.09	116.21	[59]
794	970.08	1060.28	[56]	168.6	163.74	157.6	[60]
1169.53	1184.95	1000.25	[56]	430.7	303.71	413.53	[61]
973	995.52	972.34	[57]	160.57	140.56	139.91	[62]
707	809.83	768.55	[57]	252.95	228.47	213.69	[62]
717	718.92	734.32	[57]	368	390.22	444.07	[63]
1070	1137.84	1030.68	[57]	237	269.16	268.43	[64]
740	845.65	772.83	[58]	286	235.78	244.48	[64]
291	329.67	324.4	[53]	264	242.14	231.59	[64]

Appendix B

B.1. Evaluation of Models using Bayesian method

Table B.1.: The values of some factors calculated based on the optimal parameter set

	M_1^\ddagger				M_2^\ddagger			M_3^\ddagger				Γ^\dagger MPa
	r_{ym} μm	r_y μm	$F'(r_y)^\dagger$ μm	$(V_{fv} - V_{fp})^\dagger$ %	σ_{cr} MPa	x -	X -	σ_{cr} MPa	C_h -	H_{vM} -	I_{SB} -	
D_1	6.37	39.1	328.6	0.34	519.5	7.64	46.36	114.7	0.751	2.06	4.94	198.0
			210.1	1.02								125.7
			167.1	1.71								99.5
			131.4	2.86								77.7
D_2	3.02	18.5	155.7	0.45	563.8	7.51	41.10	99.6	0.742	1.96	4.73	163.8
			99.6	1.33								104.0
			79.2	2.24								82.3
			62.3	3.74								64.2
D_3	9.21	57.7	447.7	0.47	564.6	7.72	48.46	130.7	0.778	1.74	3.93	188.2
			283.1	1.40								118.1
			235.2	2.12								97.6
			204.8	2.84								84.7
D_4	5.22	30.6	237.1	0.06	547.3	6.74	21.33	120.4	0.754	1.85	4.19	199.1
			150.0	0.17								124.9
			100.4	0.41								82.7
			88.1	0.53								72.2
D_5	4.27	23.0	151.4	0.04	496.4	6.32	14.61	76.7	0.846	1.52	3.06	138.9
			93.7	0.13								85.1

Continued on next page

B.1 Evaluation of Models using Bayesian method

Table B.1 – continued from previous page

		M_1^\ddagger			M_2^\ddagger			M_3^\ddagger				Γ^\dagger
r_{ym}	r_y	$F'(r_y)^\dagger$	$(V_{fv} - V_{fp})^\dagger$	σ_{cr}	x	X	σ_{cr}	C_h	H_{vM}	I_{SB}		
μm	μm	μm	%	MPa	–	–	MPa	–	–	–	–	MPa
		72.9	0.23									65.7
		60.8	0.32									54.4
D_6	12.35	78.2	310.2	0.08	417.9	6.69	20.48	89.9	0.766	1.94	4.52	91.5
		221.3	0.16									64.5
		150.8	0.32									43.2
D_7	12.67	80.6	319.5	0.33	505.9	6.96	24.8	106.7	0.755	1.82	4.13	89.1
		227.9	0.66									62.9
		155.3	1.33									42.0
D_8	3.39	18.6	107.7	2.13	563.0	7.17	29.76	112.6	0.737	1.81	4.14	139.0
		79.5	4.27									102.0
		65.9	6.40									84.0
		57.2	8.54									72.7
		51.1	10.67									64.6
		47.4	12.81									58.4
D_9	2.79	16.7	66.3	0.35	520.6	6.77	21.23	94.5	0.749	2.07	5.06	90.2
		47.8	0.69									64.3
		39.2	1.00									52.4
		33.0	1.35									43.7
D_{10}	12.80	79.4	517.4	0.95	507.1	7.34	35.42	91.8	0.712	2.29	6.10	153.2
		385.4	1.90									113.5
		280.6	3.80									81.9
		194.2	7.83									55.9
D_{11}	12.73	81.3	529.3	0.33	489.4	7.42	38.97	91.7	0.703	2.29	6.13	146.5
		394.3	0.65									108.5
		287.1	1.31									78.3
		198.7	2.70									53.4
D_{12}	1.53	8.25	48.8	0.09	495.3	6.11	11.58	82.8	0.765	1.80	4.16	103.3
		29.9	0.28									62.7
		21.1	0.56									43.7
		19.4	0.65									40.1
		18.0	0.75									37.0

Continued on next page

B.1 Evaluation of Models using Bayesian method

Table B.1 – continued from previous page

		M_1^\ddagger			M_2^\ddagger			M_3^\ddagger				
r_{ym}	r_y	$F'(r_y)^\dagger$	$(V_{fv} - V_{fp})^\dagger$	σ_{cr}	x	X	σ_{cr}	C_h	H_{vM}	I_{SB}	Γ^\dagger	
μm	μm	μm	%	MPa	–	–	MPa	–	–	–	MPa	
		15.8	0.93								32.3	
D_{13}	1.25	6.8	40.1	1.77	504.8	6.99	24.51	72.9	0.767	1.78	4.21	124.4
			24.6	5.30								75.5
			17.4	10.6								52.6
			16.0	12.4								48.2
			14.8	14.1								44.6
			13.0	17.7								38.9
D_{14}	3.65	23.1	91.5	2.84	585.1	7.52	38.06	86.8	0.796	1.81	3.91	69.5
			66.0	5.56								49.6
			54.1	8.06								40.4
			45.6	10.9								33.6
D_{15}	2.00	12.0	94.4	1.05	515.1	7.53	40.38	103.7	0.773	1.98	4.51	196.5
			71.1	2.11								147.3
			59.8	3.17								123.4
			52.6	4.22								108.3
			43.6	6.34								89.4
			33.9	10.57								68.8
			23.1	21.13								46.0
D_{16}	0.66	3.9	23.1	0.31	497.0	6.37	15.48	86.2	0.756	2.00	4.98	98.8
			14.2	0.94								59.9
			10.0	1.88								41.8
			7.50	3.13								30.9

[†] Calculated at different values of nanofiller content.

[‡] M_1 , M_2 , and M_3 refer to Huang and Kinloch [2] model, Williams [3] model, and Quaresimin et al. [4] model, respectively. The detail description can be found in Section 4.1.

Appendix C

Multiscale constitutive model of collagen fibers

C.1. Multiscale constitutive model of collagen fibers

Collagen fibers are assumed to have a circular cross-section of radius r_F and area measure $A_F = \pi r_F^2$. The crimped structure of collagen fibers is taken into account by considering locally periodic fibers of along-the-chord period length L_F and amplitude H_F in the current configuration (resp., $L_{F,o}$ and $H_{F,o}$ in the reference configuration).

Fibers deformation is described in terms of stretch λ_4 , physically representing the along-the-chord change of length of crimped collagen fibers. Therefore, by definition, it holds $L_F = L_F(\lambda_4) = \lambda_4 L_{F,o}$, with $\lambda_4 = \sqrt{I_4}$ and I_4 being the fourth-invariant of deformation defined on the basis of fiber direction. It is worth pointing out that, in the present along-the-fiber uniaxial traction case, fiber stretch λ_4 coincides with tissue stretch λ .

Geometric non-linearities are introduced by accounting for the functional dependence of fiber amplitude on λ_4 , namely $H_F = H_F(\lambda_4)$. Material non-linearities are accounted for by means of fibril tangent modulus E_f that depends on fibril stretch λ_f , in turn related to λ_4 by the inter-scale compatibility relationship Φ_f between microscale and mesoscale (here meso means between micro and nano):

$$\Phi_f(\lambda_4, H_F) = \frac{d\lambda_f}{d\lambda_4} = \frac{\lambda_4 \ell_{F,o}^2 + H_F \frac{dH_F}{d\lambda_4}}{\sqrt{(\lambda_F^2 \ell_{F,o}^2 + H_F^2)(\ell_{F,o}^2 + H_{F,o}^2)}}, \quad (\text{C.1a})$$

formulated by considering λ_f as coinciding with the centerline stretch of a fiber with piecewise linear shape [202].

C.1 Multiscale constitutive model of collagen fibers

Fibril stretch λ_f is associated with molecular stretch λ_m which, in turn, is function of entropy-related λ_m^s and energy-related λ_m^h molecular stretches. These functional dependences are taken into account via the inter-scale compatibility relationships Φ_{fm} (from meso- to nano-scale), Φ_{ms} and Φ_{mh} (from nanoscale to atomistic scale). On the basis of simple equilibrium conditions formulated assuming mechanisms as *in series*, the inter-scale compatibility relationships are obtained from the tangent modulus of collagen fibrils E_f , of collagen molecules E_m and of entropy-related E_m^s and energy-related E_m^h mechanisms. Accordingly, it results

$$\Phi_{fm}(\lambda_m^s, \lambda_m^h) = \frac{d\lambda_m}{d\lambda_f} = \frac{E_f(\lambda_m^s, \lambda_m^h)}{E_m(\lambda_m^s, \lambda_m^h)}, \quad (\text{C.1b})$$

$$\Phi_{ms}(\lambda_m^s, \lambda_m^h) = \frac{d\lambda_m^s}{d\lambda_m} = \frac{E_m(\lambda_m^s, \lambda_m^h)}{E_m^s(\lambda_m^s)}, \quad (\text{C.1c})$$

$$\Phi_{mh}(\lambda_m^s, \lambda_m^h) = \frac{d\lambda_m^h}{d\lambda_m} = \frac{E_m(\lambda_m^s, \lambda_m^h)}{E_m^h(\lambda_m^h)}. \quad (\text{C.1d})$$

where

$$E_f(\lambda_m^s, \lambda_m^h) = \frac{E_m(\lambda_m^s, \lambda_m^h) \Lambda_c k_c \ell_{m,o}}{[\Lambda_c k_c \ell_{m,o} + A_m E_m(\lambda_m^s, \lambda_m^h)]}, \quad (\text{C.2a})$$

$$E_m(\lambda_m^s, \lambda_m^h) = \frac{E_m^s(\lambda_m^s) E_m^h(\lambda_m^h)}{E_m^s(\lambda_m^s) + E_m^h(\lambda_m^h)}, \quad (\text{C.2b})$$

and

$$E_m^s(\lambda_m^s) = \frac{k_B T \ell_{m,o}}{\ell_p \ell_c A_m} \left[\frac{\ell_c^3}{2(\ell_c - \ell_{m,o} \lambda_m^s)^3} + 1 \right], \quad (\text{C.2c})$$

$$E_m^h(\lambda_m^h) = \frac{\ell_{m,o}}{\ell_c} \left\{ \frac{\hat{E}}{1 + \exp\{-\eta[\ell_{m,o}(\lambda_m^h - 1)/\ell_c - \varepsilon_o^h]\}} + \hat{E}_o \right\}, \quad (\text{C.2d})$$

with k_B being the Boltzmann constant and T the absolute temperature. Moreover, referring to the entropic behavior of collagen molecules, ℓ_p is the persistence length, ℓ_c the contour length, $\ell_{m,o}$ the end-to-end length in the reference configuration (resulting $\ell_{m,o} = \ell_c - \ell_{ks}$, with ℓ_{ks} being the length of molecular kinks), and A_m the cross-sectional area. Furthermore, addressing the energetic regime, \hat{E}_o and \hat{E} are respectively the low-strain and high-strain collagen tangent moduli, ε_o^h is the uncoiling strain, and η is the uncoiling resistance. Finally, with reference to inter-molecular sliding, Λ_c denotes the (mole fraction) density of inter-molecular covalent cross-links, which are modeled with a linear elastic behavior with stiffness k_c . Eqs. (C.2c) and (C.2d) are based respectively on

C.1 Multiscale constitutive model of collagen fibers

theoretical results which recover the Worm-Like-Chain model for the description of entropic elasticity, and on atomistic computations that elucidate energetic mechanisms [202].

Introducing V_F as collagen volume fraction, fiber stress P_F is introduced as:

$$P_F(\lambda_4) = V_F \int_1^{1+(\lambda_4-1)} E_F(\eta) d\eta, \quad (\text{C.3a})$$

where $E_F(\lambda_4) = C_F(\lambda_4, \lambda_m^s(\lambda_4), \lambda_m^h(\lambda_4), H_F(\lambda_4))$, with C_F being the along-the-chord tangent modulus of collagen fibers. Crimped collagen fibers are regarded as Euler-Bernoulli curvilinear beams whose material tangent modulus corresponds to the one of fibrils (i.e., E_f in Eqs. (C.2)). In particular, the incremental application of the Principle of Virtual Works gives [202]:

$$C_F = E_f \frac{\ell_F^2 + H_F^2}{\sqrt{\ell_{F,o}^2 + H_{F,o}^2}} \left[\ell_F + \frac{4H_F^2}{3r_F^2 \ell_F} (\ell_F^2 + H_F^2) \right]^{-1}, \quad (\text{C.3b})$$

where it is worth highlighting that $E_f = E_f(\lambda_m^s, \lambda_m^h)$. In order to be consistent with Eq. (C.3a), the functional dependences $\lambda_m^s = \lambda_m^s(\lambda_4)$ and $\lambda_m^h = \lambda_m^h(\lambda_4)$ are obtained from Eqs. (C.1) and the application of the chain-rule, via the inter-scale compatibility relationships:

$$\frac{d\lambda_m^s}{d\lambda_4} = \Phi_{ms}(\lambda_m^s, \lambda_m^h) \Phi_{fm}(\lambda_m^s, \lambda_m^h) \Phi_f(\lambda_4, H_F), \quad (\text{C.4a})$$

$$\frac{d\lambda_m^h}{d\lambda_4} = \Phi_{mh}(\lambda_m^s, \lambda_m^h) \Phi_{fm}(\lambda_m^s, \lambda_m^h) \Phi_f(\lambda_4, H_F). \quad (\text{C.4b})$$

Moreover, function $H_F = H_F(\lambda_4)$ is obtained from the solution of the geometric evolution equation:

$$\frac{dH_F}{d\lambda_4} = - \frac{\ell_F H_F [4(\ell_F^2 + H_F^2) - 3r_F^2]}{\lambda_4 [4H_F^2(\ell_F^2 + H_F^2) + 3\ell_F^2 r_F^2]}, \quad (\text{C.4c})$$

which gives the evolution of crimp amplitude upon fiber deformation and it is derived from a second application of the Principle of Virtual Works on a curvilinear beam model.

Bibliography

- [1] E. T. Thostenson, C. Li, and T.-W. Chou, Nanocomposites in context, *Composites Science and Technology* 65:491–516 (2005).
- [2] Y. Huang and A. Kinloch, Modelling of the toughening mechanisms in rubber-modified epoxy polymers, *Journal of materials science* 27:2753–2762 (1992).
- [3] J. Williams, Particle toughening of polymers by plastic void growth, *Composites Science and Technology* 70:885–891 (2010).
- [4] M. Quaresimin, M. Salviato, and M. Zappalorto, A multi-scale and multi-mechanism approach for the fracture toughness assessment of polymer nanocomposites, *Composites Science and Technology* 91:16–21 (2014).
- [5] A. A. Griffith, The phenomena of rupture and flow in solids, *Philosophical transactions of the royal society of london. Series A, containing papers of a mathematical or physical character* 221:163–198 (1921).
- [6] G. Irwin, Analysis of stresses and strains near the end of a crack traversing a plate, *J. Appl. Mech.* (1957).
- [7] T. L. Anderson, *Fracture mechanics: fundamentals and applications* (CRC press, 2005).
- [8] C. Miehe, F. Welschinger, and M. Hofacker, Thermodynamically consistent phase-field models of fracture: Variational principles and multi-field fe implementations, *International Journal for Numerical Methods in Engineering* 83:1273–1311 (2010).
- [9] C. Miehe, M. Hofacker, and F. Welschinger, A phase field model for rate-independent crack propagation: Robust algorithmic implementation based on operator splits, *Computer Methods in Applied Mechanics and Engineering* 199:2765–2778 (2010).

- [10] F. Amiri, D. Millán, Y. Shen, T. Rabczuk, and M. Arroyo, Phase-field modeling of fracture in linear thin shells, *Theoretical and Applied Fracture Mechanics* 69:102–109 (2014).
- [11] M. A. Msekh, J. M. Sargado, M. Jamshidian, P. M. Areias, and T. Rabczuk, Abaqus implementation of phase-field model for brittle fracture, *Computational Materials Science* 96:472–484 (2015).
- [12] S. Bordas, P. V. Nguyen, C. Dunant, A. Guidoum, and H. Nguyen-Dang, An extended finite element library, *International Journal for Numerical Methods in Engineering* 71:703–732 (2007).
- [13] N. Sukumar and J.-H. Prévost, Modeling quasi-static crack growth with the extended finite element method part i: Computer implementation, *International journal of solids and structures* 40:7513–7537 (2003).
- [14] S. Nanthakumar, T. Lahmer, and T. Rabczuk, Detection of flaws in piezoelectric structures using extended fem, *International Journal for Numerical Methods in Engineering* 96:373–389 (2013).
- [15] N. Sukumar, J. E. Dolbow, and N. Moës, Extended finite element method in computational fracture mechanics: a retrospective examination, *International Journal of Fracture* :1–18 (2015).
- [16] T. Rabczuk, G. Zi, A. Gerstenberger, and W. A. Wall, A new crack tip element for the phantom-node method with arbitrary cohesive cracks, *International Journal for Numerical Methods in Engineering* 75:577–599 (2008).
- [17] T. Chau-Dinh, G. Zi, P.-S. Lee, T. Rabczuk, and J.-H. Song, Phantom-node method for shell models with arbitrary cracks, *Computers & Structures* 92:242–256 (2012).
- [18] S. Haykin, *Neural Networks: A Comprehensive Foundation* (Prentice Hall PTR, 1999).
- [19] L. Fausett, *Fundamentals of neural networks: architectures, algorithms, and applications* (Prentice-Hall Englewood Cliffs, 1994).
- [20] M. Rafiq, G. Bugmann, and D. Easterbrook, Neural network design for engineering applications, *Computers & Structures* 79:1541–1552 (2001).
- [21] L. A. Zadeh, Fuzzy sets, *Information and control* 8:338–353 (1965).

BIBLIOGRAPHY

- [22] T. J. Ross, *Fuzzy logic with engineering applications* (John Wiley & Sons, 2010).
- [23] M. Monjezi and M. Rezaei, Developing a new fuzzy model to predict burden from rock geomechanical properties, *Expert Systems with Applications* 38:9266–9273 (2011).
- [24] T. Takagi and M. Sugeno, Fuzzy identification of systems and its applications to modeling and control, *Systems, Man and Cybernetics, IEEE Transactions on* 1:116–132 (1985).
- [25] J.-S. R. Jang, Anfis: adaptive-network-based fuzzy inference system, *Systems, Man and Cybernetics, IEEE Transactions on* 23:665–685 (1993).
- [26] S. C. Chapra and R. P. Canale, *Numerical Methods for Engineers* (McGraw-Hill Higher Education New York, 2010).
- [27] R. G. Ghanem and P. D. Spanos, *Stochastic finite elements: a spectral approach* (Springer-Verlag New York, Inc., 1991).
- [28] D. Xiu and G. E. Karniadakis, The wiener–askey polynomial chaos for stochastic differential equations, *SIAM journal on scientific computing* 24:619–644 (2002).
- [29] A. Saltelli, M. Ratto, T. Andres, F. Campolongo, J. Cariboni, D. Gatelli, M. Saisana, and S. Tarantola, *Global sensitivity analysis. The primer* (John Wiley & Sons, 2008).
- [30] R. L. Iman and W. Conover, A distribution-free approach to inducing rank correlation among input variables, *Communications in Statistics-Simulation and Computation* 11:311–334 (1982).
- [31] I. M. Sobol’, On sensitivity estimation for nonlinear mathematical models, *Matematicheskoe Modelirovanie* 2:112–118 (1990).
- [32] A. Saltelli, Making best use of model evaluations to compute sensitivity indices, *Computer Physics Communications* 145:280–297 (2002).
- [33] B. Sudret, Global sensitivity analysis using polynomial chaos expansions, *Reliability Engineering & System Safety* 93:964–979 (2008).
- [34] T. Crestaux, O. Le Maitre, and J.-M. Martinez, Polynomial chaos expansion for sensitivity analysis, *Reliability Engineering & System Safety* 94:1161–1172 (2009).
- [35] R. Cukier, H. Levine, and K. Shuler, Nonlinear sensitivity analysis of multipara-

- meter model systems, *Journal of computational physics* 26:1–42 (1978).
- [36] A. Saltelli, S. Tarantola, and K.-S. Chan, A quantitative model-independent method for global sensitivity analysis of model output, *Technometrics* 41:39–56 (1999).
- [37] F. Pianosi and T. Wagener, A simple and efficient method for global sensitivity analysis based on cumulative distribution functions, *Environmental Modelling & Software* 67:1–11 (2015).
- [38] S. M. Ross, *Introduction to probability and statistics for engineers and scientists* (Academic Press, 2009).
- [39] G. M. Hornberger and R. Spear, An approach to the preliminary analysis of environmental systems, *Journal of Environmental Management* 12:7–18 (1981).
- [40] A. Saltelli, S. Tarantola, F. Campolongo, and M. Ratto, *Sensitivity analysis in practice: a guide to assessing scientific models* (John Wiley & Sons, 2004).
- [41] B. Fisher, M. Ireland, D. Boyland, and S. Critten, Why use one model? an approach for encompassing model uncertainty and improving best practice, *Environmental Modeling & Assessment* 7:291–299 (2002).
- [42] T. Most, Assessment of structural simulation models by estimating uncertainties due to model selection and model simplification, *Computers & Structures* 89:1664–1672 (2011).
- [43] H. Keitel, A. Dimmig-Osburg, L. Vandewalle, and L. Schueremans, Selecting creep models using bayesian methods, *Materials and structures* 45:1513–1533 (2012).
- [44] K. Farrell and J. T. Oden, Calibration and validation of coarse-grained models of atomic systems: application to semiconductor manufacturing, *Computational Mechanics* 54:3–19 (2014).
- [45] E. Prudencio, P. Bauman, D. Faghihi, K. Ravi-Chandar, and J. Oden, A computational framework for dynamic data-driven material damage control, based on bayesian inference and model selection, *International Journal for Numerical Methods in Engineering* 102:379–403 (2015).
- [46] D. J. MacKay, Bayesian interpolation, *Neural computation* 4:415–447 (1992).
- [47] J. T. Oden and S. Prudhomme, Control of modeling error in calibration and validation processes for predictive stochastic models, *International Journal for*

BIBLIOGRAPHY

- Numerical Methods in Engineering 87:262–272 (2011).
- [48] J. L. Beck and K.-V. Yuen, Model selection using response measurements: Bayesian probabilistic approach, *Journal of Engineering Mechanics* (2004).
- [49] C. Chen, R. S. Justice, D. W. Schaefer, and J. W. Baur, Highly dispersed nanosilica–epoxy resins with enhanced mechanical properties, *Polymer* 49:3805–3815 (2008).
- [50] G. Ragosta, M. Abbate, P. Musto, G. Scarinzi, and L. Mascia, Epoxy-silica particulate nanocomposites: chemical interactions, reinforcement and fracture toughness, *Polymer* 46:10506–10516 (2005).
- [51] T. Hsieh, A. Kinloch, K. Masania, J. S. Lee, A. Taylor, and S. Sprenger, The toughness of epoxy polymers and fibre composites modified with rubber microparticles and silica nanoparticles, *Journal of materials science* 45:1193–1210 (2010).
- [52] M. Zamanian, M. Mortezaei, B. Salehnia, and J. Jam, Fracture toughness of epoxy polymer modified with nanosilica particles: Particle size effect, *Engineering Fracture Mechanics* 97:193–206 (2013).
- [53] B. Johnsen, A. Kinloch, R. Mohammed, A. Taylor, and S. Sprenger, Toughening mechanisms of nanoparticle-modified epoxy polymers, *Polymer* 48:530–541 (2007).
- [54] T. Hsieh, A. Kinloch, K. Masania, A. Taylor, and S. Sprenger, The mechanisms and mechanics of the toughening of epoxy polymers modified with silica nanoparticles, *Polymer* 51:6284–6294 (2010).
- [55] H.-Y. Liu, G.-T. Wang, Y.-W. Mai, and Y. Zeng, On fracture toughness of nanoparticle modified epoxy, *Composites Part B: Engineering* 42:2170–2175 (2011).
- [56] Y. Liang and R. Pearson, Toughening mechanisms in epoxy–silica nanocomposites (ESNs), *Polymer* 50:4895–4905 (2009).
- [57] P. Dittanet and R. A. Pearson, Effect of silica nanoparticle size on toughening mechanisms of filled epoxy, *Polymer* 53:1890–1905 (2012).
- [58] P. Dittanet and R. A. Pearson, Effect of bimodal particle size distributions on the toughening mechanisms in silica nanoparticle filled epoxy resin, *Polymer* 54:1832–1845 (2013).
- [59] H. Zhang, Z. Zhang, K. Friedrich, and C. Eger, Property improvements of in

- situ epoxy nanocomposites with reduced interparticle distance at high nanosilica content, *Acta Materialia* 54:1833–1842 (2006).
- [60] B. Wetzel, P. Rosso, F. Hauptert, and K. Friedrich, Epoxy nanocomposites–fracture and toughening mechanisms, *Engineering fracture mechanics* 73:2375–2398 (2006).
- [61] S. Deng, L. Ye, and K. Friedrich, Fracture behaviours of epoxy nanocomposites with nano-silica at low and elevated temperatures, *Journal of materials science* 42:2766–2774 (2007).
- [62] H. Zhang, L.-C. Tang, Z. Zhang, K. Friedrich, and S. Sprenger, Fracture behaviours of in situ silica nanoparticle-filled epoxy at different temperatures, *Polymer* 49:3816–3825 (2008).
- [63] J. Ma, M.-S. Mo, X.-S. Du, P. Rosso, K. Friedrich, and H.-C. Kuan, Effect of inorganic nanoparticles on mechanical property, fracture toughness and toughening mechanism of two epoxy systems, *Polymer* 49:3510–3523 (2008).
- [64] S. Zhao, L. S. Schadler, H. Hillborg, and T. Auletta, Improvements and mechanisms of fracture and fatigue properties of well-dispersed alumina/epoxy nanocomposites, *Composites Science and Technology* 68:2976–2982 (2008).
- [65] M. Zappalorto, A. Pontefisso, A. Fabrizi, and M. Quaresimin, Mechanical behaviour of epoxy/silica nanocomposites: Experiments and modelling, *Composites Part A: Applied Science and Manufacturing* 72:58–64 (2015).
- [66] K. Zuo, B. Blackman, J. Williams, and H. Steininger, The mechanical behaviour of ZnO nano-particle modified styrene acrylonitrile copolymers, *Composites Science and Technology* 113:9–18 (2015).
- [67] H. Fazilat, M. Ghatarband, S. Mazinani, Z. Asadi, M. Shiri, and M. Kalaei, Predicting the mechanical properties of glass fiber reinforced polymers via artificial neural network and adaptive neuro-fuzzy inference system, *Computational Materials Science* 58:31–37 (2012).
- [68] A. H. Mesbahi, D. Semnani, and S. N. Khorasani, Performance prediction of a specific wear rate in epoxy nanocomposites with various composition content of polytetrafluoroethylen (PTFE), graphite, short carbon fibers (CF) and nanotio 2 using adaptive neuro-fuzzy inference system (ANFIS), *Composites Part B: Engineering* 43:549–558 (2012).

BIBLIOGRAPHY

- [69] K. Wang, L. Chen, J. Wu, M. L. Toh, C. He, and A. F. Yee, Epoxy nanocomposites with highly exfoliated clay: mechanical properties and fracture mechanisms, *Macromolecules* 38:788–800 (2005).
- [70] J.-k. Chen, Z.-p. Huang, and J. Zhu, Size effect of particles on the damage dissipation in nanocomposites, *Composites Science and Technology* 67:2990–2996 (2007).
- [71] B. Lauke, On the effect of particle size on fracture toughness of polymer composites, *Composites Science and Technology* 68:3365–3372 (2008).
- [72] J. Williams, B. Blackman, H. Steininger, and K. Zuo, Toughening by plastic cavitation around cylindrical particles and fibres, *Composites Science and Technology* 103:119–126 (2014).
- [73] M. Zappalorto, M. Salviato, and M. Quaresimin, Influence of the interphase zone on the nanoparticle debonding stress, *Composites Science and Technology* 72:49–55 (2011).
- [74] M. Zappalorto, M. Salviato, and M. Quaresimin, A multiscale model to describe nanocomposite fracture toughness enhancement by the plastic yielding of nanovoids, *Composites Science and Technology* 72:1683–1691 (2012).
- [75] M. Salviato, M. Zappalorto, and M. Quaresimin, Plastic shear bands and fracture toughness improvements of nanoparticle filled polymers: a multiscale analytical model, *Composites Part A: Applied Science and Manufacturing* 48:144–152 (2013).
- [76] G. Scocchi, P. Posocco, A. Danani, S. Priel, and M. Fermeglia, To the nanoscale, and beyond!: multiscale molecular modeling of polymer-clay nanocomposites, *Fluid Phase Equilibria* 261:366–374 (2007).
- [77] B. Mortazavi, J. Bardon, and S. Ahzi, Interphase effect on the elastic and thermal conductivity response of polymer nanocomposite materials: 3d finite element study, *Computational Materials Science* 69:100–106 (2013).
- [78] R. Qiao and L. C. Brinson, Simulation of interphase percolation and gradients in polymer nanocomposites, *Composites Science and Technology* 69:491–499 (2009).
- [79] G. Odegard, T. Clancy, and T. Gates, Modeling of the mechanical properties of nanoparticle/polymer composites, *Polymer* 46:553–562 (2005).
- [80] S. Yu, S. Yang, and M. Cho, Multi-scale modeling of cross-linked epoxy nanocom-

- posites, *Polymer* 50:945–952 (2009).
- [81] J.-L. Tsai, S.-H. Tzeng, and Y.-T. Chiu, Characterizing elastic properties of carbon nanotubes/polyimide nanocomposites using multi-scale simulation, *Composites Part B: Engineering* 41:106–115 (2010).
- [82] Y. Chen, J. Chia, Z. Su, T. Tay, and V. Tan, Mechanical characterization of interfaces in epoxy-clay nanocomposites by molecular simulations, *Polymer* 54:766–773 (2013).
- [83] N. Sheng, M. C. Boyce, D. M. Parks, G. Rutledge, J. Abes, and R. Cohen, Multiscale micromechanical modeling of polymer/clay nanocomposites and the effective clay particle, *Polymer* 45:487–506 (2004).
- [84] M. Fermeglia and S. Pricl, Multiscale modeling for polymer systems of industrial interest, *Progress in Organic Coatings* 58:187–199 (2007).
- [85] K. Hbaieb, Q. Wang, Y. Chia, and B. Cotterell, Modelling stiffness of polymer/clay nanocomposites, *Polymer* 48:901–909 (2007).
- [86] K. Tserpes, P. Papanikos, G. Labeas, and S. G. Pantelakis, Multi-scale modeling of tensile behavior of carbon nanotube-reinforced composites, *Theoretical and Applied Fracture Mechanics* 49:51–60 (2008).
- [87] M. M. Shokrieh and R. Rafiee, Stochastic multi-scale modeling of CNT/polymer composites, *Computational Materials Science* 50:437–446 (2010).
- [88] K. Tserpes and A. Chanteli, Parametric numerical evaluation of the effective elastic properties of carbon nanotube-reinforced polymers, *Composite Structures* 99:366–374 (2013).
- [89] M. A. Bhuiyan, R. V. Pucha, J. Worthy, M. Karevan, and K. Kalaitzidou, Understanding the effect of cnt characteristics on the tensile modulus of cnt reinforced polypropylene using finite element analysis, *Computational Materials Science* 79:368–376 (2013).
- [90] S. Boutaleb, F. Zaïri, A. Mesbah, M. Naït-Abdelaziz, J.-M. Gloaguen, T. Boukharouba, and J.-M. Lefebvre, Micromechanics-based modelling of stiffness and yield stress for silica/polymer nanocomposites, *International Journal of Solids and Structures* 46:1716–1726 (2009).
- [91] A. Pontefisso, M. Zappalorto, and M. Quaresimin, An efficient RVE formulation for

BIBLIOGRAPHY

- the analysis of the elastic properties of spherical nanoparticle reinforced polymers, *Computational Materials Science* 96:319–326 (2015).
- [92] N. Vu-Bac, T. Lahmer, H. Keitel, J. Zhao, X. Zhuang, and T. Rabczuk, Stochastic predictions of bulk properties of amorphous polyethylene based on molecular dynamics simulations, *Mechanics of Materials* 68:70–84 (2014).
- [93] N. Vu-Bac, T. Lahmer, Y. Zhang, X. Zhuang, and T. Rabczuk, Stochastic predictions of interfacial characteristic of polymeric nanocomposites (PNCs), *Composites Part B: Engineering* 59:80–95 (2014).
- [94] N. Vu-Bac, R. Rafiee, X. Zhuang, T. Lahmer, and T. Rabczuk, Uncertainty quantification for multiscale modeling of polymer nanocomposites with correlated parameters, *Composites Part B: Engineering* 68:446–464 (2015).
- [95] M. Silani, H. Talebi, S. Ziaei-Rad, P. Kerfriden, S. P. Bordas, and T. Rabczuk, Stochastic modelling of clay/epoxy nanocomposites, *Composite Structures* 118:241–249 (2014).
- [96] N. Vu-Bac, M. Silani, T. Lahmer, X. Zhuang, and T. Rabczuk, A unified framework for stochastic predictions of mechanical properties of polymeric nanocomposites, *Computational Materials Science* 96:520–535 (2015).
- [97] A. Almasi, M. Silani, H. Talebi, and T. Rabczuk, Stochastic analysis of the interphase effects on the mechanical properties of clay/epoxy nanocomposites, *Composite Structures* 133:1302–1312 (2015).
- [98] T. Belytschko and T. Black, Elastic crack growth in finite elements with minimal remeshing, *International journal for numerical methods in engineering* 45:601–620 (1999).
- [99] N. Moës, J. Dolbow, and T. Belytschko, A finite element method for crack growth without remeshing, *International Journal for Numerical Methods in Engineering* 46:131–150 (1999).
- [100] N. Moës and T. Belytschko, Extended finite element method for cohesive crack growth, *Engineering fracture mechanics* 69:813–833 (2002).
- [101] T. Strouboulis, I. Babuška, and K. Copps, The design and analysis of the generalized finite element method, *Computer methods in applied mechanics and engineering* 181:43–69 (2000).

- [102] T. Strouboulis, K. Copps, and I. Babuska, The generalized finite element method: an example of its implementation and illustration of its performance, *International Journal for Numerical Methods in Engineering* 47:1401–1417 (2000).
- [103] C. Duarte, O. Hamzeh, T. Liszka, and W. Tworzydło, A generalized finite element method for the simulation of three-dimensional dynamic crack propagation, *Computer Methods in Applied Mechanics and Engineering* 190:2227–2262 (2001).
- [104] T. Belytschko, Y. Y. Lu, and L. Gu, Element-free galerkin methods, *International journal for numerical methods in engineering* 37:229–256 (1994).
- [105] T. Belytschko, Y. Lu, L. Gu, and M. Tabbara, Element-free galerkin methods for static and dynamic fracture, *International Journal of Solids and Structures* 32:2547–2570 (1995).
- [106] W. K. Liu, S. Jun, and Y. F. Zhang, Reproducing kernel particle methods, *International journal for numerical methods in fluids* 20:1081–1106 (1995).
- [107] W.-K. Liu, S. Li, and T. Belytschko, Moving least-square reproducing kernel methods (i) methodology and convergence, *Computer methods in applied mechanics and engineering* 143:113–154 (1997).
- [108] X. Zhuang, C. Augarde, and K. Mathisen, Fracture modeling using meshless methods and level sets in 3D: framework and modeling, *International Journal for Numerical Methods in Engineering* 92:969–998 (2012).
- [109] X. Zhuang, Y. Cai, and C. Augarde, A meshless sub-region radial point interpolation method for accurate calculation of crack tip fields, *Theoretical and Applied Fracture Mechanics* 69:118–125 (2014).
- [110] T. Belytschko and M. Fleming, Smoothing, enrichment and contact in the element-free galerkin method, *Computers & Structures* 71:173–195 (1999).
- [111] T. Rabczuk and T. Belytschko, Cracking particles: a simplified meshfree method for arbitrary evolving cracks, *International Journal for Numerical Methods in Engineering* 61:2316–2343 (2004).
- [112] T. Rabczuk and G. Zi, A meshfree method based on the local partition of unity for cohesive cracks, *Computational Mechanics* 39:743–760 (2007).
- [113] J.-H. Song, P. M. Areias, and T. Belytschko, A method for dynamic crack and shear band propagation with phantom nodes, *International Journal for Numerical*

BIBLIOGRAPHY

- Methods in Engineering 67:868–893 (2006).
- [114] N. Vu-Bac, H. Nguyen-Xuan, L. Chen, C.-K. Lee, G. Zi, X. Zhuang, G. R. Liu, and T. Rabczuk, A phantom-node method with edge-based strain smoothing for linear elastic fracture mechanics, *Journal of Applied Mathematics* 2013 (2013).
- [115] Y. Cai, X. Zhuang, and H. Zhu, A generalized and efficient method for finite cover generation in the numerical manifold method, *International Journal of Computational Methods* 10:1350028 (2013).
- [116] D. Benson, Y. Bazilevs, E. DeLuycker, M.-C. Hsu, M. Scott, T. Hughes, and T. Belytschko, A generalized finite element formulation for arbitrary basis functions: from isogeometric analysis to XFEM, *International Journal for Numerical Methods in Engineering* 83:765–785 (2010).
- [117] S. S. Ghorashi, N. Valizadeh, S. Mohammadi, and T. Rabczuk, T-spline based XIGA for fracture analysis of orthotropic media, *Computers & Structures* 147:138–146 (2015).
- [118] N. Nguyen-Thanh *et al.*, An extended isogeometric thin shell analysis based on kirchhoff-love theory, *Computer Methods in Applied Mechanics and Engineering* 284:265–291 (2015).
- [119] P. Areias and T. Rabczuk, Finite strain fracture of plates and shells with configurational forces and edge rotations, *International Journal for Numerical Methods in Engineering* 94:1099–1122 (2013).
- [120] P. Areias, T. Rabczuk, and D. Dias-da Costa, Element-wise fracture algorithm based on rotation of edges, *Engineering Fracture Mechanics* 110:113–137 (2013).
- [121] C. Miehe and E. Gürses, A robust algorithm for configurational-force-driven brittle crack propagation with r-adaptive mesh alignment, *International Journal for Numerical Methods in Engineering* 72:127–155 (2007).
- [122] R. De Borst and H.-B. Mühlhaus, Gradient-dependent plasticity: Formulation and algorithmic aspects, *International Journal for Numerical Methods in Engineering* 35:521–539 (1992).
- [123] S. Hosseini, J. J. Remmers, and R. Borst, The incorporation of gradient damage models in shell elements, *International Journal for Numerical Methods in Engineering* 98:391–398 (2014).

- [124] Z. P. Bazant and G. Pijaudier-Cabot, Nonlocal continuum damage, localization instability and convergence, *Journal of applied mechanics* 55:287–293 (1988).
- [125] M. J. Borden, T. J. Hughes, C. M. Landis, and C. V. Verhoosel, A higher-order phase-field model for brittle fracture: Formulation and analysis within the isogeometric analysis framework, *Computer Methods in Applied Mechanics and Engineering* 273:100–118 (2014).
- [126] D. Schillinger, M. J. Borden, and H. K. Stolarski, Isogeometric collocation for phase-field fracture models, *Computer Methods in Applied Mechanics and Engineering* 284:583–610 (2015).
- [127] J. Vignollet, S. May, R. de Borst, and C. V. Verhoosel, Phase-field models for brittle and cohesive fracture, *Meccanica* :1–15 (2014).
- [128] C. Miehe, L. Schänzel, and H. Ulmer, Phase field modeling of fracture in multi-physics problems. part I. balance of crack surface and failure criteria for brittle crack propagation in thermo-elastic solids, *Computer Methods in Applied Mechanics and Engineering* (2014).
- [129] C. Miehe, M. Hofacker, L. Schänzel, and F. Aldakheel, Phase field modeling of fracture in multi-physics problems. part II. coupled brittle-to-ductile failure criteria and crack propagation in thermo-elastic–plastic solids, *Computer Methods in Applied Mechanics and Engineering* (2014).
- [130] M. Silani, S. Ziaei-Rad, M. Esfahanian, and V. Tan, On the experimental and numerical investigation of clay/epoxy nanocomposites, *Composite Structures* 94:3142–3148 (2012).
- [131] J. Zhao, J.-W. Jiang, Y. Jia, W. Guo, and T. Rabczuk, A theoretical analysis of cohesive energy between carbon nanotubes, graphene and substrates, *Carbon* 57:108–119 (2013).
- [132] B. Arash, H. S. Park, and T. Rabczuk, Tensile fracture behavior of short carbon nanotube reinforced polymer composites: A coarse-grained model, *Composite Structures* 134:981–988 (2015).
- [133] B. Arash, H. S. Park, and T. Rabczuk, Coarse-grained model of the J-integral of carbon nanotube reinforced polymer composites, *Carbon* 96:1084–1092 (2016).
- [134] M. A. Msekh, M. Silani, M. Jamshidian, P. Areias, X. Zhuang, G. Zi, P. He,

BIBLIOGRAPHY

- and T. Rabczuk, Predictions of J integral and tensile strength of clay/epoxy nanocomposites material using phase field model, *Composites Part B: Engineering* (2016).
- [135] G. Blatman and B. Sudret, An adaptive algorithm to build up sparse polynomial chaos expansions for stochastic finite element analysis, *Probabilistic Engineering Mechanics* 25:183–197 (2010).
- [136] G. Blatman and B. Sudret, Efficient computation of global sensitivity indices using sparse polynomial chaos expansions, *Reliability Engineering & System Safety* 95:1216–1229 (2010).
- [137] J. Wall, Practical statistics for astronomers-ii. correlation, data-modelling and sample comparison, *Quarterly Journal of the Royal Astronomical Society* 37:519–563 (1996).
- [138] Y. Huang and A. Kinloch, Modelling of the toughening mechanisms in rubber-modified epoxy polymers. part i finite element analysis studies, *Journal of materials science* 27:2753–2762 (1992).
- [139] J. Lee and A. Yee, Inorganic particle toughening i: micro-mechanical deformations in the fracture of glass bead filled epoxies, *Polymer* 42:577–588 (2001).
- [140] A. Argon and R. Cohen, Toughenability of polymers, *Polymer* 44:6013–6032 (2003).
- [141] A. Kinloch, R. Mohammed, A. Taylor, C. Eger, S. Sprenger, and D. Egan, The effect of silica nano particles and rubber particles on the toughness of multiphase thermosetting epoxy polymers, *Journal of Materials Science* 40:5083–5086 (2005).
- [142] A. D5045-99, *Standard test methods for plane-strain fracture toughness and strain energy release rate of plastic materials* (ASTM International, West Conshohocken, 2014).
- [143] M. H. Beale, M. T. Hagan, and H. B. Demuth, *Neural network toolbox user's guide* (The MathWorks, Inc, 2014).
- [144] *Fuzzy logic toolbox user's guide* (The MathWorks, Inc, 2014).
- [145] M. Sarıdemir, İ. B. Topçu, F. Özcan, and M. H. Severcan, Prediction of long-term effects of ggbs on compressive strength of concrete by artificial neural networks and fuzzy logic, *Construction and Building Materials* 23:1279–1286 (2009).

- [146] B. Mortazavi, F. Hassouna, A. Laachachi, A. Rajabpour, S. Ahzi, D. Chapron, V. Toniazzi, and D. Ruch, Experimental and multiscale modeling of thermal conductivity and elastic properties of pla/expanded graphite polymer nanocomposites, *Thermochimica Acta* 552:106–113 (2013).
- [147] B. Mortazavi, O. Benzerara, H. Meyer, J. Bardon, and S. Ahzi, Combined molecular dynamics-finite element multiscale modeling of thermal conduction in graphene epoxy nanocomposites, *Carbon* 60:356–365 (2013).
- [148] R. Peng, H. Zhou, H. Wang, and L. Mishnaevsky, Modeling of nano-reinforced polymer composites: Microstructure effect on young's modulus, *Computational Materials Science* 60:19–31 (2012).
- [149] H. Ghasemi, R. Brighenti, X. Zhuang, J. Muthu, and T. Rabczuk, Optimal fiber content and distribution in fiber-reinforced solids using a reliability and nurbs based sequential optimization approach, *Structural and Multidisciplinary Optimization* 51:99–112 (2015).
- [150] H. Ghasemi, R. Rafiee, X. Zhuang, J. Muthu, and T. Rabczuk, Uncertainties propagation in metamodel-based probabilistic optimization of cnt/polymer composite structure using stochastic multi-scale modeling, *Computational Materials Science* 85:295–305 (2014).
- [151] C. Zilg, R. Mülhaupt, and J. Finter, Morphology and toughness/stiffness balance of nanocomposites based upon anhydride-cured epoxy resins and layered silicates, *Macromolecular Chemistry and Physics* 200:661–670 (1999).
- [152] A. S. Zerda and A. J. Lesser, Intercalated clay nanocomposites: morphology, mechanics, and fracture behavior, *Journal of Polymer Science Part B: Polymer Physics* 39:1137–1146 (2001).
- [153] M.-W. Ho, C.-K. Lam, K.-t. Lau, D. H. Ng, and D. Hui, Mechanical properties of epoxy-based composites using nanoclays, *Composite structures* 75:415–421 (2006).
- [154] S. Zunjarrao, R. Sriraman, and R. Singh, Effect of processing parameters and clay volume fraction on the mechanical properties of epoxy-clay nanocomposites, *Journal of materials science* 41:2219–2228 (2006).
- [155] B. Chen and J. R. Evans, Elastic moduli of clay platelets, *Scripta materialia* 54:1581–1585 (2006).

BIBLIOGRAPHY

- [156] K. M. Hamdia, T. Lahmer, T. Nguyen-Thoi, and T. Rabczuk, Predicting the fracture toughness of pncs: A stochastic approach based on ANN and ANFIS, *Computational Materials Science* 102:304–313 (2015).
- [157] R. L. Iman and J. C. Helton, An investigation of uncertainty and sensitivity analysis techniques for computer models, *Risk analysis* 8:71–90 (1988).
- [158] F. Campolongo and A. Saltelli, Sensitivity analysis of an environmental model: an application of different analysis methods, *Reliability Engineering & System Safety* 57:49–69 (1997).
- [159] J. Yang, Convergence and uncertainty analyses in monte-carlo based sensitivity analysis, *Environmental Modelling & Software* 26:444–457 (2011).
- [160] B. Efron and R. J. Tibshirani, *An introduction to the bootstrap* (Chapman & Hall, 1993).
- [161] G. Archer, A. Saltelli, and I. Sobol, Sensitivity measures, anova-like techniques and the use of bootstrap, *Journal of Statistical Computation and Simulation* 58:99–120 (1997).
- [162] F. Gan and K. Koehler, Goodness-of-fit tests based on p-p probability plots, *Technometrics* 32:289–303 (1990).
- [163] F. Pianosi, F. Sarrazin, and T. Wagener, A matlab toolbox for global sensitivity analysis, *Environmental Modelling & Software* 70:80–85 (2015).
- [164] M. Albdiry, B. Yousif, H. Ku, and K. Lau, A critical review on the manufacturing processes in relation to the properties of nanoclay/polymer composites, *Journal of Composite Materials* 47:1093–1115 (2013).
- [165] Bray, DJ and Dittanet, P and Guild, FJ and Kinloch, AJ and Masania, K and Pearson, RA and Taylor, AC, The modelling of the toughening of epoxy polymers via silica nanoparticles: The effects of volume fraction and particle size, *Polymer* 54:7022–7032 (2013).
- [166] K. M. Hamdia, M. A. Msekh, M. Silani, N. Vu-Bac, X. Zhuang, T. Nguyen-Thoi, and T. Rabczuk, Uncertainty quantification of the fracture properties of polymeric nanocomposites based on phase field modeling, *Composite Structures* 133:1177–1190 (2015).
- [167] J. Berriot, F. Lequeux, L. Monnerie, H. Montes, D. Long, and P. Sotta, Filler–

- elastomer interaction in model filled rubbers, a 1 h nmr study, *Journal of Non-Crystalline Solids* 307:719–724 (2002).
- [168] J. Berriot, F. Martin, H. Montes, L. Monnerie, and P. Sotta, Reinforcement of model filled elastomers: characterization of the cross-linking density at the filler–elastomer interface by 1 h nmr measurements, *Polymer* 44:1437–1447 (2003).
- [169] A. Bansal, H. Yang, C. Li, K. Cho, B. C. Benicewicz, S. K. Kumar, and L. S. Schadler, Quantitative equivalence between polymer nanocomposites and thin polymer films, *Nature materials* 4:693–698 (2005).
- [170] S. Watcharotone, C. D. Wood, R. Friedrich, X. Chen, R. Qiao, K. Putz, and L. C. Brinson, Interfacial and substrate effects on local elastic properties of polymers using coupled experiments and modeling of nanoindentation, *Advanced Engineering Materials* 13:400–404 (2011).
- [171] A. Pontefisso, M. Zappalorto, and M. Quaresimin, Influence of interphase and filler distribution on the elastic properties of nanoparticle filled polymers, *Mechanics Research Communications* 52:92–94 (2013).
- [172] H. Wang, H. Zhou, R. Peng, and L. Mishnaevsky, Nanoreinforced polymer composites: 3D FEM modeling with effective interface concept, *Composites Science and Technology* 71:980–988 (2011).
- [173] O. Garcia-Cabrejo and A. Valocchi, Global sensitivity analysis for multivariate output using polynomial chaos expansion, *Reliability Engineering & System Safety* 126:25–36 (2014).
- [174] A. Hansbo and P. Hansbo, A finite element method for the simulation of strong and weak discontinuities in solid mechanics, *Computer methods in applied mechanics and engineering* 193:3523–3540 (2004).
- [175] P. Areias and T. Rabczuk, Quasi-static crack propagation in plane and plate structures using set-valued traction-separation laws, *International journal for numerical methods in engineering* 74:475–505 (2008).
- [176] T.-T. Le, J. Guilleminot, and C. Soize, Stochastic continuum modeling of random interphases from atomistic simulations. application to a polymer nanocomposite, *Computer Methods in Applied Mechanics and Engineering* 303:430–449 (2016).
- [177] Y. Li, A. M. Waas, and E. M. Arruda, A closed-form, hierarchical, multi-interphase

BIBLIOGRAPHY

- model for composites-Derivation, verification and application to nanocomposites, *Journal of the Mechanics and Physics of Solids* 59:43–63 (2011).
- [178] F. Bondioli, V. Cannillo, E. Fabbri, and M. Messori, Epoxy-silica nanocomposites: Preparation, experimental characterization, and modeling, *Journal of applied polymer science* 97:2382–2386 (2005).
- [179] Z. Dominkovics, J. Hári, J. Kovács, E. Fekete, and B. Pukánszky, Estimation of interphase thickness and properties in pp/layered silicate nanocomposites, *European Polymer Journal* 47:1765–1774 (2011).
- [180] D. Xiu and G. E. Karniadakis, Modeling uncertainty in flow simulations via generalized polynomial chaos, *Journal of computational physics* 187:137–167 (2003).
- [181] H. G. Matthies and A. Keese, Galerkin methods for linear and nonlinear elliptic stochastic partial differential equations, *Computer Methods in Applied Mechanics and Engineering* 194:1295–1331 (2005).
- [182] S.-K. Choi, R. V. Grandhi, R. A. Canfield, and C. L. Pettit, Polynomial chaos expansion with latin hypercube sampling for estimating response variability, *AIAA journal* 42:1191–1198 (2004).
- [183] M. Berveiller, B. Sudret, and M. Lemaire, Stochastic finite element: a non intrusive approach by regression, *European Journal of Computational Mechanics/Revue Européenne de Mécanique Numérique* 15:81–92 (2006).
- [184] S. S. Isukapalli, *Uncertainty analysis of transport-transformation models*, PhD thesis, The State University of New Jersey, 1999.
- [185] S. Huang, S. Mahadevan, and R. Rebba, Collocation-based stochastic finite element analysis for random field problems, *Probabilistic Engineering Mechanics* 22:194–205 (2007).
- [186] K. M. Hamdia, X. Zhuang, P. He, and T. Rabczuk, Fracture toughness of polymeric particle nanocomposites: Evaluation of models performance using bayesian method, *Composites Science and Technology* 126:122–129 (2016).
- [187] J. Guillemot and C. Soize, On the statistical dependence for the components of random elasticity tensors exhibiting material symmetry properties, *Journal of elasticity* 111:109–130 (2013).
- [188] M. Grigoriu, Probabilistic models for stochastic elliptic partial differential equati-

- ons, *Journal of Computational Physics* 229:8406–8429 (2010).
- [189] P. Fratzl, *Collagen: structure and mechanics* (Springer Science & Business Media, 2008).
- [190] J. A. Niestrawska, C. Viertler, P. Regitnig, T. U. Cohnert, G. Sommer, and G. A. Holzapfel, Microstructure and mechanics of healthy and aneurysmatic abdominal aortas: experimental analysis and modelling, *Journal of The Royal Society Interface* 13 (2016).
- [191] A. M. Robertson, X. Duan, K. M. Aziz, M. R. Hill, S. C. Watkins, and J. R. Cebal, Diversity in the strength and structure of unruptured cerebral aneurysms, *Annals of biomedical engineering* 43:1502–1515 (2015).
- [192] M. Carmo, L. Colombo, A. Bruno, F. Corsi, L. Roncoroni, M. Cuttin, F. Radice, E. Mussini, and P. Settembrini, Alteration of elastin, collagen and their cross-links in abdominal aortic aneurysms, *European journal of vascular and endovascular surgery* 23:543–549 (2002).
- [193] A. Brüel, G. Ørtoft, and H. Oxlund, Inhibition of cross-links in collagen is associated with reduced stiffness of the aorta in young rats, *Atherosclerosis* 140:135–145 (1998).
- [194] P. Panwar, G. Lamour, N. C. Mackenzie, H. Yang, F. Ko, H. Li, and D. Brömme, Changes in structural-mechanical properties and degradability of collagen during aging-associated modifications, *Journal of Biological Chemistry* 290:23291–23306 (2015).
- [195] O. Andriotis, S. Chang, M. Vanleene, P. Howarth, D. Davies, S. Shefelbine, M. Buehler, and P. Thurner, Structure–mechanics relationships of collagen fibrils in the osteogenesis imperfecta mouse model, *Journal of The Royal Society Interface* 12:20150701 (2015).
- [196] G. A. Holzapfel, T. C. Gasser, and R. W. Ogden, A new constitutive framework for arterial wall mechanics and a comparative study of material models, *Journal of elasticity and the physical science of solids* 61:1–48 (2000).
- [197] J. Schröder and P. Neff, Invariant formulation of hyperelastic transverse isotropy based on polyconvex free energy functions, *International journal of solids and structures* 40:401–445 (2003).

BIBLIOGRAPHY

- [198] T. C. Gasser, R. W. Ogden, and G. A. Holzapfel, Hyperelastic modelling of arterial layers with distributed collagen fibre orientations, *Journal of the royal society interface* 3:15–35 (2006).
- [199] F. Maceri, M. Marino, and G. Vairo, Age-dependent arterial mechanics via a multiscale elastic approach, *International Journal for Computational Methods in Engineering Science and Mechanics* 14:141–151 (2013).
- [200] M. Marino and G. Vairo, Computational modeling of soft tissues and ligaments. In: Jin Z, editor, *Computational Modeling of Biomechanics and Biotribology in the Musculoskeletal System* 81:141–172 (2014).
- [201] D. Bianchi, M. Marino, and G. Vairo, An integrated computational approach for aortic mechanics including geometric, histological and chemico-physical data, *Journal of biomechanics* 49:2331–2340 (2016).
- [202] M. Marino and P. Wriggers, Finite strain response of crimped fibers under uniaxial traction: An analytical approach applied to collagen, *Journal of the Mechanics and Physics of Solids* 98:429–453 (2017).
- [203] Y. Lanir, A structural theory for the homogeneous biaxial stress-strain relationships in flat collagenous tissues, *Journal of biomechanics* 12:423–436 (1979).
- [204] K. M. Hamdia, M. Silani, X. Zhuang, P. He, and T. Rabczuk, Stochastic analysis of the fracture toughness of polymeric nanoparticle composites using polynomial chaos expansions, *International Journal of Fracture* 206:215–227 (2017).
- [205] K. A. Hansen, J. A. Weiss, and J. K. Barton, Recruitment of tendon crimp with applied tensile strain, *Journal of Biomechanical Engineering* 124:72–77 (2002).

Ehrenwörtliche Erklärung

Ich erkläre hiermit ehrenwörtlich, dass ich die vorliegende Arbeit ohne unzulässige Hilfe Dritter und ohne Benutzung anderer als der angegebenen Hilfsmittel angefertigt habe. Die aus anderen Quellen direkt oder indirekt übernommenen Daten und Konzepte sind unter Angabe der Quelle gekennzeichnet.

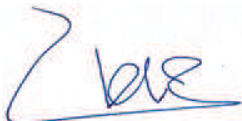
Weitere Personen waren an der inhaltlich-materiellen Erstellung der vorliegenden Arbeit nicht beteiligt. Insbesondere habe ich hierfür nicht die entgeltliche Hilfe von Vermittlungs-bzw. Beratungsdiensten (Promotionsberater oder anderer Personen) in Anspruch genommen. Niemand hat von mir unmittelbar oder mittelbar geldwerte Leistungen für Arbeiten erhalten, die im Zusammenhang mit dem Inhalt der vorgelegten Dissertation stehen.

Die Arbeit wurde bisher weder im In- noch im Ausland in gleicher oder ähnlicher Form einer anderen Prüfungsbehörde vorgelegt.

Ich versichere ehrenwörtlich, dass ich nach bestem Wissen die reine Wahrheit gesagt und nichts verschwiegen habe.

Weimar, 13 June 2017

Khader Hamdia



Curriculum Vitae

Khader M. Hamdia

Institute of Structural Mechanics

Bauhaus-Universität Weimar

Email: khader.hamdia@uni-weimar.de

Date of Birth: 26.03.1981

Place of Birth: Gaza, Palestine

Education

- Ph.D student: Institute of Structural Mechanics, Bauhaus-Universität Weimar, Germany, 2013-present.
- M.Sc: Master in Civil Engineering, The Islamic University of Gaza; Gaza, Palestine, 2010
- B.Sc: Bachelor in Civil Engineering, The Islamic University of Gaza; Gaza, Palestine, 2004

Publications

Doctoral phase

1. K. M. Hamdia, M. Silani, X. Zhuang, P. He, and T. Rabczuk, Stochastic analysis of the fracture toughness of polymeric nanoparticle composites using polynomial chaos expansions, *International Journal of Fracture* (2017).
2. K. M. Hamdia, X. Zhuang, P. He, and T. Rabczuk, Fracture toughness of polymeric particle nanocomposites: Evaluation of models performance using Bayesian method, *Composites Science and Technology* 126:122-129 (2016).

3. K. M. Hamdia, M. A. Msekh, M. Silani, N. Vu-Bac, X. Zhuang, T. Nguyen-Thoi, and T. Rabczuk, Uncertainty quantification of the fracture properties of polymeric nanocomposites based on phase field modeling, *Composite Structures* 133:1177-1190 (2015).
4. K. M. Hamdia, T. Lahmer, T. Nguyen-Thoi, and T. Rabczuk, Predicting the fracture toughness of PNCs: A stochastic approach based on ANN and ANFIS, *Computational Materials Science* 102:304-313 (2015).
5. K. M. Hamdia, H. Ghasemi, X. Zhuang, N. Alajla, and T. Rabczuk. Sensitivity and uncertainty analysis for flexoelectric nanostructures, *Computer Methods in Applied Mechanics and Engineering*, 337:95-109(2018).

Master phase

6. K. M. Hamdia, M Arafa, and M Alqedra, Structural damage assessment criteria for reinforced concrete buildings by using a Fuzzy Analytic Hierarchy Process, *Underground Space* (2018).
7. K. M. Hamdia, M. Arafa, M. Alqedra, Criteria weighting system for assessment of RC buildings using fuzzy analytic hierarchy process, *Journal of Al Azhar University Engineering Sector* , JAUES , ISSN 1110- 6409, Dec 2010.
8. K. M. Hamdia, M. Arafa, M. Alqedra, Fuzzy based structural assessment criteria for reinforced concrete buildings in Gaza Strip, *Proceedings of the third International Conference on Engineering and Gaza Reconstruction at Islamic University Gaza-Palestine*, October 2010.
9. K. M. Hamdia, Methods for seismic retrofit of historic unreinforced masonry buildings, *Proceedings of the second International Conference on Architectural conservation at Islamic University Gaza-Palestine*, April 2010